

**Faculty of Science and Engineering**

**Natural Gas Processing for Removal of Sour Gases and their  
Storage for Production of LNG and its gasification**

**Firas Nayyef Hasan Alnili**

**This Thesis is presented for the Degree of**

**Doctor of Philosophy**

**Of**

**Curtin University**

**March 2020**

## Declaration

To the best of my knowledge and belief this thesis contains no material previously published by any other person except where due acknowledgment has been made.

This thesis contains no material which has been accepted for the award of any other degree or diploma in any university.

Signature:

Date: **04 Jan 2021**

## Copyright

I acknowledged that I have obtained the approval from the copyright owners to use any of my published work such as journal and conference papers for this thesis where the ownership is held by Elsevier and CSIRO Publishing. The permission to utilise the published material by the author has been stated in the copyright link below:

<https://www.elsevier.com/about/our-business/policies/copyright#Author-rights>

<https://s100.copyright.com/CustomAdmin/PLF.jsp?ref=8005a8c9-7b07-427e-b123-7e8a928f1772>

<https://s100.copyright.com/AppDispatchServlet#formTop>

Signature:

Date: **04 Jan 2021**

## Author's Biography

Firas Nayyef Hasan Alnili completed his Bachelor's degree in Chemical Engineering (Hons) from University of Baghdad in Iraq in 2005. He also completed his Master's degree in Chemical Engineering from the same University (Baghdad) in 2008. He worked as a lecturer at Al-Muthanna University in Iraq from 2008 to 2014. In December 2014, he commenced his PhD research in natural gas processing at Curtin University. He received a scholarship from the Ministry of Higher and Scientific Research of Iraq and Al-Muthanna University, Iraq to pursue his postgraduate study.

Journal publications (published):

Alnili, F. and Barifceni, A., 2018. Efficient separation scheme for binary mixture of CO<sub>2</sub> and H<sub>2</sub>S using aromatic components. *Separation Science and Technology*, 53(2), pp.312-319.

Alnili, F. and Barifceni, A., 2018. Simulation study of sweetening and dehydration of natural gas stream using MEG solution. *The Canadian Journal of Chemical Engineering*, 96(9), pp.2000-2006.

Alnili, F., James, P. and Barifceni, A., 2019. Natural gas sweetening using low temperature distillation: simulation and configuration. *Separation Science and Technology*, pp.1-8.

Alnili, F., Al-Yaseri, A., Roshan, H., Rahman, T., Verall, M., Lebedev, M., Sarmadivaleh, M., Iglauer, S. and Barifceni, A., 2018. Carbon dioxide/brine wettability of porous sandstone versus solid quartz: An experimental and theoretical investigation. *Journal of colloid and interface science*, 524, pp.188-194.



## Manuscripts

1. Firas Alnili, Biao Sun, Ahmed Barifcani, Vishnu Pareek, *Pilot plant of new design of Ambient Air Vaporizer (AAV): Design and construction*. To be submitted to another journal.
2. Biao Sun, Firas Alnili, Ahmed Barifcani, Vishnu Pareek, *Experimental Study of a Cryogenic Ambient Air Vaporizer*. To be submitted to another journal.

# Dedication

*To my wife Noor and my boys Mohammed, Adam and Noah for their  
greatest support and patience.*

*I would like to dedicate my thesis to my Parent for their encouragement  
and help*

## **Abstract**

Natural gas is currently an important and popular fossil fuel and will likely continue to be in the future. In addition, natural gas can be considered as a source of hydrocarbons for petrochemical industries. Despite the fact that natural gas is mostly considered a “clean” fuel compared to other fossil fuels, the natural gas found in reservoir deposits is not necessarily “clean” and free of impurities. Natural gas consists primarily of methane, but it also contains considerable amounts of light and heavier hydrocarbons as well as contaminating compounds of CO<sub>2</sub>, N<sub>2</sub>, H<sub>2</sub>S, and other impurities. These impurities are undesirable compounds and cause several technical problems such as corrosion and environment pollution. However, many natural gas streams in different areas contain huge quantities of H<sub>2</sub>S and CO<sub>2</sub>.

This thesis discusses many aspects of natural gas processing namely sour gases separation, CO<sub>2</sub> sequestration for EOR, and natural gas regasification after liquefaction.

Many natural gas streams in different areas contain huge quantities of H<sub>2</sub>S and CO<sub>2</sub>. Many technologies can be used to purify natural gas from acid gases. These technologies include amine absorption, the adsorption process, cryogenic processes, and membranes. In this thesis, two technologies of sour gases removal processes have been simulated using HYSYS and the results have been extensively discussed. On the other hand, increases in CO<sub>2</sub> emissions represent a formidable problem given the increases in energy demand and high levels of industry-dependent fossil fuel consumption. Various strategies such as the capture and storage of CO<sub>2</sub> in geological formations can be adopted to minimise the CO<sub>2</sub> emissions into the atmosphere. For this purpose, an experimental study of effect the porosity in real rock in underground reservoir on CO<sub>2</sub> injection has been conducted to examine the suitability of a particular reservoir in WA for CO<sub>2</sub> reinjection by studying the wettability properties of CO<sub>2</sub>/brine/Sandstone. Finally, an innovative finned vaporizer with invasive defrosting method has been tested experimentally in a pilot-scale forced-draft AAV unit through vaporizing liquid nitrogen (LN<sub>2</sub>) at certain operating pressures. Different operating conditions, including operating capacity, natural/forced convections and air relative humidity, have been tested in the system. Defrosting was performed by using a hot MEG-water solution cycle.

## Table of Contents

|  |    |
|--|----|
| 1. Chapter one. Introduction to the Research .....       | 1  |
| 1.1. Background .....                                    | 1  |
| 1.2. Aims and Objectives of the Research.....            | 3  |
| 1.3. Significance of the Research .....                  | 3  |
| 1.4. Thesis Chapter Outline .....                        | 4  |
| 2. Chapter two: Literature review .....                  | 7  |
| 2.1. Natural gas processing and sour gases removal ..... | 7  |
| 2.1.1. An Overview .....                                 | 7  |
| 2.1.2. Natural gas processing .....                      | 9  |
| 2.1.3. Gas sweetening processes .....                    | 12 |
| 2.1.3.2. Amine Processes.....                            | 14 |
| 2.1.4. Ryan Holmes Process.....                          | 22 |
| 2.2. Natural gas Liquefaction .....                      | 36 |
| 2.2.1. Natural gas pre-treatment.....                    | 37 |
| 2.2.2. Cold box .....                                    | 37 |
| 2.2.3. Fractionation .....                               | 39 |
| 2.2.4. Liquefaction .....                                | 40 |
| 2.2.5. Storage .....                                     | 40 |
| 2.2.6. Loading and transportation .....                  | 40 |
| 2.3. LNG regasification .....                            | 42 |
| 2.3.1. Open Rack Vaporizer (ORV).....                    | 42 |
| 2.3.2. Submerged Combustion Vaporizers (SCV).....        | 44 |
| 2.3.3. Intermediate Fluid Vaporizer .....                | 45 |
| 2.3.4. Ambient Air Vaporizer .....                       | 48 |

|        |   |    |
|--------|---|----|
| 2.4.   | CO <sub>2</sub> Reinjection for storage and EOR purposes.....   | 49 |
| 2.4.1. | WETTABILITY AND CONTACT ANGLE DETERMINATION ....  | 51 |
| 2.4.2. | Effect of temperature on contact angle .....  | 52 |
| 2.4.3. | Effect of pressure on contact angle .....   | 53 |
| 2.4.4. | Effect of pressure and temperature on interfacial tension.....  | 53 |
| 2.4.5. | Effect of CO <sub>2</sub> injection on permeability .....   | 53 |
| 3.     | Chapter 3: Efficient separation scheme for binary mixture of CO <sub>2</sub> and H <sub>2</sub> S using aromatic components ..... | 55 |
| 3.1.   | Introduction .....  | 55 |
| 3.1.1. | Process description.....  | 57 |
| 3.2.   | Numerical implementation .....  | 60 |
| 3.2.1. | Selection of equation of state .....  | 60 |
| 3.2.2. | Algorithm and basic equation used for simulation .....  | 61 |
| 3.3.   | Process Performance .....   | 62 |
| 3.4.   | Result and discussion .....   | 64 |
| 3.4.1. | Solvents Quantity .....   | 64 |
| 3.4.2. | Relative Volatility .....   | 64 |
| 3.4.3. | Energy Consumption.....   | 68 |
| 3.4.4. | Effect of Solvents on Phase Diagram.....  | 68 |
| 3.4.5. | CO <sub>2</sub> and H <sub>2</sub> S Purities and Recoveries.....   | 70 |
| 3.5.   | Conclusions .....   | 72 |
| 4.     | Chapter 4: Natural Gas Sweetening Using low temperature Distillation: Simulation and Configuration.....                           | 73 |
| 4.1.   | Introduction .....  | 73 |
| 4.2.   | Process description .....   | 75 |
| 4.3.   | Simulation & methodology .....  | 78 |

|        |  |     |
|--------|--|-----|
| 4.4.   | Results and discussion.....  | 81  |
| 4.4.1. | CO <sub>2</sub> freezing inhibition .....  | 81  |
| 4.4.2. | H <sub>2</sub> S removal and column duty .....   | 82  |
| 4.4.3. | CO <sub>2</sub> Recovery and column .....  | 85  |
| 4.4.4. | Effect of the feed stream CO <sub>2</sub> composition on the energy requirements<br>86   |     |
| 4.5.   | Conclusions and further work .....   | 87  |
| 5.     | Chapter 5: Simulation Study of Sweetening and Dehydration of Natural Gas<br>Stream Using MEG Solution .....                                | 89  |
| 5.1.   | Introduction .....   | 89  |
| 5.2.   | Process description .....  | 90  |
| 5.3.   | Numerical implementation .....   | 92  |
| 5.3.1. | Algorithm and basic equation used for simulation .....   | 92  |
| 5.3.2. | Selection of equation of state .....   | 95  |
| 5.4.   | Steady state simulation and optimization .....   | 95  |
| 5.4.1. | Process performance .....  | 96  |
| 5.5.   | Results and discussion.....  | 97  |
| 5.5.1. | H <sub>2</sub> S Removal.....  | 100 |
| 5.5.2. | CO <sub>2</sub> Removal .....  | 100 |
| 5.5.3. | Water content .....  | 101 |
| 5.5.4. | Hydrate formation analysis .....   | 102 |
| 5.6.   | Conclusions .....  | 104 |
| 6.     | Chapter 6: Carbon dioxide/brine wettability of porous sandstone versus solid<br>quartz: An experimental and theoretical investigation..... | 105 |
| 6.1.   | Introduction .....   | 105 |
| 6.2.   | Experimental methodology .....   | 106 |

|            |   |     |
|------------|---|-----|
| 6.3.       | Results .....   | 110 |
| 6.4.       | Discussion .....  | 114 |
| 6.5.       | Conclusions .....   | 120 |
| 7.         | Chapter 7: Experimental Study of a Cryogenic Ambient Air Vaporizer..... | 121 |
| 7.1.       | Introduction .....  | 121 |
| 7.2.       | Flow scheme and control system.....                                     | 124 |
| 7.3.       | Operating data analysis (Commissioning operation) .....                 | 130 |
| 7.3.1.     | Design modifications .....  | 135 |
| 7.4.       | Operating data analysis (Normal operation).....                         | 138 |
| 7.4.1.     | Liquid nitrogen flow .....  | 139 |
| 7.4.2.     | Air flow .....  | 141 |
| 7.4.3.     | Temperature profile on fins.....  | 142 |
| 7.4.4.     | Defrosting process.....   | 143 |
| 7.5.       | Discussion .....  | 145 |
| 7.5.1.     | Overall heat transfer coefficient.....                                  | 145 |
| 7.5.2.     | Air humidification.....   | 147 |
| 7.5.3.     | Frost formation.....  | 150 |
| 7.6.       | Conclusions .....   | 151 |
| 8.         | Chapter 8: Conclusions and recommendations .....                        | 152 |
| 8.1.       | Conclusions .....   | 152 |
| 8.2.       | Recommendations .....   | 153 |
| 9.         | References .....  | 154 |
| Appendix 1 | :Statement of Contributions of Others.....                              | 163 |
| Appendix 2 | :Equipment used in LNG vaporization (Chapter 7) .....                   | 168 |

## List of Figures

|  |           |
|--|-----------|
| Figure 2-1. Natural gas sweetening Processes .....   | 13        |
| Figure 2-2 Amine Gas sweetening process .....  | 15        |
| Figure 2-3. Principal scheme of the Ryan-Holmes process for Natural Gas sweetening (Holmes&Ryan, 1982) .....   | 19        |
| Figure 2-4. Block diagram of CoolEnergy's technology.....  | 20        |
| Figure 2-5. CFZ Column & VLE data .....  | 21        |
| Figure 2-6. Carbon dioxide & Methane Phase Envelope.....   | 24        |
| <i>Figure 2-7. CO<sub>2</sub> Solubility Vs Temperature .....</i>  | <i>26</i> |
| Figure 2-8. Ryan-Holmes CO <sub>2</sub> Recovery Unit (Holmes and Ryan 1982b) .....  | 26        |
| Figure 2-9. CO <sub>2</sub> /Ethane Relative Volatilities Vs Temperature .....   | 27        |
| Figure 2-10. Process configuration proposed by Berstad (Berstad, Neksa, and Anantharaman 2012).....  | 29        |
| Figure 2-11. Part 1 of ZareNezhad process.....   | 31        |
| Figure 2-12. Part 2 of ZareNezhad process.....   | 32        |
| Figure 2-13. Process Configuration from Finn & O'Brien.....  | 33        |
| Figure 2-14. Conventional Ryan-Holmes Process Modelled by (Sun et al. 2015)....  | 35        |
| Figure 2-15. Natural gas pre-treatment diagram .....   | 38        |
| Figure 2-16. ConocoPhillips optimized cascade® process.....  | 39        |
| Figure 2-17. LNG transportation tank by Moss Maritime [42] .....   | 41        |
| Figure 2-18. Open rack Vaporizer flow scheme .....   | 44        |
| Figure 2-19. Submerged Combustion Vaporizer (SCV).....   | 45        |
| Figure 2-20. Glycol-water Intermediate Fluid Vaporizer Integration with Different Heat Sources Intermediate Fluid (Hydrocarbon) in Rankine Cycle ..... | 47        |
| Figure 3-1. Process flow diagram of CO <sub>2</sub> /H <sub>2</sub> S separation .....   | 58        |
| Figure 3-2. Effect of various CO <sub>2</sub> concentrations in mole% on solvent amount (%)  | 64        |



|   |    |
|---|----|
| Figure 3-3. Relative volatility of CO <sub>2</sub> to H <sub>2</sub> S for various EB concentrations.....                       | 66 |
| Figure 3-4. Relative volatility of CO <sub>2</sub> to H <sub>2</sub> S for various M-Xylene concentrations.                     | 66 |
| Figure 3-5. Relative volatility of CO <sub>2</sub> to H <sub>2</sub> S for various O-Xylene concentrations.                     | 67 |
| Figure 3-6. Relative volatility of CO <sub>2</sub> to H <sub>2</sub> S for various Toluene concentrations....                   | 67 |
| Figure 3-7. Amount of duty required for separation H <sub>2</sub> S from 90 mol% of CO <sub>2</sub> ....                        | 68 |
| Figure 3-8. Phase diagram of 90% CO <sub>2</sub> and 10% H <sub>2</sub> S .....   | 69 |
| Figure 3-9. Phase diagram of 90% CO <sub>2</sub> and 10% H <sub>2</sub> S in 20% solvent .....                                  | 69 |
| Figure 4-1. Process flow diagram .....  | 80 |
| Figure 4-2. T-100 tray temperatures. ....   | 81 |
| Figure 4-3. T-101 tray temperatures. ....   | 82 |
| Figure 4-4. Effect of the toluene flow rate on the reboiler and condenser duties.....   | 83 |
| Figure 4-5. Effect of the reflux ratio on the column duty. ....   | 84 |
| Figure 4-6. Effect of the toluene flow rate on the distillate H <sub>2</sub> S content. ....                                    | 84 |
| Figure 4-7. Effect of the n-butane flow rate on the distillate ethane Mole%.....  | 85 |
| Figure 4-8. Effect of the n-butane flow rate on the CO <sub>2</sub> purity.....   | 85 |
| Figure 4-9. Effect of the feed stream CO <sub>2</sub> content on the T-104 duty. ....   | 86 |
| Figure 4-10. Required n-butane flow rates for 5000 kgmole/hr of feed stream containing different CO <sub>2</sub> contents ..... | 87 |
| Figure 5-1. Acid gas removal process based on absorption in MEG solution.....   | 91 |
| Figure 5-2. Process flow diagram by HYSYS .....   | 92 |
| Figure 5-3. . MEG absorber menu .....   | 97 |
| Figure 5-4. MEG regenerator menu .....  | 97 |
| Figure 5-5. Effect of (80% MEG) circulation flowrate on sour gas mole% in the treated gas stream.....                           | 98 |
| Figure 5-6. Relationship between (80% MEG) rate and reboiler temperature. ....  | 99 |
| Figure 5-7. Relationship between MEG concentration and reboiler temperature. ....   | 99 |

|  |     |
|--|-----|
| Figure 5-8. The relationship between H <sub>2</sub> S (ppm) in the sweet gas stream and inlet MEG flow rate (m <sup>3</sup> /h) for various inlet MEG temperatures (°C).....   | 100 |
| Figure 5-9. Relationship between CO <sub>2</sub> concentration in the sweet gas stream as a function of MEG flow rate and temperature .....  | 101 |
| Figure 5-10. The relationship between H <sub>2</sub> O mole percent in sweet gas and MEG rate .....  | 102 |
| Figure 5-11. . HYSYS Hydrate Package Utility .....   | 103 |
| Figure 5-12. . Hydrate formation phase diagram .....   | 103 |
| Figure 6-1. Atomic force microscopy image of the sandstone surfaces investigated; different heights are coloured differently (black is 0 nm, white is 3500 nm).....  | 108 |
| Figure 6-2. SEM images of the sandstone samples; a and b are the raw images and c and d are the segmented images. Grey shows the grains, while blue shows the pores. ....  | 109 |
| Figure 6-3. Schematic diagram of the high temperature/high pressure contact angle measurement apparatus used for contact angle measurements. ....  | 110 |
| Figure 6-4. Advancing water contact angles for sandstone/CO <sub>2</sub> /DI water as a function of pressure and temperature; RMS = 540 nm, SD = 3 (where SD is the standard deviation). ....                                      | 112 |
| Figure 6-5. Receding contact angles for sandstone/CO <sub>2</sub> /DI water as a function of pressure and temperature; RMS = 540 nm, SD = 3. ....  | 113 |
| Figure 6-6. Advancing contact angles for sandstone/CO <sub>2</sub> /DI water and sandstone/CO <sub>2</sub> /brine (20 wt% CaCl <sub>2</sub> ) as a function of pressure at a temperature of 323 K; RMS = 540 nm, SD = 3.....       | 113 |
| Figure 6-7. Receding contact angles for sandstone/CO <sub>2</sub> /DI water and sandstone/CO <sub>2</sub> /brine water (20 wt% CaCl <sub>2</sub> ) as a function of pressure at a temperature of 323 K; RMS = 540 nm, SD = 3. .... | 114 |
| Figure 6-8. Forces acting on quartz (top) and sandstone (bottom). ....   | 118 |
| Figure 6-9. Water droplet on a sandstone sample in the presence of air under atmospheric conditions after exposure times of 2 min (top) and 4 min (bottom)....   | 119 |

|   |     |
|---|-----|
| Figure 6-10. Comparison of the equilibrium contact angles obtained through laboratory experiments, the Cassie–Baxter method, and the present method at a temperature of 323 K. .... | 119 |
| Figure 7-1 P&ID diagram of the pilot-scale experiment .....   | 124 |
| Figure 7-2. Flow scheme and schematic Diagram of finned tube design. ....   | 125 |
| Figure 7-3. Schematic Diagram of phase separator .....  | 127 |
| Figure 7-4. Thermocouple for measuring the LN2 temperature at AAV inlet. ....   | 127 |
| Figure 7-5. Distribution of thermocouples on vaporizer.....   | 129 |
| Figure 7-6. Site photo of the system of ambient air vaporizer.....  | 130 |
| Figure 7-7. AAV inlet and outlet temperature profile test #6.....   | 133 |
| Figure 7-8. Frost formation from test #6.....   | 133 |
| Figure 7-9. Fin average temperature .....   | 134 |
| Figure 7-10. Temperature Sensors and globe valve location.....  | 134 |
| Figure 7-11. Spray head for air humidification.....   | 135 |
| Figure 7-12. . Thermocouple of measuring LN2 inlet temperature .....  | 136 |
| Figure 7-13. . LN2 line insulation.....   | 137 |
| Figure 7-14. History of operating pressure and nitrogen flow rate of Test #7 .....  | 139 |
| Figure 7-15. Temperatures of nitrogen inlet and outlet. ....  | 140 |
| Figure 7-16. The temperatures and relative humidity of air flow in Test #7 & 8....  | 142 |
| Figure 7-17. The temperatures and relative humidity of air flow in Test #10. ....   | 142 |
| Figure 7-18. AAV Fin temperature profile in Test #6 and Test #10.....   | 143 |
| Figure 7-19. MEG flow rate and temperature change during defrosting process....   | 144 |
| Figure 7-20. Temperature change of fin surface and Nitrogen outlet during defrosting process.....   | 145 |
| Figure 7-21. Overall heat transfer coefficient changing with time in Test #7 .....  | 146 |
| Figure 7-22. Humidity ratio change of air flow with time.....   | 148 |
| Figure 7-23. Energy balance between nitrogen flow and air flow.....   | 149 |

|   |     |
|---|-----|
| Figure 7-24. Frost formation on the AAV in Test #6. ....            | 150 |
| Figure 7-25. Frost formation in Test #10 (a) and Test #12 (b). .... | 151 |

### **List of Tables**

|   |     |
|---|-----|
| Table 2-1. Pounds of air pollutants produces per billion Btu of energy [3].....   | 8   |
| Table 2-2. Typical Natural gas composition (mole %).....  | 9   |
| Table 2-3. Molar composition for Berstad feed stream. ....  | 28  |
| Table 2-4. Operating conditions and other specifics for the Berstad process operation<br>.....                          | 30  |
| Table 3-1. The operating parameters were applied in simulation process.....   | 59  |
| Table 3-2. Process Optimization Results .....   | 63  |
| Table 3-3. Purities, Recoveries of CO <sub>2</sub> , and H <sub>2</sub> S for various CO <sub>2</sub> concentrations .. | 71  |
| Table 4-1. Columns Conditions .....   | 77  |
| Table 4-2. Column compositions (mole%) .....  | 78  |
| Table 4-3. Feed stream details .....  | 79  |
| Table 5-1. Natural gas stream composition and associated flow rates. ....   | 90  |
| Table 5-2. Specifications for Base Case CO <sub>2</sub> removal.....  | 91  |
| Table 6-1. Chemical Purities.....   | 111 |
| Table 7-1. Details of instrumentation used in the AAV system .....  | 128 |
| Table 7-2 . Operating condition (Test #1-6). ....   | 132 |
| Table 7-3. Operating conditions in different tests (7-12).....  | 138 |
| Table 7-4. Operating conditions of defrosting in different tests .....  | 139 |
| Table 7-5. Overall heat transfer coefficient during LN <sub>2</sub> evaporation.....                                    | 147 |

## Nomenclature

### Chemical formulas

|                  |                                 |
|------------------|---------------------------------|
| C1               | Methane                         |
| C2               | Ethane                          |
| C3               | propane                         |
| C4               | butane                          |
| C4-C15           | Gasoline                        |
| C5 <sup>+</sup>  | pentane and heavier hydrocarbon |
| CO               | Carbon monoxide                 |
| CO <sub>2</sub>  | Carbon dioxide                  |
| H <sub>2</sub> O | Water                           |
| H <sub>2</sub> S | Hydrogen Sulfide                |
| SO <sub>2</sub>  | Sulphur dioxide                 |
| O <sub>2</sub>   | Oxygen                          |
| N <sub>2</sub>   | Nitrogen                        |
| NO <sub>2</sub>  | Nitrogen dioxide                |
| EB               | Ethylbenzene                    |
| O-Xylene         | Ortho Xylene                    |
| M-Xylene         | Meta Xylene                     |
| MEG              | Mono Ethylene Glycol            |
| DEG              | Di Ethylene Glycol              |
| TEG              | Tri Ethylene Glycol             |

### **Unit of measurements**

|                |                     |
|----------------|---------------------|
| mg             | microgram           |
| b              | bar                 |
| kg             | kilogram            |
| kJ             | Kilojoule           |
| kWh            | Kilowatt-hour       |
| L              | Litre               |
| lb             | Pound               |
| m <sup>3</sup> | Cubic meter         |
| °C             | Degree Celsius      |
| ppm            | part per million    |
| TCF            | Trillion Cubic Feet |

### **Symbols in equations**

|             |                                       |
|-------------|---------------------------------------|
| $g$         | Gas phase                             |
| $\ell$      | Liquid phase                          |
| $\theta_a$  | Advancing Contact Angle               |
| $\theta_r$  | Receding Contact Angle                |
| $\gamma$    | Interfacial Tension                   |
| $F$         | Total Free Energy                     |
| $\tilde{r}$ | Average Pore Radius                   |
| $\tilde{h}$ | Capillary Rise                        |
| $f_i$       | Fractional projected area of material |

### **Standard abbreviations**

|      |                              |
|------|------------------------------|
| EOS  | Equation of State            |
| PR   | Peng Robinson                |
| SRK  | Soave Redlich Kwong          |
| EOR  | Enhance Oil Recovery         |
| RV   | Relative Volatility          |
| AGRU | acid gas removal unit        |
| CNG  | Compressed natural gas       |
| DHU  | Dehydration Unit             |
| LNG  | Liquefied natural gas        |
| LPG  | Liquefied petroleum gas      |
| CGS  | Carbon Geo-Storage           |
| TOC  | Total Organic Content        |
| RMS  | Root Mean Square             |
| XRD  | X-ray diffraction            |
| AFM  | Atomic Force Microscope      |
| SEM  | Scanning Electron Microscopy |

# **1. Chapter one. Introduction to the Research**

## **1.1. Background**

The rapidly increasing in energy demands and to reduce the greenhouse gases (GHG) impact on the environment, researchers have put major efforts for a potential alternative energy source. As for the fundamental criteria of desirable energy alternatives, the capability of providing adequate quantity of energy with high quality, economic viability and environmental friendly are the major considerations. Renewable energy potential such as the solar energy and the wind energy are unable to meet the total global demand of energy at the present stage. They need long time to be further researched. Consequently, the only supply of energy that is able to fulfil the aforementioned requirements and to satisfy the total global demand of energy at the present stage is natural gas. In addition to its principal significance as a fuel, natural gas can also be the source of hydrocarbons for the petrochemical industries as raw material. Although natural gas is considered as a clean fossil fuel in comparison to other fossil fuels such as crude oil and coal, however, natural gas recovered from well heads normally contains corrosive and contaminant sour gases. These gases are commonly known as Carbon Dioxide (CO<sub>2</sub>) and Hydrogen Sulfide (H<sub>2</sub>S). The sour gases in the stream of natural gas cannot be only harmful to the environment, but could also reduce the heating value of natural gas products and must therefore be removed. Originally, sour gases treatment has been done by Claus process. Many sour gases removal methods have been previously addressed such as chemical absorption by amine, physical absorption and membrane treatment. All these conventional treatment methods are driven by many limitations and the energy consumption can be considered as the main challenge facing such techniques especially when the removed CO<sub>2</sub> needs further processing before undergoing sequestration. An alternative technique has been introduced in sour gases removal which is the low temperature distillation separation represented by Ryan Holmes process [1]. The extractive distillation process of Ryan Holmes emphasises on producing Methane and avoiding the CO<sub>2</sub> freezing simultaneously. In addition, Ryan Holmes process also addresses the Azeotropic nature of separation of a mixture of CO<sub>2</sub> and Ethane. When sour gases removal process is completed, further processes needs to be completed for both sweet and sour gases stream. For transportation and storage of natural gas purposes, sweet natural gas stream needs to be cooled down to -161 °C in a liquefaction process. Liquefaction processes is a process to transform



natural gas (NG) into a liquefied natural gas (LNG) to reduce the volume about 600 times making the resource easier to store and transport through marine shipments to the consuming natural gas countries. The major use for LNG today is for power generation resulting from the growing power demand especially in the Southeast Asian region. The imported LNG needs to be regasified through a vaporization process to transform LNG from liquid to gaseous state to produce natural gas to supply sale gas in pipelines for power plant generation. Numerous methods of regasification and the selection of the optimum process depends on many factors such as site location, climate conditions, and throughput capacities [2]. Traditionally, three types of vaporizers have been used in the regasification terminals, Open Rack Vaporizer (ORV), Submerged Combustion Vaporizer (SCV) and Intermediate Fluid Vaporizer (IFV). In addition to these vaporizers, other type of vaporizers represented by Direct Air Vaporizer and Ambient Air Vaporizer (AAV) have been recently used in small regasification terminals. The AAV can be considered as a low fuel consumption and a low operating cost terminals due to the low grade heat recovery from AAV to regasify LNG. In addition, AAV is environmentally friendly due to the lower air emissions resulting from reducing the fuel used to vaporize LNG [3].

The stream of sour gases that has been removed from the stream of natural gas needs to be treated before proceeding to further stages. Recently, CO<sub>2</sub> emission to the atmosphere has been classified as the main cause of climate change. These changes are continuously increasing due to increasing the energy demands. Geological storage of CO<sub>2</sub> (GCS), also known as carbon sequestration, is a crucial strategy to reduce the increasing CO<sub>2</sub> emission to the atmosphere [4]. CO<sub>2</sub> geological storage, is a process where CO<sub>2</sub> emitted from different sources such as power plants generation or CO<sub>2</sub> separated from streams of natural gas is separated from the other component (e.g. H<sub>2</sub>S) to meet the CO<sub>2</sub> sequestration standard, compressed, and finally reinjected underground. CO<sub>2</sub> can also be used for the enhanced oil recovery (EOR) to make the injection process more economical. The primary problem with geological carbon storage is that CO<sub>2</sub> density is lower than the formation brine and flows upward to the surface. However, many mechanisms can prevent CO<sub>2</sub> flowing upward and leaking to the surface. These mechanisms represented by structural trapping, residual trapping, dissolution trapping and minerals trapping (Al-Yaseri et al. 2016). The nature of reservoir storage also plays an important role in CO<sub>2</sub> injection underground to ensure the stored CO<sub>2</sub> remains in the reservoir. Wettability of the rock has a significant impact on the CO<sub>2</sub> trapping mechanism.

## **1.2. Aims and Objectives of the Research**

Three objectives were targeted in this research and as listed below:

1. Employing Ryan Holmes process for sour gas removed from a stream of natural gas and discover the economical and processing advantages as this process offers a clean and efficient separation method compared with many other conventional processes. In this concept, a simulation study was conducted to improve and reach the optimum conditions of sour gas separation using Ryan Holmes process as a base case, also adopting different process configurations and using different solvents to prevent CO<sub>2</sub> freezing and Azeotrope nature of CO<sub>2</sub>.
2. Removed CO<sub>2</sub> from such processes needs to be reinjected to the underground to control the environment emissions and address climate changes. Injection of CO<sub>2</sub> to the underground either for storage or to enhance oil recovery can be considered as an effective procedure to reduce CO<sub>2</sub> in the atmosphere. Conduct an experimental study of effect the porosity in the real rock in underground reservoir on CO<sub>2</sub> injection and examine the suitability of a particular reservoir in WA for CO<sub>2</sub> reinjection by studying the wettability properties of CO<sub>2</sub>/brine/Sandstone.
3. It has been noted that the worldwide consumption of LNG has increased significantly as a result of increasing the energy demands. LNG is considered as a clean fuel and it is an efficient alternative fuel source. LNG regasification is an essential procedure before it can be used as a sale gas or in power generation plants. In this part of the research, a pilot plant has been designed, constructed and operated in order to test the efficiency of a modified ambient air vaporizer located in Technology Park at Curtin University facilities and fully funded by Woodside Energy Company in Australia. The main big challenge of this pilot plant was to operate the vaporizer continuously and circulate the defrosting process during the LNG operation.

## **1.3. Significance of the Research**

Due to the numerous methods of natural gas treatment processes, choosing the process relies on many factors such as feed stock flowrate, compositions of sour gases, location, economic aspect and government regulations. These factors have a huge influence on selection of the process. These numerous methods have been well illustrated in the literature. However, when the feed stock contains high concentration of CO<sub>2</sub> and H<sub>2</sub>S (depending on the amount of sour gases in natural gas),

many challenges remain and difficulties appear. Recruitment of Ryan-Holmes process for removing different concentration of sour gases to produce a sweet natural gas stream is considered to be valuable for natural gas treatment development. In addition, adopting MEG instead of amine to remove sour gases from natural gas in a conventional absorption process and investigate the advantages of using MEG in terms of sour gases recovery, energy consumption and dehydration (H<sub>2</sub>O removal) of natural gas.

On the other hand, CO<sub>2</sub> produced from the natural gas treatment process needs to be reinjected to the underground as a safety procedure for environment protection purposes. Measuring the contact angle of Sandstone rock taken from a certain reservoir in Western Australia can help to predict the suitability of injection CO<sub>2</sub> in this reservoir. Experimental study of the effect of temperature, pressure, and salinity on the contact angle of CO<sub>2</sub>/ Brine has been discussed in this research.

Furthermore, vaporization is one of the most important processes in LNG terminal operation. Basically there are three main types of LNG vaporizers ORV, SCV, IFV and AAV (Ambient Air Vaporizer) has granted attention in the recent years and can be considered as a greenest technology in LNG regasification. In order to explore the feasibility of continuous operation of LNG regasification, a pilot plant of AAV with innovative continuous operation adopting a defrosting duct in the middle of the vaporizer has been designed, installed and operated.

#### **1.4. Thesis Chapter Outline**

This research consists of three topics as mentioned in research objectives. This thesis contains published and unpublished work.

The content of this thesis is presented in a hybrid format. **Chapters 3, 4, 5 and 6** contents are referred to journal articles that have been published in the *Journal of Separation Science and Technology*, *Canadian Journal of Chemical Engineering* and *Journal of Colloid and Interface Science* respectively. The presentation of the content is partially adjusted to be consistent with the research flow and thesis style

## **Chapter one:**

Introduction. This chapter provides a brief overview of the three topics including the significance and the objectives of this research.

## **Chapter two**

Literature review. This chapter presents the literature review of sour gas separation technology and emphasise on low temperature distillation separation, also presents an overview of liquefied natural gas (LNG) regasification techniques and presents the advantages and disadvantages for each process. Lastly, part of chapter two, presents an overview of the CO<sub>2</sub> sequestration and the effect the wettability on geological storage of CO<sub>2</sub>.

Chapter **Three** through to chapter **eight** detail the theoretical and the experimental work of the above three objectives.

## **Chapter Three**

"Efficient separation scheme for binary mixture of CO<sub>2</sub> and H<sub>2</sub>S using aromatic components." *Separation Science and Technology* 53, no. 2 (2018): 312-319.

This chapter consists an efficient separation scheme for binary mixture of CO<sub>2</sub> and H<sub>2</sub>S using aromatic components. Different solvents (ethylbenzene, o-xylene, m-xylene, and toluene) and operating conditions (temperature, pressure, and reflux ratio) for separating CO<sub>2</sub> from H<sub>2</sub>S at different concentrations have been simulated through distillation using Aspen HYSYS software.

**This Chapter is an exact copy of the journal paper referred to above.**

## **Chapter Four**

"Natural gas sweetening using low temperature distillation: simulation and configuration." *Separation Science and Technology* 55, no. 8 (2020): 1569-1576.

In chapter 4, a theoretical simulation results of sour gas removal from stream of natural gas using low temperature distillation is optimized.

**This Chapter is an exact copy of the journal paper referred to above.**

## **Chapter Five**

"Simulation study of sweetening and dehydration of natural gas stream using MEG solution." *The Canadian Journal of Chemical Engineering* 96, no. 9 (2018): 2000-2006.

This chapter contains the results of simulation of the gas sweetening process by using the Aspen HYSYS V.7.3 program. Moreover, in this simulation work, MEG (Mono Ethylene Glycol) was selected as an absorbent for the gas sweetening process: it achieved high acid gas removal and reduced the water content from a stream of natural gas.

**This Chapter is an exact copy of the journal paper referred to above.**

### **Chapter Six**

"Carbon dioxide/brine wettability of porous sandstone versus solid quartz: An experimental and theoretical investigation." *Journal of colloid and interface science* 524 (2018): 188-194.

Chapter 6 discusses an experimental study of wettability of CO<sub>2</sub>/Brine in Sandstone rock to explore the suitability of injection the CO<sub>2</sub> produces from the natural gas treatment process in a certain reservoir in Western Australia.

**This Chapter is an exact copy of the journal paper referred to above.**

### **Chapter Seven**

In Chapter 7, an innovative ambient air vaporizer of a pilot scale was designed, constructed and operated at Curtin University by applying an intrusive defrosting process which could remove frost effectively and ensure a continuous regasification process. Results of a pilot plant of AAV (Ambient Air Vaporizer) have been discussed.

### **Chapter Eight:**

Conclusions and recommendations. This chapter concludes the overall findings based on the results presented from Chapters 3 to 7. Further, recommendations for future studies have been proposed based on the new knowledge gaps found.

## **2. Chapter two: Literature review**

### **2.1. Natural gas processing and sour gases removal**

#### **2.1.1. An Overview**

Natural gas needs have been growing over the past two decades due to the rapidly increase in demand of industrial and domestic utilization. Natural gas is the most efficient and cleanest fossil fuel due to low atoms ratio of H/C. In addition, natural gas cannot be used only as a primary fuel but also as a source of hydrocarbons for petrochemical and industrial chemicals [5]. As a fuel, natural gas is expected to rapidly grow due to the ability of providing a sustainable energy needed for industry development and reducing the greenhouse gas emission. Increasing Carbone Dioxide emission produced from combustion of fossil fuel such as coal and petroleum products have encouraged researchers to develop a clean and sustainable fuel that has less impact on the environment. Thus natural gas can be considered as an alternative source of fuel which meets the requirements of residential, industrial and transportation specifications. Table 1 shows the Carbone Dioxide produced from coal and petroleum product which is higher than the amount produced from natural gas by 1.5-1.8 times [5]. Natural gas can be found in large volume in crude oil wells either onshore or offshore as an associated gas, gas wells or condensate gas. Natural gas mainly contains more than 70% of Methane in addition to other hydrocarbons such as Ethane, Propane, Butane and heavy hydrocarbon (C5-C10). However, natural gas doesn't come in a pure form of hydrocarbon, it also consists various contaminants such as water, Nitrogen, Mercury, Helium, and sour gas such as Carbone Dioxide and Hydrogen Sulfide. CO<sub>2</sub> is considered as a major greenhouse gas that cause emission and lower the efficiency of transportation, production and storage of natural gas [5, 6]. Over the world, natural gas composition substantially varies based on the location where it has been taken. Table 2 shows some typical gas compositions. Once natural gas has been extracted from the well it is transported through a pipeline to a processing facility where the contaminants are removed in multiple purification processes to produce LNG, sales gas, natural gas liquids and other products. The inlet stream of natural gas from the well is a combination of both the gaseous and liquid phases. Various equipment such as a slug catchers, high pressure separators and a compressors are involved in the processing of the inlet stream. The slug catcher is found to ascertain the liquid slurry is removed and the gas stream then compressed via compressors and directed for further treatment [6].

Table 2-1. Pounds of air pollutants produced per billion Btu of energy [3].

Source: Energy Information Administration (1998)

| Contaminant     | Natural gas* | Coal**  | Crude oil*** |
|-----------------|--------------|---------|--------------|
| Carbon Dioxide  | 17,000       | 164,000 | 208,000      |
| Carbon Monoxide | 40           | 33      | 208          |
| Nitrogen Oxides | 92           | 448     | 457          |
| Sulfur Oxide    | 0.6          | 1122    | 2591         |
| particulates    | 7.0          | 84      | 2477         |
| Formaldehyde    | 0.75         | 0.22    | 0.221        |
| Mercury         | 0.00         | 0.0007  | 0.016        |

\* Natural gas burned in uncontrolled residential gas burners.

\*\* Oil is # 6 fuel oil at 6.287 million Btu per barrel and 1.03% sulfur with postcombustion removal of pollutants.

\*\*\* Bituminous coal at 12,027 Btu per pound and 1.64% sulfur with no postcombustion removal of pollutants.

Table 2-2. Typical Natural gas composition (mole %)

Source: U.S. Bureau of Mines (1972) and Jones et al. (1999).

|                     | Canada | Western Colorado | Southern Kansas | Vietnam | Tunisia | New Mexico | Texas |
|---------------------|--------|------------------|-----------------|---------|---------|------------|-------|
| Helium              | 0.0    | 0.0              | 0.45            | 0.0     | 0.0     | 0.0        | 1.8   |
| Nitrogen            | 3.2    | 26.10            | 14.65           | 0.21    | 16.903  | 0.68       | 25.6  |
| Carbon Dioxide      | 1.7    | 42.66            | 0.0             | 0.06    | 13.588  | 0.82       | 0.0   |
| Hydrogen Sulfide    | 3.3    | 0.0              | 0.0             | 0.0     | 0.092   | 0.0        | 0.0   |
| Methane             | 77.1   | 29.98            | 72.89           | 70.85   | 63.901  | 96.91      | 65.8  |
| Ethane              | 6.6    | 0.55             | 6.27            | 13.41   | 3.349   | 1.33       | 3.8   |
| Propane             | 3.1    | 0.28             | 3.74            | 7.5     | 0.960   | 0.19       | 1.7   |
| Butane              | 2.0    | 0.21             | 1.38            | 4.02    | 0.544   | 0.05       | 0.8   |
| Pentane and heavier | 3.0    | 0.25             | 0.62            | 2.64    | 0.630   | 0.02       | 0.5   |

### 2.1.2. Natural gas processing

Natural gas is used as a fuel or as a petrochemical feedstock. Therefore, there are three basic reasons for processing raw natural gas which are listed below:

1. Purification and/or removal of materials, valuable or not, that inhibit the use of the gas as an industrial or residential fuel.
2. Separation the components that have greater value as petrochemical feedstocks, stand alone fuels (e.g., propane), or industrial gases (e.g., ethane, helium).
3. Liquefaction. Decreasing the gas volume for storage or transportation.



Based on the situation, process may be classified as a purification, separation or liquefaction. For instant, removing small amount of H<sub>2</sub>S or venting to the atmosphere, this is purification process. But if a large amount of H<sub>2</sub>S is removed and then converted to a sulfur element then the process is separation.

#### **2.1.2.1. Mercury removal**

Presence of mercury in natural gas can cause two major problems: corrosion of aluminium and environment pollution. Mercury has to be removed from natural gas to prevent corrosion in aluminium equipment and avoid downstream poisoning [7]. The removal process for mercury from natural gas can be classified into two processes: **Non-regenerative and Regenerative** processes. From a health perspective, mercury can cause a serious damage to the brain and kidneys. Disposal of the residue must be in a sanitary lined landfill. Existing thermal treatment processes can treat up to 150 tonnes of waste per day with over 99.9% recovery of elemental mercury at an estimated cost of \$125 to \$225 per ton of material, such as mercury scavenger catalyst or contaminated soil [5, 7].

#### **2.1.2.2. Acid gas sweetening and removal of contaminant**

Natural gas usually consists of large amounts of acid gases such as CO<sub>2</sub> and H<sub>2</sub>S. In addition to acid gases, natural gas may contain other contaminants such as carbonyl sulphide (COS), Mercaptans (R-SH) and carbon disulfide (CS<sub>2</sub>). Acid gases can cause an extensive damage to natural gas pipelines and equipment if not properly removed. The combustion of sulfur compounds produce serious air pollutants and eventually produces acid rain when combined with water. In addition, these sulfur compounds are corrosive to metals and equipment that handle and transport natural gas. Furthermore, Carbon Dioxide is non-flammable gas and large quantities are undesirable in natural gas [6]. Therefore, removing sour gases is a major concern in natural gas processing. Specifications for the allowable concentrations of CO<sub>2</sub> and H<sub>2</sub>S is usually specified by regulators influenced by safety and product values. A number of methods of acid gas removal from stream of natural gas have been explored and many are commercially performed daily. These processes include chemical absorption, physical absorption, adsorption, cryogenic distillation and membrane technology among others. The chemical absorption processes consist of amine contacting through the use of chemical reagents, MEA, DGA, DEA, MDEA and other amine mixtures [5]. Adsorption is a physical-chemical phenomenon in which the gas is concentrated on the surface of a solid to remove impurities. Selecting sweetening process is subjected to many factors such as the concentration of

sour gases in the natural gas, the allowable acid gases in the final products, economic factors and many other factors. Figure 1 describes the more important processes in natural gas sweetening.

### **2.1.2.3. Dehydration**

Natural gas usually has water content in a liquid or vapour phase from the source or as a result of sweetening process using chemical solvent (Amine Solution). Removing water content from stream of natural gas is necessary for many reasons:

1. Water can combine with natural gas to form solid gas hydrate that causes plugging in pipeline and valve fittings.
2. Water may condense in the pipeline causing erosion, corrosion and slug flow.
3. Water vapour causes decrease natural gas heating value.
4. Water can cause a serious damage in liquefaction process of natural gas as liquefaction freezes water molecules into solid particles which can have disastrous consequences [5, 6].

The sweetened gas stream follows the processing chain to the dehydration unit with the aim to reduce the level of  $H_2O$  to a certain level. Water content in natural gas can be removed by several methods. Glycol dehydration, solid desiccant dehydration, and cooling the gas which are considered to be the most common methods. The first two methods utilize mass transfer of the water molecule into a liquid solvent (glycol solution) or a crystalline structure (dry desiccant). The third method employs cooling below the initial dew point, by expansion and/or refrigeration, to condense the water molecule to the liquid phase with the subsequent injection of an inhibitor to prevent hydrate formation.

Several other dehydration technologies such as membranes, vortex tube and supersonic processes are less commonly used.

### **2.1.2.4. Nitrogen Removal**

Nitrogen rejection unit (NRU) is used to remove nitrogen from LNG to insure:

1. Producing high quality stream of natural gas.

2. Removing nitrogen from LNG so that the nitrogen can be used for enhanced oil recovery (EOR) operation.
3. Separating helium from nitrogen in a helium recovery operation.

There are three common methods for removal of nitrogen from LNG:

1. Cryogenic distillation.
2. Pressure swing adsorption.
3. Membrane separation.

#### **2.1.2.5. Liquefaction.**

Liquefied natural gas (LNG) has become helpful since the transportation of natural gas over long distances through pipelines is economically not feasible. LNG is liquefied Methane that has been cooled down to  $-161^{\circ}\text{C}$  where the state of the gas has changed from gas phase to liquid phase. This phase change will reduce the volume of LNG by a factor of 600 which insures reliable economical transportation and storage. All contaminants should be removed prior to liquefaction process to avoid any issues in downstream processes. In addition, water content also need to be removed before liquefaction process to prevent ice formation and possible blockage in the cold section.

#### **2.1.3. Gas sweetening processes**

There are several processes for natural gas sweetening. Because the presence of  $\text{CO}_2$  and  $\text{H}_2\text{S}$  in the raw gas to be processed and the allowable acid gas levels in the final product vary substantially, no single process is markedly superior in all circumstances, and, consequently, many processes are presently in use. Figure 2-1 illustrates the more important processes and are grouped into the generally accepted categories.

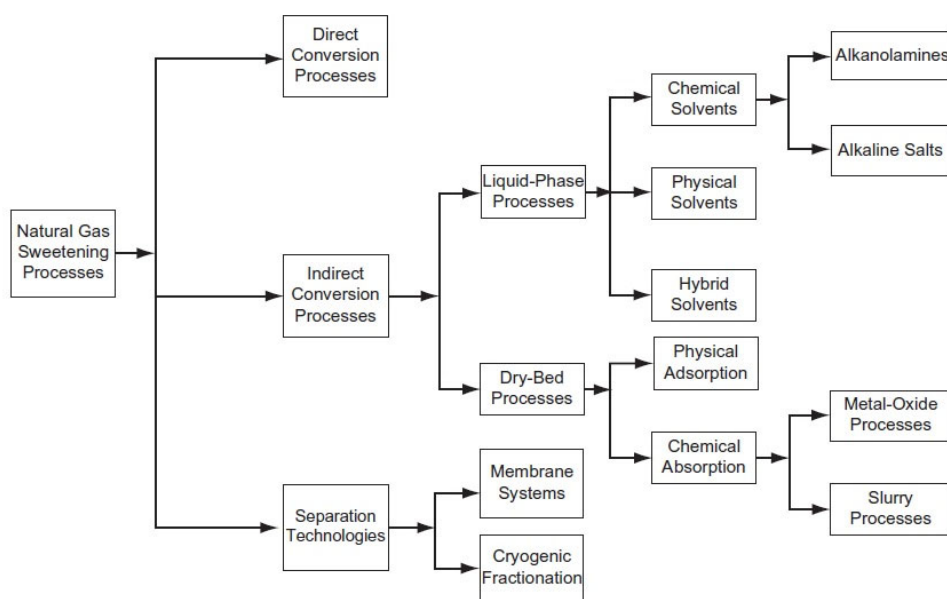


Figure 2-1. Natural gas sweetening Processes

### 2.1.3.1. Liquid Phase Treatment Processes

Liquid-phase absorption processes are classified into three categories: chemical solvents, physical solvents, and hybrid solvents that contain both amines and a physical solvents.

In chemical solvent processes, absorption of the acid gases is achieved mainly by use of alkanolamines or alkaline salts of various weak acids such as sodium and potassium salts of Carbonate [8].

Chemical absorption processes chemically absorb the H<sub>2</sub>S, CO<sub>2</sub>, and to some extent COS. Organic sulfur components do not chemically react with the solvent. Chemical solvents are specifically suitable when contaminants at relatively low partial pressure have to be removed to very low concentrations.

In physical solvent processes, which use organic solvents, no chemical reaction occurs, and acid gas/organic sulfur components removal depending entirely on the physical absorption. Physical solvents tend to be favoured over chemical solvents when the partial pressure of the contaminants is high, the treated gas specification is moderate, and large gas volumes have to be purified [8]. Unlike chemical solvents, physical solvents are noncorrosive, requiring only carbon steel material

equipment. In addition, physical solvents can usually be stripped of impurities by reducing the pressure without the addition of heat [6, 9].

### **2.1.3.2. Amine Processes**

Chemical absorption involves contacting the sour gas with a solvent such as an alkanolamine in a contacting tower on the basis of a difference in density between the liquid and the gas [5, 6]. Different amines can be selected depending on the composition and operating conditions of the feed gas to meet the product gas specification.

The sour gas flows into the lower part of the absorber or contactor. Solvent rich water with no trace of sour gas is pumped into the absorber near the top. As the solution of lean solvent flows down from tray to tray, it is in close contact with the sour gas as it flows upward through the liquid on each tray. When the gas reaches the top of the vessel, the concentrations of  $H_2S$  and  $CO_2$  are reduced to a very minimal and acceptable level. The solvent rich stream that has now incorporated the sour gas is circulated through to a regeneration tower where the solvent is stripped from the sour gas and directed back towards the absorber column to be contacted with a fresh stream of sour gas. A typical schematic of the chemical absorption process is shown in Figure -2 below.

#### **Limitation:**

The limitations of absorption process are briefly described as follows. The solvent used in absorption process such as amines and Benfield solution cause corrosion of the units [10]. When the solvent reacts with some corrosion inhibitors, it will cause erosion of the unit, high tendency for foaming and solid suspension thus reduce  $CO_2$  solvent loading and require injection of antifoaming agents to reduce the surface tension of the solvent and to ensure better contact between the solvent and the  $CO_2$ , the regenerated solution leaving the stripper is at its saturated temperature and partially vaporize at the pump suction, resulting in vibration and excessive wear of the pump impellers. Moreover, since all of the solvents cannot be recycled back to the absorber column, the disposal of the solvents causes environmental hazards and thus gives the common disadvantages of using the absorption process.

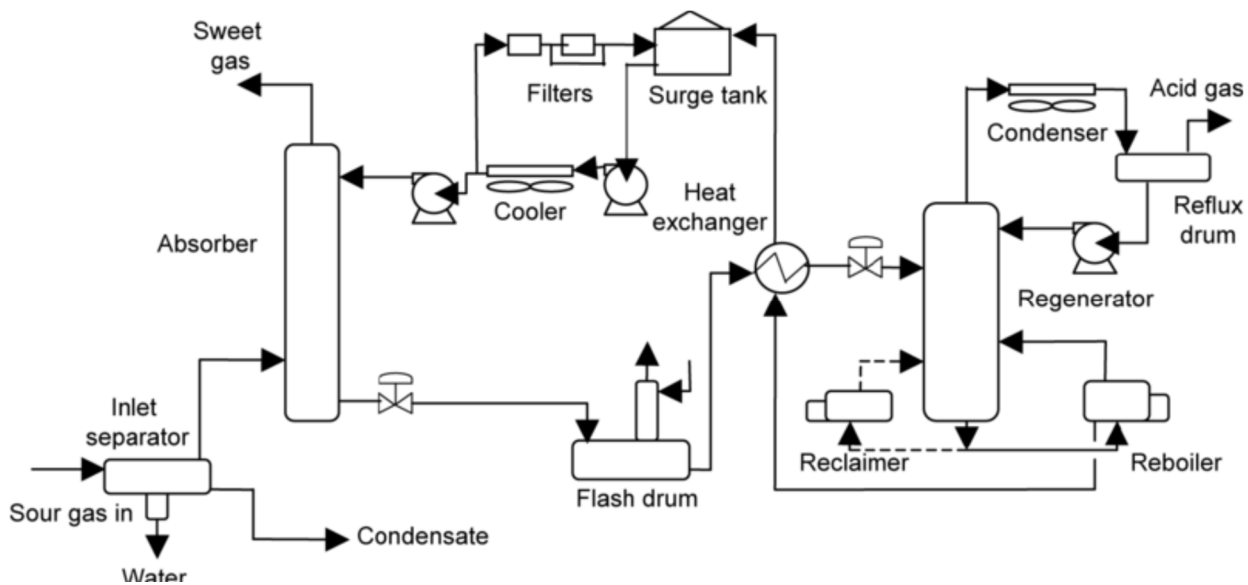


Figure 2-2 Amine Gas sweetening process

### 2.1.3.3. Adsorption Process

In gas separation application, the process of adsorption is described as the adhesion or retention of selective components of feed gas stream brought into contact to the surface of certain solid adsorbent as the result of the force of field at the surface. As the surface of an adsorbing material may exhibit different affinities for the various components of a fluid, it offers a straightforward means of purification (removal of undesirable components from a fluid mixture) as well as a potentially useful method of bulk separation (separation of a mixture into two or more streams of enhanced value)[12].

The primary requirement for an economic adsorption separation process is an adsorbent with sufficient selectivity, capacity and service life. Adsorption selectivity may depend either on the difference in utilization of the adsorption equilibrium or, less commonly, on a difference in kinetics. The main advantage of physical adsorption methods is its low energy requirement for the regeneration of the sorbent material with short period of time associated with the change in pressure [13].

The widely used adsorption processes include metal oxides (metal organic frame works), molecular sieves (zeolites, activated carbon) and promoted hydrotalcites based processes. Zeolite systems can produce nearly pure streams of CO<sub>2</sub>, but are high energy expensive due to the requirements of vacuum pumps and dehumidification equipment. As most effective adsorbent, the use of

hydrotalcites at high temperatures (177-327°C) is widely used for adsorption of CO<sub>2</sub> in combustion or gasification chambers. However, more studies are still required to decrease the pressure difference requirement and enhance the capacity of current adsorbents [14].

Once saturation of the adsorbent is reached, regeneration is carried out by either applying heat or by lowering pressure (concentration). Based on regeneration methods, adsorption process is most commonly divided into temperature swing adsorption (TSA), pressure swing adsorption (PSA) and displacement desorption.

### **Limitation:**

The disadvantages and the limitations of adsorption process are summarized below:

TSA

- Thermal aging of adsorbent
- Inefficiency in energy usage due to heat loss
- Unstable for rapid cycling

PSA

- Very low pressure may be required
- More expensive
- Desorbate recover at low purity

Displacement desorption

- Product separation and recovery needed

#### **2.1.3.4. Membrane technology**

Membrane systems, which consist of semipermeable elements (polymeric membranes), separate gases by selective permeation of the gas constituents in contact with the membrane. The gases dissolve in the membrane material and move across the membrane barrier under imposed partial pressure gradient, which is established by feeding high-pressure gas to one side of the membrane while maintaining the permeate side at much lower pressure [15]. Membranes technology for the purpose of gas separation usually fall into three distinct categories defined by the materials of production which include polymeric, inorganic and mixed matrix membranes. Membrane technologies can also be segregated by the mechanism through which gas is transported through the

membrane, for example, sorption–diffusion, solution diffusion and molecular sieving. Membranes are used widely for the removal of CO<sub>2</sub> from natural gas. These systems can handle higher CO<sub>2</sub> concentration (around 85%) compared to amine systems at high pressures in the range of 200 psia to 1,200 psia.

The important criteria for selecting membrane materials for gas separation are based on the following key factors (a) intrinsic membrane permselectivity (b) ability of the membrane material to resist swelling induced plasticization (chemical resistance, which is quite rare but mostly fulfilled by inorganic membranes) and (c) ability to process the membrane material into a useful asymmetric morphology with good mechanical strength under adverse thermal and feed mixture conditions

Membranes generally are not effective for the removal of H<sub>2</sub>S and other sulfur species because of the very low outlet concentrations required. Membrane systems have major advantages, as a smaller footprint is needed. These systems are cleaner, need low maintenance, have lower capital and operating costs, require lower energy, and are environmentally friendly.

### **Limitation and challenges**

The application of membranes today for CO<sub>2</sub> separation in natural gas processing is mainly used for moderate-volume gas streams. For large-volume gas streams, membrane separation today cannot yet compete with the standard amine absorption as the flux and selectivity of the membranes are too low for processing large gas volumes.

Membranes are used in situations where the produced gas contains high levels of CO<sub>2</sub>.

However, a key sensitivity with these current membranes is that they must be protected from the heavier C<sub>5</sub>+ hydrocarbons present in wet natural gas streams. Exposure to these compounds immediately degrades performance and can cause irreversible damage to the membranes. Thus, in order to fully exploit the use of membranes in natural gas purification, development of more selective, higher-flux and cost effective new membranes are still of critical concerns. And hence, the outcome will make membrane processes much more competitive with other technologies such as amine absorption for large scale systems [15].



### **2.1.3.5. Cryogenic Technologies**

Cryogenic CO<sub>2</sub> removal technology is not new to the oil and gas industry ([16]. Produced hydrocarbons must be sweetened from such impurities as Carbon Dioxide, Hydrogen Sulphide, oxides of Nitrogen and others. The original 21 flue mixture produced from a reservoir, especially in the case of tertiary oil recovery, may contain over 40 mol% CO<sub>2</sub> [17]. The above mentioned acid gases lower the heating value of the gas mixture and must therefore be removed from the stream of mainly Methane and other hydrocarbon gases prior to commercial use as a fuel. On the other hand, trapped acid gases are marketable themselves and are required to be of high purity for such implementations as in the food industry, for example. Cryogenic distillation is considered as one of the most successful methods for separation of CH<sub>4</sub>-CO<sub>2</sub> mixtures with content of Carbon Dioxide varying between 5 and 95 mol%. However, operating temperatures below -60 °C often lead to solid CO<sub>2</sub> formation and consequently plugging of the tower and the flow lines. Eggeman et.al. [18] have claimed that this is a major obstacle in the light hydrocarbon/CO<sub>2</sub> separation process due to the unreliable prediction of CO<sub>2</sub> freeze out temperatures made by several conventional simulation programs. Operating at pressures higher than 40 to 50 bar will result in higher process temperatures, but this may also result in the formation of inseparable supercritical CH<sub>4</sub>-CO<sub>2</sub> fluids. Therefore the operating conditions are limited within a relatively narrow range between the critical state of the feed mixture and freezing conditions of Carbon Dioxide. Besides, if performed as a single distillation column, this will result in the production of a Methane stream containing up to 10 to 15% CO<sub>2</sub> while the sales gas specification of about 2 to 4% is usually desired for pipeline gas specification. Helium and Natural Gas liquids recovery processes require less than 1% Carbon Dioxide content; ultra-pure product require less than 100 ppm CO<sub>2</sub> as specified for use in Natural Gas liquefaction plants and Nitrogen rejection process [19].

#### **2.1.3.5.1. Ryan Holmes Process**

In order to improve the efficiency and effectiveness of separation, Ryan and Holmes proposed the injection of heavier hydrocarbons into the distillation column. These additives are said to shift the CO<sub>2</sub> freezing point, therefore allowing for better separation at lower temperatures and prevention of plugging. The principal scheme for a legacy Ryan-Holmes distillation process is presented in Figure 2-3 [1, 20]

The process is applicable for Methane separation from mixtures containing acid gases such as Carbon Dioxide, for a wide range of compositions. The produced overhead stream is enriched in Methane and substantially free of acid gas components. The bottom products contain mainly CO<sub>2</sub> and other acid gases, higher alkanes and preferably not more than 1 mol% of Methane. Although the tower is operated at pressure-temperature conditions at which solid CO<sub>2</sub> can potentially form, the solids formation is avoided by introduction of 5 to 30 moles of non-polar additives such as C<sub>2</sub>-C<sub>5</sub> hydrocarbons per 100 moles of feed into the column. The additives can be optionally introduced externally and/or as a recycled fraction of the bottom products.

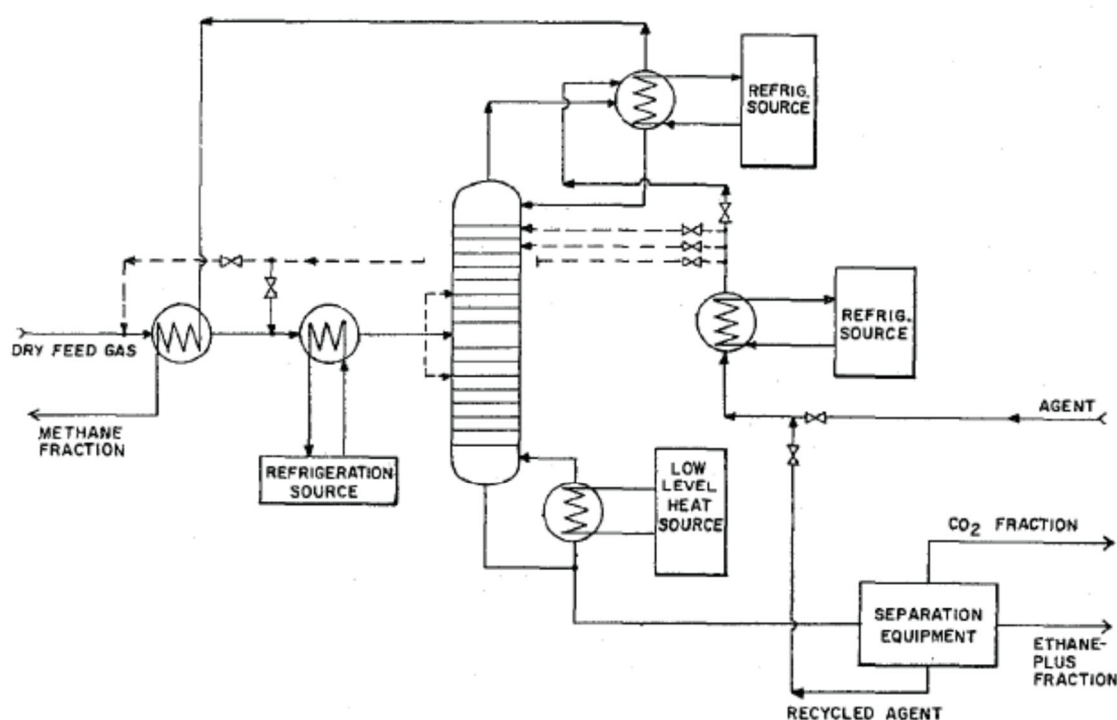


Figure 2-3. Principal scheme of the Ryan-Holmes process for Natural Gas sweetening (Holmes&Ryan, 1982)

There are a number of difficulties associated with the separation of the Ethane-CO<sub>2</sub> and Propane-CO<sub>2</sub> azeotropic mixtures. However, additives could be used to resolve this problem. Ancillary CO<sub>2</sub> purification requirements have motivated further research in this field. Numerous improvements (O'Brien et al., 1983 & 1987) [21, 22] have been made to this process recently including recycling of heavier hydrocarbon fractions [17], distribution of distillation and CO<sub>2</sub> concentration zones [23], multistage distillation [24, 25], thermal coupling, and the introduction of other substances for shifting the CO<sub>2</sub> freezing point [26, 27] [28].

Modified Ryan-Holmes processes are successfully implemented in industrial processing of Natural Gas for Methane-Carbon Dioxide separation due to the significant difference in volatilities of components; however, it is not suitable for non-hydrocarbon sources such as IGCC and Oxyfuel process gases. The main reason is that all of the above mentioned processes involve the use of additives, mainly hydrocarbons, in order to improve separation, and therefore the recovered CO<sub>2</sub> must be separated from them in the subsequent stages.

#### 2.1.3.5.2. Cryocell® Technology

One of the latest improvements to Natural Gas sweetening technologies was made by Amin et al. in 2005. The technology known as CryoCell® has been patented ( Hart & Amin, 2007; Amin & Kennaird, 2008) [29] [30]. Cold liquid hydrocarbons C<sub>2</sub>-C<sub>4</sub> are utilised for CO<sub>2</sub> absorption in conjunction with the Joule-Thomson expansion effect in order to cool the feed gas down to temperatures where CO<sub>2</sub> freezes out and precipitates at the bottom of the vessel. CO<sub>2</sub> is then heated and can be pumped to appropriate pressure and sequestered. The process is highly scalable and applicable to a wide range of tasks, easily operatable and inexpensive. Due to the absence of chemicals involved in gas treatment, no corrosion issues are involved. This technology has been tested for a number of years at the 2 mmscfd CoolEnergy demonstration site in Dongara, Western Australia launched in 2006, and the block diagram of the process is shown in Figure 2-4

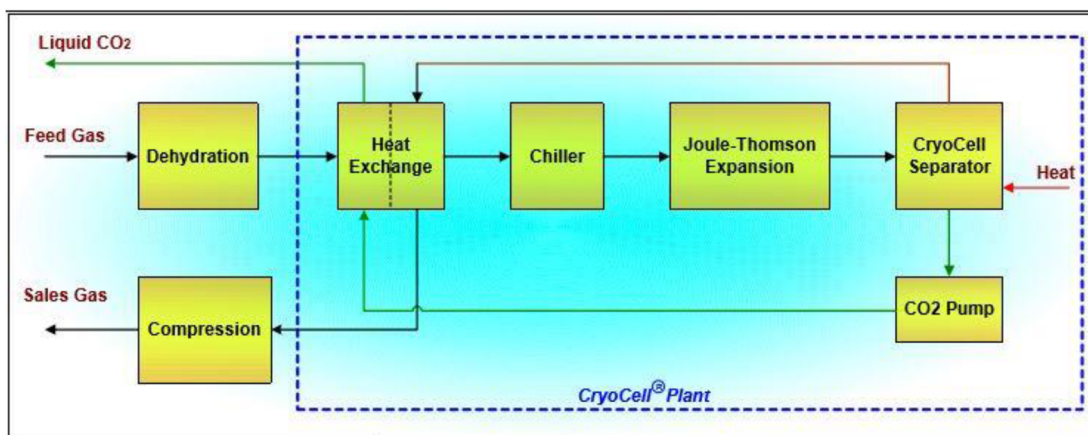


Figure 2-4. Block diagram of CoolEnergy's technology

The CryoCell step reduces CO<sub>2</sub> concentration down to less than 3 mol%, and the CryoZorb™ utilises absorption by cold Methanol to further reduce CO<sub>2</sub> to ppm level. Further information about this technology can be found in (Amin et al., 2005) [31].

### 2.1.3.5.3. Controlled Freezing Zone

Another low temperature process for separation of CO<sub>2</sub> is the Controlled Freezing Zone (CFZ) technology by Exxon [26]. In this process the CO<sub>2</sub> freezing is not avoided, but permitted in a controlled manner. Therefore the method consists of two separate parts. In the first stage CO<sub>2</sub> is condensed in a manner similar to the one described above. Up to 15% of CO<sub>2</sub> may still remain in the gas phase, mixed with hydrocarbons in the product gas stream from this stage. In the second stage, the overhead gas stream from the distillation tower is directed into the freezing zone, engineered in such a way as to prevent the introduction of solids in the distillation zone. There, the gaseous mixture is brought in contact with at least one cold liquid sprayed through nozzles placed in the upper part in order to solidify CO<sub>2</sub> in a form resembling snow. The liquid sprayed into the freezing zone is conventionally a C<sub>1</sub>-rich stream containing 3-8 mol% of CO<sub>2</sub> [32] and is in counter current to the distillation zone product stream. A second spraying liquid could be liquefied Nitrogen as when the CFZ method is applied for the Nitrogen rejection unit as described by Potts and Thomas (1992) [33], or any other highly volatile component. A second distillation zone may be added for further purification of the overhead stream from the freezing zone. The schematic illustrated in Figure 2-5 outlines the general formation of the controlled freezing zone technology that was initially proposed by Valencia and Denton in 1985 [26].

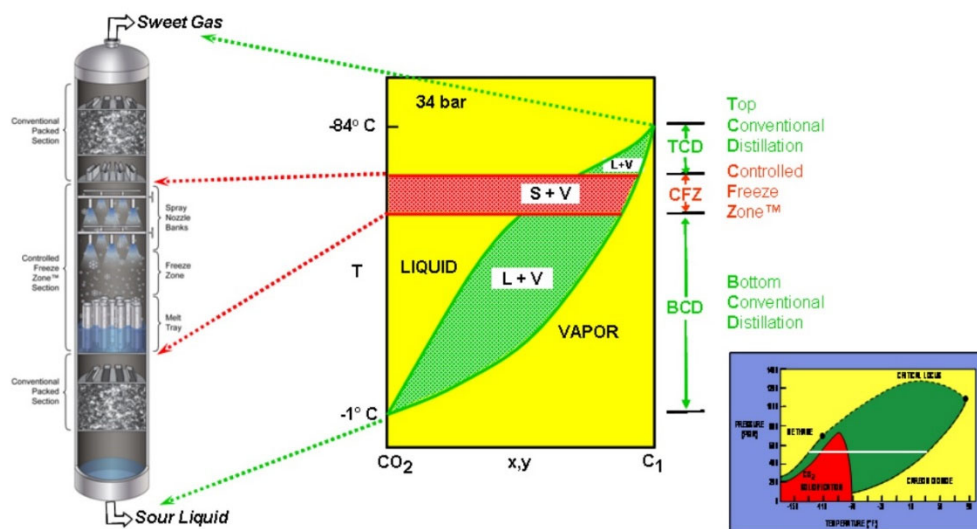


Figure 2-5. CFZ Column & VLE data

During start-up it is essential to prevent freezing outside the freezing zone, and therefore substantially pure Methane stream must be used while the tower is chilled to the low operating

temperatures. Another way to avoid CO<sub>2</sub> solidification at this stage is to inject small quantities of heavier hydrocarbons such as Propane or Butane or Methanol. This leads to the use of other techniques for CO<sub>2</sub> removal before the column reaches the required conditions. One of the methods is described in [32] and utilises pressure-temperature swing adsorption on Linde molecular sieves. The Methane-rich stream can then be condensed and used as a spraying liquid in the freezing zone of the tower. During continuous operation, the adsorption stripping section can be utilised for additional purification of the overhead product stream; however introduction of this supplementary unit will inevitably increase the capital cost.

The CFZ technique can produce an overhead product enriched in Methane and containing 700 ppm to 2 mol% CO<sub>2</sub> and bottoms composition ranging from 0.5 to 1 mol% Methane in CO<sub>2</sub> from a feed composition of 15 to 65 mol% [32]. This method of CH<sub>4</sub>-CO<sub>2</sub> separation is usually associated with liquefied Natural Gas production [34] and utilises the so-called Cold Energy of LNG [35] produced at -160 °C. Despite the possibility to obtain high purity products, this method is not suitable for non-hydrocarbon sources such as IGCC and Oxyfuel gases.

#### **2.1.4. Ryan Holmes Process**

Ryan-Holmes process was originally designed and developed for processing sour gases from Enhanced Oil Recovery (EOR) fields. The most prominent problem for separating CO<sub>2</sub> from light hydrocarbons is complicated by two major factors and they are as follows. The existence of an azeotrope between CO<sub>2</sub>, ethane and H<sub>2</sub>S and ethane as well as the relatively high freezing point of CO<sub>2</sub> (Holmes and Ryan 1982a). The fundamental feature of the Ryan-Holmes process solves these problems by the addition of an extractive solvent in order to avoid CO<sub>2</sub> freeze up and break the CO<sub>2</sub>/ethane azeotrope. This process is a series of distillation columns operating at low temperatures to separate the feed gas components into relatively pure methane and CO<sub>2</sub>, ethane and propane plus products.

The Ryan-Holmes process has been reported to be superior to other processes in treating high CO<sub>2</sub> natural gas from EOR operations. There are several natural gas processing plants that have implemented the Ryan-Holmes process including the Seminole Unit which is owned and operated by the Amerada Hess Company, the ARCO owned Willard Unit, the GMK South Field, operated by Mobil Oil Corporation, and the Wasson Denver Unit, operated by Shell Oil. In addition, Ryan-Holmes process has the advantage of requiring lower dehydration and energy requirement relative to

the amine process, non-corrosiveness, the use of NGL based solvents, and high pressure of the rejected acid gas product which leads to potential in sequestration and applicability of a synergistic principles. Another benefit offered by the Ryan-Holmes process is the high hydrocarbon liquid recovery, which is essential for EOR operations is to increase the revenue of the plant due to the decreasing methane content. Moreover, with the Ryan-Holmes process, a high-pressure  $CO_2$  stream is produced which is more suitable for  $CO_2$  injection for EOR and the possibility for significant synergies within process scheme.

#### **2.1.4.1. Process foundation**

The founding principles of the Ryan-Holmes process is based on lowering or “shifting” of the freezing point characteristic of carbon dioxide. The initial design by (Holmes and Ryan 1982) [20] claimed to have the capacity to drastically improve the efficiency and the effectiveness of the hydrocarbon methane separation. The patented design flow scheme proposed by (Holmes and Ryan 1982) [20] for methane separation is shown in Figure 2-3.

The process aims to reduce the freezing temperature of  $CO_2$  through the addition of an external agent in a form of extractive distillation. As reported by (Katz 1959) [36], the possibility of separating methane from  $CO_2$  is close to impossible without overstepping the  $CO_2$  solid region as shown in

Figure 2-6. This is conducted through the addition of ethane and a mixture of other heavier hydrocarbons at the top of the distillation column. This increases the solubility of carbon dioxide in the liquid phase, increases operating temperatures and raises the critical pressure locus in order to increase relative volatility and make separation easier. This is illustrated in Figure 6 as the dry feed gas enters the column at a mid-point area. The external additive is added at the top of the column as seen in stream 70 at a flowrate of 5-30 moles of additive per 100 moles of feed gas. The amount of additive circulated will be affected by factors such as the composition of the feed stream, the operating pressure and the desired purity of the methane overhead (Holmes and Ryan 1982) [20]. The bottoms stream which contains the separated carbon dioxide and heavier hydrocarbons require further treatment in the subsequent low temperature distillation columns. The patent also states that

the possible distribution of the additive at feed stages of more than one can have positive effects on the results achieved (Holmes and Ryan 1982b)[1].

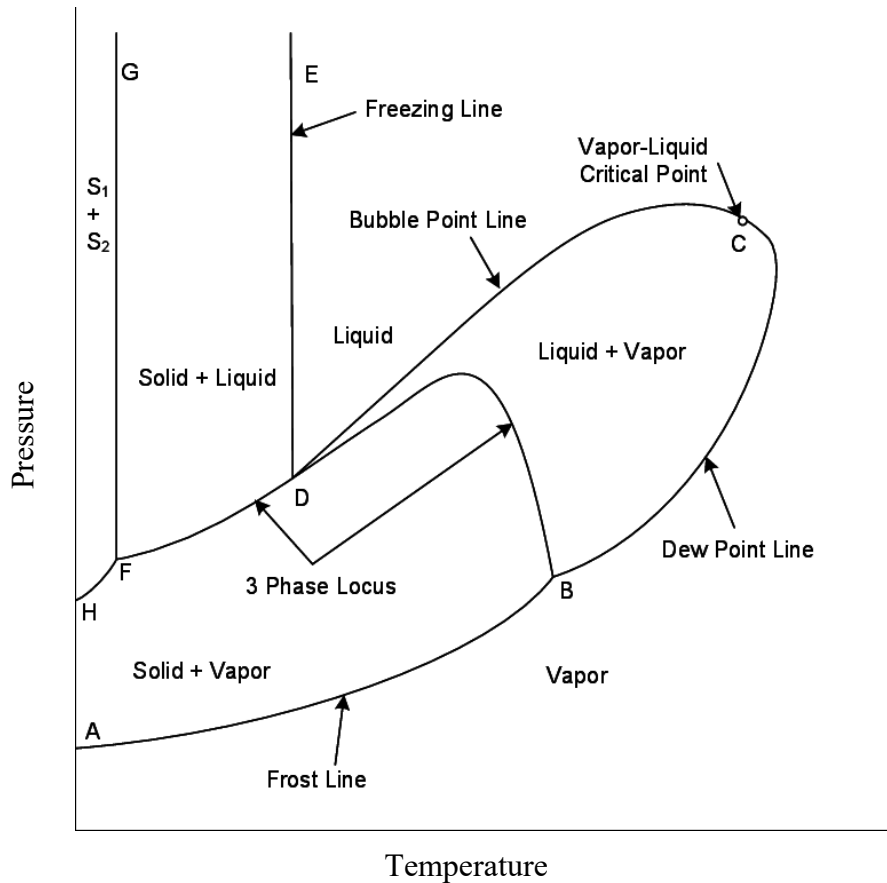


Figure 2-6. Carbon dioxide & Methane Phase Envelope

The proposed technology was then subjected to simulation trials employing the PROCESS Simulation Program from Simulation Sciences, Inc. The equation of state that was seen to be utilised in this study was the Soave-Redlich-Kwong equation of state for the prediction of the vapour-liquid equilibria and thermodynamic data concerning the methane/carbon dioxide system (Holmes and Ryan 1982) [20].

In the preliminary stage of the simulation, the feed stream utilised a binary system of methane and carbon dioxide with the component n-butane being added as the solid-preventing agent with the operating pressure set to 500 psia. The results from the simulation proved that with the addition of the butane component the mixture could be moved away from the solids formation zone [20]. Further simulation work at a pressure of 600 psia indicated that the process could still be conducted

for pressures higher than the initial run due to the addition of the additive agent but at lower circulation rate in comparison. The first run utilised an additive circulation rate of 540 moles/hr into the condenser and 160 mole/hr into the first tray. However, the simulated run at a higher pressure of 600 psia only required a butane circulation rate of 160 moles/hr added to the condenser and the same amount added to the first tray [20]. Subsequently, an additional simulation conducted with an inlet composition consisting of components such as nitrogen, ethane and heavier hydrocarbons at a pressure of 600 psia indicated that once again the operating line for the demethaniser column was moved away from the solids formation zone due to the addition of the butane component [1]. The simulation specified that the amount of carbon dioxide present in the overhead to be 0.98 mole% and the amount of methane in the bottoms product to be 0.32 mol% with an additive flow rate of 160 moles/hr and a feed stream flow rate of 2000 moles/hr. The graphically represented results for the simulated can be found in Figure 2-7 below indicating the freezing point depression of the carbon dioxide.

A second patent (US4350511) published later in 1982 addresses this issue in detail and produces a solution to combat the azeotrope. (Holmes and Ryan 1982b) [1] claims that the formation of the azeotrope can be prevented, again, through the addition of an agent in to the distillation column. (Holmes and Ryan 1982b) [1] elaborates further on the technology stating that the distillative agent required to separate the ethane/ $CO_2$  azeotrope is often found in the feed stream of the column, hinting that components such as butane are viable options [1]. This offers the opportunity for process integration as the agent can be separated from the bottoms stream at a later stage in the process scheme and reinjected in to the distillation column. This form of azeotrope prevention can not only aid in purer overhead product, the overall energy efficiency of the process can be improved in many instances in comparison to a separation study without the addition of an agent. The addition of the agent allows for the separation to occur at higher temperatures and therefore reduce the operating cost of the column [1].

A process flow scheme for the separation of an ethane/ $CO_2$  mixture is displayed in Figure 2-8 below.



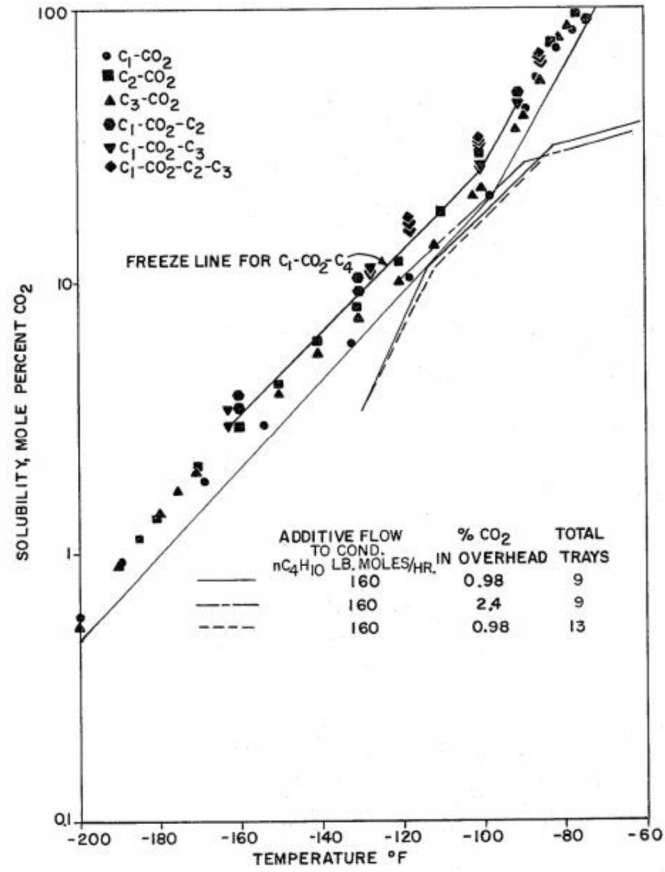


Figure 2-7. CO<sub>2</sub> Solubility Vs Temperature

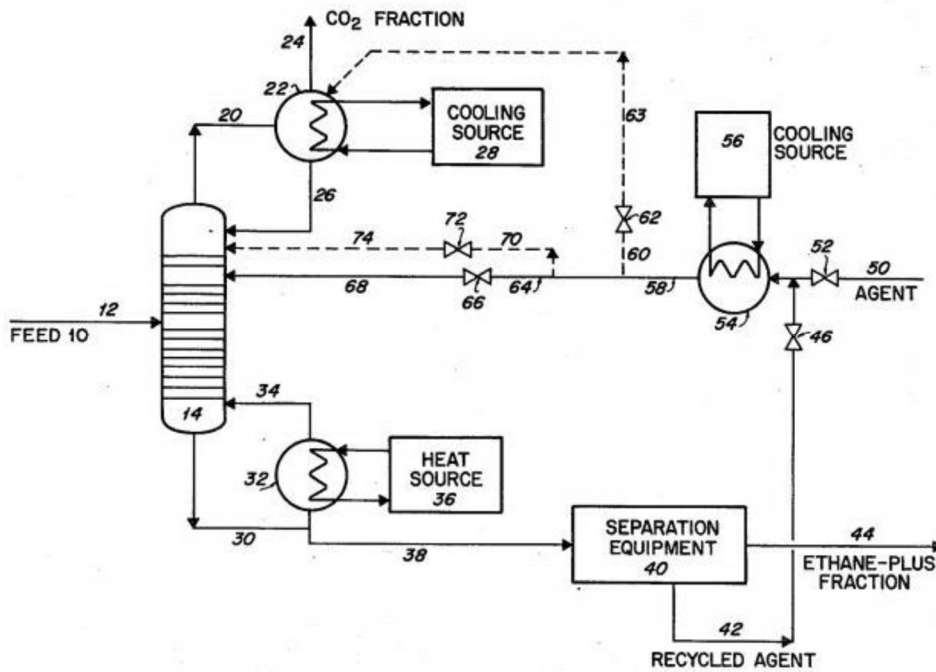


Figure 2-8. Ryan-Holmes CO<sub>2</sub> Recovery Unit (Holmes and Ryan 1982b)

In the flow scheme displayed above, the bottoms stream containing ethane and the heavier hydrocarbon components undergo further separation which the recycled additive agent is then added back into the  $CO_2$  recovery column through either stream 74, 68 or a combination of both. The additive enters the distillation column at the 6th stage from the top with the majority of the composition consisting of propane plus components, 99.8 mol% to be precise (Holmes and Ryan 1982b). With reference to Figure 8 displaying the vapor-liquid equilibria data for a binary mixture of carbon dioxide and ethane at a base case pressures of 578 psia and 335 psia, it can be deduced that the azeotropic characteristic exhibited by the binary mixture can be eliminated through the introduction of additives. From analysing the vapour-liquid equilibria data in Figure 8, it can be concluded that the addition of the additive agent has drastically improved the separation of the carbon dioxide and ethane mixture in that the formation of the azeotrope at the one third ethane two thirds carbon dioxide point. To further this notion, Figure 2-9 is displayed consisting of the relative volatilities of carbon dioxide to ethane.

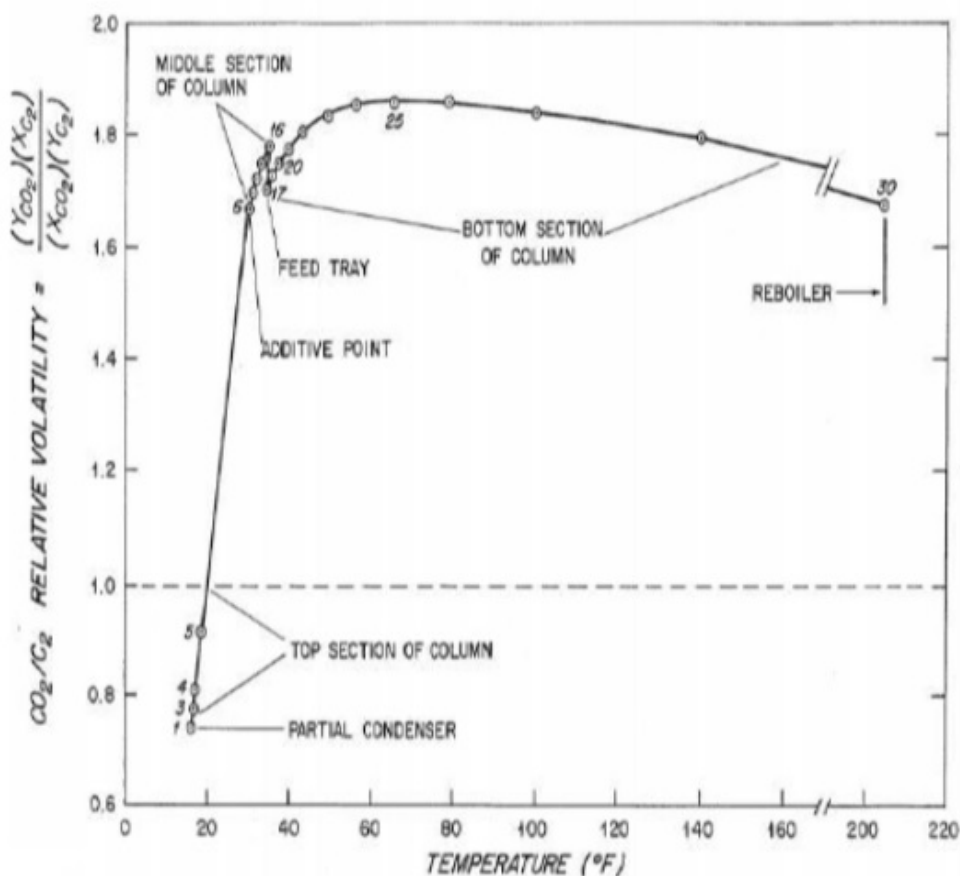


Figure 2-9.  $CO_2$ /Ethane Relative Volatilities Vs Temperature

#### 2.1.4.2. Low temperature distillation

In 2012 Berstad, Neksa, and Anantharaman [37] have conducted a study that elaborates further on the concept of using the Ryan-Holmes process as a foundation in designing systems for a form of extractive distillation in conjunction with low-temperature distillation. With the specification for the concentration of  $CO_2$  in the sale gas set to 100 ppm, the study presents a design scheme allowing the delivery of natural gas product for liquefaction at a high enough pressure of 40 bar and a temperature of  $-88^\circ C$ . The process described utilises the additive technique patented by (Holmes and Ryan 1982a) in that an additional solvent consisting mainly of heavier hydrocarbons are recirculated through the  $CO_2$  recovery columns to combat the inevitable formation of the  $CO_2$ /ethane azeotrope and to address the objective of aiding the freezing point depression of  $CO_2$ . The proposed process addresses the issue of natural gas sweetening for a feed stream with a high carbon dioxide concentration.

The feed stream composition subject to the low-temperature distillation process is indicated in Table 2-3 below as extracted from (Berstad, Neksa, and Anantharaman 2012).

Table 2-3. Molar composition for Berstad feed stream. [37]

| Component      | Mole % |
|----------------|--------|
| <b>CH4</b>     | 0.397  |
| <b>C2H6</b>    | 0.035  |
| <b>C3H8</b>    | 0.024  |
| <b>i-C4H10</b> | 0.009  |
| <b>n-C4H10</b> | 0.009  |
| <b>i-C5H12</b> | 0.006  |
| <b>n-C5H12</b> | 0.006  |
| <b>n-C6H14</b> | 0.002  |
| <b>CO2</b>     | 0.506  |
| <b>N2</b>      | 0.005  |
| <b>H2S</b>     | 0.000  |
| <b>H2O</b>     | 0.000  |

The assumptions implemented in the lead up to the design have been described as follows. The composition of the feed gas was given in the earlier table. The model also assumes that the treatment and removal of water along with hydrogen sulfide is conducted in the upstream processes claiming that despite the possibility of removing both  $CO_2$  and  $H_2S$  in the low-temperature distillation process, only the removal of  $CO_2$  was to be considered. The process inlet flowrate utilised a molar flowrate of 24,800  $kmol/h$  of natural gas devoid of water and  $H_2S$  [37].

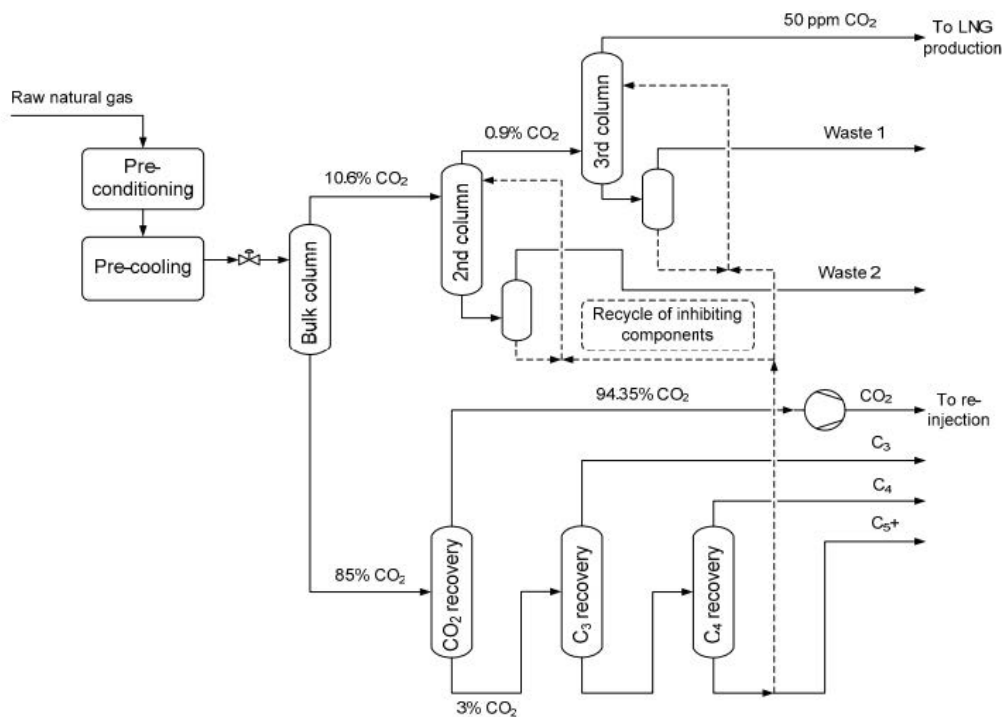


Figure 2-10. Process configuration proposed by Berstad (Berstad, Neksa, and Anantharaman 2012)

Figure 2-10 above depicts the process flow scheme employed by (Berstad, Neksa, and Anantharaman 2012) in the conducted study. The pre-conditioned natural gas passes through auxiliary refrigeration cycles to a temperature of  $10^{\circ}C$  and throttled to a pressure of 40 bar prior to entry into the displayed Bulk column. The Bulk column in this instance represents the preliminary stage in the carbon dioxide separation process in which the concentration of  $CO_2$  in the overhead stream is reduced to 10.6% from 50.6%  $CO_2$  whereas the  $CO_2$  concentration in the bottoms stream has been stated to be 85% leading to the suggestion that further purification of both the overhead and bottoms streams have to be conducted in order to meet the pipeline gas specification for methane and to increase purity of  $CO_2$  for reinjection. With regards to the finer details of the Bulk column, it

is claimed by (Berstad, Neksa, and Anantharaman 2012) [37] that the need for recirculation of hydrocarbon additives was not found to be present in order to avoid the formation of solid carbon dioxide.

The overhead product from the Bulk column is then directed to a secondary low-temperature distillation column with the aim of lowering the carbon dioxide content to a concentration of 0.9%. Proceeding this step, the overhead product undergoes further treatment in the third low-temperature distillation column where the LNG specification of 50 ppm is achieved. Both the secondary and tertiary low-temperature distillation columns require the addition of a recirculating inhibitor in order to avoid potential freezing out of carbon dioxide inside the column. These additional streams consist mainly of pentane and hexane components, aiding in the freezing point depression operation [37].

The operating conditions and other specifics relating to the operation of the design scheme as whole have been displayed in Table 2-4 below.

Table 2-4. Operating conditions and other specifics for the Berstad process operation

|                                 | Unit | Bulk column | 2 <sup>nd</sup> column | 3 <sup>rd</sup> column | CO <sub>2</sub> recovery column | C <sub>3</sub> recovery column | C <sub>4</sub> recovery column |
|---------------------------------|------|-------------|------------------------|------------------------|---------------------------------|--------------------------------|--------------------------------|
| Theoretical stages <sup>1</sup> |      | 19          | 14                     | 62                     | 62                              | 62                             | 77                             |
| Feed stage no. (from top)       |      | 4           | 4                      | 10                     | 34                              | 20                             | 20                             |
| Additive feed stage no.         |      | n/a         | 1                      | 57                     | n/a                             | n/a                            | n/a                            |
| Pressure                        | bar  | 40          | 40                     | 40                     | 30                              | 16                             | 10                             |
| Condenser temperature           | °C   | -67.5       | -86.9                  | -88.0                  | -6.2                            | 48.3                           | 74.0                           |
| Condenser duty                  | MW   | 48.1        | 14.9                   | 11.0                   | 54.7                            | 6.4                            | 4.5                            |
| Reflux ratio                    |      | 1.69        | 1.57                   | 1.61                   | 1.52                            | 2.80                           | 2.41                           |
| Reboiler temperature            | °C   | 7.9         | 0.0                    | 3.0                    | 109.9                           | 117.8                          | 125.0                          |
| Reboiler duty                   | MW   | 40.4        | 11.4                   | 11.3                   | 87.8                            | 7.4                            | 5.7                            |

<sup>1</sup> Including condenser and reboiler stages

As seen in the above table, the overhead product from the tertiary low-temperature distillation column containing mostly methane will have to undergo further refrigeration in order to undergo liquefaction as the temperature for liquefaction of methane is  $-160^{\circ}\text{C}$  [38]. A critical analysis of the CO<sub>2</sub>, C<sub>3</sub>, C<sub>4</sub> recovery columns and possibly the tertiary low-temperature distillation column indicates that the number of theoretical stages is quite high leading to the question of economic viability which consequently doesn't seem to be addressed in the paper. This could be the defining

factor in ascertaining the economic feasibility of the process and whether or not the main features can be tailored to a suitable and appropriate advantage.

The modelling of the low-temperature distillation process in this instance was conducted using ASPEN Hysys platform assuming steady state operation. The equation of state employed for the purpose of this simulation was claimed to have been the Peng-Robinson equation of state. The study also provides assumed efficiencies of the pumps and compressors.

Another Study conducted by (ZareNezhad and Hosseinpour 2009) [39] explored the possibility of utilising and implementing the technique of extractive distillation for producing  $CO_2$  enriched injection gas in field of enhanced oil recovery. The modelling of the process involved rigorous tray-by-tray calculations employed with the view of designing a process flow scheme containing a demethaniser column and a  $CO_2$  stripping column addressing the sharp separation of carbon dioxide from ethane due to the presence of an azeotrope. The occurrence of the azeotrope in this instance is avoided, based on the extractive distillation technique patented by Ryan-Holmes, through the use of an additional agent from within the system. A process schematic for the proposed process is displayed in Figure 2-11 below.

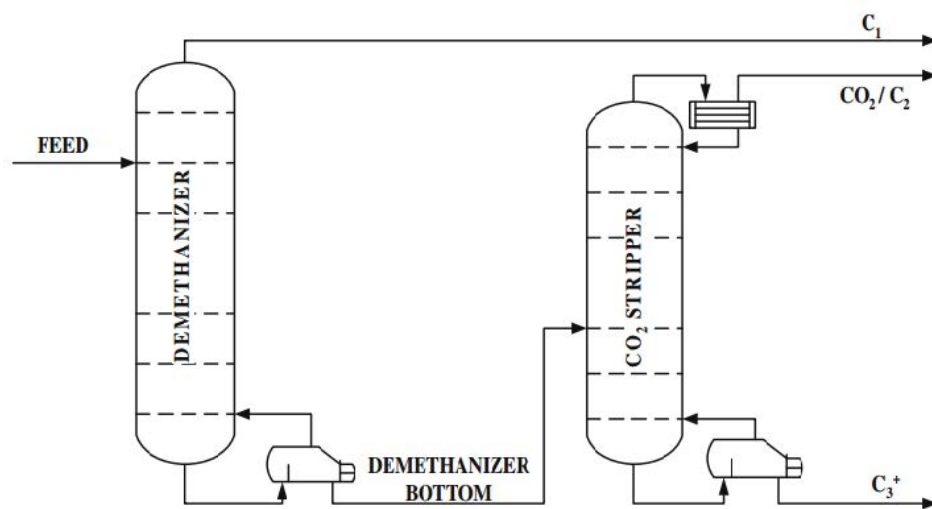


Figure 2-11. Part 1 of ZareNezhad process

The feed stream containing  $CO_2$  along with hydrocarbons undergoes conventional distillation in which the majority of the methane component is separated into the overhead product, leaving the demethaniser bottom stream to consist largely of carbon dioxide, ethane and heavier hydrocarbons [39]. The bottoms stream composition comprises of 26.24% ethane and 57.36% carbon dioxide.

However, the required amount of purity of carbon dioxide has yet to be reached (>95%) in order for the product to be considered suitable for EOR.

The second stage in the extractive distillation process involves the addition of heavier hydrocarbons in order to avoid the azeotrope formation and ensure a high level of separation. A process schematic extracted from the study is displayed in Figure 2-12 below highlighting the recirculation of the additive solvent in the extractive distillation process.

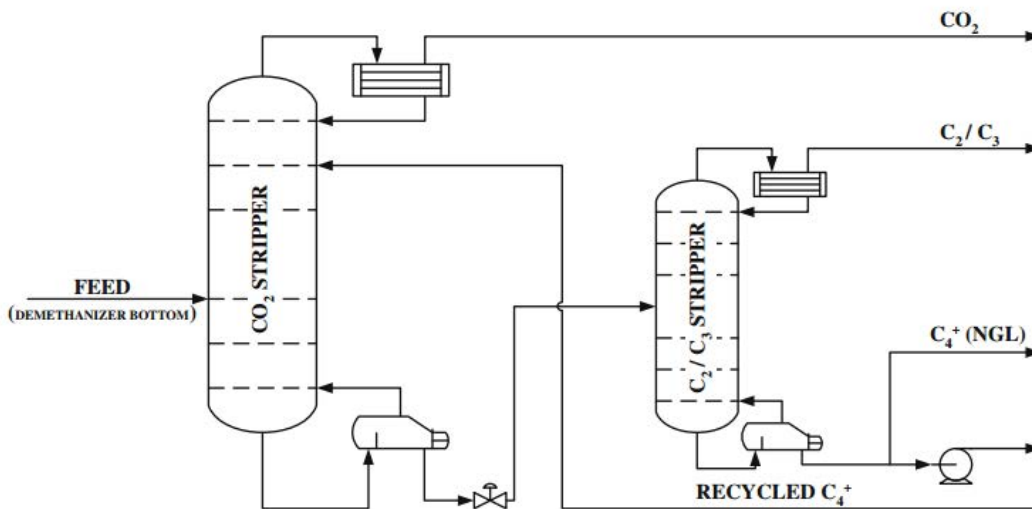


Figure 2-12. Part 2 of ZareNezhad process

In the above figure, the recovered C<sub>2</sub>+ components are redirected to a third distillation column which then separates the ethane from propane and heavier components. From the products of the third column, the overhead product contains mainly ethane and propane whereas the bottoms product is partially redirected into the CO<sub>2</sub> stripping column to act as the additional agent as per the concept explained by (Holmes et al 1982) [1].

Further studies into the realm of extractive distillation and the Ryan-Holmes process is found in the GPA annual conference proceedings 2014 by (Finn and O'Brien 2015) [40]. The paper presents the commercial application of the Ryan-Holmes process at the Seminole plant in Texas, USA. The objective of this plant is to separate carbon dioxide from natural gas for enhanced oil recovery injection. The process utilises a scheme built up of four distillation columns as shown in the Figure 2-13 below

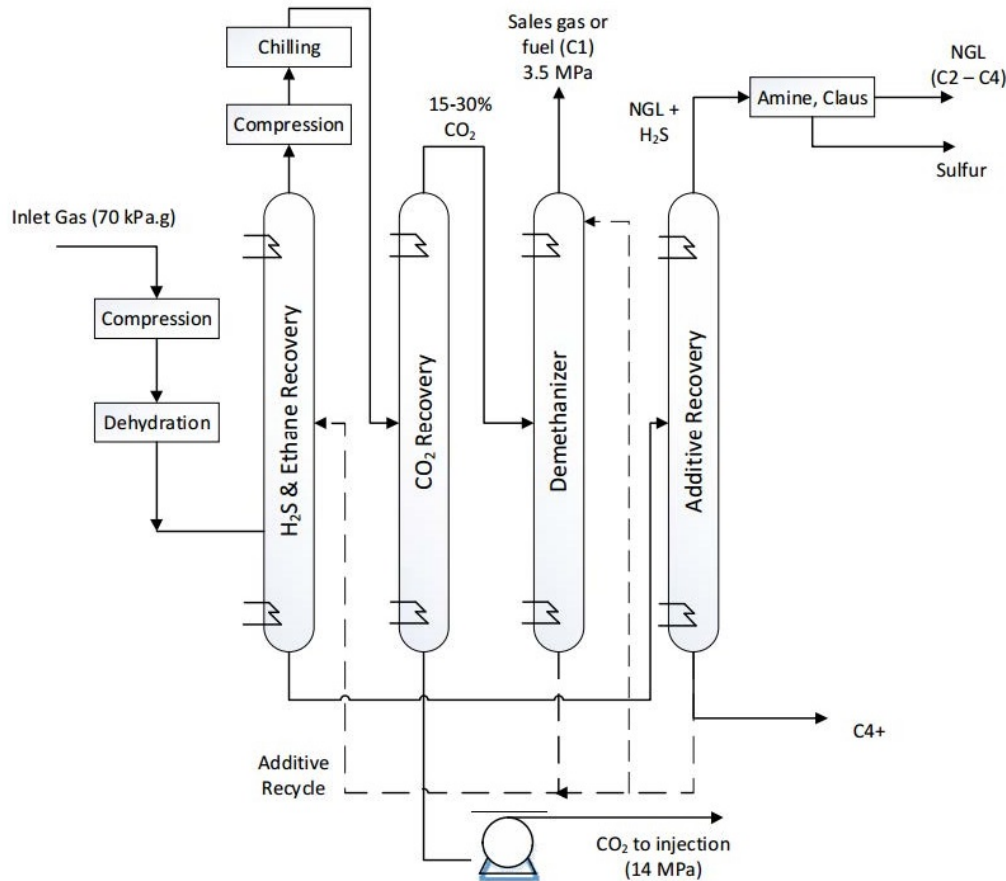


Figure 2-13. Process Configuration from Finn & O'Brien

In this process, the bottoms product from the first column contain predominantly the NGL that is to be further refined to meet commercial specifications. The overhead product undergoes further compression to a pressure of 40 bar. The azeotrope that forms in the presence of carbon dioxide and ethane is overcome in this instance through the addition of recycled butane and heavier hydrocarbon solvents [40].

In the subsequent column, after compression to 40 bar, the majority of the carbon dioxide required for the enhanced oil recovery injection is recovered in the bottoms product which is further adjusted to a pressure of 14 MPa for injection (Finn and O'Brien 2015). The overhead product contains between 15-30 mol% carbon dioxide with the reasoning being that this is the lowest possible purity attainable with the  $-40^{\circ}\text{C}$  propane refrigeration in the condenser. The study acknowledges that the carbon dioxide content can be reduced with the employment of an ethane or ethylene refrigeration system while reducing the refrigeration duty consumed in the system. However, due to the complexity this places on the flowsheet in conjunction with the fact that the bottoms product meets



the specification for oil field injection, this prospect was set aside. The overhead product from the  $CO_2$  recovery column is then directed towards a demethaniser column where it is fractionated into a methane stream containing low carbon dioxide contents. The freezing of carbon dioxide in this column is avoided again through the addition of butane and heavier hydrocarbon solvents recycled from the bottoms product derived from the additive recovery column [40].

The more recent article published in the Canadian Journal of Chemical Engineering conveys an innovative and improved outlook on the typical three tower Ryan-Holmes or the so called low-temperature distillation process in 2015. The study by (Sun et al. 2015) [41] addresses one of the major drawbacks associated with the commercialisation of the low-temperature distillation process for the removal of  $CO_2$  from natural gas in the form of the high refrigeration duties imposed on the system resulting in the relatively large operational costs. The study presents an improvement made on the conventional three tower process through the addition of intermediate reboilers in the stripping section of the carbon dioxide recovery column in conjunction with the utilisation of the overhead vapour from the demethaniser column to essentially pre-cool the feed gas [41].

The study emphasises that an innovative method of reducing energy consumption lies in the employment of intermediate condensers and reboilers in columns that typically exhibit a large temperature differential from the bottom to the top. The study claims that while the addition of intermediate reboilers and condensers induces very minimal changes in the respective total duties, the requirement for both refrigerant and heating mediums in the condenser and reboiler can be greatly reduced. The process scheme utilises, like in many other prior studies the circulation of butane and a combination of heavier hydrocarbon components with the objective of avoiding the freezing of the carbon dioxide in the demethaniser column. The same recycled hydrocarbon solvent is utilised in the carbon dioxide recovery column using an inlet stream at the top of the column in order to break the  $CO_2$ /ethane azeotrope and obtain a carbon dioxide stream with a purity high enough of EOR injection. The bottoms product consisting of the separated carbon dioxide, hydrogen sulfide and the additive hydrocarbon solvent among other hydrocarbons becomes the feed for the  $CO_2$  recovery column.

The preliminary process flow diagram employed by (Sun et al. 2015) in the comparison study of the three tower low-temperature flow scheme is displayed below in Figure 2-14. The scheme is designed with the intended purpose of comparison with the intermediate reboiler concept being explored.

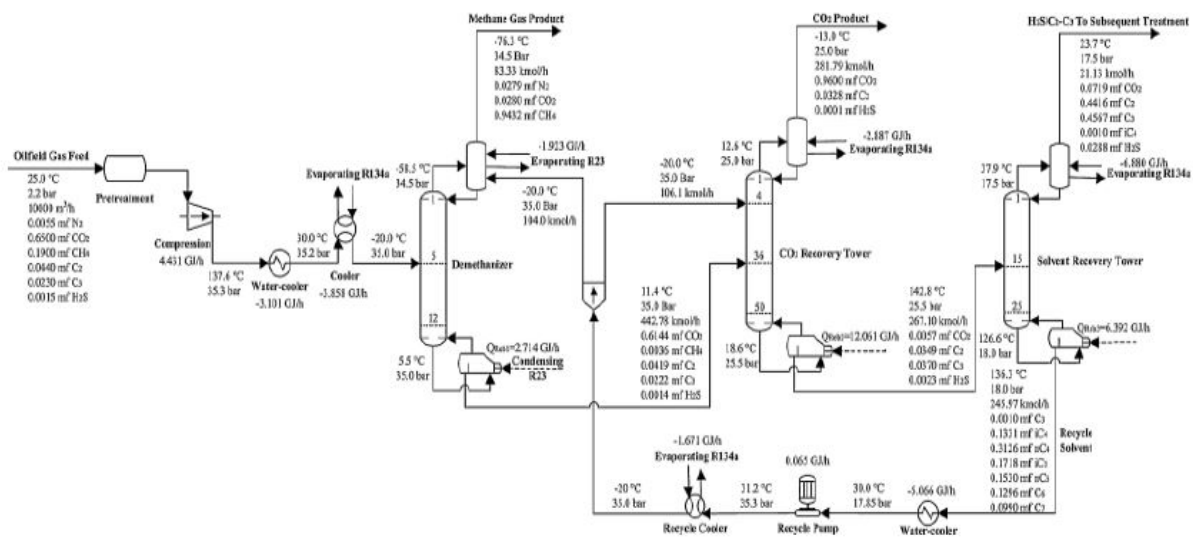


Figure 2-14. Conventional Ryan-Holmes Process Modelled by (Sun et al. 2015)

The process configuration shown above claimed to have achieved a purity of 96% mol carbon dioxide in the overhead stream, attaining the minimum level of purity required for the stream to be considered viable for EOR. The stream emerges from the column at a temperature of  $-13^{\circ}\text{C}$  and a pressure of 25.0 bar. The overhead product from demethaniser column contains a methane content of 94.32% mol which although can be considered to be relatively pure, the presence of a fraction of carbon dioxide means that further treatment will be required before the methane stream can be considered viable for liquefaction. The second stage of the modelling of the process takes place in the form of the implementation of the intermediate reboilers placed in the stripping section of the carbon dioxide recovery column. As mentioned prior, the utilisation of the  $-70$  to  $-80^{\circ}\text{C}$  overhead vapor from the demethaniser to pre-cool the feed gas is also displayed in the reconfigured process scheme [41]. This ensures that the cooling requirement for the refrigeration system is drastically reduced. The modelling software used in the conduction of the simulation was the ProMax3.2 in conjunction with the Soave-Redlich-Kwong property package.

## 2.2. Natural gas Liquefaction

As a gas, natural gas can only be transported from one place to another through pipelines, which limits the number of end users. To overcome this transportation difficulty, natural gas is fractionated to methane, ethane, propane, butane and heavier hydrocarbons. The methane gas is converted to Liquefied Natural Gas (LNG). LNG is methane gas that has been cooled to approximately -160 degrees Celsius where the state of the gas changes from the gas phase to the liquid phase. This phase change reduces the volume of the LNG by 600 times in order to ease the transportation of the natural gas over long distances and make it more economical. On the other hand, the fractionated hydrocarbons are very valuable by-products of natural gas processing where they can be sold as feedstock for the production of petrochemicals, fertilizers, methanol, GTL and acetic acid.

The process of producing LNG begins with processing the raw feed gas to remove all contaminants such as carbon dioxide, hydrogen sulfide, mercury, helium and nitrogen, which may cause difficulties downstream. Next, dehydration is needed to remove water and ensure that even small amounts of water vapour are not present where freezing of water vapour could lead to ice formation and possible blocking in the cold section. Then, the dry sweet gas is cooled by refrigerant streams to separate heavier hydrocarbons. Selecting the appropriate refrigerant depends on multiple factors such as the process temperature requirements, availability of the refrigerant, economics and the refrigerant operating experience. Refrigeration and liquefaction of the process gas is achieved in what is so called cascade process using three refrigerants where each refrigerant has its own operational temperature range. Compressors and heat exchangers are used to circulate and liquefy the natural gas as well as exchanging heat between refrigerants and the natural gas. Cascade refrigeration is usually used where the process desired temperature is very low. After the liquefaction process, the resulting LNG is stored in insulated atmospheric tanks. These tanks are designed to maintain the LNG at very low temperature (-160°C). Then, LNG can be loaded and transported globally using specially designed ships. At its destination, LNG is off loaded and transferred to insulated storage tanks. When LNG is needed, it has to go through regasification process to be converted to its original state (gas) for distribution and use. The heavier hydrocarbons separated during the cooling process are: fractionated to recover ethane, propane and butane as well as meeting the LNG Btu requirements. Ethane can be either utilized as a feedstock for petrochemical plants or reinjected into the gas stream to be liquefied. On the other hand, propane and butane are exported as Liquefied Petroleum Gases (LPG). The remaining hydrocarbons (pentane plus) are exported as Natural Gasoline products (NGL). These heavy hydrocarbons (C5+)

have high freezing points and must be removed to very low temperature levels to avoid freezing and later possible plugging of process equipment during liquefaction.

### **2.2.1. Natural gas pre-treatment**

The liquefaction process requires all contaminants and components that solidify at liquefaction temperatures to be removed from the system prior to liquefaction process. Natural gas consists of three phases before it reaches the plant battery-limit. As shown in Figure 2-15, natural gas, water and condensate are separated in a separator (slug catcher). Water is removed from the bottom of the separator and sent to the waste water treatment area, if the treatment is desired, while condensate is heated to remove any residual gas. Natural gas is further treated through absorption columns to remove carbon dioxide and hydrogen sulfide by utilizing the amine washing method. This step is essential to prevent freezing of carbon dioxide during liquefaction process. Also, removing water vapour from the gas stream to prevent icing later in the process, as illustrated in Figure 2-15. Similarly, removing mercury that causes equipment damage especially to the brazed aluminium heat exchangers usually used in the cold section of LNG processing.

### **2.2.2. Cold box**

The treated natural gas enters the cold box which consists of three stages of pure component cascade refrigerants as illustrated in Figure 2-16. The first cooling stage uses propane as refrigerant and cools the natural gas to about  $-35^{\circ}\text{C}$  and also cools the other refrigerants to the same temperature. The availability and price of propane make it very economical to be used as a refrigerant in the first stage. After that, natural gas will go to the second cooling stage which has ethylene refrigerant. Ethylene cools the natural gas to around  $-95^{\circ}\text{C}$  and also can be condensed by propane.

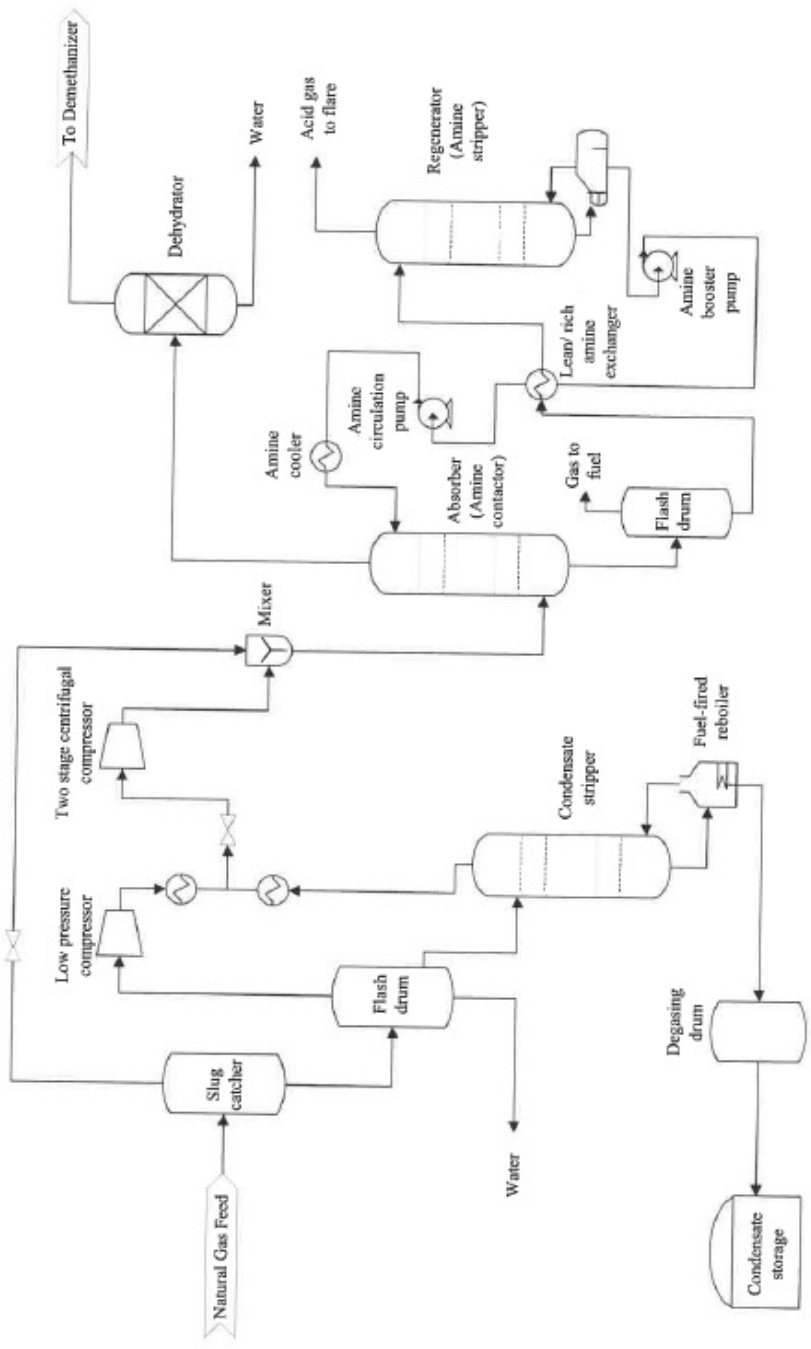


Figure 2-15. Natural gas pre-treatment diagram

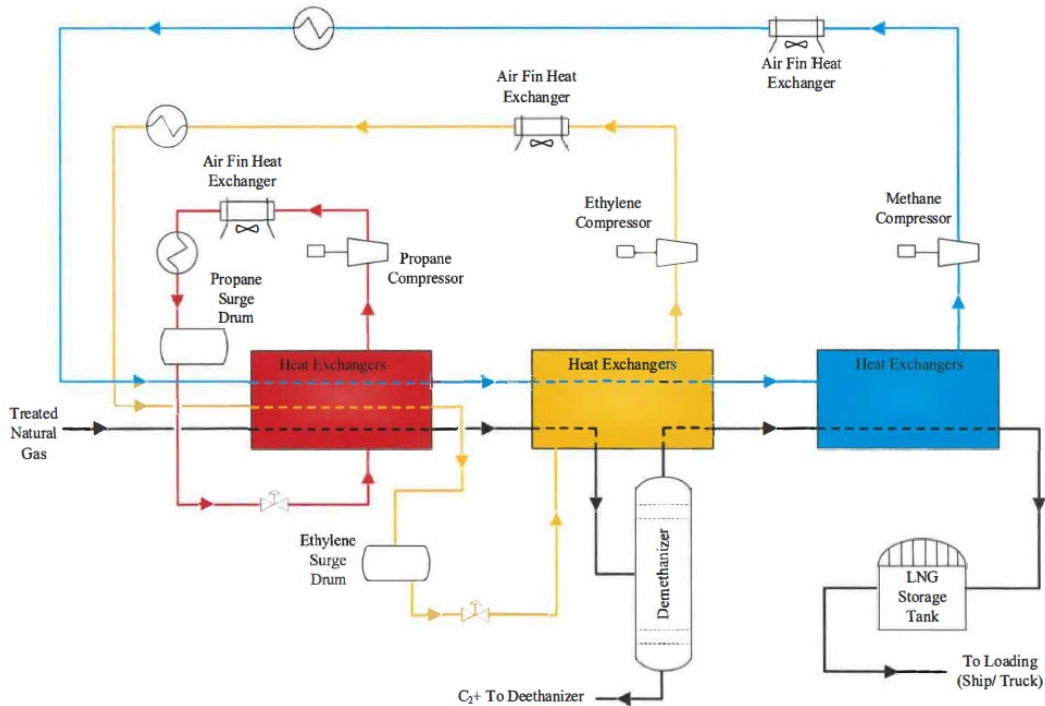


Figure 2-16. ConocoPhillips optimized cascade® process

### 2.2.3. Fractionation

The maximum contents of ethane, propane, butane and heavier hydrocarbons are defined by the LNG specification and its heating value. In order to meet the LNG specification requirements, C<sub>2</sub>+ (ethane, propane, butane and heavier components) must be separated through Demethanizer fractionation column. After the treatment section, the treated natural gas is sent to the demethanizer fractionation column where methane from the top of the demethanizer is taken through gas liquefaction process while the bottom of the demethanizer will contain the C<sub>2</sub>+ products. C<sub>2</sub>+ is separated into components through three different processes. First, the bottom of the demethanizer is sent to the deethanizer distillation column to separate ethane from the C<sub>2</sub>+ mixture. Ethane is produced at the top of the column while propane and heavier hydrocarbons exit the deethanizer column from the bottom. The bottom stream of the deethanizer is fed to the depropanizer column in order to separate propane from the mixture. Butane and heavier hydrocarbons exit the depropanizer column as bottom product and fed to the debutanizer column. Same concept as the previous two processes where butane is the top product of the debutanizer while pentane in addition to the heavier hydrocarbons exits the debutanizer as bottom products.

#### **2.2.4. Liquefaction**

Being extracted from the top of the demethanizer, the methane gas flows to the liquefaction section of the plant for sub-cooling in order to liquefy the natural gas (LNG). This part consists of a refrigeration stage that has methane as refrigerant. The gas leaves the condensate drum at about  $-95^{\circ}\text{C}$  and is sub-cooled by methane to  $-155^{\circ}\text{C}$ . Within this stage, the gas flows through thin tubes which are constantly immersed in pure fluid coolant (methane). The heat from the gas is absorbed by the coolant which will evaporate the coolant while the gas is cooled and condensed to liquid. It is worth mentioning that the nitrogen leaving the top part of the demethanizer has some methane. This excess nitrogen is removed in a double-column nitrogen rejection unit (Cryogenic distillation) where LNG is extracted from the bottom of the low-pressure nitrogen removal column and sent the liquefaction section.

#### **2.2.5. Storage**

There are several types of LNG storage tanks where the choice of the storage tank design is governed by safety and operational considerations, plant location, layout constraints and engineering design standards. LNG formed in liquefaction process is stored at atmospheric pressure in a double-walled insulated tanks that feature innovative and safe designs. The inner tank's walls must withstand the cryogenic temperatures where they are composed of either aluminium or stainless steel while the outer walls of the tanks are made of concrete. LNG tanks are built mostly on piles and have a 75 to 100 cm of perlite insulation between inner and outer walls in addition to an isolated base as well as floating roof. Also, LNG tanks are equipped with prestressed concrete outer shell to contain any leak. Other single-containment storage tanks are surrounded by dikes that provide secondary containment, isolating LNG spills safely. The temperature of boiling LNG at atmospheric pressure ( $-160^{\circ}\text{C}$ ) remains constant as long as the LNG vapour is removed from the tank to the vapour recovery unit where it returns as liquid back to the tank from that unit. All LNG tanks are designed with relief valves. These relief valves will release the excess pressure if there is an upset with the vapour recovery unit. Relief valves are usually set to open if the pressure exceeds 5 bar.

#### **2.2.6. Loading and transportation**

Truck transport and marine carriers are the two possible options for transporting LNG. Liquefied natural gas is transferred from the storage tanks to the dedicated truck or ship by specially designed

pumps and loading arms that can withstand the cryogenic temperatures. Thus, the road movement of LNG is a straightforward process and no new technology is required in this regard. The major consumer of trucked LNG is the vehicle fuel stations. On the other hand, LNG carriers are mostly double-hulled ships designed for safe and efficient transportation of the cryogenic liquid. Figure 2-17 shows spherical aluminium tanks that are designed by Moss Maritime [42] where its insulation system maintains the LNG temperature to prevent heat inflow from the surroundings which would evaporate the liquid; nevertheless, during sea transport, some of the LNG evaporates to form boil-off vapour. Some LNG carriers are equipped with vapour recovery units while others utilize these vapours as fuel.

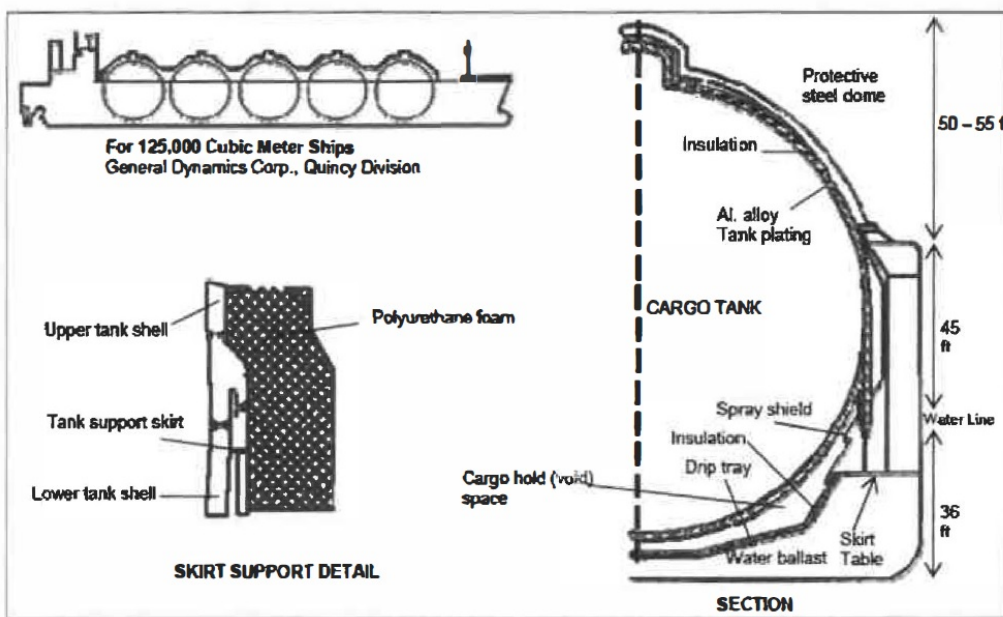


Figure 2-17. LNG transportation tank by Moss Maritime [42]



### **2.3. LNG regasification**

Natural gas can be liquefied at approximately -161 °C slightly above the atmospheric pressure, but this can likewise be achieved by cooling down the natural gas at very high pressure in order to produce liquefied natural gas (LNG). Liquefaction of natural gas makes the transportation considerably more efficient because it hugely reduces the volume of natural gas by 600 times [1]. To return the LNG to the gaseous state, LNG vaporizers are used for the vaporization at the gas receiving terminals [2]. Numerous factors of selecting proper regasification methods have been taken into consideration such as plant site location, weather conditions, throughput capacities, etc. Nowadays, three main different types of vaporizers have been widely used in LNG regasification terminals (1) Open rack vaporizer (ORV), (2) Submerged combustion vaporizer (SCV) and (3) Intermediate fluid vaporizer. Increased energy costs associated with recent developments in environmental regulations have challenged LNG terminal developers to select greener technologies to re-gasify LNG, such as the ambient air vaporizer (AAV) [3].

In this study, an innovative ambient air vaporizer has been designed, constructed and operated. The fins on the AAV were modified by adding a separate channel in the middle of each fin to allow the hot fluid to flow through. The objectives of this study are to investigate the possibility of continuous LNG regasification process without stopping the process for defrosting.

#### **2.3.1. Open Rack Vaporizer (ORV)**

An Open Rack Vaporizer (ORV) is a heat exchanger that uses seawater as the source of heat. ORVs are well proven technology and have been widely used in Japan, Korea and Europe for LNG terminals. The preferred seawater temperature for ORV operation is above 5°C. .

ORV units are generally constructed of aluminium alloy for mechanical strength suitable to operate at the cryogenic temperature. The material has high thermal conductivity which is effective for heat transfer equipment. The tubes are arranged in panels, connected through the LNG inlet and the regasified product outlet piping manifolds and hung from a rack (Figure 2-18). The panels are coated externally with zinc alloy, provide corrosion protection against seawater. ORVs require regular maintenance to keep the finned tube surface clean.

The panel arrangement feature provides ease of access for maintenance. Depending on the design of the units, it is also possible to isolate sections of the panels and vary the load on the units. The unit can be turndown to accommodate fluctuations in gas demand, gas outlet temperature and seawater temperature.

For large regasification terminals where significant amounts of water are required, in-depth evaluation and assessment of the seawater system must be performed. Often, late design changes are very difficult and costly to implement, thereby, the key issues and design parameter must be established early in the project, such as:

- Is the seawater quality suitable for operating an ORV system?
- Does the seawater containing significant amounts of heavy metal ions? These ions will attack the zinc aluminium alloy coating and will shorten its life.
- Does the seawater contain significant amount of sand and suspended solids? Excessive sediment will cause jamming of the water trough and the tube panel. Proper seawater intake filtration system must be designed to prevent silts, sands and sea life from reaching the seawater pumps and exchangers.
- The design must consider the environmental impacts of the seawater intake and outfall system, and minimize the destruction of marine life during the construction period and normal plant operation.
- Chlorination of the seawater is necessary to slow down marine growth. However, residual chlorine in the seawater effluent can impact the marine life and the usage must be minimized.
- Seawater discharge temperature must comply with local regulation. The temperature drop of seawater is typically limited to 5°C in most locations.
- Location of the seawater intake and outfall must be studied to avoid cold seawater recirculation.
- If site is located in a cold climate region, supplementary heating may be necessary to maintain the outlet gas temperature. Boiloff gas from LNG storage tanks can be used as fuel to these heaters.
- Is a backup vaporization system provided? This may be necessary during partial shutdown of the seawater system or during peaking demand operation.

Is the regasification facility located close to a waste heat source, such as a power plant? Heat integration using waste heat can reduce regasification duty and would minimize the environmental impacts.

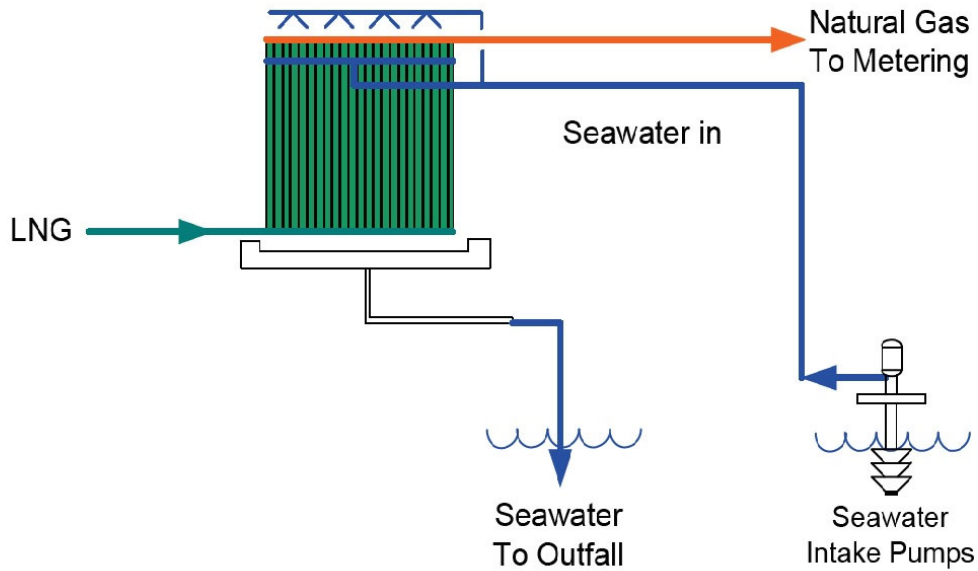


Figure 2-18. Open rack Vaporizer flow scheme

### 2.3.2. Submerged Combustion Vaporizers (SCV)

A typical SCV system is shown in Figure 2-19. LNG flows through a stainless steel tube coil that is submerged in a water bath which is heated by direct contact with hot flue gases from a submerged gas burner. Flue gases are sparged into the water using a distributor located under the heat transfer tubes. The sparging action promotes turbulence resulting in a high heat transfer rate and a high thermal efficiency (over 98%). The turbulence also reduces deposits or scales that can build up on the heat transfer surface.

Since the water bath is always maintained at a constant temperature and has high thermal capacity, the system copes very well with sudden load changes and can be quickly started up and shutdown.

The bath water is acidic as the combustion gas products ( $\text{CO}_2$ ) are condensed in the water. Caustic chemical such as sodium carbonate and sodium bicarbonate can be added to the bath water to control the pH value and to protect the tubes against corrosion. The excess combustion water must be neutralized before being discharged to the open water.

To minimize the NO<sub>x</sub> emissions, low NO<sub>x</sub> burners can be used to meet the 40 ppm NO<sub>x</sub> limit. The NO<sub>x</sub> level can be further reduced by using a Selective Catalytic Reduction (SCR) system to meet the 5 ppm specification if more stringent emission requirements are needed, at a significant cost impact.

SCV units are proven equipment, are very reliable and have very good safety records. Leakage of gas can be quickly detected by hydrocarbon detectors which will result in a plant shutdown. There is no danger of explosion, due to the fact that the temperature of the water bath always stays below the ignition point of natural gas.

The controls for the submerged combustion vaporizers are more complex when compared to the open rack vaporizers (ORV). The SCV has more pieces of equipment, such as the air blow, sparging piping and the burner management system which must be maintained. SCVs are compact and do not require much plot area when compared to the other vaporizer options.

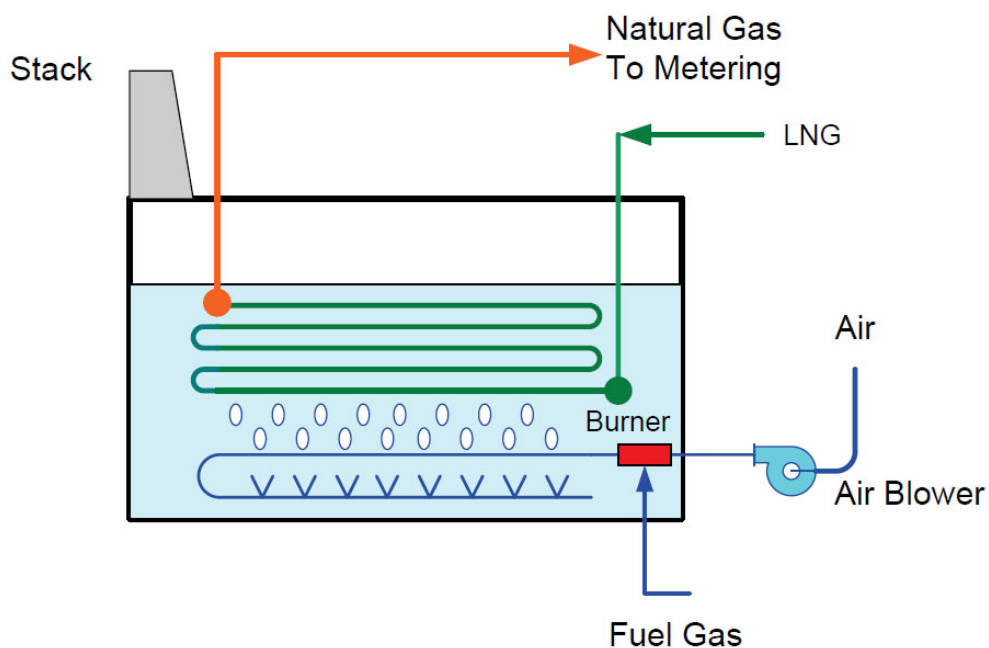


Figure 2-19. Submerged Combustion Vaporizer (SCV)

### 2.3.3. Intermediate Fluid Vaporizer

This LNG vaporizing via intermediate fluid utilizes Heat Transfer Fluid (HTF) in a closed loop to transfer heat to vaporize LNG. Three types of Heat Transfer Fluids are typically utilized for LNG vaporization:

- Glycol-Water
- Hydrocarbon Based HTF (Propane, Butane or Mixed Refrigerant)
- Hot Water

#### **2.3.3.1. Glycol-water Intermediate Fluid Vaporizer**

This system typically uses glycol-water as an intermediate heat transfer fluid. Ethylene glycol or propylene glycol or other low freezing heat transfer fluids are suitable for this application. Heat transfer for LNG vaporization occurs in a shell and tube exchanger. Warm glycol-water flows through the intermediate fluid vaporizers where it rejects heat to vaporize LNG.

A simplified process sketch of these various heating options is shown in Figure 2-20. The IFV is a conventional shell and tube exchanger which is also known as Shell and Tube Vaporizer (STV). These glycol-water IFVs are very compact exchangers (vertical shell and tube design) due to the high heat transfer coefficients and the large temperature approach.

Currently, glycol-water intermediate fluid LNG vaporizers account for a small fraction (around 5%) of total LNG regasification markets worldwide. Some of the operating plants utilize air heater and reverse cooling tower as the source of heat.

There are several options to warm the glycol-water solution prior to recycling it back into the shell and tube LNG vaporizers, such as:

- Air heater
- Reverse cooling tower
- Seawater heater
- Waste heat recovery system or fired heater

Using air for heating will generate water condensate, especially in the equatorial regions. The water condensate is of rain water quality which can be collected and purified for in-plant water usage and/or export as fresh raw water. Conventional air fin type exchanger consists of fin tubes are not designed for ice build-up. With the use of an intermediate fluid such as glycol-water, the glycol temperature can be controlled at above the water freezing temperature hence avoiding the icing problems.

Similarly, the reverse cooling tower design, which extracts ambient heat by direct contact with cooling water via sensible heat and water condensation, would require an intermediate fluid. The heat of the cooling water can be transferred to the intermediate fluid by a heat exchange coil.

Seawater may be also be used. However, the use of seawater is more prone to exchanger fouling, and the exchanger (plate and frame type) need to be cleaned periodically. The plate and frame exchangers are very compact and low cost. Typically, spare seawater exchangers are provided for this option.

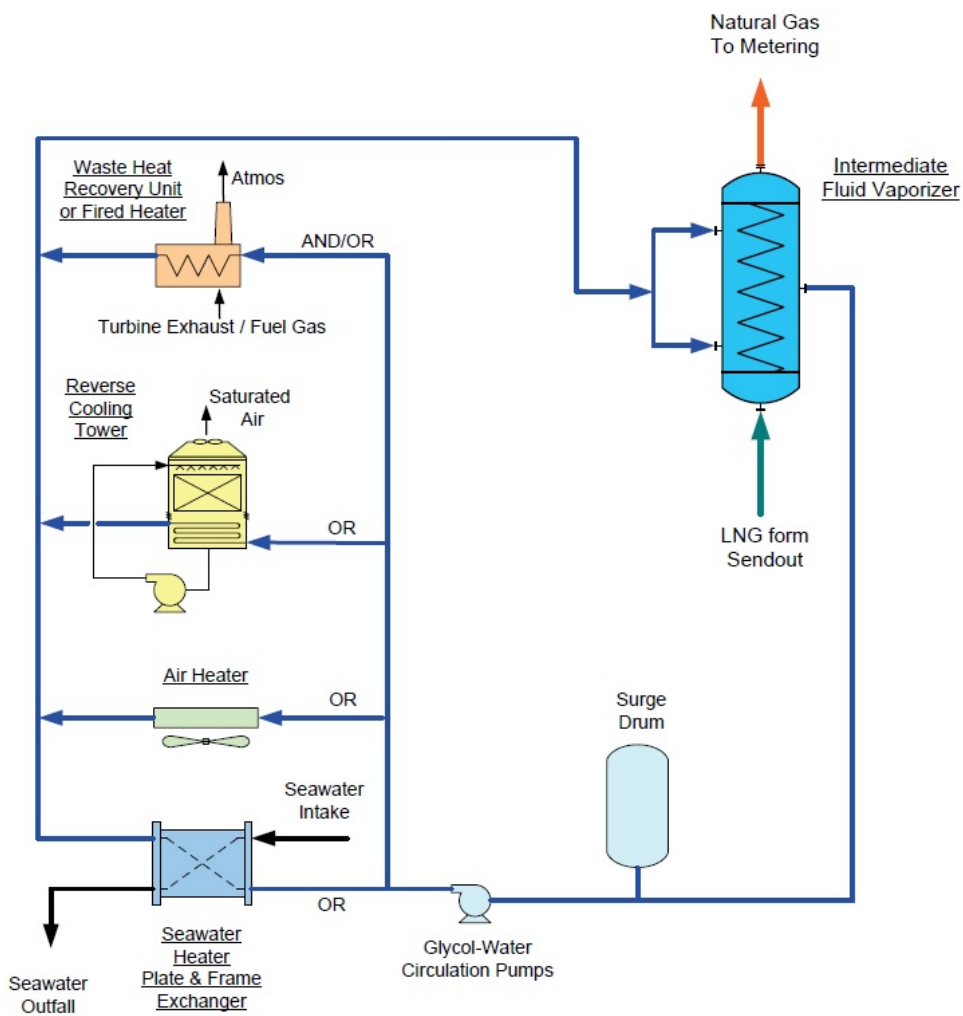


Figure 2-20. Glycol-water Intermediate Fluid Vaporizer Integration with Different Heat Sources Intermediate Fluid (Hydrocarbon) in Rankine Cycle

### 2.3.4. Ambient Air Vaporizer

Various papers have been published previously presenting differences between the fuel gas fired SCV, open rack vaporizers (ORV) utilizing sea water and specific ambient air based technologies. It is generally well understood that the recovery of low grade heat from ambient air to re-gasify LNG results in lower fuel consumption and operating cost [2]. In addition to savings in the operating cost, the reduced energy usage could result in lower air emissions making the overall terminal more environmentally friendly.

It is also generally understood that the capital cost for the ambient air based technologies is higher because of the addition of equipment, such as auxiliary heater to provide supplement heat due to limited ambient conditions [3]. AAV is widely used in small and medium gas terminal stations due to the low operating cost and high environmental sustainability [2]. Many ambient air based technologies have been developed recently to demonstrate the overall savings in fuel gas and reduced environmental emissions [3, 4]. The heat transfer performance of AAV could be easily affected by ambient conditions and operation parameters, e.g. temperature and humidity of the ambient air. Various approaches have been proposed recently for using ambient air as a source of heat to re-gasify LNG. The approaches can be classified into two basic methods for recovering low level heat from ambient air i.e. indirect contact and direct contact methods. The indirect contact approach utilizes a closed loop of intermediate fluid that is heated by ambient air and then exchange heat with LNG in specially designed shell and tube heat exchangers [ref]. The direct contact approach utilizes ambient air directly to re-gasify LNG in finned-tube heat exchangers.

There are two common types of direct contact ambient air vaporizers Natural Draft Ambient Air Vaporizer (NDAAV) and Forced Draft Ambient Air Vaporizer (FDAAV). NDAAV utilizes the natural draft based on density difference of warm and cold ambient air. FDAAV utilizes electrical fans to force ambient air across the finned-tube exchanger. [1, 4, 5] presented series of papers of both simulation and experimental on heat transfer performance of natural-draft AAV. They used LN<sub>2</sub> (Liquid nitrogen) as working fluid instead of LNG for safety reasons. [7] Conducted an experimental study of natural draft AAV using different cryogenic fluid and ground clearance to investigate the effect of such variables on the frost formation and heat transfer. Increasing the AAV ground clearance or cryogenic fluid flow rate could increase the frost formation. Many studies have been presented on the behaviour of frost formation. [8] Showing through performed an

experimental study of natural convection AAV that the amount of frost formed on the cryogenic surface was not enough as in refrigeration temperature due to the fact that the water-vapour could be condensed before reaching the surface of vaporizer (Cryogenic surface). This results can explain the different between the Cryogenic and refrigeration temperatures in terms of frost formation. Moreover, density and thermal conductivity of cryogenic frost could have a different temperature correlation in comparison with the refrigeration frost conditions.

To avoid dense ice build-up on the surface of the heat exchanger tubes, defrosting with a 4-8 hour cycle is typically required [any reference]. Long operating cycles lead to dense ice on the exchanger tubes, requiring longer defrosting time. Defrosting requires the exchanger to be placed on a standby mode, and can be completed by natural draft convection or force draft air fans. The use of forced-draft fans can reduce the defrosting time but would require additional fan horsepower. The reduction in defrosting time is typically not significant as the heat transfer is limited by the ice layers which act as an insulator. [8, 9] have patented an innovative fin design by adding a separate channel for defrosting fluid to decrease defrosting period and delay the frost formation by drying the fin surface and the air passage. Other defrosting studies have focused on using electric heating, preheating air inlet [11].

#### **2.4. CO<sub>2</sub> Reinjection for storage and EOR purposes**

To reduce CO<sub>2</sub> emissions into the atmosphere, different scenarios are proposed to capture and store carbon dioxide (CO<sub>2</sub>) in geological formations (CCS). Storage strategies include CO<sub>2</sub> injection into deep saline aquifers [43, 44], depleted gas and oil reservoirs [45] [46], and coal seams [47]. Even though the volumetric CO<sub>2</sub> storage capacity is the highest in aquifers, CO<sub>2</sub> storage by means of CO<sub>2</sub>-enhanced gas and oil recovery (CO<sub>2</sub>-EGR and CO<sub>2</sub>-EOR) is more economically viable.

In reservoir engineering, it has been well-identified that interfacial interactions, i.e., wettability, capillarity, interfacial tension, and mass transfer, control the flow behaviour and the displacement in porous media. Particularly, wettability has been known as one of the most important factors determining the residual saturation, the capillary pressure, and the relative permeability functions [7,8]. This means that the process of CO<sub>2</sub> storage in hydrocarbon reservoirs and in deep saline aquifers is influenced by gas/liquid/rock interfacial interactions [9–11]. The relation between the interfacial interactions (interfacial tension, capillarity, and wettability) is represented by the Young–Laplace equation:



$$P_c = P_{nw} - P_w = 2\gamma_{aq,CO_2} \cos \theta / R \quad 2.1$$

where  $P_c$  is the capillary pressure,  $P_{nw}$  and  $P_w$  are the pressures in the non-wetting and wetting phases, respectively,  $\gamma_{aq,CO_2}$  is the interfacial tension between the aqueous phase and the  $CO_2$ -rich phase,  $R$  is an effective pore radius corresponding to the narrowest pore throat along the entire  $CO_2$  flow path [Ref] and  $\theta$  is the contact angle related to the reservoir wettability

Wettability can be considered an important factor which influences the residual saturation, capillary pressure, and relative permeability, which in turn control the flow in porous rocks [12–15]. In addition, interfacial interactions can have a significant impact on the process of  $CO_2$  storage in hydrocarbon reservoirs and in saline aquifers [14,16,17], where the relation between the interfacial interactions (interfacial tension, capillarity, and wettability) is represented by the Young–Laplace equation.

Roughness of the surface can also influence the apparent contact angle at the boundary between the liquid and the surface, and many examples have been given where wetting of the rough surfaces proved to be difficult because of their large apparent contact area [19,20]. Moreover, theoretically, the contact angle increases with increase in the surface roughness for oil-wet surfaces and decreases with increase in the surface roughness for water-wet surfaces [12–23]. However, these effects are still poorly understood, as many other studies have shown both increasing and decreasing trends with increasing surface roughness [24–26].

The contact angles are often measured on pure mineral samples to investigate the fundamental phenomena behind wettability variations with state variables; however, such measurements might not be representative of an actual reservoir rock with inherent heterogeneities. In fact, very little work has been conducted on wettability measurements of heterogeneous reservoir samples where surface roughness, interfacial tensions, mineral surfaces, and the pore system play key roles. Therefore, we measured the contact angle of  $CO_2$ /brine on a porous sandstone surface under reservoir conditions and analysed the dependency of the contact angle on the pore fraction where the pressure, temperature, and brine salinity were varied. We also developed a physical model to describe the observed phenomena.

#### 2.4.1. WETTABILITY AND CONTACT ANGLE DETERMINATION

Wettability of reservoir rocks is determined by a complex relationship of interfacial interactions between the rock, composed of a wide variety of minerals, and the reservoir fluids that occupy the irregular pore space. Experimentally, the wettability is only determined in the laboratory because no experimental method exists for in-situ measurements. Different techniques, either quantitative or qualitative, have been developed to evaluate the wettability of a rock-fluid system, namely the Amott test, the U.S. Bureau of Mines (USBM) test, and contact-angle measurements. The Amott and USBM methods give a quantitative value of the wettability of a core only at atmospheric conditions. The contact-angle method allows the determination of the wettability of a specific surface also at high pressures and elevated temperatures [29]. To avoid complications due to surface roughness and heterogeneity during the experiments and data processing, the experimental determination of the contact angle is commonly conducted on idealized and polished surfaces. Although the wettability determination on a polished or rough surface leads to an “apparent contact angle”, this apparent contact angle is a good representative value of the average wettability of the real surface. Therefore, experimentally determined contact angles are widely used to characterize the wettability of complicated systems, in particular at high pressures and elevated temperatures [13, 28, 30].

For the characterization of the surface wettability by means of the contact angle, Young’s equation is applied:

$$\gamma_{lv} \times \cos\theta_y = \gamma_{sv} - \gamma_{sl} \quad 2.2$$

Where  $\gamma_{lv}$ ,  $\gamma_{sv}$  and  $\gamma_{sl}$  are the interfacial tensions or surface energies between the aqueous phase and the gas phase, the solid and the gas phase, and the solid and the aqueous phase, respectively, and  $\theta_y$  is the Young’s contact angle, which is a unique contact angle at equilibrium and is determined through the densest fluid phase. Commonly, the product  $\gamma_{lv} \cos\theta$  refers to the adhesion force [31], which is used in reservoir engineering for the calculation of the capillary number. Based on the capillary number, the residual saturations and relative permeabilities are determined [32].

However, in practice, many metastable states of a droplet/bubble on a solid exist, which might lead to an inequality of the experimentally determined contact angle,  $\theta$ , with the Young’s contact angle,  $\theta_y$ . In general, the contact angles formed by expanding and contracting a liquid droplet/gas bubble are described as the advancing contact angle  $\theta_a$  and the receding contact angle  $\theta_r$ , respectively.

Differences in the receding and advancing contact angle result from surface roughness and/or heterogeneity [33]. The difference between the advancing and the receding angle is called the contact angle hysteresis ( $H$ ):

$$H = \theta_h - \theta_r \quad 2.3$$

On ideal surfaces, there is no contact angle hysteresis, and the experimentally determined contact angle is equal to Young's contact angle,  $\theta_Y$ .

The contact angle between the three phases determines whether a reservoir rock is water-wet ( $\theta < 75^\circ$ ), intermediate-wet ( $75^\circ < \theta < 105^\circ$ ) or oil/gas-wet ( $\theta > 105^\circ$ ). The contact angle can be experimentally determined in a pendant/sessile drop cell that is adapted to allow the analysis of a captured bubble/sessile drop at a rock surface. The contact angle method is based on image analysis of high-resolution photographs of the droplet/bubble on the rock surface.

#### 2.4.2. Effect of temperature on contact angle

It was reported that contact angle increases with temperature [Yang et al., 2008, Farokhpoor et al., 2013]; however, there are other works [De Ruijter et al., 1998, Saraji et al., 2014, Arif et al., 2016] showing that the contact angle decreases with temperature. Further, Roshan et al. [2016] observed theoretically (Eq.3) that contact angle is a function of temperature through several parameters, among which are the dielectric constant of the solution  $D_f$ , the interfacial tension  $Y_{lg}$  between the fluids, the density difference between the phases  $\Delta\rho$  and temperature ( $T$ ) itself. The effect of temperature on  $D_f$  [Floriano and Nascimento, 2004] is insignificant compared to its effect on the density difference and interfacial tension between fluids [ref].



Thus, three parameters compete against each other contact angle decreases with temperature and with increases in  $\Delta\rho$  by temperature, but increases because of a decrease in  $Y_{lg}$  with temperature [Sarmadivaleh et al., 2015, Al-Yaseri et al., 2016a]; however, in one case, the contact angle increased with temperature, which shows the effect of temperature on  $Y_{lg}$  over-compensated for the effect of density difference and temperature and, thus, caused the contact angle to increase. A further change in contact angle can take place as a result of a microscopic change in the van der Waals potential caused by temperature. However, this effect is neglected herein, as these microscopic variations are not yet fully understood [Roshan et al., 2016].

### **2.4.3. Effect of pressure on contact angle**

Increasing pressure significantly reduces the density difference and causes the contact angle to increase [Al-Yaseri et al., 2016a]. This is well supported by much literature data [Dickson et al., 2006, Ameri et al., 2013, Saraji et al., 2013b, Arif et al., 2016] and molecular dynamics data [Jung and Wan 2012, Iglauer et al., 2012b, McCaughan et al., 2013, Sedghi et al., 2014, Chen et al., 2015]. Furthermore, pressure has a profound effect on contact angle, both on charged and neutral surfaces. When examining Eq. 2.2 clearly several parameters are a function of pressure. For instance, the increase in pressure slightly affects the interfacial tension between the fluids [Hjelmel and et al., 1986] along with the dielectric constant of the liquid phase  $D_f$  [Floriano and Nascimento 2004]; however, the main effect primarily occurs through the change in the density difference of the phases by pressure [Georgiadis et al., 2010].

### **2.4.4. Effect of pressure and temperature on interfacial tension**

Increasing pressure significantly reduces the CO<sub>2</sub>-water interfacial tension. This is well supported by much literature data [Chun and Wilkinson 1995, Park et al., 2005, Georgiadis et al., 2010, Nielsen et al., 2012, Sarmadivaleh et al., 2015, Arif et al., 2016] and molecular dynamics data [Iglauer et al., 2012b, Tsuji et al., 2013]. Furthermore, it was reported that CO<sub>2</sub>-water interfacial tension increases with increasing temperature [Chun and Wilkinson 1995, Park et al., 2005, Georgiadis et al., 2010, Iglauer et al., 2012b, Tsuji et al., 2013, Sarmadivaleh et al., 2015, Arif et al., 2016]. However, little literature data have shown a constant relation of IFT with increasing temperature [Tsuji et al., 2013, Nielsen et al., 2012].

### **2.4.5. Effect of CO<sub>2</sub> injection on permeability**

It is important to understand the nature of the interaction between fluid and rock in order to safely store CO<sub>2</sub> in the ground [Sayegh et al., 1990, Nightingale et al., 2009, Carroll et al., 2011]. Such interactions, on the other hand, affect the aquifer permeability and consequently the injectivity [Wiese et al., 2010]. Therefore, permeability and permeability alteration should be carefully evaluated to properly design CO<sub>2</sub> injection projects, because injected CO<sub>2</sub> dissolves in reservoir in-situ water to produce a weak carbonic acid [Nightingale et al. 2009, Carroll et al., 2011, Iglauer 2011]. This acid reacts with rock minerals leading to ionic dissolution-precipitation as well as forming secondary minerals [Worden and Smith, 2004]. Therefore, sandstone formations are considered to be the best candidates for CO<sub>2</sub> sequestration [IPCC 2005]. However, sandstone typically contains components (cements, clays) other than quartz [Delle et al., 2013], and these

impurities usually have a substantially higher reactivity in an acidic environment than quartz [Fischer et al., 2010; Carroll et al., 2011], especially in the carbonate brine (live brine) at reservoir condition, which has low pH (about 3 to 4) [Schaeff and McGrail, 2004, Sigfusson et al., 2015]. Also, CO<sub>2</sub> can be trapped in the pore spaces of rock for several hundreds of years [Ballentine et al., 2001].

### **3. Chapter 3: Efficient separation scheme for binary mixture of CO<sub>2</sub> and H<sub>2</sub>S using aromatic components**

#### **3.1. Introduction**

With fossil-fuel consumption accounting for more than 80% of energy use, CO<sub>2</sub> concentration in the atmosphere is bound to increase [48] [49, 50]. This increase in CO<sub>2</sub> concentration is considered the main cause of climate change and the increase in global temperatures [51-53]. However, once CO<sub>2</sub> is captured and transported, it can be injected underground for storage [54] and/or enhanced oil recovery processes (EOR) [55, 56]. Moreover, in EOR, it is preferred that CO<sub>2</sub> containing less than 100 PPM H<sub>2</sub>S [57] is injected, as it might be a safety hazard [58] and corrosive [59]. On the other hand, high-purity hydrogen sulfide can be converted to hydrogen fuel and sulfur through photoelectrochemical processes and other methods [60].

Several experimental and theoretical researchers have focused on the reactive absorption of H<sub>2</sub>S and CO<sub>2</sub> from gas mixtures containing small or trace amounts of H<sub>2</sub>S or both gasses. These researchers have mostly been driven by the need for natural gas sweetening [61]. Adsorption has also been studied both experimentally and theoretically as a method for removing trace amounts of H<sub>2</sub>S from biogas or other gas mixtures containing CO<sub>2</sub> [62], ion exchange resins [63], or centrifugation [64]. In addition, separating CO<sub>2</sub>/H<sub>2</sub>S using ionic liquids at room temperature has been reported. For example, separating CO<sub>2</sub>/H<sub>2</sub>S using ([bmim][MeSO<sub>4</sub>]) based on a modified RK (Redlich-Kwong) EOS [65].

Few studies have reported on separating binary mixtures of CO<sub>2</sub> and H<sub>2</sub>S. [66] investigated separating the binary mixture of H<sub>2</sub>S and CO<sub>2</sub> using pressure swing adsorption (PSA) in molecular sieves 4A, 5A, and 13X.

Separating a mixture of CO<sub>2</sub>/H<sub>2</sub>S into two products through distillation is difficult and complicated because of the converging relative volatility of the two gases [67]. The relative volatilities of CO<sub>2</sub>

and H<sub>2</sub>S are close, especially when the CO<sub>2</sub> concentration goes beyond 80% [67] [57]; as a result, the separation process can be complicated and several separating stages will be required [57]. However, adding a solvent (agent) to the distillation column during separation can better facilitate this procedure.

| Nomenclatures               |                                 |
|-----------------------------|---------------------------------|
| CO <sub>2</sub>             | Carbon dioxide                  |
| H <sub>2</sub> S            | Hydrogen Sulfide                |
| EOR                         | Enhance Oil Recovery            |
| C <sub>3</sub> <sup>+</sup> | Propane and Heavier Hydrocarbon |
| RV                          | Relative Volatility             |
| PR                          | Peng Robinson                   |
| SRK                         | Soave Redlich Kwong             |
| EOS                         | Equation of State               |
| EB                          | Ethylbenzene                    |
| O-Xylene                    | Ortho Xylene                    |
| M-Xylene                    | Meta Xylene                     |

Furthermore, many solvents have been used in distilling CO<sub>2</sub>/H<sub>2</sub>S to improve the separation process and reduce costs and energy consumption [57]; however, solvent selection requires many considerations such as relative volatility, the low freezing point, and H<sub>2</sub>S/ agent separation [57, 67]. Yao et al. [59] added hydrocarbons (C<sub>3</sub><sup>+</sup>) as solvents (agents) to the distillation column (above the feeding point) to increase the relative volatility of CO<sub>2</sub>/H<sub>2</sub>S. However, there are many disadvantages to using such agents (alkanes) as solvents. These disadvantages include [68] poor selectivity between CO<sub>2</sub> and H<sub>2</sub>S compared to other solvents, such as aromatic solvents that require a higher

reflux rate and a higher solvent circulation rate. Accordingly, the refrigeration duty will be higher; and [68] the low molecular weight of alkanes also leads to a significant loss in the solvents.

Aromatic compounds are very effective solvents in CO<sub>2</sub>/H<sub>2</sub>S separation because of their high molecular weight and low freezing points. Separation occurs best when the solvent molecular weight is between 90 and 125 and the freezing point is below -45 °C; this avoids solvent solidification [59]. In addition, because of these solvents' high selectivity, the circulation rate and overhead reflux ratio of the distillation column can be reduced. Accordingly, the regeneration requirement and reflux rates will be reduced [59].

In this work, different solvents and operating conditions for separating a CO<sub>2</sub>-H<sub>2</sub>S binary mixture have been simulated by distillation using Aspen HYSYS software. Furthermore, three aromatic compounds have been evaluated for increasing the relative volatility of CO<sub>2</sub>/H<sub>2</sub>S, reducing the quantity of the solvent required and the energy consumption.

### **3.1.1. Process description**

Separating liquid mixtures through distillation depends on differences in the components' volatility. The separation becomes easier as the relative volatilities increase. As shown in Figure 3-1, the gas feed stream (1) at 1000 kgmole/hr enters the middle of the first distillation column (T-100) at -15°C and 10 bar with CO<sub>2</sub> contents from 10-90 mol%. The first distillation column has 30-40 theoretical stages and operates at 7 bar. In case of O-Xylene, the first column (T-101) operates at 20 bar to prevent freezing of the agent (O-Xylene), this is because of the freezing point of O-xylene (-25 °C) is higher than the other solvents. Aspen HYSYS simulation was used in the steady state mode and the Peng-Robinson equation of state was applied for the dynamic studies. The solvent at 8°C and 8 bar was fed to stage 2 near the top of the column, as this is the location where the relative volatility of CO<sub>2</sub> to H<sub>2</sub>S has to be increased [57]. The amount of solvent added was based on the CO<sub>2</sub> concentration in the feed [57]. Although it is possible to add the solvent to the top of the column,



including into the condenser, this is not usually preferable because the agent cannot then be separated efficiently from the overhead product. Thus, adding the solvent at a point below the column top is desirable for additive separation from the desired overhead product [57]. The overhead product of the first distillation column is CO<sub>2</sub>, which has less than 100 ppm H<sub>2</sub>S. The bottom product enters the heat exchanger to increase the stream temperature and then enters the second distillation column (T-101), which is a solvent recovery column. The solvent recovery column has 10 theoretical stages and operates at 5 bar. The reflux ratio and H<sub>2</sub>S mole fraction in the bottom stream were selected to set the column specs. The reflux ratio and H<sub>2</sub>S mole fraction were set at 0.6 and 10<sup>-5</sup> respectively. The top product of the second column is a pure H<sub>2</sub>S and the bottom product is the aromatic solvent. Afterward, the solvent is recycled to the first distillation column. Operating parameters of the process are presented in Table 3-1.

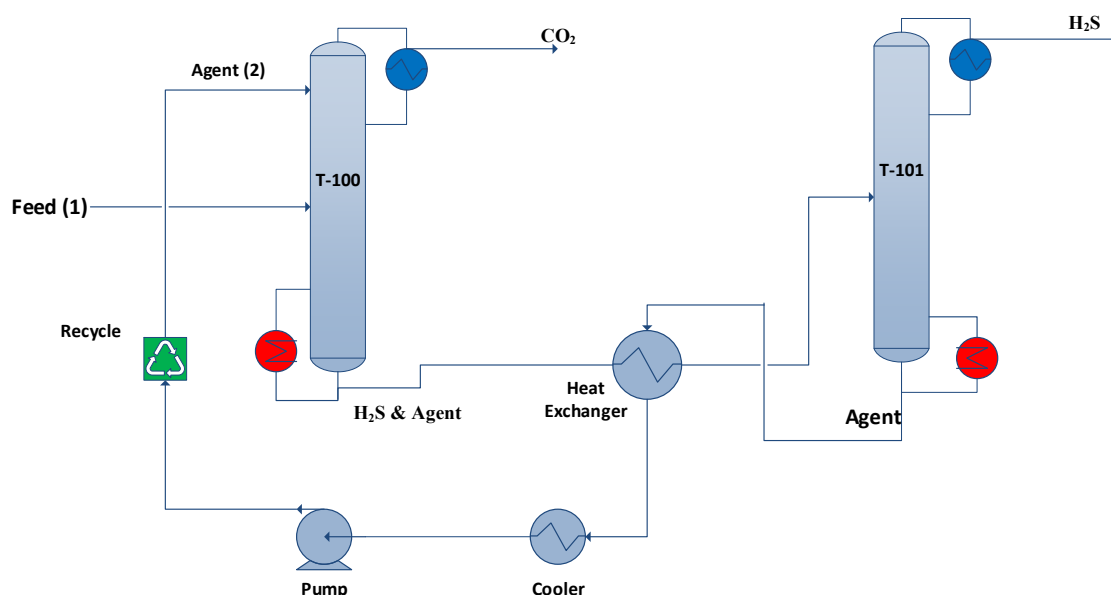


Figure 3-1. Process flow diagram of CO<sub>2</sub>/H<sub>2</sub>S separation

Table 3-1. The operating parameters were applied in simulation process

| T-100  |                         |          |       |         |
|--|-------------------------|----------|-------|---------|
|  | M-Xylene                | O-Xylene | E.B   | Toluene |
| Feed ( CO <sub>2</sub> & H <sub>2</sub> S) (Kgmole/hr) | 1000                    | 1000     | 1000  | 1000    |
| CO <sub>2</sub> /H <sub>2</sub> S Composition          | 90/10                   | 90/10    | 90/10 | 90/10   |
| Feed Temp. (°C)  | -10                     | -10      | -10   | -10     |
| Feed Pressure (bar)                                    | 10                      | 21       | 10    | 10      |
| Feed stage point                                       | 15                      | 20       | 20    | 20      |
| Agent (Kgmole/hr)                                      | 310                     | 410      | 430   | 400     |
| Agent Temp. (°C)                                       | 8                       | 8        | 8     | 8       |
| Agent Pressure (bar)                                   | 10                      | 21       | 10    | 10      |
| Agent stage point                                      | 2 (Below the condenser) | =        | =     | =       |
| Theoretical stages                                     | 30                      | 40       | 40    | 40      |
| Column Pressure (bar)                                  | 8                       | 20       | 8     | 8       |
| Column Overhead Temp. (°C)                             | -45                     | -20      | -52   | -52     |
| Column Bottom Temp. (°C)                               | 60                      | 160      | 50    | 66      |
| Overhead H <sub>2</sub> S (ppm)                        | 70                      | 70       | 70    | 70      |
| Bottom CO <sub>2</sub> (ppm)                           | 0                       | 0        | 0     | 0       |
| Reflux Ratio   | 1                       | 1        | 1     | 1       |

### 3.2. Numerical implementation

In this study, the distillation processes in Figure 3-1 have been simulated using Aspen HYSYS 7.2, which is a set of comprehensive process-modeling tools used by the world's leading oil and gas producers, refineries, and engineering companies for process simulation and process optimization in design and operation. The Peng-Robinson (PR) equation of state has been selected for all simulation calculations.

#### 3.2.1. Selection of equation of state

The thermodynamic model has a huge impact on such kind of simulation process. HYSYS provides enhanced equations of state (PR and SRK) for the strict treatment of hydrocarbon systems and sour gases separation. For oil, gas, and petrochemical applications, the Peng–Robinson EOS (PR) and Soave Redlich Kwong (SRK) are usually recommended [65, 69]. The PR and Soave Redlich Kwong equations of state have been enhanced to yield accurate phase equilibrium calculations for systems ranging from low-temperature cryogenic systems to high-temperature, high-pressure reservoir systems [69]. In addition, Vitu, S. et al. [70] used PR EOS to predict the phase equilibria of CO<sub>2</sub> and Hydrocarbon system and found accurate results in many cases. Moreover, Jaubert et al. [71] have chosen PR EOS to predict the phase equilibria of syntheses petroleum fluids ( Alkanes, aromatics, CO<sub>2</sub>, H<sub>2</sub>S, N<sub>2</sub> and more) and they reported that the model was a successful due to the high accuracy results for nonpolar compounds using PR EOS. In 2008, Privat et al. [72] have added H<sub>2</sub>S group for their model to calculate the temperature dependent binary interaction parameters ( $K_{ij}$ ) and they obtained an accurate behavior prediction of the system containing H<sub>2</sub>S. The PR equation of state in HYSYS simulation applies a functionality to some specific component-component interaction parameters. Key component receiving special treatment include He, H<sub>2</sub>, N<sub>2</sub>, CO<sub>2</sub>, H<sub>2</sub>S, MEG, TEG, CH<sub>3</sub>OH and more. For other EOS model,  $K_{ij}$  will be generated automatically by HYSYS for improved VLE property predictions. Last and not least, PR EOS has been relied on in

this simulation process due to the compatibility of this model to describe and predict the CO<sub>2</sub>, H<sub>2</sub>S and aromatic compounds thermodynamic properties.

### **3.2.2. Algorithm and basic equation used for simulation**

#### **3.2.2.1. CO<sub>2</sub> separation column**

A distillation column was selected for simulating the CO<sub>2</sub> separation column.

*Column specs:* Two specs should be defined for the distillation column until the degree of freedom becomes zero. The reflux ratio and H<sub>2</sub>S mole fraction in the top product were selected as column specs.

*Solving methods:* Inside-out: With the “inside-out” based algorithms, simple equilibrium and enthalpy models are used in the inner loop to solve the overall component and heat balances as well as any specifications. The outer loop updates the simple thermodynamic models with rigorous model calculations. The inside-out algorithm has become one of the most popular methods because of its robustness and its ability to solve a wide variety of columns [69].

#### **3.2.2.2. Heaters and Coolers**

The heater and cooler operations are one-sided heat exchangers. The inlet stream is heated (or cooled) to the desired outlet conditions while the energy stream provides (or absorbs) the enthalpy difference between the two streams. These operations are useful to discover the energy required to cool or heat a process stream with a utility and without focusing the conditions of the utility itself [69].

#### **3.2.2.3. Pumps**

The pump operation is used to increase the pressure of an inlet liquid stream. Depending on the supplied information, the pump calculates either an unknown pressure, temperature, or pump efficiency [69].

#### **3.2.2.4. Recycle**

The capability of any Flowsheet simulator to solve recycles reliably and efficiently is critical. In this respect, HYSYS has inherent advantages over other simulators, having the unique ability to back-

calculate through many operations in a non-sequential manner, which allows many problems with recycling loops to be solved explicitly

The recycle installs a theoretical block in the process stream. The feed into the block, also known as the calculated recycle stream, and the product is the assumed recycle stream [69].

### **3.3. Process Performance**

The aim of this optimization work is to study the effect of various types of solvents on different concentrations of CO<sub>2</sub> and H<sub>2</sub>S. Therefore, the optimization section will apply various solvents with various quantities that can be achieved by entering them into simulation tools and changing the CO<sub>2</sub>-H<sub>2</sub>S stream compositions as can be shown in table2. The following optimizations steps are assumed:

1. Using 10-90 mol% CO<sub>2</sub> concentrations in inlet stream.
2. Investigating 0, 10, 20 and 40 mol% of Ethylbenzene.
3. Investigating 0, 10, 20 and 40 mol% of O-Xylene.
4. Investigating 0, 10, 20 and 40 mol% of M-Xylene.
5. Investigating 0, 10, 20 and 40 mol% of Toluene.

Table 3-2. Process Optimization Results

| 10/90 mol% CO <sub>2</sub> /H <sub>2</sub> S (1000 kgmole/hr)    | Ethylbenzene | M-Xylene | O-Xylene | Toluene |
|--|--------------|----------|----------|---------|
| Solvent Quantity (kgmole/hr)                                     | 120          | 80       | 130      | 140     |
| Solvent Regeneration column Duty (MW)                            | 1.2          | 1        | 2.7      | 1.4     |
| No. of Trays (T-100)   | 20           | 20       | 20       | 20      |
| Reflux Ratio(T-100)  | 1.5          | 1.5      | 1.5      | 1.5     |
| (T-100) Top Temp(°C)   | -52          | -45      | -20      | -52     |
| (T-100) Pressure (bar)   | 8            | 9        | 20       | 8       |
| <b>50/50 mol% CO<sub>2</sub>/H<sub>2</sub>S (1000 kgmole/hr)</b> |              |          |          |         |
| Solvent Quantity (kgmole/hr)                                     | 260          | 230      | 250      | 290     |
| Solvent Regeneration column Duty (MW)                            | 2.6          | 2        | 2.8      | 2.2     |
| No. of Trays (T-100)   | 30           | 30       | 30       | 30      |
| Reflux Ratio(T-100)  | 1.5          | 1.5      | 1.5      | 1.5     |
| (T-100) Top Temp(°C)   | -52          | -45      | -20      | -52     |
| (T-100) Pressure (bar)   | 8            | 9        | 20       | 8       |
| <b>90/10 mol% CO<sub>2</sub>/H<sub>2</sub>S (1000 kgmole/hr)</b> |              |          |          |         |
| Solvent Quantity (kgmole/hr)                                     | 430          | 310      | 410      | 400     |
| Solvent Regeneration column Duty (MW)                            | 2.9          | 2.5      | 3.3      | 2.5     |
| No. of Trays (T-100)   | 30           | 30       | 30       | 30      |
| Reflux Ratio(T-100)  | 1.5          | 1.5      | 1.5      | 1.5     |
| (T-100) Top Temp(°C)   | -52          | -45      | -20      | -52     |
| (T-100) Pressure (bar)   | 8            | 9        | 20       | 8       |

### 3.4. Result and discussion

#### 3.4.1. Solvents Quantity

As can be seen in Figure 3-2, the solvent's amount has to be increased with increasing CO<sub>2</sub> concentration in the feed stream and this is consistent with the previous literature [59, 67]. The amount of solvent added will be dependent upon factors such as the feed's composition, operating pressure, throughput of the column, recovery of overhead, and bottoms product desired [57]. Based on the results shown in Figure 3-2, the amount of solvent required for m-Xylene was about 22.5% lower than that required for toluene at 90 mol% CO<sub>2</sub>. This is because of the difference in the solvent's properties such as freezing point and molecular weight [59].

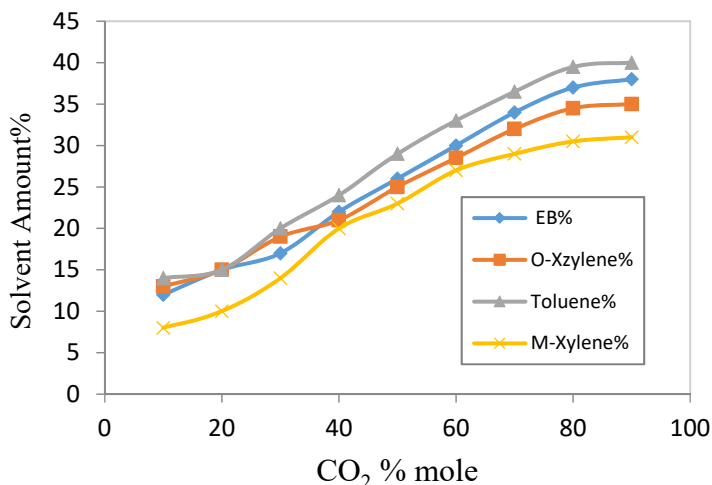


Figure 3-2. Effect of various CO<sub>2</sub> concentrations in mole% on solvent amount (%)

#### 3.4.2. Relative Volatility

The relative volatility is a measure comparing the vapor pressures of the components in a liquid mixture of chemicals. This measure is widely used in designing large industrial distillation processes. In effect, the relative volatility indicates the ease or difficulty of using distillation to

separate more volatile components from those that are less volatile. The relative volatility of two components can be expressed as the ratio of their K values:

$$\alpha_{ij} = \frac{K_i}{K_j} = \frac{(y_i/x_i)}{(y_j/x_j)} \quad (9)$$

Where:

$\alpha$  = Relative Volatility

K = Equilibrium Constant

y = Vapour phase component fraction

x = Liquid phase component fraction

Figures 3.3-3.5 show the relative volatility of carbon dioxide to hydrogen sulfide at different concentrations of Ethylbenzene, m-Xylene, o-Xylene, and toluene respectively. As can be noticed in Figure 3-3, the relative volatility of CO<sub>2</sub> to H<sub>2</sub>S was 1.2 at high concentration of CO<sub>2</sub> and with no agent present; however, the relative volatility increases by approximately 50% when a 40% concentration of ethylbenzene is added. Figure 3-4 shows that by adding 40% of m-Xylene, the relative volatility increases by approximately 60% in comparison to when no solvent is present. In Figure 3-5, the relative volatility increases by 63% when a 40% concentration of o-Xylene is added. Figure 3-6 shows that the relative volatility of CO<sub>2</sub> to H<sub>2</sub>S increases by about 55% when 40% toluene is added. Increases in the relative volatility of CO<sub>2</sub> to H<sub>2</sub>S using aromatic compounds are as a result of properties such as molecular weight, freezing point, and volatility. In addition, it was noticed that easier separation can occur at the high relative volatility of CO<sub>2</sub> to H<sub>2</sub>S [59].



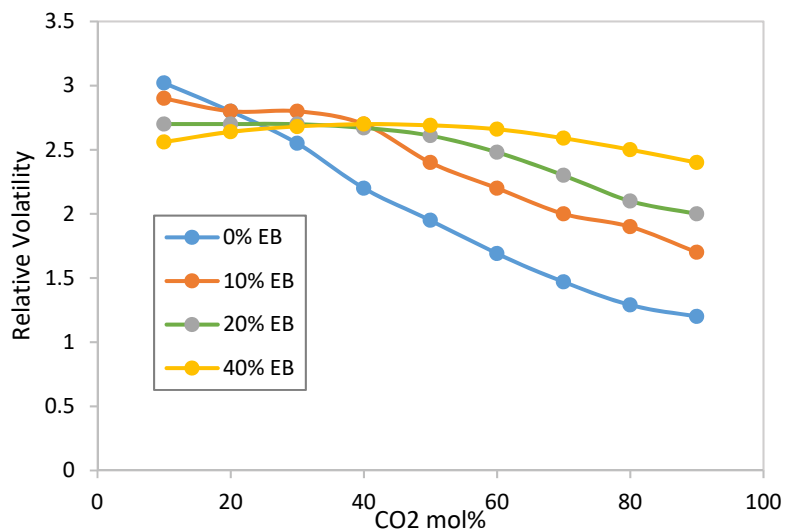


Figure 3-3. Relative volatility of CO<sub>2</sub> to H<sub>2</sub>S for various EB concentrations.

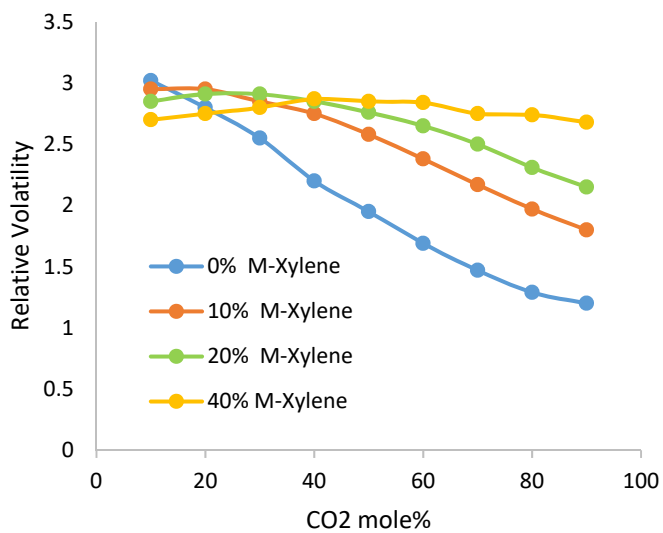


Figure 3-4. Relative volatility of CO<sub>2</sub> to H<sub>2</sub>S for various M-Xylene concentrations.

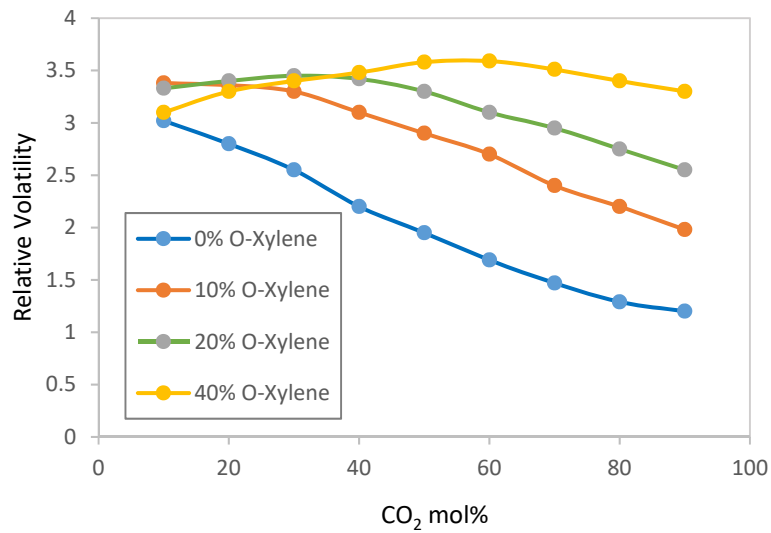


Figure 3-5. Relative volatility of CO<sub>2</sub> to H<sub>2</sub>S for various O-Xylene concentrations.

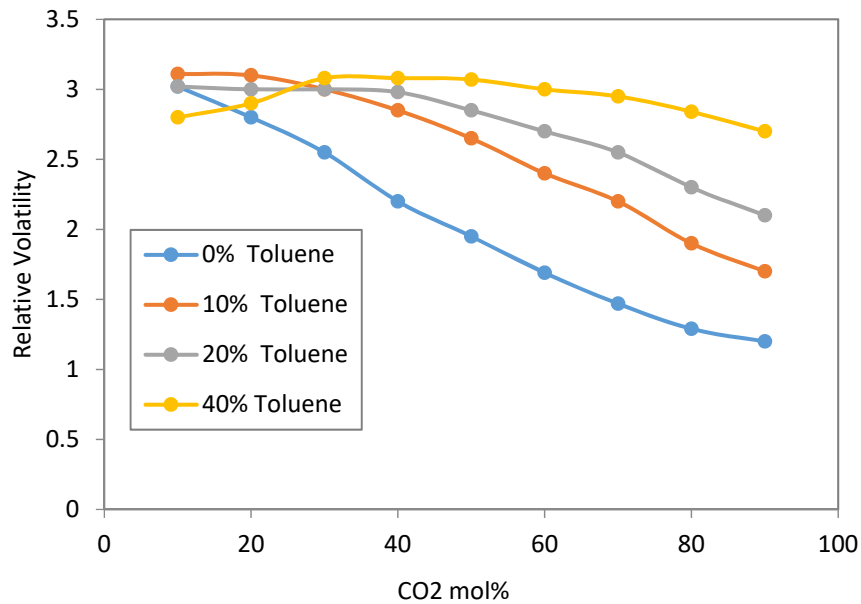


Figure 3-6. Relative volatility of CO<sub>2</sub> to H<sub>2</sub>S for various Toluene concentrations.

### 3.4.3. Energy Consumption

Figure 3-7 shows that the total duty required to separate H<sub>2</sub>S from a binary mixture that contains 90 mol% of CO<sub>2</sub> decreases from o-Xylene to m-Xylene solvent. The amount of total duty required by m-Xylene is 29.77% lower than that of o-Xylene. This is because the freezing point of m-Xylene (-48°C), which is much lower than the freezing point of o-Xylene (-24°C), makes the separation process easier [57].

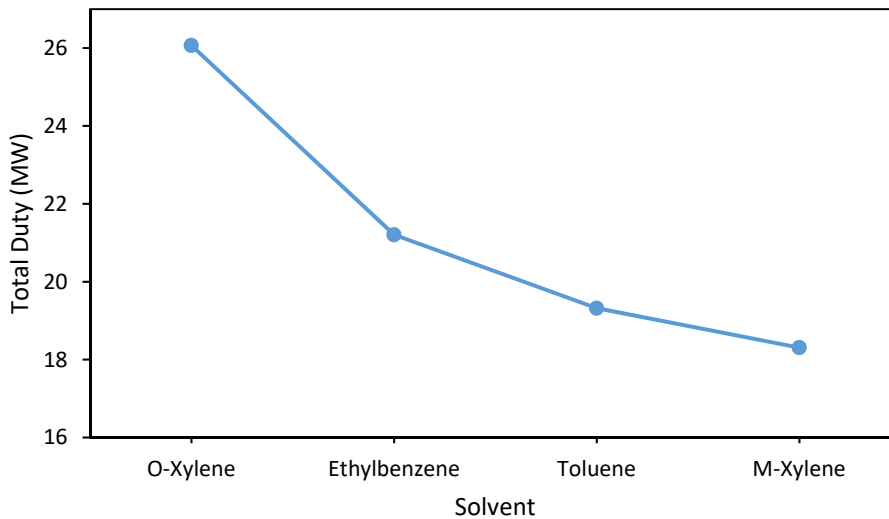


Figure 3-7. Amount of duty required for separation H<sub>2</sub>S from 90 mol% of CO<sub>2</sub>

### 3.4.4. Effect of Solvents on Phase Diagram

Figure 3-8 displays the practical difficulty of obtaining a substantially complete separation of carbon dioxide from hydrogen sulfide in a binary mixture. It can be seen that the bubble and dew points plot for the pure binary at 10 bar tends to pinch together. This separation becomes difficult at 80% carbon dioxide or higher [57, 59]. Thus, the overhead product from a column would normally be limited to about 80% carbon dioxide, unless many of theoretical stages are added to the column

[57]. To solve this issue (i.e. the separation), a solvent is added into these gas mixture to increase the relative volatility. As can be seen in Figure 3-9, when 20% solvent is added, it widens the phase diagram of CO<sub>2</sub>-H<sub>2</sub>S, which eases the separation process.

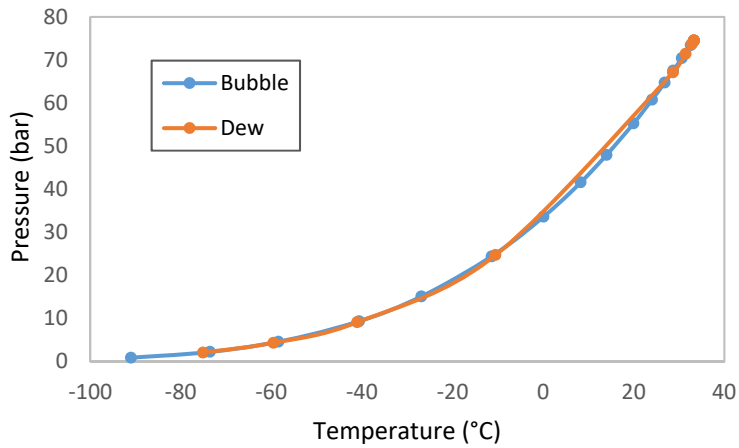


Figure 3-8. Phase diagram of 90% CO<sub>2</sub> and 10% H<sub>2</sub>S

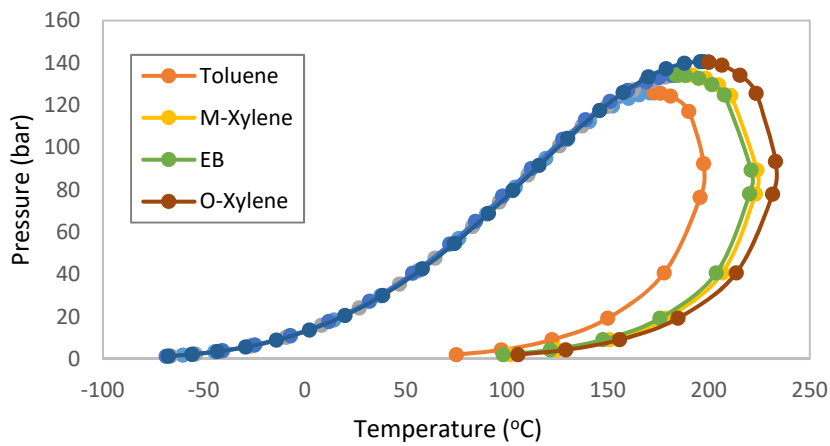


Figure 3-9. Phase diagram of 90% CO<sub>2</sub> and 10% H<sub>2</sub>S in 20% solvent

### 3.4.5. CO<sub>2</sub> and H<sub>2</sub>S Purities and Recoveries

As can be seen in Figure 3-9 and Table 3-3, the purities and recoveries of H<sub>2</sub>S and CO<sub>2</sub> using aromatic compounds are quite high (greater than 99.9%) in comparison to the results, which have been done in other separation processes such as PSA (18). This is because the selectivity of aromatic compounds for H<sub>2</sub>S is high. The highest purity and recovery for CO<sub>2</sub> using PSA were 92% and 93% respectively while for H<sub>2</sub>S were 71% and 91% respectively. In addition, the low H<sub>2</sub>S purity and recovery obtained with SPA could be due in part to another factor affecting the PSA system performance. One such factor could be the purge-to-feed ratio, which is the ratio of desorption purge flow rate to the feed flow rate during adsorption [66]. Furthermore, the properties of aromatics compounds, such as freezing points, high selectivity, and the molecular weights, also have an effect to obtain a high purity and recovery for CO<sub>2</sub> and H<sub>2</sub>S.

Table 3-3. Purities, Recoveries of CO<sub>2</sub>, and H<sub>2</sub>S for various CO<sub>2</sub> concentrations

| 10% CO <sub>2</sub>                               | Ethylbenzene    | M-Xylene       | O-Xylene            | Toluene          |
|---|-----------------|----------------|---------------------|------------------|
| <b>H<sub>2</sub>S ppm (CO<sub>2</sub> Purity)</b> | 80<br>( >99.9%) | 80<br>(>99.9%) | 80<br>( >99.9%)     | 80<br>( >99.9%)  |
| <b>CO<sub>2</sub> Recovery (%)</b>                | 99.99<br>99.99  | 99.99<br>99.99 | 99.99<br>99.99      | 99<br>98         |
| <b>H<sub>2</sub>S Recovery</b>                    | 0               | 0              | 0                   | 0                |
| <b>H<sub>2</sub>S Purity (CO<sub>2</sub> ppm)</b> |                 |                |                     |                  |
| 50% CO <sub>2</sub>                               |                 |                |                     |                  |
| <b>H<sub>2</sub>S PPM (CO<sub>2</sub> Purity)</b> | 80<br>(>99.9%)  | 80<br>(>99.9%) | 80(>99.9%)<br>99.99 | 80(>99.9%)<br>99 |
| <b>CO<sub>2</sub>Recovery (%)</b>                 | 99.99           | 99.99          | 99.99               | 98               |
| <b>H<sub>2</sub>S Recovery</b>                    | 99.99           | 99.99          | 0                   | 0                |
| <b>H<sub>2</sub>S Purity (CO<sub>2</sub> ppm)</b> | 0               | 0              |                     |                  |
| 90% CO <sub>2</sub>                               |                 |                |                     |                  |
| <b>H<sub>2</sub>S PPM (CO<sub>2</sub> Purity)</b> | 70<br>(>99.9%)  | 70<br>(>99.9%) | 70(>99.9%)          | 70(>99.9%)       |
| <b>CO<sub>2</sub>Recovery (%)</b>                 | 99.99           | 99.99          | 99.99               | 99               |
| <b>H<sub>2</sub>S RECOVERY (%)</b>                | 99.99<br>0      | 99.99<br>0     | 99.99<br>0          | 98<br>0          |
| <b>H<sub>2</sub>S Purity (CO<sub>2</sub> ppm)</b> |                 |                |                     |                  |

### 3.5. Conclusions

Although separating H<sub>2</sub>S/CO<sub>2</sub> from gaseous mixtures has been presented before, demonstrations for CO<sub>2</sub>/H<sub>2</sub>S as a binary mixture reported in the literature are limited. In this study, new solvents have been used to separate the carbon dioxide from hydrogen sulfide in a distillation column by simulation using Aspen HYSYS to improve the separation process. It is difficult to separate CO<sub>2</sub> from H<sub>2</sub>S using standard distillation columns with no solvent, especially at high concentrations of CO<sub>2</sub>, because of their low relative volatility. Aromatic compounds have been used as solvents to increase the relative volatility between CO<sub>2</sub> and H<sub>2</sub>S. In this study, m-Xylene has shown to be highly efficient as a solvent for separating CO<sub>2</sub> from H<sub>2</sub>S because of the significant effect on relative volatility and low quantity required for high CO<sub>2</sub> recovery also low energy is required to regenerate the solvent. When selecting solvents, the effect of the agent on relative volatility, the low freezing point of the solvent to avoid solid formation in the column, and the ease of separation of the solvent from H<sub>2</sub>S to recover the solvent and recirculate it to the first distillation column are some factors for consideration. It is important to achieve a high purity of CO<sub>2</sub> for EOR purposes and hydrogen sulfide converted processes.

## 4. Chapter 4: Natural Gas Sweetening Using low temperature Distillation: Simulation and Configuration

### 4.1. Introduction

- **Motivation**

Recently, the demand of natural gas has been dramatically increased. In fact, natural gas plays an important role in the world economy and industry due to the widely used as an industrial and domestic fuel. The stream originating from the wellhead tends to contain a mixture of hydrocarbons in addition to considerable amounts of sour gases, such as CO<sub>2</sub> and H<sub>2</sub>S. As such, the reduction and removal of CO<sub>2</sub> and H<sub>2</sub>S from natural gas has become an integral process associated with reducing the probability of solidification during refrigeration, while simultaneously increasing the heating value of the liquefied natural gas (LNG) [73]. According to pipeline specifications, natural gas must contain <2 vol% CO<sub>2</sub>, while for the liquefaction process, natural gas must contain no more than 50 and 2 ppm of CO<sub>2</sub> and H<sub>2</sub>S, respectively [73]. To date, a range of sweetening methods have been employed, including commercial methods for sour gas removal, such as chemical absorption, physical adsorption, membrane and cryogenic processes [74]. However, the most commonly employed chemical absorption process based on amine solvents requires large solvent volumes at high CO<sub>2</sub> concentrations and it produces CO<sub>2</sub> at low pressures, thereby resulting in a greater compression power downstream [75]. In contrast, low-temperature distillation processes, which are seen as the future of natural gas processing, have the potential to avoid these issues by producing high-pressure CO<sub>2</sub> suitable for EOR while assisting in the liquefaction process [76]. Such low-temperature processes typically begin with the methane component being separated from the ethane-containing feed stream, while the CO<sub>2</sub> and C<sub>3</sub><sup>+</sup> components compose the bottom products [77]. Ethane and CO<sub>2</sub> are then separated in a CO<sub>2</sub> recovery column [20]; however, the operation of this process is hindered by two limiting factors, namely the solidification of CO<sub>2</sub> at cryogenic temperatures [20] and the formation of an azeotrope between CO<sub>2</sub> and ethane because of their relative volatility value approaching unity.7-8].



- **Literature survey**

A number of studies have thus been carried out to address both of these limiting factors. For example, Holmes et al. avoided the freezing out of CO<sub>2</sub> by adding n-butane, which shifted the system operating conditions away from critical conditions [6, 7]. This process utilises recycled n-butane from downstream separation equipment to maximise the efficiency and economy of the separation process. Several other studies conducted since the advent of the above Ryan-Holmes process have indicated that utilising one or a combination of C<sub>3</sub>–C<sub>6</sub> species can aid in reducing the freezing point of CO<sub>2</sub> and preventing solid formation.

Similar to the work conducted on the freezing point depreciation of CO<sub>2</sub> in a demethaniser, Holmes et al. addressed azeotrope formation through the addition of a combination of heavier hydrocarbons, such as propane, n-butane, n-pentane, and n-hexane [7]. They also reported that the most efficient separation of CO<sub>2</sub> and ethane occurred when the agents were added close to the condenser [1].

Lastari et al. explored the use of single-component solvent streams (C<sub>3</sub>–C<sub>5</sub>) to separate a binary feed stream of CO<sub>2</sub> and ethane. This was based on a simulation study of extractive distillation [3]. They found that the minimum solvent volume required decreased with the use of heavier hydrocarbons, with the propane to n-pentane series being examined. Propane was the least desirable solvent for this process because of its high relative volatility and its presence in relatively large quantities in the overhead product, which resulted in the requirement for a significantly higher reflux ratio to achieve the desired product compositions [75]. In contrast, reduced volumes of n-pentane were required, and this solvent exhibited the lowest energy requirement. A further study into the feasibility of a varied-composition additive stream was also reported by Lastari et al., which led to the claim that mixed components containing lower levels of n-propane were favourable in terms of the solvent volume required [65]. Berstad et al. utilised a different approach in avoiding the formation and freeze-out of azeotropes through the recycling of pentane and hexane in an unconventional column configuration [10]. They used a scheme consists of six distillation columns simulated by HYSYS with the ability to separate a feed stream containing 50 mole% of CO<sub>2</sub> into a methane stream containing 50 ppm CO<sub>2</sub> and a high purity CO<sub>2</sub> stream fit for reinjection.. These results indicated that additional columns aid in the separation of propane and heavier compounds. Furthermore, Kobayashi et al. experimentally implemented n-pentane as the additive agent to combat the formation of the azeotrope between CO<sub>2</sub> and ethane [11].

The removal of H<sub>2</sub>S from natural gas through distillation is challenging because of the relatively close volatilities of CO<sub>2</sub> and H<sub>2</sub>S at medium and high CO<sub>2</sub> concentrations, which mean that

additional stages of separation are required, and the process becomes more complicated [57]. Thus, the separation of H<sub>2</sub>S from CO<sub>2</sub> and other natural gas components can be aided by the addition of a solvent to alter the relative volatilities of the components. For example, Yao et al. experimentally employed heavy (C<sub>3</sub><sup>+</sup>) hydrocarbons, although this led to a poor selectivity between H<sub>2</sub>S and CO<sub>2</sub> [13]. Alternatively, aromatic compounds were found to be particularly efficient and effective solvents for separation of the two gases because of their high molecular weights and relatively low freezing points [59]. In addition, Alnili et al. explored in a simulation study the use of xylene as a potential agent in the separation process, and successfully achieved sufficient separation of H<sub>2</sub>S from CO<sub>2</sub> [14].

- **Contribution**

After a broad analysis of low temperature separation technologies in sour gas removal from natural gas, a major gap in the research was discovered. Previous research included process schemes designed for the removal of either CO<sub>2</sub> or H<sub>2</sub>S but in no case have both been seen to be removed in a single process flowsheet. The simulation based study presented here addresses this gap in conveying a flow sheet that removes both CO<sub>2</sub> and H<sub>2</sub>S simultaneously using the low temperature distillation process.

Sour gas separation is also explored following the addition of various solvents, and these solvents are evaluated with regard to their efficiency in achieving the required levels of separation. In addition, the product stream compositions are analysed as a factor of the solvent flow rate. We also analyse the energy consumption of the distillation columns and tabulate these results against the CO<sub>2</sub> composition of the feed stream. Finally, the effect of different reflux ratios on the composition of the top product in the CO<sub>2</sub> recovery column is evaluated in conjunction with the CO<sub>2</sub> purity.

## **4.2. Process description**

The selection of a suitable process configuration for the removal of CO<sub>2</sub> and H<sub>2</sub>O was achieved through careful examination of the literature.

A simplified process flow diagram is given in Figure 4-1 above, where the overall process flow scheme includes the implementation of seven distillation columns operated under varying operating conditions (i.e., pressure, temperature, and reflux ratio). As indicated, the dehydrated feed stream enters the process at the C<sub>3</sub><sup>+</sup> removal column, in which propane and heavier hydrocarbons are

separated from the sour gases, methane and ethane. The distillate from the  $C_3^+$  removal column becomes the feed stream for the demethaniser column, with the primary objective of separating methane from ethane,  $CO_2$ , and  $H_2S$ . An n-butane additive is then added to the top of the column with the aim of decreasing the freezing temperature of  $CO_2$  to prevent freeze-out. Methane and nitrogen exit the column as the distillate, leaving the bottoms stream containing  $CO_2$ ,  $H_2S$ , ethane, and n-butane.

The separation of  $H_2S$  from the remainder of the stream is then carried out using the subsequent column. In this case, an external agent (i.e., toluene) is added to the column to address the issue regarding the similar volatilities of  $H_2S$  and  $CO_2$ , and to improve separation. The toluene stream is introduced towards the top of the column and can be detected in the bottoms product along with the separated  $H_2S$  and n-butane, while the column distillate is composed of  $CO_2$  and ethane. Separation of the toluene from  $H_2S$  is achieved using a recovery column, thereby allowing this solvent to be recycled. Similarly, n-butane is separated from  $H_2S$  using an n-butane recovery column.

The distillate from the  $H_2S$  separation column is then employed as the feed for the  $CO_2$  and ethane separation column. As in the case of  $H_2S$ , the similar volatilities of the two components result in the formation of an azeotrope containing 33.3 mol/mol ethane and 66.6 mol/mol  $CO_2$  at the top of the column under normal operating conditions. The addition of n-butane as a solvent alleviates this issue by increasing the relative volatilities of the two components. This column allows the complete separation of  $CO_2$  from ethane under the appropriate operating conditions, giving a  $CO_2$  distillate and a bottoms product containing n-butane and the separated ethane. This solvent is then recovered using a conventional distillation column where pure ethane exits as the distillate and the solvent becomes the bottoms product. The solvent is then recycled back into the  $CO_2$  separation column to complete the separation cycle. Details regarding the columns employed and the obtained product compositions are listed in Table 4-1 and Table 4-2, respectively.

Table 4-1. Columns Conditions

| Conditions            | Units | T-100  | T-101 | T-102  | T-103 | T-104  | T-105  | T-106 |
|-----------------------|-------|--------|-------|--------|-------|--------|--------|-------|
| Theoretical Stage     | -     | 30     | 60    | 50     | 16    | 24     | 50     | 40    |
| Feed Stage            | -     | 17     | 30    | 30     | 8     | 12     | 25     | 20    |
| Additive Feed Stage   | -     | -      | 2     | 2      | -     | -      | 3      | -     |
| Condenser Pressure    | bar   | 37     | 35    | 14     | 5     | 6      | 25     | 6     |
| Reboiler Pressure     | bar   | 38     | 35    | 15     | 6     | 7      | 26     | 7     |
| Condenser Temperature | °C    | -54.43 | -92   | -34.57 | 41.87 | -20.45 | -15.56 | -35   |
| Reboiler Temperature  | °C    | 125.5  | 23.46 | 104.2  | 187.7 | 62.99  | 67.88  | 79.44 |
| Condenser Duty        | MW    | 14.04  | 7.514 | 4.499  | 3.972 | 3.847  | 4.252  | 2.77  |
| Reboiler Duty         | MW    | 19.99  | 8.039 | 10.68  | 8.451 | 1.032  | 5.971  | 3.401 |
| Reflux Ratio          | -     | 1      | 2     | 2      | 1     | 2      | 2      | 1     |

Table 4-2. Column compositions (mole%)

|                       | <b>T-100</b> |        | <b>T-101</b> |        | <b>T-102</b> |        | <b>T-103</b> |        | <b>T-104</b> |        | <b>T-105</b> |        | <b>T-106</b> |        |
|-----------------------|--------------|--------|--------------|--------|--------------|--------|--------------|--------|--------------|--------|--------------|--------|--------------|--------|
|                       | Top          | Bottom | Top          | Bottom | Top          | Bottom | Top          | Bottom | Top          | Bottom | Top          | Bottom | Top          | Bottom |
| <b>C<sub>1</sub></b>  | 0.817        | 0.00   | 0.99         | 0.0239 | 0.046        | 0.00   | 0.00         | 0.00   | 0.00         | 0.00   | 0.1025       | 0.00   | 0.00         | 0.00   |
| <b>C<sub>2</sub></b>  | 0.0837       | 0.0005 | 0.00         | 0.29   | 0.57         | 0.00   | 0.00         | 0.00   | 0.00         | 0.00   | 0.0033       | 0.33   | 0.9991       | 0.00   |
| <b>C<sub>3</sub></b>  | 0.0035       | 0.458  | 0.00         | 0.0166 | 0.00         | 0.0181 | 0.0347       | 0.00   | 0.115        | 0.00   | 0.00         | 0.00   | 0.00         | 0.00   |
| <b>iC<sub>4</sub></b> | 0.00         | 0.1725 | 0.00         | 0.00   | 0.00         | 0.00   | 0.00         | 0.00   | 0.00         | 0.00   | 0.00         | 0.00   | 0.00         | 0.00   |
| <b>nC<sub>4</sub></b> | 0.00         | 0.2571 | 0.00         | 0.37   | 0.00         | 0.4    | 0.77         | 0.00   | 0.00         | 1.0    | 0.0031       | 0.67   | 0.0008       | 1.00   |
| <b>iC<sub>5</sub></b> | 0.00         | 0.0086 | 0.00         | 0.00   | 0.00         | 0.00   | 0.00         | 0.00   | 0.00         | 0.00   | 0.00         | 0.00   | 0.00         | 0.00   |
| <b>nC<sub>5</sub></b> | 0.00         | 0.0680 | 0.00         | 0.00   | 0.00         | 0.00   | 0.00         | 0.00   | 0.00         | 0.00   | 0.00         | 0.00   | 0.00         | 0.00   |
| <b>nC<sub>6</sub></b> | 0.00         | 0.0348 | 0.00         | 0.00   | 0.00         | 0.00   | 0.00         | 0.00   | 0.00         | 0.00   | 0.00         | 0.00   | 0.00         | 0.00   |
| <b>CO<sub>2</sub></b> | 0.0598       | 0.00   | 0.00         | 0.2074 | 0.4          | 0.00   | 0.00         | 0.00   | 0.00         | 0.00   | 0.891        | 0.00   | 0.00         | 0.00   |
| <b>H<sub>2</sub>S</b> | 0.027        | 0.00   | 0.00         | 0.094  | 0.00         | 0.102  | 0.196        | 0.00   | 0.884        | 0.00   | 0.00         | 0.00   | 0.00         | 0.00   |
| <b>N<sub>2</sub></b>  | 0.0082       | 0.00   | 0.099        | 0.00   | 0.00         | 0.00   | 0.00         | 0.00   | 0.00         | 0.00   | 0.00         | 0.00   | 0.00         | 0.00   |
| <b>Toluene</b>        | 0.00         | 0.00   | 0.00         | 0.00   | 0.00         | 0.48   | 0.0005       | 1.0    | 0.00         | 0.00   | 0.00         | 0.00   | 0.00         | 1.00   |

### 4.3. Simulation & methodology

The distillation process outlined in Figure 4-1 was developed with the aid of Aspen HYSYS, a simulation software containing comprehensive tools for process simulation. The aim of this study was to produce high purity gas products and high recovery of sour gases. To do so, a scheme with optimum operation conditions was presented with view of reducing cost and energy consumption. The EOS utilised for all calculations in the study was the PR EOS. The feed compositions and essential data employed for the simulation are displayed in Table 4-3.

Table 4-3. Feed stream details

|  |        |
|--|--------|
| Feed Flow rate (kgmole/h)                  | 5000   |
| Temperature (°C)                           | -40    |
| Pressure (bar)                             | 39     |
| CH <sub>4</sub> (mol/mol)                  | 0.7749 |
| C <sub>2</sub> H <sub>6</sub> (mol/mol)    | 0.0794 |
| C <sub>3</sub> H <sub>8</sub> (mol/mol)    | 0.0298 |
| i-C <sub>4</sub> H <sub>10</sub> (mol/mol) | 0.0100 |
| n-C <sub>4</sub> H <sub>10</sub> (mol/mol) | 0.0148 |
| i-C <sub>5</sub> H <sub>12</sub> (mol/mol) | 0.0005 |
| n-C <sub>5</sub> H <sub>12</sub> (mol/mol) | 0.0039 |
| n-C <sub>6</sub> H <sub>14</sub> (mol/mol) | 0.0020 |
| CO <sub>2</sub> (mol/mol)                  | 0.0513 |
| H <sub>2</sub> S (mol/mol)                 | 0.0256 |
| N <sub>2</sub> (mol/mol)                   | 0.0078 |

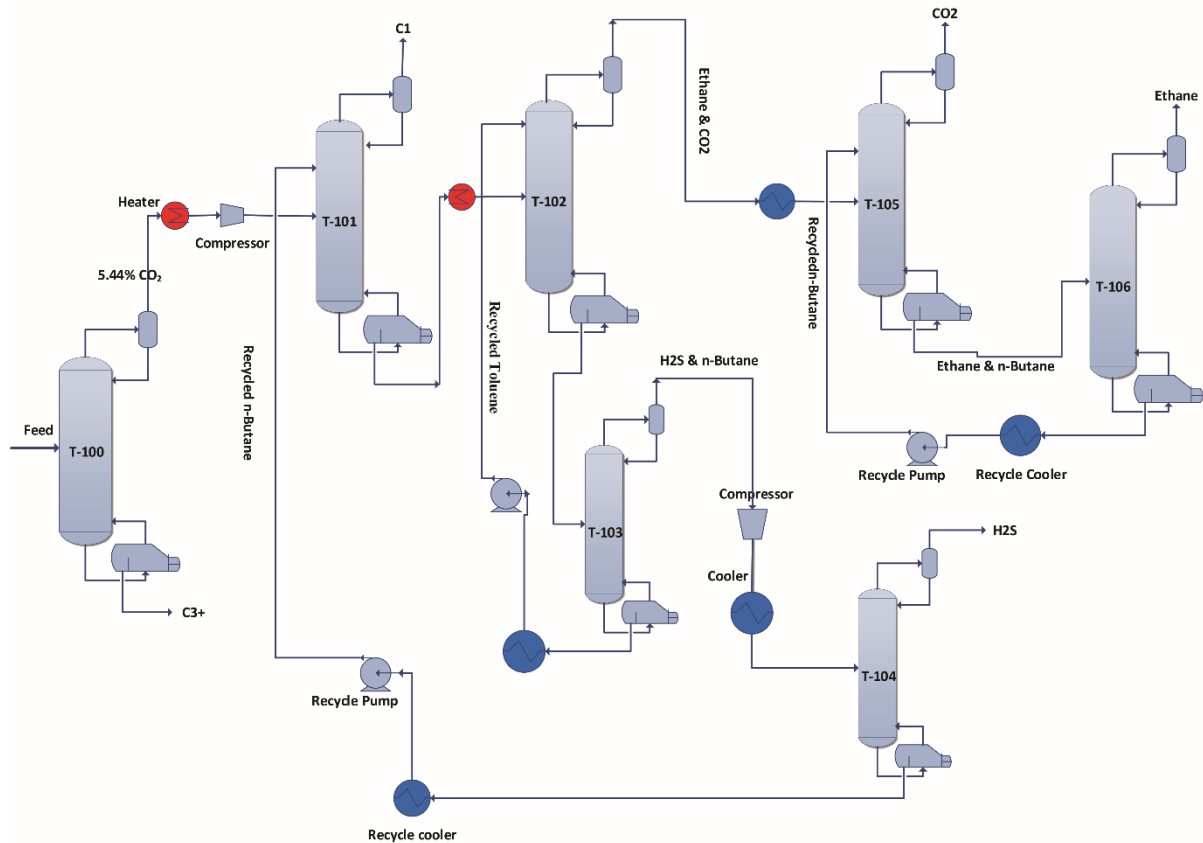


Figure 4-1. Process flow diagram

Selection of the correct thermodynamic model is of particular importance to the process being simulated. In this case, the PR and Soave Redlich Kwong (SRK) EOS were provided by the HYSYS platform for implementation in the treatment of systems containing hydrocarbons and in the separation of the sour gases present in natural gas. We note that the PR and SRK equations are typically recommended for use in oil, gas, and petrochemical processes [65]. Both EOS have been enhanced to produce precise phase equilibrium calculations enveloping low-temperature cryogenic systems to the higher pressure and temperature reservoir systems [78].

In the modelling work carried out by Vitu et al. to predict the phase equilibria of CO<sub>2</sub> and hydrocarbon systems using the PR EOS, particularly accurate results were obtained in various cases [16]. In addition, Jaubert et al. selected the PR EOS to predict the phase equilibria of synthesised petroleum fluids (i.e., alkanes, aromatics, CO<sub>2</sub>, H<sub>2</sub>S, and N<sub>2</sub>, among others), and they reported that the model was successful due to the high accuracy observed for nonpolar compounds [17]. Furthermore, in 2008, Privat et al. included the H<sub>2</sub>S group in their model to calculate the

temperature-dependent binary interaction parameters ( $K_{ij}$ ), and they reported an accurate behaviour prediction of H<sub>2</sub>S-containing systems [18]. We therefore selected the PR EOS for our simulation process due to the compatibility of this model in describing and predicting the thermodynamic properties of CO<sub>2</sub>, H<sub>2</sub>S, and aromatic compounds.

#### 4.4. Results and discussion

##### 4.4.1. CO<sub>2</sub> freezing inhibition

We initially examined the inhibition of CO<sub>2</sub> freezing. In this context, it should be noted that for column T-100, a distillate temperature below  $-56\text{ }^{\circ}\text{C}$  would result in freezing of the CO<sub>2</sub> present in the feed stream. Optimisation of the feed stage, number of stages, condenser pressure, and reboiler pressure ensured that the distillate temperature did not drop below this critical value, thereby preventing the requirement for a tray-by-tray analysis. The tray temperatures for the T-100 column are outlined in Figure 4-2.

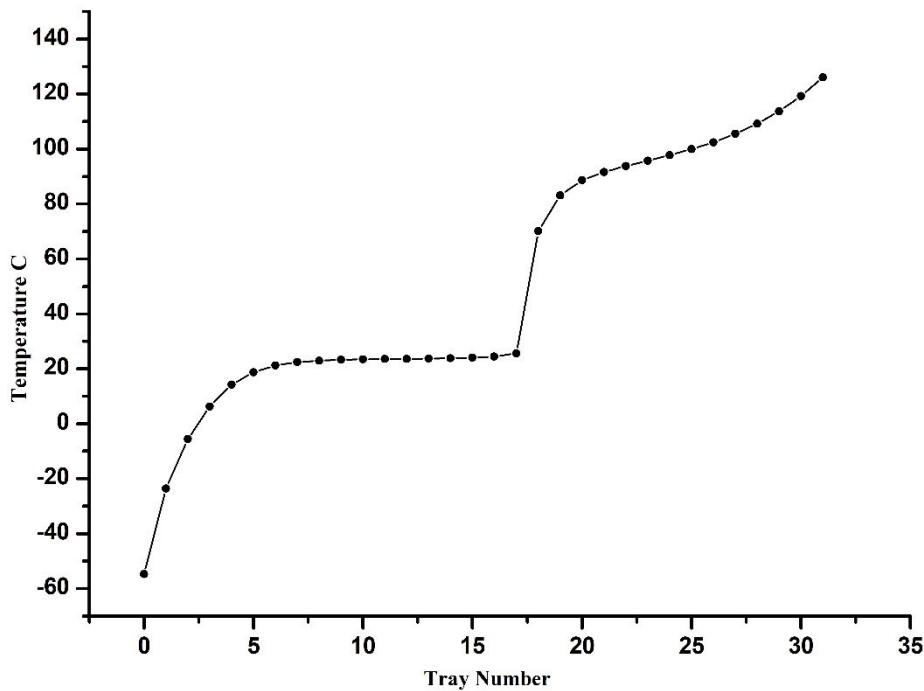


Figure 4-2. T-100 tray temperatures.

The separation of methane from ethane and from the sour gases was achieved using the demethaniser column T-101. However, with the distillate temperature of the demethaniser reaching  $-92\text{ }^{\circ}\text{C}$ , it was



necessary to address the issue of CO<sub>2</sub> freeze-out. As previously described in the literature [3, 18], the use of heavier hydrocarbons significantly lowers the freezing temperature of CO<sub>2</sub>, and so we employed an n-butane additive to successfully prevent freezing during the described process. The solidification temperature of CO<sub>2</sub> at the various column trays was then calculated using the CO<sub>2</sub> freeze-out utility with the PR EOS, then compared to the actual tray temperatures indicated in the column parameters. The result of the comparison can be seen in Figure 4-3, which indicates that the actual tray temperatures appear higher than the predicted freeze-out temperatures, thereby confirming that solidification should be prevented.

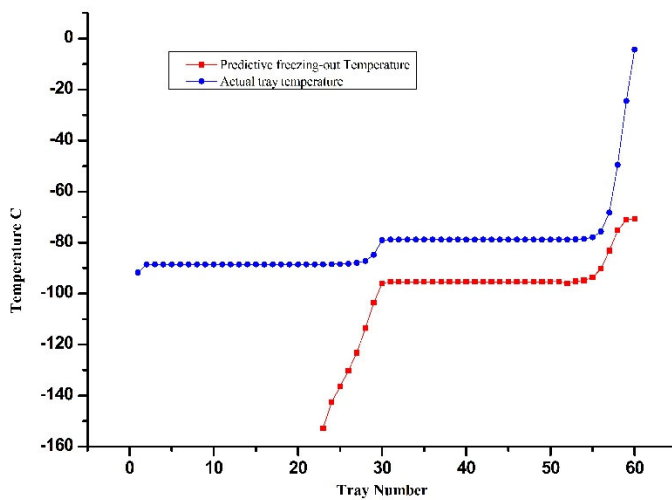


Figure 4-3. T-101 tray temperatures.

#### 4.4.2. H<sub>2</sub>S removal and column duty

As previously mentioned, toluene was used as an additive in the removal of H<sub>2</sub>S, as the aromatic nature of toluene enables it to separate H<sub>2</sub>S from CO<sub>2</sub> [12, 14]. The effect of the toluene flow rate and column (T-102) reflux ratio on the H<sub>2</sub>S content in the distillate and on the respective condenser and reboiler duties were then examined, as outlined in Figure 4-4 and Figure 4-5, respectively. It can be notified that the condenser duty is nearly constant in respect to the toluene flowrate and it belongs to the fact that the light components involved in the condensed are less effect than the heavy components that involved in the reboiler with respect to the solvent flowrate.

A sharp decline in H<sub>2</sub>S flowrate occurred at toluene flowrate between 600-650 kgmole/hr. In addition, the H<sub>2</sub>S flowrate was found to remain relatively constant between flow rates of 650 and 900 kgmole/h (Figure 4-6), which allows for choosing of the solvent flow rate whilst ensuring that

the respective duties of the column remain at a minimum (see Figure 4-4). As the flowrate of the solvent increased, larger circulation rate and reboiler power requirement are needed, thus 600-650kgmole/hr of toluene is recommended without having any detrimental effect on the separation process.

In contrast, the reflux ratio of the column was found to exhibit a larger influence on the condenser and reboiler duties. More specifically, upon varying the reflux ratio between 1.5 and 2.8, both the condenser and reboiler duties increased linearly. Although we reduced the reflux ratio into lower than 1.5 (which in turn reduced the column duty), the H<sub>2</sub>S content in the distillate was increased. Since variation of the reflux ratio more than 1.5 had little effect on gas separation, a value of 1.5 was employed whilst ensuring minimum condenser and reboiler duties, as indicated in Figure 4-5.

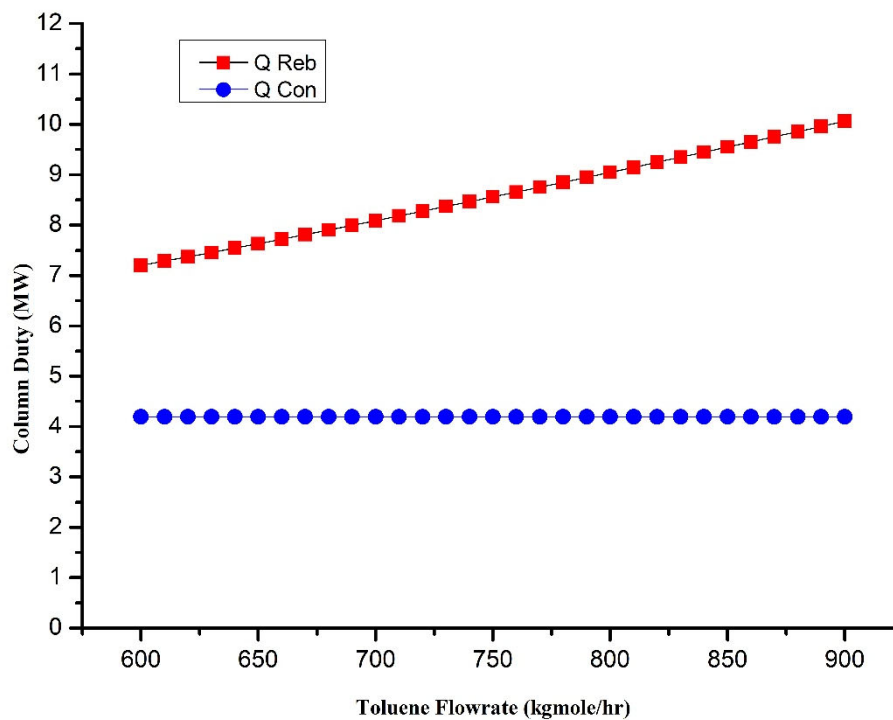


Figure 4-4. Effect of the toluene flow rate on the reboiler and condenser duties.

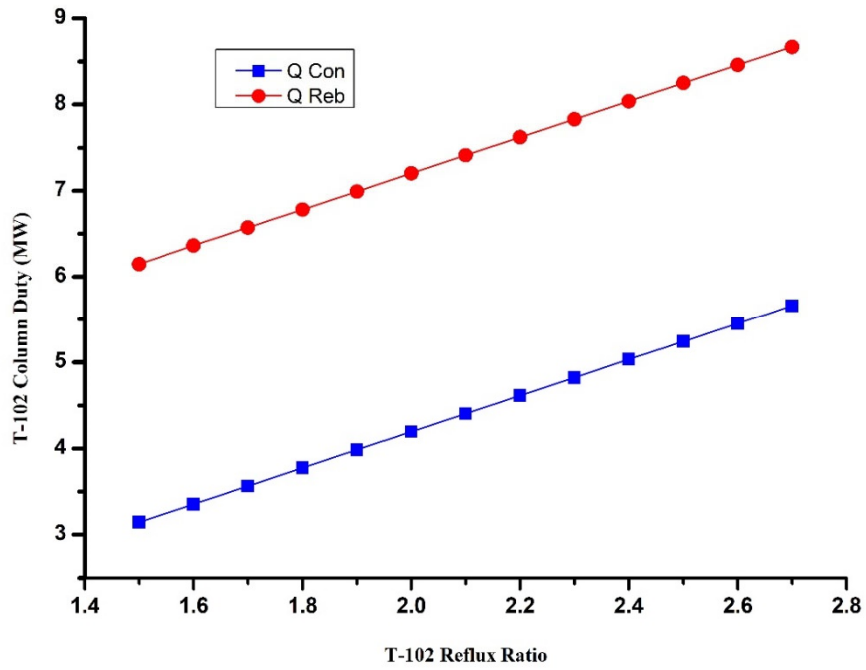


Figure 4-5. Effect of the reflux ratio on the column duty.

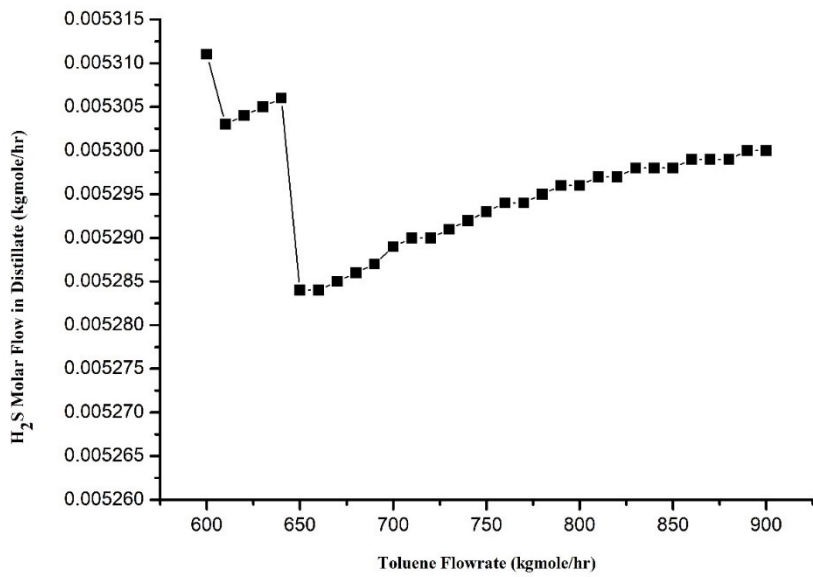


Figure 4-6. Effect of the toluene flow rate on the distillate H<sub>2</sub>S content.

### 4.4.3. CO<sub>2</sub> Recovery and column

One of the key points to consider in the separation of CO<sub>2</sub> from ethane is the addition of n-butane as an additive. Thus, using the CO<sub>2</sub>/ethane mixture derived from the H<sub>2</sub>S separation column along with n-butane as the solvent, we examined the effect of the solvent flow rate on the distillate and bottoms product compositions (see Figure 4-7 and Figure 4-8, respectively).

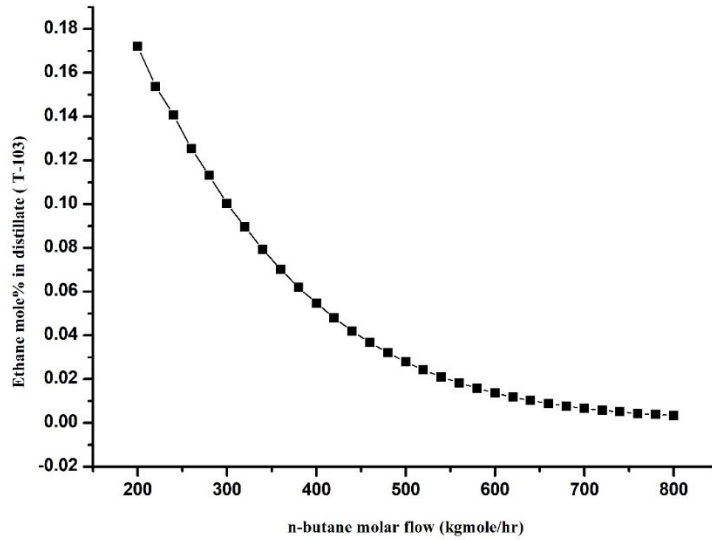


Figure 4-7. Effect of the n-butane flow rate on the distillate ethane Mole%.

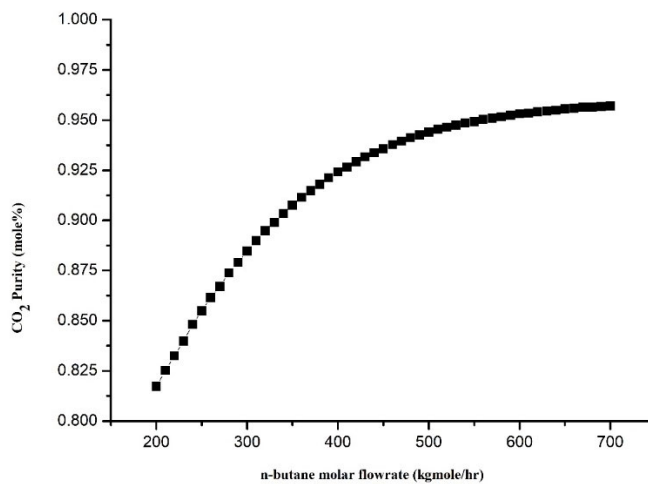


Figure 4-8. Effect of the n-butane flow rate on the CO<sub>2</sub> purity.

As indicated, an increased n-butane flow rate had a significant effect on the amount of ethane present in the column distillate. More specifically, upon increasing the solvent flow rate from 200 to 800 kgmole/h, the ethane mole fraction was reduced from 0.17 to 0.0033 (Figure 4-8). In addition, a lower reflux ratio in the column resulted in a reduced separation within the column. As such, a reflux ratio of 2 was employed. A CO<sub>2</sub> purity of ~ 90 mole% was achieved under these conditions, as shown in Figure 4-8. Furthermore, upon increasing the n-butane flow rate above 800 kgmole/h, the separation plateaued, thereby indicating that higher amounts of solvent had little effect on the CO<sub>2</sub> purity. To conclude, the n-butane flowrate can be in the range of 600-800 kgmole/hr that can guarantee distillate stream with less ethane and high purity of CO<sub>2</sub>.

#### 4.4.4. Effect of the feed stream CO<sub>2</sub> composition on the energy requirements

In the presence of varying levels of CO<sub>2</sub> in the feed stream, many conventional means of CO<sub>2</sub> removal are unsuccessful. Thus, in the proposed process, a range of feed streams with different CO<sub>2</sub> contents (i.e., 3–30 mole%) were employed. Interestingly, high levels of separation were achieved for all concentrations; however, the potential increase in the column duties upon increasing the CO<sub>2</sub> content was a concern. We therefore examined the increase in the duties of the condenser and the reboiler upon increasing the CO<sub>2</sub> content to achieve as low of CO<sub>2</sub> concentration in the product gas as required in NG specifications, as outlined in Figure 4-9.

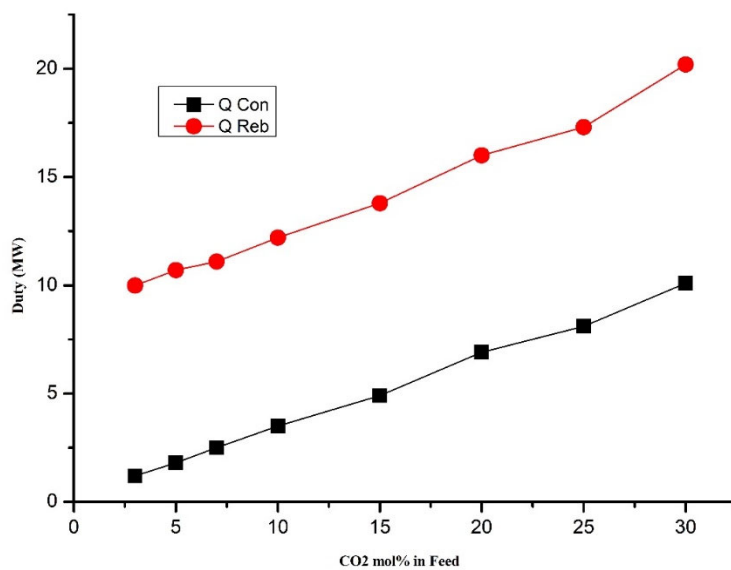


Figure 4-9. Effect of the feed stream CO<sub>2</sub> content on the T-104 duty.

As shown in Figure 4-9, both the condenser and reboiler duties increase proportionally to the increase in the feed stream CO<sub>2</sub> content. This can be accounted for by considering the relatively difficult task of separating larger quantities of CO<sub>2</sub> from the smaller quantities of ethane. Increased quantities of n-butane were also required to achieve the same level of separation (see Figure 4-10).

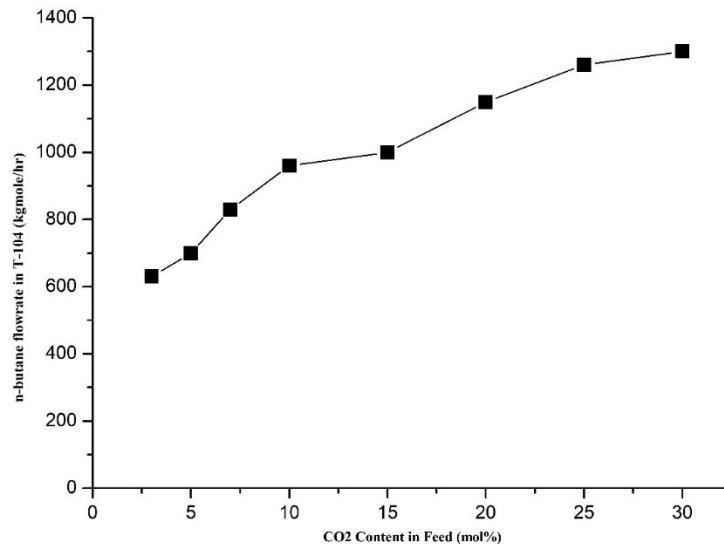


Figure 4-10. Required n-butane flow rates for 5000 kgmole/hr of feed stream containing different CO<sub>2</sub> contents

#### 4.5. Conclusions and further work

The separation of CO<sub>2</sub> from stream of natural gas is challenging due to the presence of an ethane-CO<sub>2</sub> azeotrope and due to the freezing of CO<sub>2</sub> at the low temperatures required for distillation. We herein presented a modified scheme for the separation of sour gases based on an existing scheme of Ryan-Holmes. The first column employed during the process successfully separated propane and heavier hydrocarbons from the lighter hydrocarbons and sour gases, while methane was subsequently separated in the presence of an n-butane additive to reduce the freezing temperature of CO<sub>2</sub> and avoid blockages in the low-temperature equipment. We also found that toluene was an excellent solvent for the separation of H<sub>2</sub>S from CO<sub>2</sub> and other constituents, while n-butane was a suitable solvent in the separation of CO<sub>2</sub> from ethane. A great advantage of this process lies in the production of high purity of CO<sub>2</sub> at the high pressure required for enhanced oil recovery processes. Importantly, the reported process produced pure methane and ethane containing <50 ppm CO<sub>2</sub>, with high purity (>90%) of CO<sub>2</sub> stream. For comparative purposes, simulations based on the same feed

conditions and product recoveries should be conducted using conventional sour gas removal techniques to determine the economic feasibility of the reported process. Moreover, optimisation of the overall process with respect to the energy consumption should be explored in the near future to give a more synergistic process simulation. We also note that sizing of the equipment in conjunction with a reasonable estimate of the total energy consumption should lead to a better understanding of the costs involved in implementing the process commercially.

## 5. Chapter 5: Simulation Study of Sweetening and Dehydration of Natural Gas Stream Using MEG Solution

### 5.1. Introduction

In recent decades, the demand for natural gas has increased dramatically [68]. This rising demand is due to requirement energy and at the same time the efforts to tackle the environmental impacts such as global greenhouse gas emissions and alternative energy has become crucial objective for researchers. In addition to the importance as a fuel, natural gas is also considered as a source of hydrocarbons for many petrochemicals processes. Natural gas is also considered as the main source for methane which is an important component for producing many products such as syngas and pure hydrogen. In addition to the importance as a fuel, natural gas is also considered as a source of hydrocarbons for many petrochemicals processes, syngas and hydrogen production [13]. Although natural gas can be considered as a clean fuel when compared to other fossil fuels, it contains impurities that need to be removed to meet gas pipeline specifications and to increase the heating value of the natural gas [13, 68]. [79] reported that gas contracts regulation restrict hydrogen sulfide (H<sub>2</sub>S) content are 4 ppm and carbon dioxide (CO<sub>2</sub>) content 2 mol% in natural gas stream. In fact, there are several technologies for acid gas removal from natural gas for example, chemical and physical absorption[80], membrane separation[81], pressure-swing adsorption (PSA)[82], membrane contactors [83], and cryogenic/low-temperature separation methods [84]. In addition, natural gas is usually dehydrated to avoid pipeline corrosion or plugging due to hydrate formation [85]. There are three major processes for natural gas dehydration (1) Direct cooling, (2) absorption and (3) adsorption [86]. The most common process for natural gas dehydration is normally carried out by absorption using tri-ethylene glycol.

In this paper, the process is computationally simulated and optimized due to the high cost of testing at large scale. However, this study will focus on adopting MEG solution gas process to dehydrate and remove sour gases from stream of natural gas and investigate the effect of MEG concentration and MEG inlet temperature on the treated gas stream properties.



## 5.2. Process description

Natural gas feed compositions were selected in this work are listed in Table 5-1, and following operating conditions are considered: 55 bar pressure, 30°C temperature and a molar flowrate of 5000 kgmole/hr. The process flow diagram in Figure 5-1 shows the principal flow sheet of the MEG plant for acid gas and water removal, including MEG regeneration column.

An absorption and desorption process for CO<sub>2</sub> removal using a MEG solution has been simulated. The absorption column had 40 stages, and various concentration, temperature and pressure scenarios were analysed. The thermodynamical properties of this mixture were estimated using the Peng-Robinson equation of state (implemented in Aspen HYSYS 7.2). Specifications for the calculation are listed in

Table 5-2 and the associated process flow diagram is shown in Figure 5-2.

Table 5-1. Natural gas stream composition and associated flow rates.

| <b>Component</b>                      | <b>mol%</b> | <b>kgmole/hr</b> |
|---------------------------------------|-------------|------------------|
| <b>H<sub>2</sub>S</b>                 | 2.9         | 145              |
| <b>CO<sub>2</sub></b>                 | 10          | 500              |
| <b>N<sub>2</sub></b>                  | 0.1         | 5                |
| <b>CH<sub>4</sub></b>                 | 72          | 3600             |
| <b>C<sub>2</sub>H<sub>6</sub></b>     | 7           | 350              |
| <b>C<sub>3</sub>H<sub>8</sub></b>     | 5           | 250              |
| <b>i-C<sub>2</sub>4H<sub>10</sub></b> | 0.7         | 35               |
| <b>n-C<sub>4</sub>H<sub>10</sub></b>  | 0.7         | 35               |
| <b>i-C<sub>5</sub>H<sub>12</sub></b>  | 0.3         | 15               |
| <b>n-C<sub>5</sub>H<sub>12</sub></b>  | 0.3         | 15               |
| <b>H<sub>2</sub>O</b>                 | 1           | 50               |
| <b>Total</b>                          | 100         | 5000             |

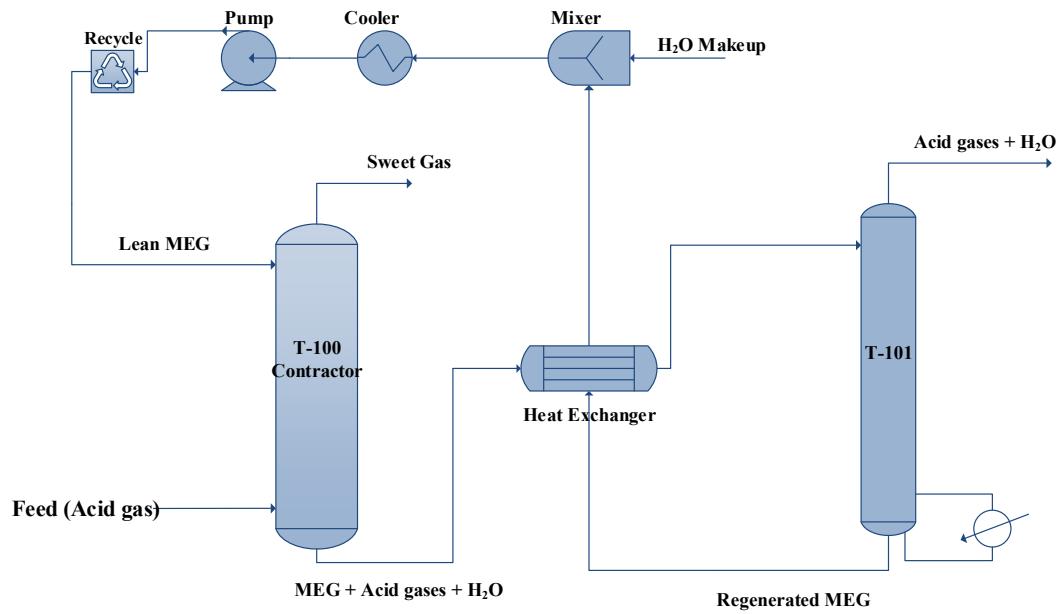


Figure 5-1. Acid gas removal process based on absorption in MEG solution.

Table 5-2. Specifications for Base Case CO<sub>2</sub> removal

|   |                         |
|---|-------------------------|
| Inlet gas temperature                   | 30 °C                   |
| Inlet gas pressure                      | 52 bar                  |
| Inlet gas flow                          | 5000 kgmole/hr          |
| CO <sub>2</sub> in inlet gas            | 5 mol %                 |
| H <sub>2</sub> S in inlet gas           | 2.8 mol %               |
| Water in inlet gas                      | 1 mol %                 |
| Lean amine temperature                  | 20 °C                   |
| Lean amine pressure                     | 52 bar                  |
| Lean amine rate                         | 1000 m <sup>3</sup> /hr |
| MEG content in lean MEG                 | 80 mass %               |
| Number of stages in absorber            | 40                      |
| Number of stages in regeneration column | 20                      |
| Reflux ratio in stripper                | 0.8                     |
| Reboiler temperature                    | 126 °C                  |

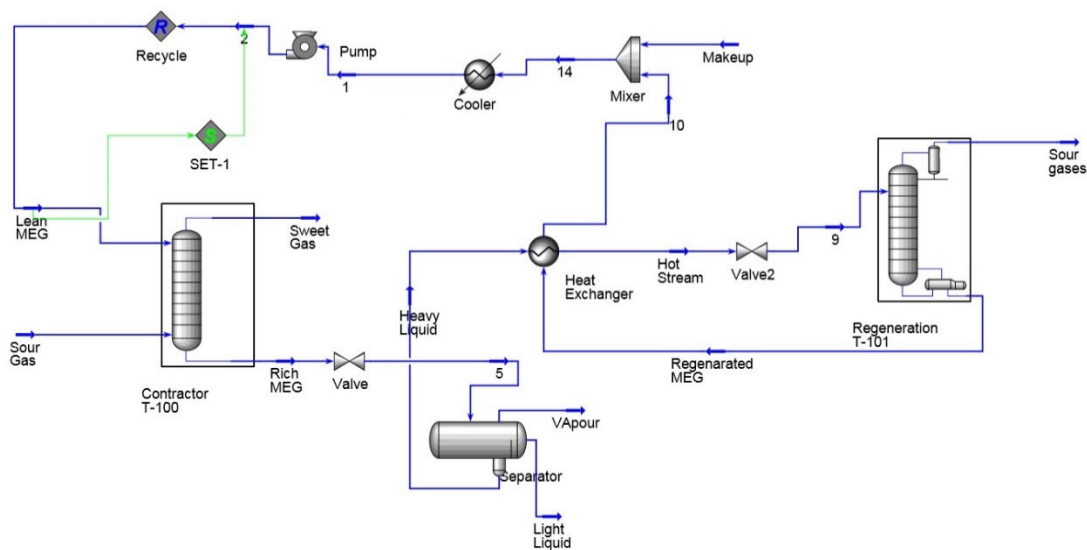


Figure 5-2. Process flow diagram by HYSYS

### 5.3. Numerical implementation

In this study, the separation processes (Figure 5-2) have been simulated using Aspen HYSYS 7.2, which is a set of comprehensive process-modeling tools used by the world’s leading oil and gas producers, refineries, and engineering companies for process simulation and process optimization in design and operation. The Peng Robinson (PR) equation of state has been selected for all simulation calculations.

#### 5.3.1. Algorithm and basic equation used for simulation

##### 5.3.1.1. Absorber

An absorber was selected for acid gas removal.

##### 5.3.1.2. MEG Regeneration column

A distillation column was selected for simulating the MEG recovery column.

*Column specs:* Two specs should be defined for the distillation column until the degree of freedom becomes zero. The reflux ratio and column duty were selected as column specs.

*Solving methods:* Inside-out: With the “inside-out” based algorithms, simple equilibrium and enthalpy models were used in the inner loop to solve the overall component and heat balances as well as any specifications. The outer loop updates the simple thermodynamic models with

rigorous model calculations. The inside-out algorithm has become one of the most popular methods because of its robustness and its ability to solve a wide variety of columns.

### **5.3.1.3. Heat Exchanger**

The heat exchanger performs two-sided energy and material balance calculations. The heat exchanger is very flexible and can solve for temperatures, pressures, heat flows (including heat loss and heat leak), material stream flows, or UA. In HYSYS, you choose the Heat Exchanger Model for your analysis. Your choices include an End Point analysis design model, an ideal ( $Ft=1$ ) counter-current Weighted design model, a Steady State rating method, and a Dynamic rating method for use in dynamic simulations. The dynamic rating method is available as either a Basic or Detailed model and can also be used in steady state mode for heat exchanger rating. The unit operation also allows the use of third party heat exchanger design methods via OLE Extensibility [69].

Some of the key features included in the dynamic heat exchanger operation include:

- A pressure-flow specification option that realistically models flow through the heat exchanger according to the pressure network of the plant. Possible flow reversal situations can therefore be modelled.
- The choice between a Basic and Detailed heat exchanger model. Detailed heat exchanger rating information can be used to calculate the overall heat transfer coefficient and pressure drop across the heat exchanger.
- A heat loss model that accounts for the convective and conductive heat transfer that occurs across the heat exchanger shell wall [69].

### **5.3.1.4. Heater and Cooler**

The heater and cooler operations are one-sided heat exchangers. The inlet stream is heated (or cooled) to the desired outlet conditions while the energy stream provides (or absorbs) the enthalpy difference between the two streams. These operations are useful to discover the energy required to cool or heat a process stream with a utility and without focusing the conditions of the utility itself [69].

The Heater and Cooler calculations are based on the energy balance between the inlet and process streams. The energy balances are shown as follows:

$$\mathbf{Heat}_{inlet} + \mathbf{Duty}_{Cooler} = \mathbf{Heat}_{outlet} \quad \mathbf{For\ Heater} \quad \mathbf{5.1}$$

$$\mathbf{Heat}_{inlet} - \mathbf{Duty}_{Cooler} = \mathbf{Heat}_{outlet} \quad \mathbf{For\ cooler} \quad \mathbf{5.2}$$

The enthalpy or heat flow of the energy stream is added to the Heater process side holdup:

$$\mathbf{M(H}_{in} - \mathbf{H}_{out}) + \mathbf{Q}_{Heater} = \rho \frac{d(\mathbf{VH}_{out})}{dt} \quad \mathbf{For\ Heater} \quad \mathbf{5.3}$$

$$\mathbf{M(H}_{in} - \mathbf{H}_{out}) + \mathbf{Q}_{Heater} = \rho \frac{d(\mathbf{VH}_{out})}{dt} \quad \mathbf{For\ Cooler} \quad \mathbf{5.4}$$

Where:

M= flow rate

ρ= Density

H= Enthalpy

Q<sub>Heater</sub>= Heater Duty

V= Volume shell

### 5.3.1.5. Pump

Increasing in the pressure of outlet liquid stream can be taken place by using a pump. Depending on the supplied information, the pump calculates either an unknown pressure, temperature, or pump efficiency [69].

**Theory:** The following equations and assumptions are used by HYSYS in order to calculate the unknown pump variables.

Equation (5) is used to calculate the ideal power of the pump required to raise the pressure of the liquid:

$$\mathbf{Power\ Required}_{ideal} = \frac{(\mathbf{P}_{out} - \mathbf{P}_{in}) \times \mathbf{FlowRate}}{\mathbf{Liquid\ Density}} \times \mathbf{100\%} \quad \mathbf{5.5}$$

Where:

P<sub>out</sub> = Pump outlet pressure

P<sub>in</sub> = Pump inlet pressure

The actual power of the pump can be calculated as below:

$$\text{Efficiency}(\%) = \frac{\text{Power Required}_{ideal}}{\text{Power Required}_{actual}} \quad 5.6$$

When the efficiency is less than 100%, the temperature of the outlet stream will be raised by the excess energy [69].<sup>[11]</sup>

The actual power of the Pump can be calculated by combining equations (5 and 6):

$$\text{Power Required}_{actual} = \frac{(P_{out} - P_{in}) \times \text{FlowRate} \times 100\%}{\text{Liquid Density} \times \text{Efficiency}(\%)} \quad 5.7$$

### 5.3.2. Selection of equation of state

HYSYS provides enhanced equations of state (PR and Soave-Redlich-Kwong (SRK)) for strict treatment of hydrocarbon systems and sour gases separation. For oil, gas, and petrochemical applications, the PR EOS and SRK are usually recommended [65, 69]. The PR and SRK equations of state have been enhanced to yield accurate phase equilibrium calculations for systems ranging from low-temperature cryogenic systems to high-temperature, high-pressure reservoir systems [69]. In addition, Vitu, S. et al. used PR EOS to predict the phase equilibria of CO<sub>2</sub> and Hydrocarbon system and found an accurate results in many cases. Moreover, Jaubert et al. have chosen PR EOS to predict the phase equilibria of syntheses petroleum fluids (Alkanes, aromatics, CO<sub>2</sub>, H<sub>2</sub>S, N<sub>2</sub> and more) and they reported that the model was successful due to the high accuracy results. In 2008, Privat et al. have added H<sub>2</sub>S group for their model to calculate the temperature dependent binary interaction parameters (*K<sub>ij</sub>*) and they obtained an accurate behavior prediction of the system containing H<sub>2</sub>S. In contrast, Glycol fluid package provided by HYSYS is a common package to deal with natural gas dehydration by TEG and it is not recommended for using with MEG. However, even though the MEG is non-polar component, but the process operate at 30 °C and 49 bar which is far from the critical conditions of MEG, T<sub>c</sub>= 429 °C and P<sub>c</sub>= 65 bar.

### 5.4. Steady state simulation and optimization

In this study, Aspen HYSY V.7.3 is used to simulate and optimize the acid gas sweetening process plant. The MEG is adopted as an absorbent for acid gases from sour gas stream. Providing a stream compositions of natural gas is the first step of the simulation work as listed in Table 5-1. The second

step of the simulation work is choosing the fluid package that is suitable to the system and Peng-Robinson fluid package was selected in this study as shown in Figure 5-2.

The inlet gas separator is quite necessary to remove impurities such as solid particulates and liquid and this step is assumed to be done before the gas stream enters to the absorber. Some specification needs to be specified for MEG absorber column such as stream inlet temperature and pressure, absorber column number of stages and absorber pressure, Figure 5-3 shows MEG absorber menu. Moreover, absorbent regeneration column is a crucial part of sweetening process to regenerate the absorbent (MEG) and it can be installed after the heat exchanger as can be seen in Figure 4 in MEG regenerator column menu.

The simulation process was done successfully and Figure 5-2 shows the process flow diagram of the sour gas removal process plant. In order to avoid any problems that may be caused by the rich MEG impurities that can cause a serious problem to the process and might damage the equipment, it is recommended to install a flash tank for the rich MEG stream before the heat exchanger. Moreover, the SET function is a useful function provided by HYSYS to set the temperature and the pressure of lean MEG. In addition, water make up stream must be added to the process to substitute any losses in water to avoid any built up of MEG/ water concentrations in the process. Therefore, the concentration of MEG solution in the process can be maintained and supported using water make up stream. Finally, the simulation process was completed and the process accomplished high acid gas removal and reduced the water content in the sweet gas stream which will be discussed in the results and discussion

#### **5.4.1. Process performance**

Aspen HYSYS V.7.3 is used to simulate the acid gas sweetening plant. MEG solution is used as an absorbent for sour gases from natural gas stream. Natural gas stream compositions were firstly provided to the program to start the simulation work as listed in Table 5-1 and Peng-Robinson EOS fluid package has been used.

MEG absorber is the main important equipment of this process plant and it also needs some specifications to be identified such as stream temperature and pressure, Figure 5-3 shows MEG

absorber menu. Moreover, MEG regenerator column is used to regenerate rich MEG after the MEG heat exchanger as shown in Figure 5-4 in MEG regenerator column menu.

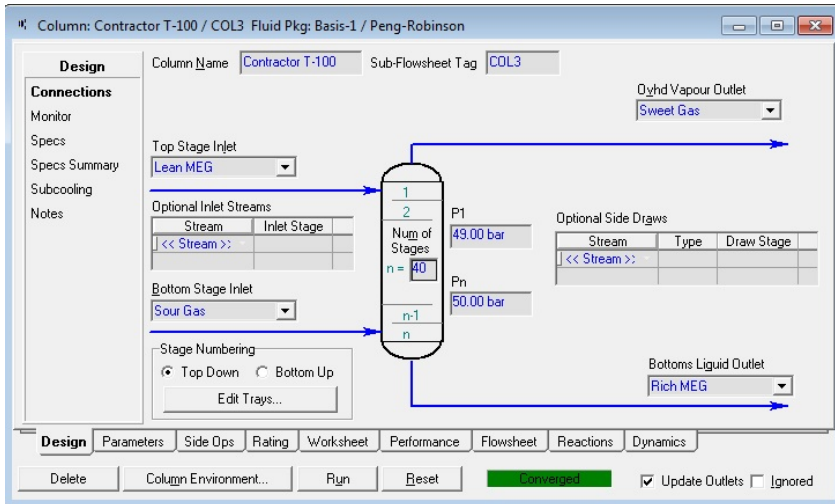


Figure 5-3. . MEG absorber menu

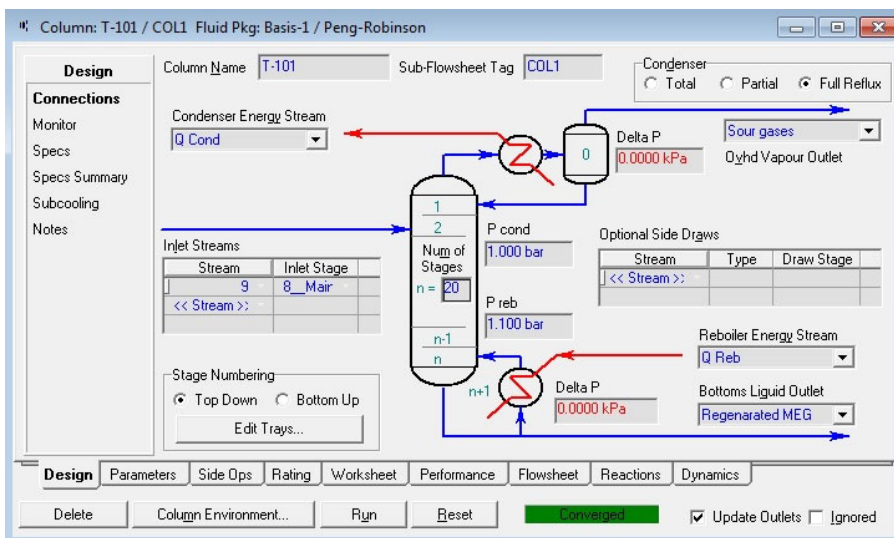


Figure 5-4. MEG regenerator menu

## 5.5. Results and discussion

Increasing the MEG circulation rate increases acid gas removal and decreases the water content in the sweetened gas as can be seen in Figure 5-5. Moreover, at MEG flow rates of (900 m<sup>3</sup>/h) the H<sub>2</sub>S amount in the sweet gas reduced to 2.5 ppm as can be noticed in Figure 5-5. However, the



optimum MEG rate was (1000 m<sup>3</sup>/h) which resulted in 1 ppm H<sub>2</sub>S and 0.03% CO<sub>2</sub> in the treated gas stream, also the optimum liquid residence time on the tray has been achieved. The total recovery of CO<sub>2</sub> and H<sub>2</sub>S were 98% and 99.7% respectively. On the other hand, the regeneration reboiler temperature is decreased when the MEG concentration is reduced due to the high boiling point of MEG (when compared with water, Figure 5-6). In addition, the regenerated MEG temperature decreased when the lean MEG rate increased that is because of the increasing of MEG residence time inside the column (less reboiler effects) as shown in Figure 5-7. To conclude, it is not recommended to increase the regeneration reboiler temperature (more than 140 °C) because of the degradation of MEG can occur. However, cost and economic terms should be taken into consideration for MEG process because any increasing of MEG flowrate and/or inlet temperature leads to increase process operation cost [68].

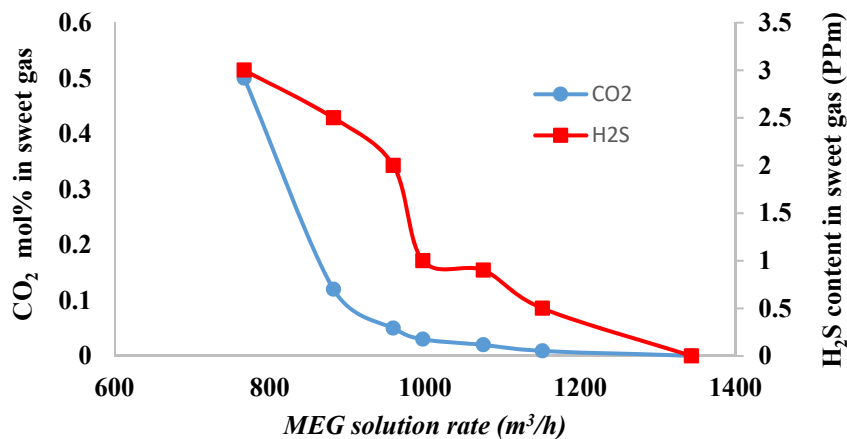


Figure 5-5. Effect of (80% MEG) circulation flowrate on sour gas mole% in the treated gas stream.

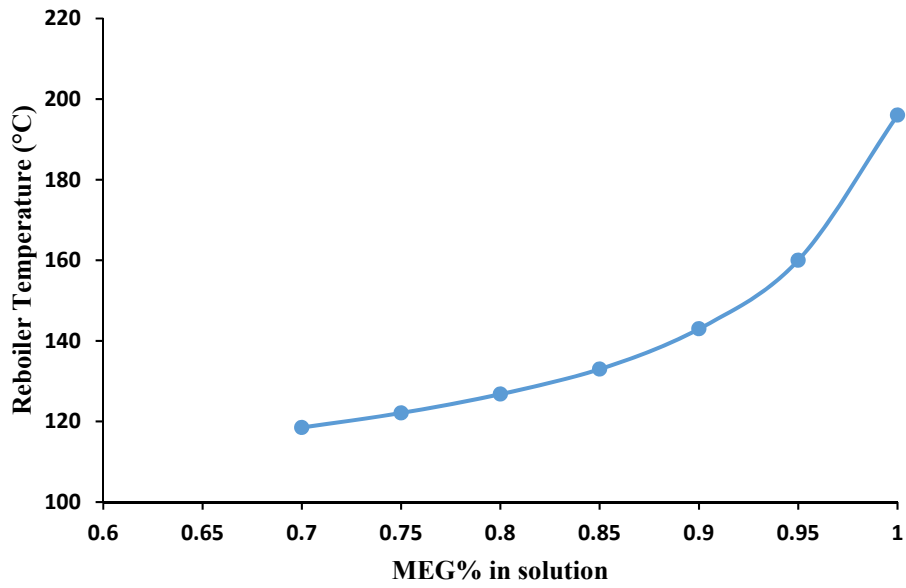


Figure 5-6. Relationship between (80% MEG) rate and reboiler temperature.

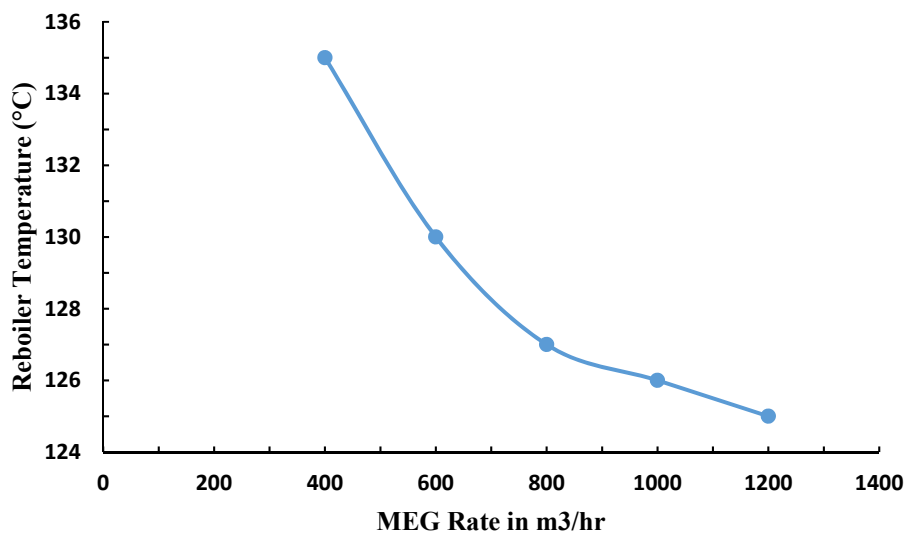


Figure 5-7. Relationship between MEG concentration and reboiler temperature.

### 5.5.1. H<sub>2</sub>S Removal

Removing of H<sub>2</sub>S from the gas stream was more efficient at higher MEG flow rates at all MEG feed temperatures as shown in Figure 5-8. Note, however, increasing the MEG flow rate will increase the process operational costs due to high duty requirement in reboiler. We thus conclude that using (80% MEG) at 20 °C is optimal with respect to H<sub>2</sub>S removal.

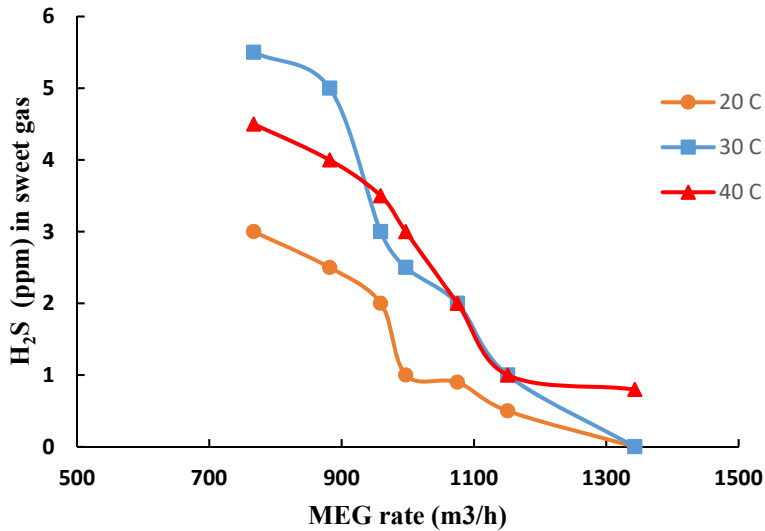


Figure 5-8. The relationship between H<sub>2</sub>S (ppm) in the sweet gas stream and inlet MEG flow rate (m<sup>3</sup>/h) for various inlet MEG temperatures (°C).

### 5.5.2. CO<sub>2</sub> Removal

In addition, Removing CO<sub>2</sub> from the gas stream is also more efficient at higher MEG flow rates and lower MEG temperatures. As can be seen in Figure 5-9, CO<sub>2</sub> mol% in sweet gas stream is 0.4 mol% at 800 m<sup>3</sup>/hr MEG flow rate and 40 °C MEG feed temperature and reduces to 0.04 mol% when the MEG flow rate is increased to 1150 kgmole/hr.

However, increasing the MEG flow rate and inlet temperature will increase the reboiler duty. To conclude, using 1000 m<sup>3</sup>/hr as a MEG flow rate at 20 C as a MEG inlet temperature can be considered as an optimum choice in order of CO<sub>2</sub> removal as can be noticed in Figure 5-9 where the CO<sub>2</sub> mol% is 0.03 .

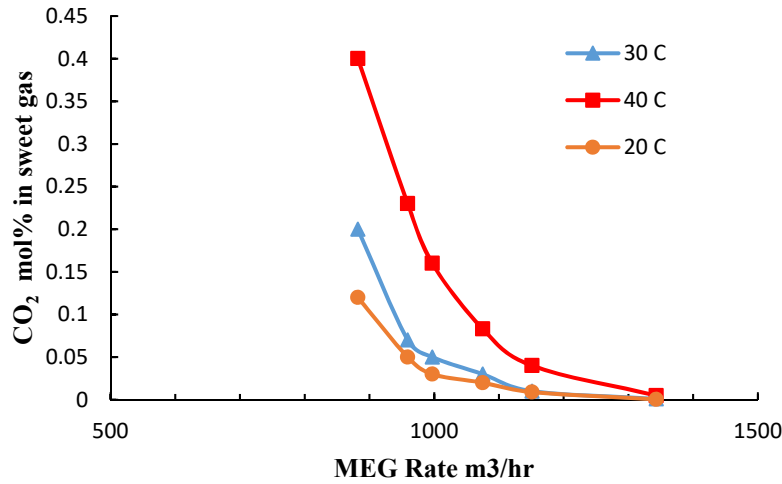


Figure 5-9. Relationship between CO<sub>2</sub> concentration in the sweet gas stream as a function of MEG flow rate and temperature

### 5.5.3. Water content

Water content in the treated natural gas stream is also reduced with increasing MEG flowrate and MEG inlet temperature. However, MEG at 20 °C gives the lowest water content in treated gas stream in minimum MEG rate. Figure 5-10 shows that water content at 20 °C and 1350 kgmole/hr MEG flowrate is 0.028 mol% while it is 0.08 mol% at the same flowrate and at 40 °C. Increasing the MEG inlet temperature increases the water mole% in the dry gas stream as can be seen in the Figure 5-10. In addition, increasing in MEG flowrate decreases the water content in the treated gas stream. The water mole% in treated gas stream at 20 C and 1000 kgmole/he flowrate is less than 0.03 mol% and is recommended due to a reasonable MEG flowrate and temperature.

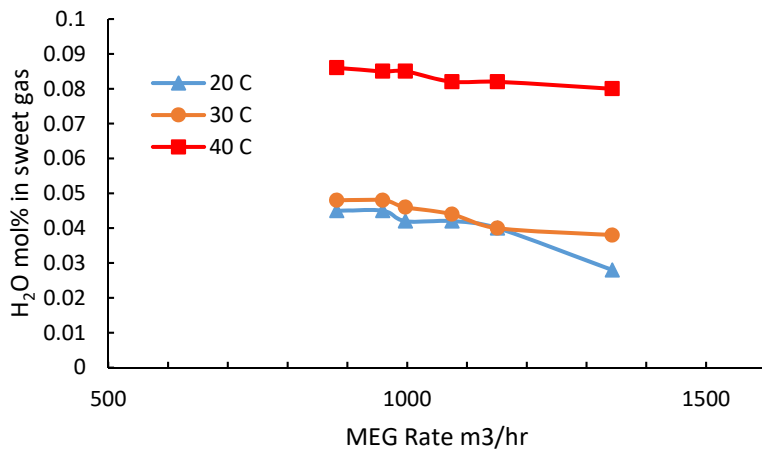


Figure 5-10. The relationship between H<sub>2</sub>O mole percent in sweet gas and MEG rate

#### 5.5.4. Hydrate formation analysis

Gas hydrate, which are also known as gas clathrate, are crystalline compounds that form when gas molecules (guests) are entrapped by hydrogen bond in water molecules (host) under favourable conditions of high pressure and low temperature [72].

There are two types of gas hydrate commonly associated with natural gas processing, type I and type II. The third hydrate type is called type H, but it is less commonly encountered. Common gas molecules of hydrate type I are; methane, ethane, carbon dioxide, and hydrogen sulphide. While, type II are; nitrogen, propane, and isobutane [87].

It is a significance requirement to prevent hydrate formation due to corrosion damage in the pipelines and equipment of gas transport system and flow blockage of gas in the pipeline [88].

To prevent hydrate formation, it is compulsory to check the natural gas stream to obtain hydrate formation temperature and operate the process above this temperature. HYSYS has capability to predict whether hydrate formation is possible or not by Hydrate utility package as can be seen in Figure 5-11. The following results were obtained:

1. Hydrate Formation Flag: Will not Form.
2. Hydrate Formation Type: No type Form.
3. Equilibrium Phase: Vapour Phase.

The phase diagram is shown in Figure 5-12. On the phase diagram, it can be noticed that the hydrate formation temperature is 9 °C at 50 bar pressure in the dehydrated gas stream which is below the treated gas stream temperature and this means dry gas can be safely transformed beyond this temperature without hydrate formation.

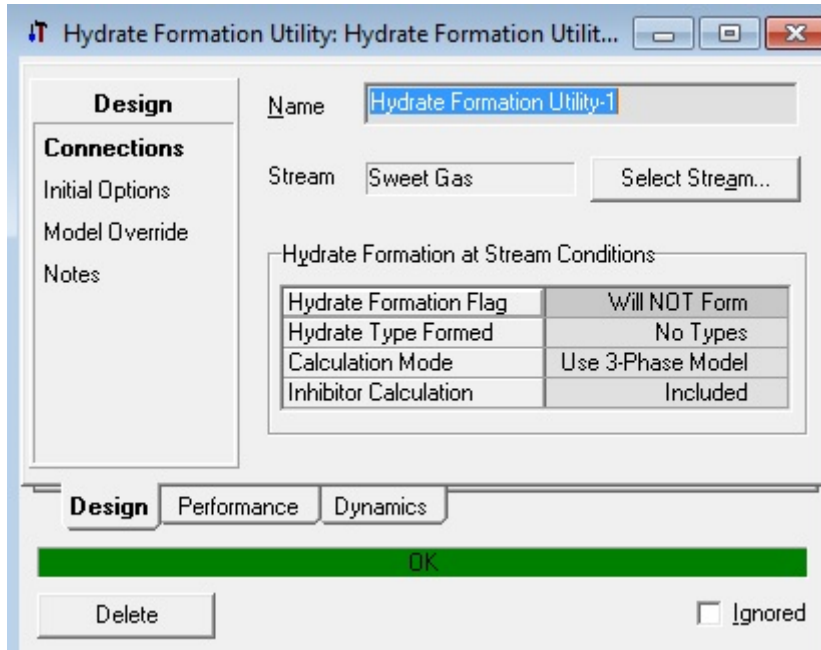


Figure 5-11. . HYSYS Hydrate Package Utility

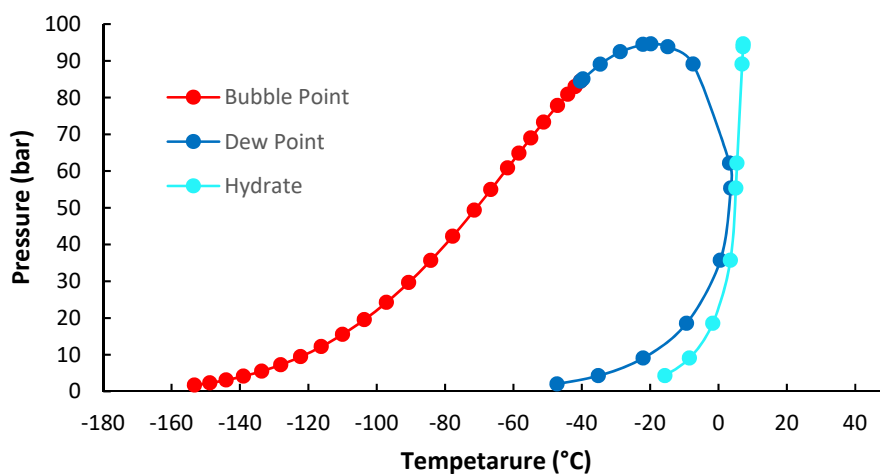


Figure 5-12. . Hydrate formation phase diagram

## 5.6. Conclusions

Natural gas stream usually contains high amount of sour gases that should be removed to meet natural gas requirements. In addition, natural gas is also saturated with water in the reservoir and this water content must be dehydrated to meet the pipeline specification. However, this problem can be solved by installing appropriate gas dehydration and sweetening plant. This simulation work was designed using Aspen HYSYS to remove sour gases and water content from a stream of natural gas and the process has met the specifications and the standards of pipelines. PR equation of state has been used due containing enhanced binary interaction parameters for all hydrocarbons–non-hydrocarbons components pairs and the high accuracy results. Moreover, in this study, the simulation work achieved high acid gases and water content removal using MEG solution rate at different temperatures and concentrations. Reducing the water content to a pipeline specification can eliminate the dehydration unit that used in conventional natural gas dehydration and then reduce the capital cost. It can be argued that (80% MEG) concentration with 1000 m<sup>3</sup>/h circulation rate at 20 °C achieved the optimum sour gases removal and dehydration. Value below this it might not be able to remove sour gases and water content. The total recovery of CO<sub>2</sub> and H<sub>2</sub>S were 98% and 99.7% respectively which are higher than the total recovery of CO<sub>2</sub> using the commercial Selexol process which is less than 95%. Furthermore, forty trays for amine contactor tower have achieved high acid gases and water content removing. MEG process plant is also performed by adopting several MEG concentrations and temperatures and several process parameters are examined for instance, water content, sour gases removal and rich MEG temperature. Many other selection specifications, such as MEG properties and economic terms, are considerations that can play a crucial role in MEG concentration and flow rate selection. Cost, energy study can be considered as a future work to examine the efficiency and the reliability of this process as an alternative to the conventional Amine process.

## **6. Chapter 6: Carbon dioxide/brine wettability of porous sandstone versus solid quartz: An experimental and theoretical investigation**

### **6.1. Introduction**

Increase in CO<sub>2</sub> emission seems to be formidable due to increase in energy demand and industry-dependent fossil fuel consumption [89]. Various strategies in particular capture and storage of CO<sub>2</sub> in geological formations have been adopted to minimize such CO<sub>2</sub> emission into the atmosphere. The techniques used to store the CO<sub>2</sub> underground include CO<sub>2</sub> injection into deep aquifers [90], depleted gas and oil reservoirs [91] and storage of CO<sub>2</sub> in coal seam formations underground [92]. While aquifers have the highest volumetric CO<sub>2</sub> storage capacity, CO<sub>2</sub> storage for enhance oil recovery (EOR) is more attractive alternative due to economic viability.

In this context, reducing CO<sub>2</sub> emissions by carbon geo-storage has been specified as a viable option [54, 93]. Combination between carbon geostorage (CGS) and hydrocarbon recovery scheme can be adopted to improve oil and gas recovery [54, 94]. In particular, in CGS, CO<sub>2</sub> is collected from large point-source emitters, compressed and injected deep underground into geological formations [54]. Basically, the main problem with CGS can be briefly defined by the density of CO<sub>2</sub>. The lower CO<sub>2</sub> density compare to that of formation brine density causes the CO<sub>2</sub> to flow upward which in turn increases the change of CO<sub>2</sub> leaking through caprock. Four mechanisms are considered to prevent CO<sub>2</sub> surface leaking: a) structural trapping [95], b) residual trapping [96] , c) dissolution trapping [97] and d) mineral trapping [98] .

Wettability can be considered as an important influential factor in determining residual saturation, capillary pressure and relative permeability which also control the flow in porous rocks [99-102]. In addition, interfacial interactions have a significant impact on the process of CO<sub>2</sub> storage in hydrocarbon reservoir and in saline aquifers [101, 103, 104] where the relation between the interfacial interactions (interfacial tension, capillarity, and wettability) is represented by the Young–Laplace equation [105].

Roughness of the surface can also influence the apparent contact angle at the boundary between liquid and the surface, and many examples have been given where wetting the rough surfaces proves to be difficult because of their large apparent contact area [106, 107]. Moreover, theoretically the contact angle increase with increasing the surface roughness for oil wet surfaces and decrease with increasing the surface roughness for water wet surfaces [108-110]. However, the effects are still



poorly understood where many other studies have shown both increasing and decreasing trends with increasing surface roughness [111-113].

The contact angles are often measured on pure mineral samples to investigate the fundamental phenomena behind wettability variations with state variables however such measurements might not be representative of an actual reservoir rock with inherent heterogeneities. In fact very little work has been conducted on the wettability measurements of heterogeneous reservoir samples where surface roughness, interfacial tensions mineral surface and pore system play key roles. Therefore we have measured the contact angle of CO<sub>2</sub>/brine on a porous sandstone surface at reservoir conditions and analysed the dependency of contact angle on pore fraction where the pressure, temperature and brine salinity are varied. We have also described the observed phenomena by developing a physical model.

## **6.2. Experimental methodology**

A sandstone sample from well 2 in Warro gas field was used for this study. The Warro field is situated in a convenient location onshore in the Perth Basin, approximately 200 kilometres north of Perth, Australia with in-place reserve estimation of 7-10 TCF and a big 1-3 TCS possible recoverable gas. The field structure is a large, simple, closed, growth-type anticline with not major faulting activities. Warro-2 well was drilled to check the productivity potential of Yarragadee formation and has reached to the depth 4854m by early 1978.

The well has undergone a considerable number of tests including fracturing, wireline logging, conventional and side wall coring, formation pressure, and temperature analysis. Several conventional cores were cut. We have used a core sample from the depth of 3836.2m with porosity and air permeability of 9.6% and 0.5 MD respectively. The composition of the sandstone sample was measured via XRD with a Bruker-AXS D9 Advance Diffractometer (quartz 90 wt%, Kaolin 3.3 wt%, Felspar 6.7 wt%), which indicated that the sandstone sample was composed mainly of quartz. The RMS surface roughness (540 nm) was measured with an Atomic Force Microscope, instrument model AFM DSE 95-200, Figure 6-1. In addition, the scanning electron microscopy-energy dispersive x-ray spectroscopy (SEM) was used to estimate surface solid fraction ( $f = 0.65$ ) using Avizo software (the raw images were filtered using non-local mean filter, then segmented using watershed segmentation methods), Figure 6-2.

The sample was cleaned for 5min in an air plasma to remove surface contamination [114], following Iglauer et al.'s [115] and Sarmadivaleh et al.'s [116] procedure. This cleaning process is an important step to avoid significant systematic errors [115, 117]. The cleaned sample was then placed inside a pressure chamber (Figure 6-3) at a set temperature (296, 323 and 343K). Subsequently CO<sub>2</sub> was injected into the chamber by a high precision syringe pump (ISCO 500D; pressure accuracy of 0.1% FS) and pressure was increased to a target value (0.1, 5, 10, 15, 20 MPa). It should be noted that brine was saturated with CO<sub>2</sub> using a mixing reactor [118] although the earlier studies showed that the contact angle is not influenced by such CO<sub>2</sub>-brine solubility equilibration [119].

When the pressure reached the set pressure, a single deionised (DI) water or brine (20 wt% CaCl<sub>2</sub>) droplet (average volume of a single drop was  $\sim 6 \pm 1 \mu\text{L}$ ) was passed onto the sandstone via a needle. Moreover, the tilting-plate technique was applied to measure the contact angle [120-122], as this technique can simultaneously measure advancing and receding events under the same circumstances. An earlier study [121] proved that the tilting plate method offers more reliable data than the sessile drop technique. In this study, a tendency angle of  $\alpha = 12^\circ$  for the sample, which was placed on a metal platform into the pressure chamber, was attained. Under such a condition, the slightest movement of the droplet from the upper side to the lower side of the substrate will occur as result of the gravitational force.

The measurement of the advancing water contact angle ( $\theta_a$ ) was achieved at the front of the droplet prior to droplet movement, and the measurement of the receding ( $\theta_r$ ) water contact angle was attained at the trailing edge of the droplet. In this case, the gravity is pointless, as the radius of the water droplet contact length was  $\approx 1.7 \pm 0.2 \text{ mm}$  under the capillary length. The entire process was recorded with a high-resolution camera (Basler scA 640–70 fm, pixel size = 7.4  $\mu\text{m}$ ; frame rate = 71 fps; Fujinon CCTV lens: HF35HA-1B; 1:1.6/35 mm), and the extracted images taken from the video were used to measure  $\theta_a$  and  $\theta_r$  [123].

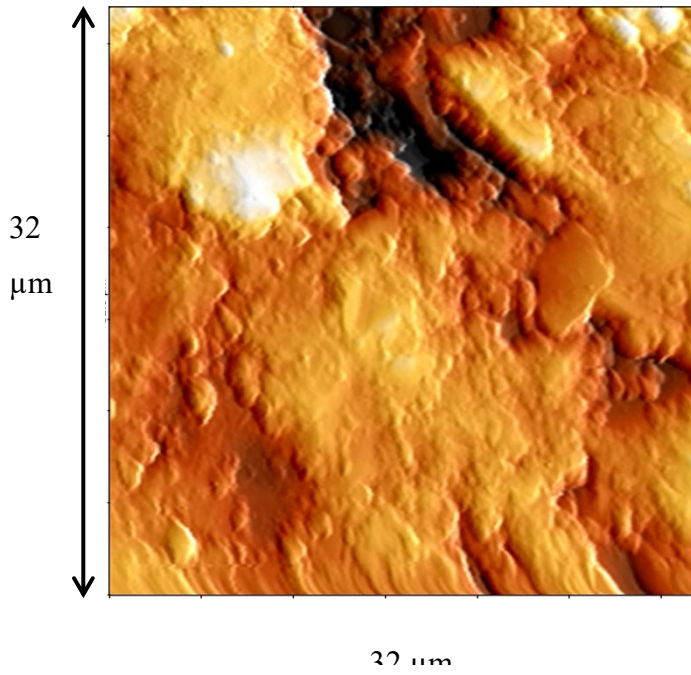
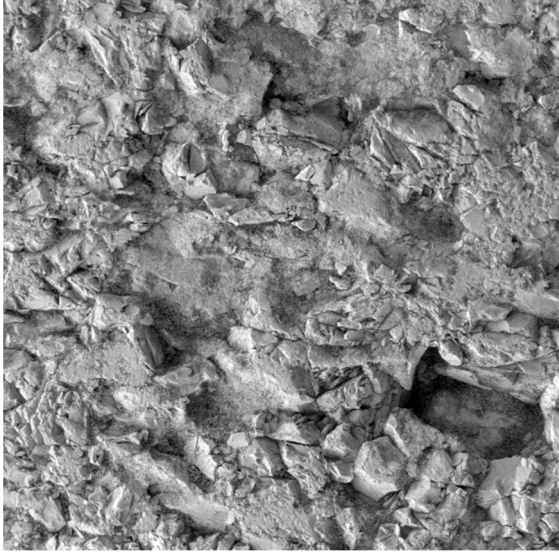
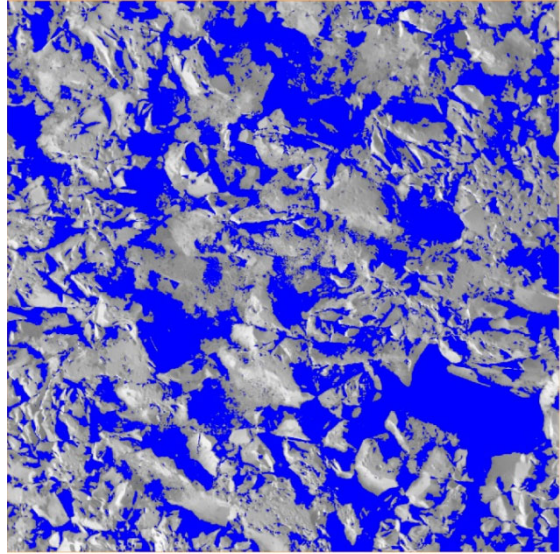


Figure 6-1. Atomic force microscopy image of the sandstone surfaces investigated; different heights are coloured differently (black is 0 nm, white is 3500 nm).



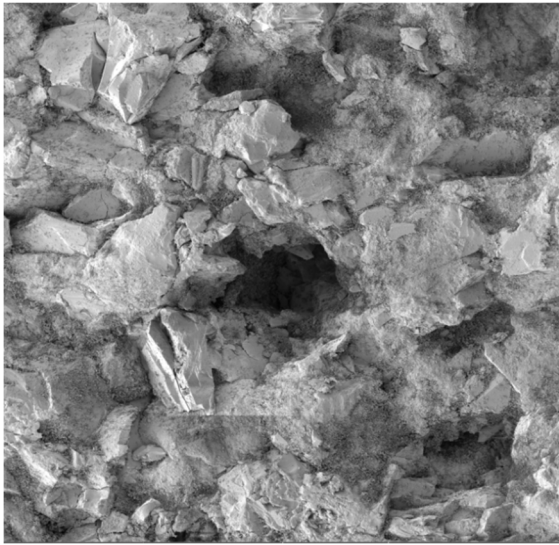
400  $\mu\text{m}$

a



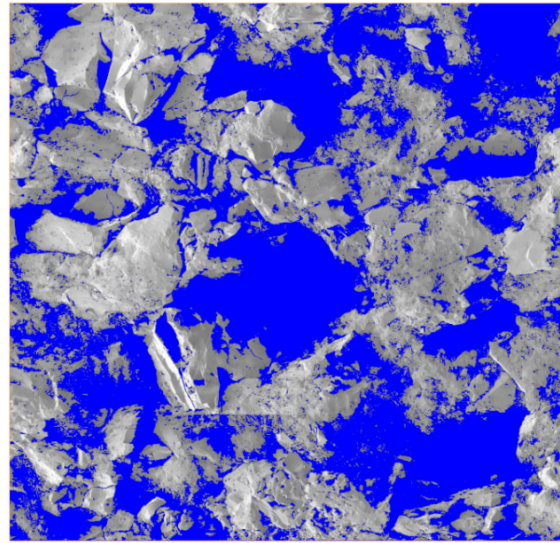
400  $\mu\text{m}$

c



400  $\mu\text{m}$

b



400  $\mu\text{m}$

d

Figure 6-2. SEM images of the sandstone samples; a and b are the raw images and c and d are the segmented images. Grey shows the grains, while blue shows the pores.

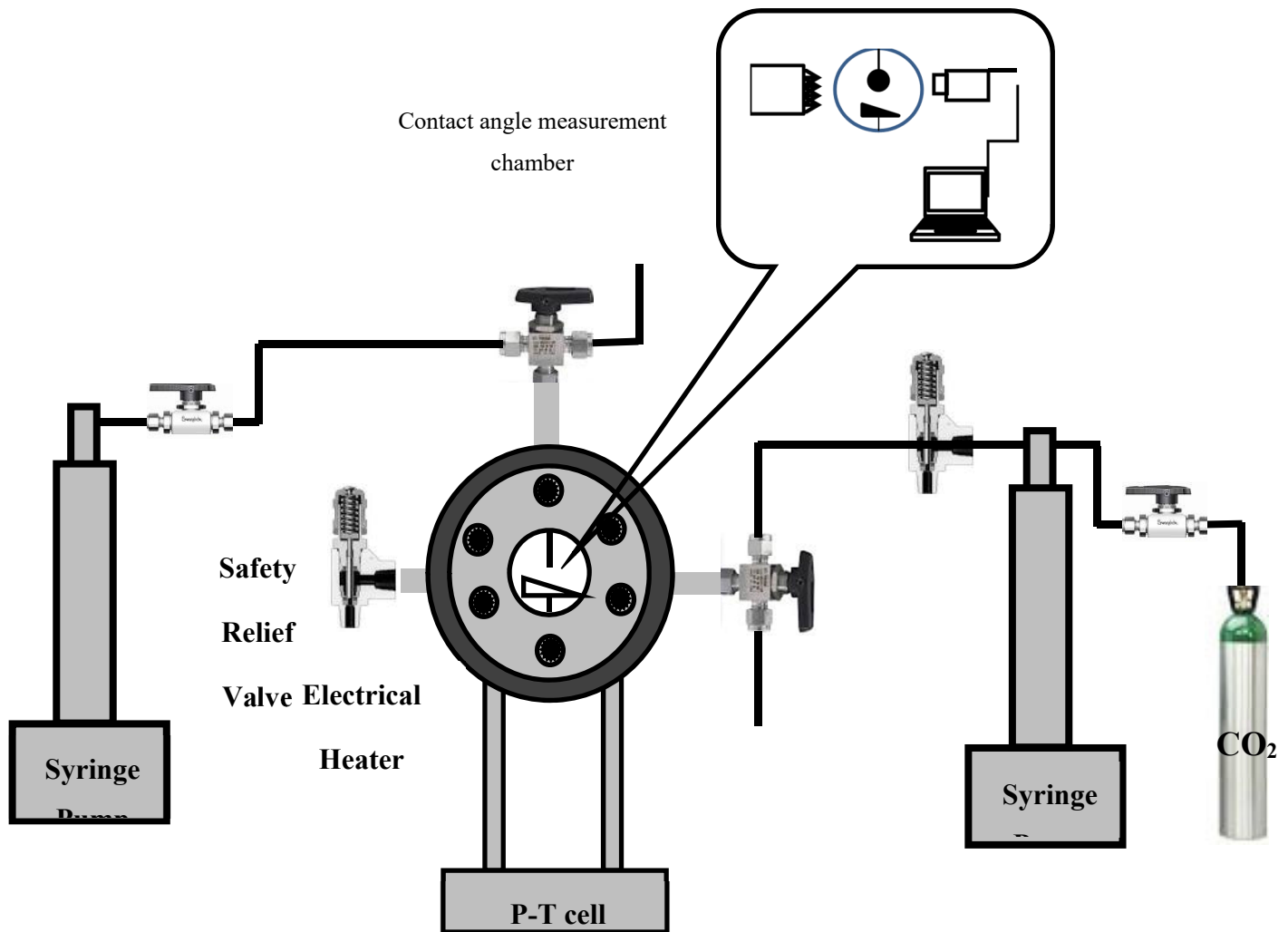


Figure 6-3. Schematic diagram of the high temperature/high pressure contact angle measurement apparatus used for contact angle measurements.

### 6.3. Results

Water contact angle  $\theta$  was measured at various pressures (0.1, 5, 10, 15, and 20) MPa and temperatures (296, 323 and 343) K on a sandstone surface (RMS surface roughness 540 nm). Advancing and receding contact angles at ambient conditions ( $T = 296$  K and 0.1 MPa CO<sub>2</sub> pressure) were close to zero as previously reported [115, 124]. However, advancing and receding contact

angles were increased with increasing pressure (Figure 6-4 and Figure 6-5 respectively) which is consistent with measurements reported in the literature data [108, 115, 116, 119]. The advancing-receding contact angle of quartz [108] was also plotted along with those of sandstone for the comparison. Iglauer et al. [125] explained this behaviour by rapid increase in CO<sub>2</sub> density with pressure, which strengthens the intermolecular interactions between CO<sub>2</sub> and quartz, and thus leads to de-wetting of the surface [105, 123]. Furtherer, advancing and receding contact angles were observed to increase with increasing temperature (Figure 6-4 and Figure 6-5) [105, 108, 116, 126].

The effect of salinity on contact angle was also investigated at 323 K and various pressure (5, 10, 15 and 20) MPa. DI water and 20 wt% CaCl<sub>2</sub> were used to observe the effect of ion concentration on sandstone contact angle. The advancing and receding contact angles were increased by ~ 10° and ~ 12° respectively when 20% CaCl<sub>2</sub> was used compare to DI water at 5 MPa (Figure 6-6 and Figure 6-7). The advancing and receding contact angles were also increased when CaCl<sub>2</sub> was used for all other pressures 10, 15, 20 MPa (Figure 6-6 and Figure 6-7). Thus more concentrated brine resulted in higher contact angles when compared to DI-water, consistent with previous studies [108, 117, 126, 127]. Chemicals purity are presented in Table 6-1

Table 6-1. Chemical Purities

| Chemical Name     | Source of Supply          | State  | Purity (wt. %)                            |
|-------------------|---------------------------|--------|---|
| CO <sub>2</sub>   | BOC Australia             | Gas    | ≥ 0.999                                   |
| CaCl <sub>2</sub> | Scharlab, Spain           | Powder | ≥ 0.995                                   |
| DI Water          | David Gray's<br>Deionized | Liquid | <sup>a</sup> Conductivity (0.02<br>mS/cm) |

<sup>a</sup> The conductivity of DI water was measured with Multiparameter (HI 9823) at T= 294 K.

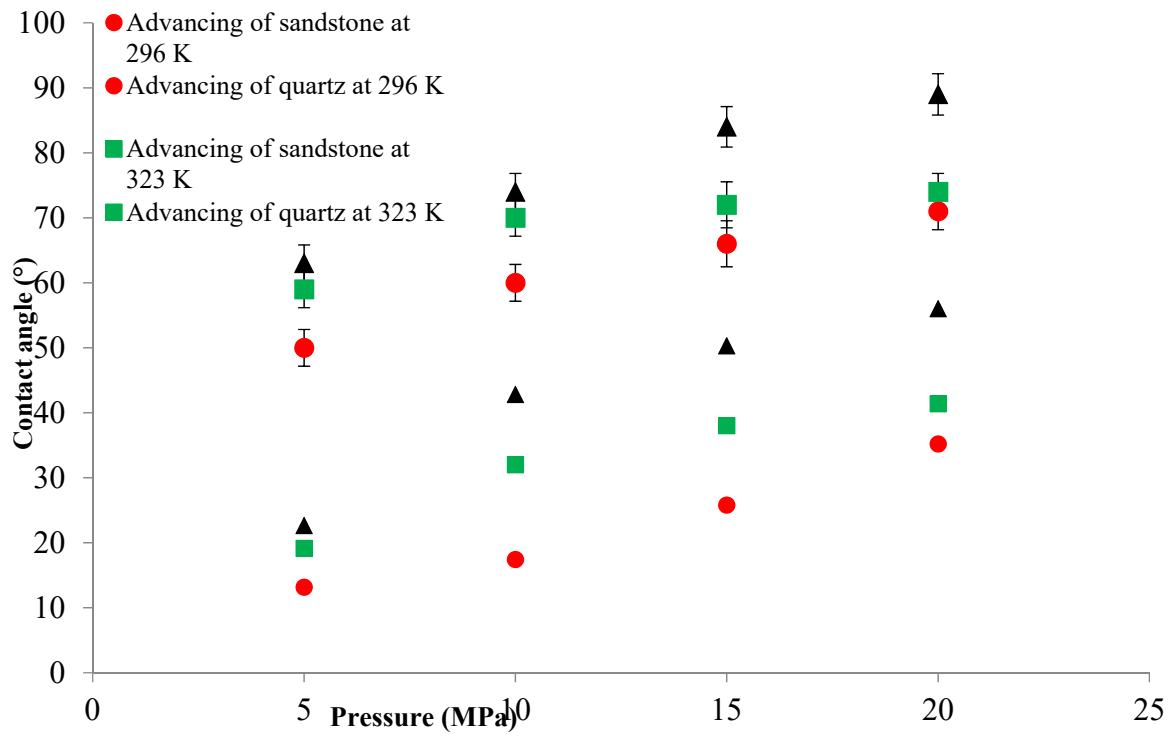


Figure 6-4. Advancing water contact angles for sandstone/CO<sub>2</sub>/DI water as a function of pressure and temperature; RMS = 540 nm, SD = 3 (where SD is the standard deviation).

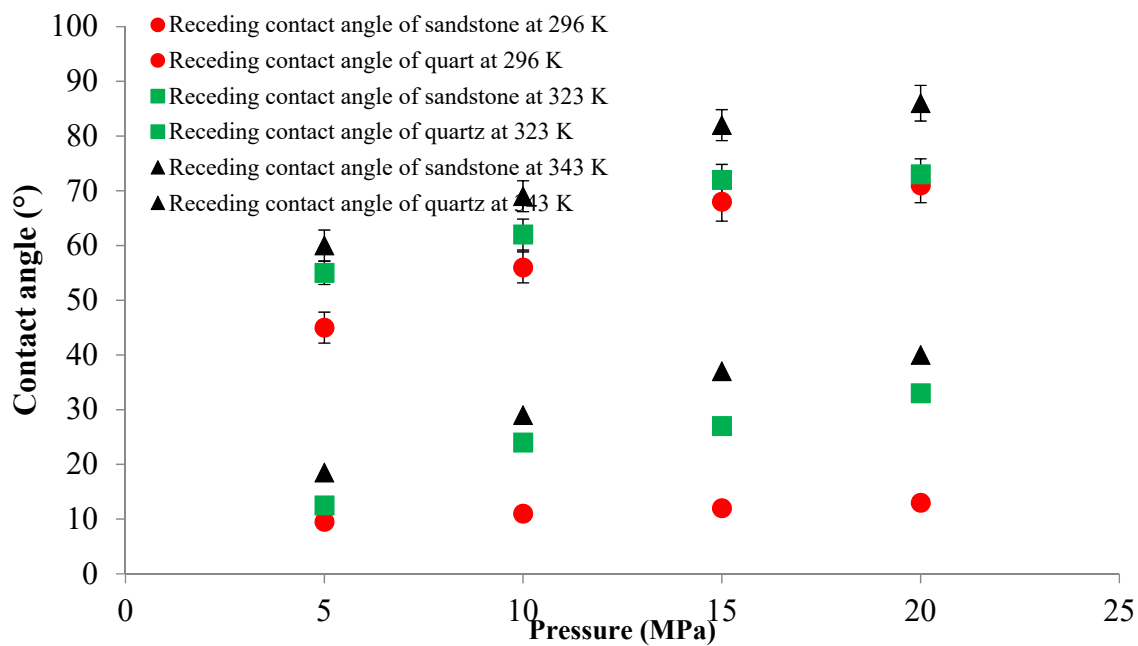


Figure 6-5. Receding contact angles for sandstone/CO<sub>2</sub>/DI water as a function of pressure and temperature; RMS = 540 nm, SD = 3.

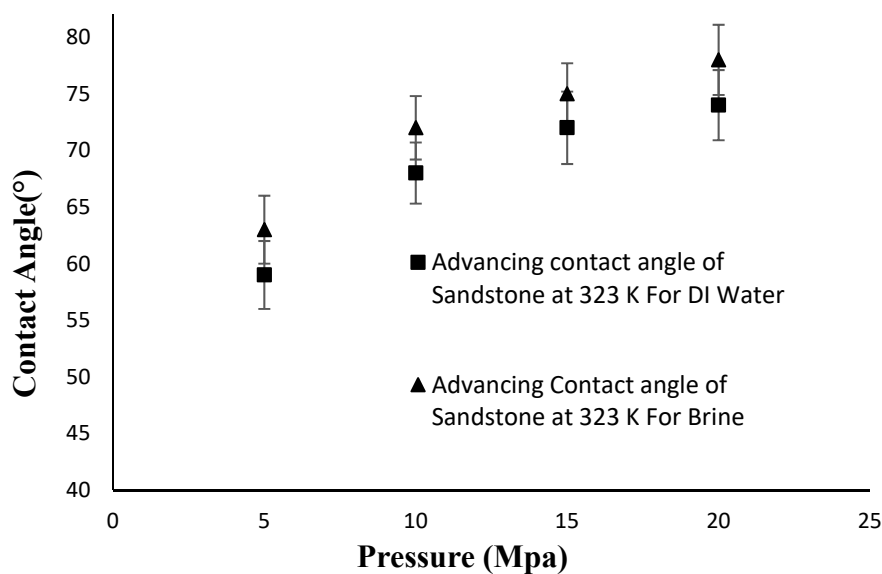


Figure 6-6. Advancing contact angles for sandstone/CO<sub>2</sub>/DI water and sandstone/CO<sub>2</sub>/brine (20 wt% CaCl<sub>2</sub>) as a function of pressure at a temperature of 323 K; RMS = 540 nm, SD = 3.



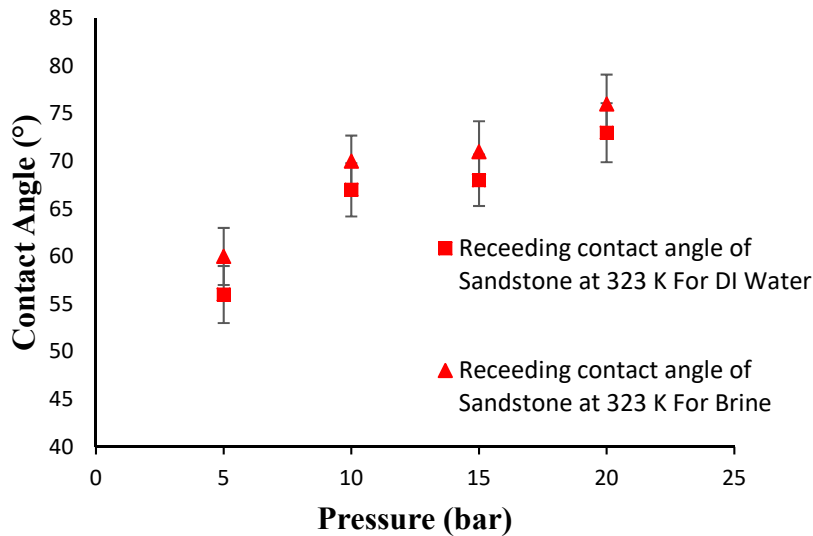


Figure 6-7. Receding contact angles for sandstone/CO<sub>2</sub>/DI water and sandstone/CO<sub>2</sub>/brine water (20 wt% CaCl<sub>2</sub>) as a function of pressure at a temperature of 323 K; RMS = 540 nm, SD = 3.

#### 6.4. Discussion

We recall the contact angle measurements of pure quartz at different pressure and temperature [108] which are consistent with other literature [45, 128] and presented in Figure 6 along with contact angle measurements of porous sandstone. It can be seen from Fig. 6 that the water contact angle of sandstone is consistently higher than that of pure quartz (which has no pores) regardless of the pressure and temperature of the system, and these data are consistent with the porous sandstone contact angle data presented by Cassie et al. [106]. While pressure increases the contact angle for both sandstone and quartz, this effect is more pronounced at lower temperatures. Temperature has a minimal effect on the contact angle. It increases only slightly with increasing temperature.

To analyse such differences between the contact angles of sandstone and quartz caused by the presence of pores, we assume that sandstone is mainly composed of quartz, i.e. the pores are also filled with CO<sub>2</sub> at the beginning of the experiment. Further, the TOC was very low (0.16 wt%) [129] for the selected sandstone sample, which makes it more suitable for CO<sub>2</sub> storage [44]. Notably, Arif et al. [130] observed a clear relationship between the TOC and CO<sub>2</sub>-wettability of the rock, whereby a high TOC content can lead to a high water–CO<sub>2</sub> contact angle (lower water wettability).

When a drop of a liquid, in the presence of another fluid (liquid or gas), is dispended on a solid surface with no/minimal electric potential, the droplet spreads across the solid surface, until the minimum free energy is reached [131].

This is related to the cohesion forces in the fluids and adhesion forces between the fluid material and the solid surface. If the energy dissipation due to the movement of the contact line by hysteresis is neglected, and the free energy change due to an infinitesimal increase in the base area of the droplet on the solid surface (surrounded by another fluid) is considered, , the free energy of the system can be calculated as follows [131]:

$$dF = \gamma_{LG} \cos \theta dA - \gamma_{SG} dA + \gamma_{SL} dA \quad 6.1$$

where  $\gamma$  is the interfacial tension or surface free energy,  $F$  is total free energy of the system,  $\theta$  is contact angle of the droplet and  $dA$  is the infinitesimal surface area (s, g and l represent the solid, fluid (gas or liquid) and liquid phases). When the minimum energy is reached and equilibrium is established, Eq. (6.1) turns to a special case, the Young's equation [105].

When the solid quartz surface is considered (Figure 6-8), the Young's equation is assumed to explain the force equilibrium in the droplet [123]:

$$\gamma_{LG} \cos \theta = \gamma_{SG} - \gamma_{SL} \quad 6.2$$

When pores exist within the substrate on the other hand, extra capillary forces driven by water movement into pores are created (if the substrate is water-wet). We call this force  $f$  herein (Figure 6-8). This force is a resultant of the capillary pressure ( $\Delta p$ ) acting on pores underneath the droplet ( $\phi.dA$ ). The infinitesimal capillary force acting on pore space can then be written as

$$f = \Delta p(\phi.dA) \quad 6.3$$

Where  $\Delta p$  is the capillary pressure. The energy associated with the infinitesimal capillary rise ( $f_c$ ) then takes the form:

$$f_c = \Delta p(\phi.dA).\tilde{h} \quad 6.4$$

where  $\tilde{h}$  is the average capillary rise in the pore system. Substituting capillary pressure with  $\frac{2\gamma_{LG} \cos \theta}{\tilde{r}}$  (where  $\tilde{r}$  is the average pore radius) yields:

$$f_c = \frac{2\gamma_{LG} \cos \theta}{\tilde{r}} \tilde{h}(\phi, dA) \quad 6.5$$

Therefore the free energy equation takes the form:

$$dF = \gamma_{LG} \cos \theta dA - \gamma_{SG} dA + \gamma_{SL} dA + f_c \quad 6.6$$

Thus the energy equilibrium equation ( $dF \rightarrow 0$ ) yields:

$$\gamma_{LG} \cos \theta = \gamma_{SG} - \gamma_{SL} - \frac{2\phi\gamma_{LG} \cos \theta}{\tilde{r}} \tilde{h} \quad 6.7$$

Eq. 6.7 illustrates that the contact angle of porous sandstone must be higher than that of pure quartz if other thermodynamic variables such as pressure and temperature are unchanged. This is supported by the experimental data of the porous sandstone investigated in this study when compared to that of solid quartz reported by Al-Yaseri et al [108]. In addition, the experimental contact angle reported by Kaveh et al [132] for porous Sandstone Bentheimer were higher than the contact angle for pure quartz reported by Al-Yaseri et al [108], Espenosa et al [128] and Chiquet et al [45]. In all cases, the contact angle of sandstone is consistently higher than that of quartz.

In order to justify our approach, we have taken images from a water droplet on the sandstone samples after 2 and 4 mins (Figure 6-9). It is evident from this figure that water started to migrate into the pores clearly demonstrating that a capillary force is active.

With increasing elapsed time, more water infiltrated, and the contact angle reduced significantly from 55° to 45° showing that the capillary driven force ( $f$ ) is weakened with time until reach equilibrium (Figure 6-9) e.g. it is noted that at equilibrium, the contact angle of porous sandstone is still higher than pure quartz.

However, if pore walls are hydrophilic however the contact angle will stay unchanged if pores are hydrophobic and no water entry occurs [133].

It is thus clear that porous water-wet substrates exhibit higher water contact angles (when compared with the identical surface without pores).

We furthermore conclude that the amount of surface pores (porosity fraction), the pore throat diameter and height of fluid infiltration play important roles in the magnitude and kinetics of contact angle variation on porous surfaces, caused by the driving capillary forces.

We now consider the Cassie-Baxter equation (Eq. 6.8) to assess its accuracy in predicting measured sandstone contact angle data. We also consider the effect of pressure and temperature on fluids interfacial tension to assess its contact angle prediction (Figure 6-10). As seen from Figure 6-10, Cassie-Baxter equation can predict the trend of the contact angle changes but the obtained values for contact angles are significantly out of range. We then use the same set of variables (porosity= 9.6%) assuming that  $h$  is known (= 0.5 mm from Fig. 6.7) to predict the sandstone contact angles (also plotted on Fig. 8) by our newly derived equation (Eq. 6.7). It is seen from Figure 6-10 that the predicted contact angle of our equation is closer to the measured value with a same trend of that of Cassie-Baxter equation.

$$\cos \theta_c = f \cos \theta - (1 - f) \quad 6.8$$

Where  $\theta_c$  is the predicted Cassie-Baxter contact angle,  $f$  is the fractional projected area of material,  $\theta$  is the smooth area contact angle and the  $(1 - f)$  term is thought to reflect the contribution of air remaining under the drop [134].

The only parameter which externally influences the contact angle in the Cassie–Baxter equation is porosity, which means that the analysed prediction is the best outcome of this model for the current data set. Our equation however takes into account the pore radius and water infiltration height along with the porosity. Porosity and average pore radius data are often available for tested samples, but not the infiltration height. While having this parameter will significantly improve model predictions of a porous substrate, the wettability information is required to estimate this parameter precisely. The other approach is to use correlation based estimations of  $h$  which can be obtained with data sets of a particular substrate. For instance, the correlation of  $h$  can be calculated with respect to other state variables and the results can be applied to new data sets. Determining such a correlation or an alternative physical equation as a function of state variables will therefore be a future research direction.

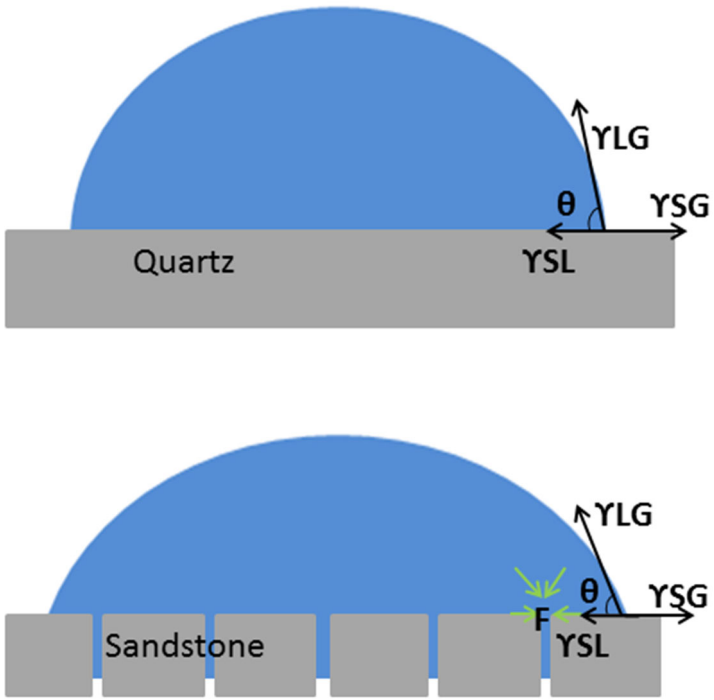


Figure 6-8. Forces acting on quartz (top) and sandstone (bottom).

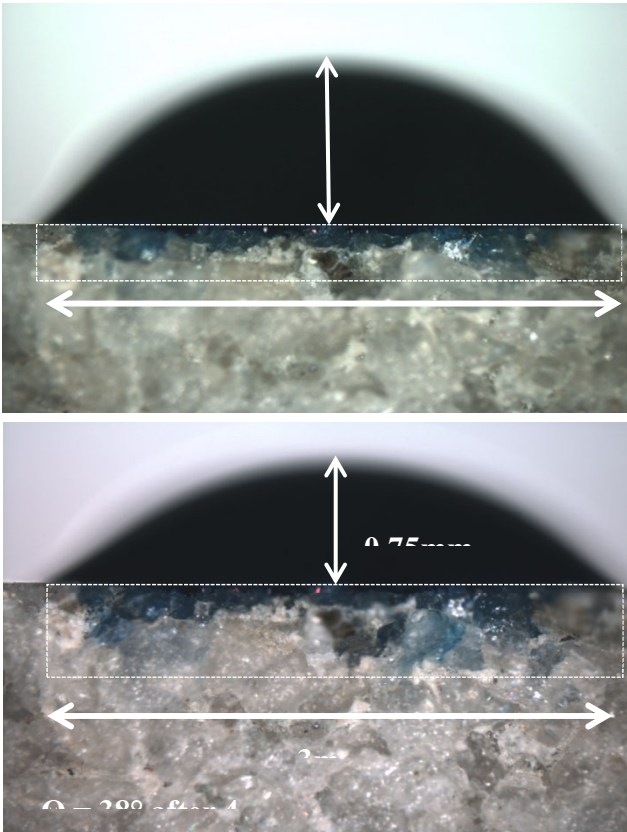


Figure 6-9. Water droplet on a sandstone sample in the presence of air under atmospheric conditions after exposure times of 2 min (top) and 4 min (bottom).

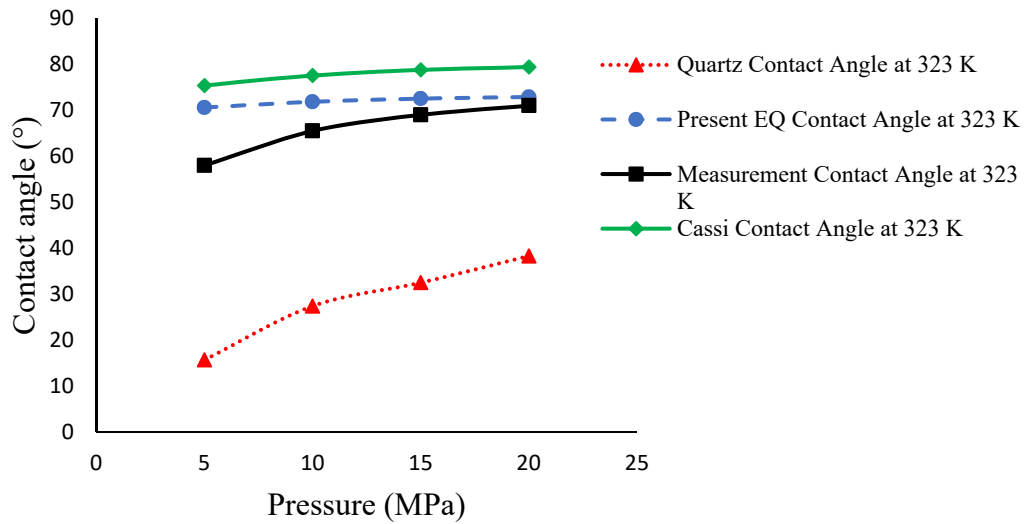


Figure 6-10. Comparison of the equilibrium contact angles obtained through laboratory experiments, the Cassie–Baxter method, and the present method at a temperature of 323 K.

## 6.5. Conclusions

Pore systems and surface roughness are considered to be fundamental factors which influence the variations in the wettability of reservoir rock with inherent heterogeneities. The advancing-receding contact angles of brine/CO<sub>2</sub> and sandstone as a function of pressure, temperature, and salinity were investigated in this study. The results were then compared with the contact angles of pure quartz samples measured at the same pressure, temperature, and salinity. It was found that the contact angle of sandstone was systematically higher than that of pure quartz at any pressure or temperature because of the presence of pores in sandstone. The contact angles also increased with increase in pressure and temperature and decreased with increase in the salinity. In addition, the contact angles of porous sandstone determined using the Cassie–Baxter equation were consistent with those determined using our new derived model (Eq. 7). Increase in the contact angle due to the presence of pores was linked to the capillary-driven forces acting at the surface pore throats and were mathematically formulated. The imaging of water entry into the substrate pores with optical microscopy confirmed the validity of the analytical approach adopted. Further studies should be conducted on pore rocks with different pore sizes and structures to better understand the variations in wettability in the presence of porosity.

## **7. Chapter 7: Experimental Study of a Cryogenic Ambient Air Vaporizer**

### **7.1. Introduction**

LNG (Liquefied Natural Gas) is globally acknowledged as a clean fuel for both large-scaled industrial production and other sales gas purposes. It has been noted that the overall world consumption of LNG in recent years was increased remarkably. The total world LNG exports in 2016 was 346.6 bcm (billion cubic meters) which has been increased by 16.5% compared with that of 2010 [135]. The total number of LNG receiving terminals all over the world was increased in the meanwhile. Regasification is one of the most important procedure in LNG terminal operations. Essentially, there are three main different types of vaporizers in LNG industry, i.e. ORV (Open Rack Vaporizer), SCV (Submerged Combustion Vaporizer) and IFV (Intermediate Fluid Vaporizer). ORVs and SCVs are widely used in Asia and Europe[136, 137]. Most current US LNG terminals utilize SCVs or IFVs with fired heaters. However, these units are not environmentally sustainable, as they produce large amounts of emissions, such as exhaust gas and processed cold sea water. It is thought that the released cold and chlorinated sea water from ORV can have a negative impact on the marine environment by killing marine life[138]. Increased energy costs and concerns about environmental issues have led the LNG industry to look into other alternative vaporization systems by using greener technologies. One of the promising alternatives is the ambient air technology. Some large LNG projects have selected ambient-air based approaches instead of traditional regasification technologies, such as Dahej LNG terminal [139] in India, Oregon LNG import terminal [140-142] and Corpus Christi Liquefaction project [143] in America.

AAV (Ambient Air Vaporizer) technology has obtained an increasing attention in recent years, and is highlighted as the greenest technology for LNG regasification[137, 138]. As the heat source is obtained directly from ambient air without any intermediate fluid, its effluent is only cold and humid air which can be dispersed and have no harmful effect on the environment. However, there are two main concerns when using AAVs, i.e. footprint and frost formation. Because AAV uses warm and low-energy-grade ambient air which is not as high as ORV and SCV in terms of heat transfer rate, it requires several banks of AAV stacks working together in order to deliver the desired amount of



LNG output. This could occupy much larger footprint than ORVs and SCVs. Frost formation due to water vapour condensing and solidification could reduce heat transfer significantly, thus operation shutdown and defrosting vaporizers must be performed periodically. The LNG station generally has different banks of AAVs working in shifts by putting some in idle for defrosting naturally. If applying some innovative defrosting technology, a non-stop vaporization process could be achieved by performing defrosting intermittently and shortening the defrosting process largely. The whole footprint can therefore also be reduced in the meanwhile.

Both numerical and experimental studies on AAVs have been conducted to investigate its heat transfer behaviour and frost formation mechanism. Jeong, Chung, et al.[144-146] conducted series of studies of both simulations and experimental work on heat transfer performance of natural-draft AAV. They used LN<sub>2</sub> (Liquid nitrogen) as working fluid. Heat transfer coefficients of inside & outside the pipe and non-dimensionless number were evaluated by performing CFD studies. Heat transfer performance of different fin configurations (i.e. fin length and thickness), length of finned tube loops and operations in different seasons were compared and optimized. Liu, Jiao and Wang [147] performed a CFD study on heat transfer performance in LNG AAV by using a coupled numerical models. The model combined LNG boiling phase change with air natural convection to investigate the factors such as air temperature, LNG flow rate and finned tube distribution in a bundle. Pandey, Singh, Shah and Acharya[148] performed an experimental study on a natural-draft AAV at different operating capacities and AAV ground clearance to investigate the effect on heat transfer and frost formation. The rate of frost formation could be increased either by increasing the flow rate of cryogenic fluid or reducing the ground clearance of AAV stack. The behaviours of frost formation in cryogenic (temperature below approx. -150°C) and refrigeration (temperature above -20°C) temperatures could be different from each other. Through conducting an experimental study of frost formation on vertical cryogenic surfaces under natural convection conditions by Liu, Dong and Li [149], water vapour could be condensed before reaching the cryo-surface, thus the amount of frost formed was not as much as that obtained in refrigeration temperatures. They also observed and tested that oxygen in air could be condensed on cryo-surface[149, 150] before frost crystals appeared if surface temperature is lower than -165°C. Moreover, physical properties of cryogenic frost, such as density and thermal conductivity could have different temperature correlations compared with refrigeration conditions[151]. In AAV operation, defrosting process is usually performed periodically by putting the AAV stacks in idle and undergoing de-icing naturally. Several

innovated design of fins by conducting invasive defrosting have been patented[152, 153]. Through providing a separate channel and introducing hot fluid in it, this could shorten the defrosting period, remove the frost more effectively, and also dry out the fin surface and air passage to delay frost formation in the next cycle. Some studies were focused upon defrosting by modifying the hydrophobic or hydrophilic properties of metal surfaces. Other defrosting methods[154] such as electric heating, ultrasonic vibration, dehumidifying or preheating inlet air and hot water/gas defrosting, were investigated by using an air source heat pump (ASHP) system rather than cryogenic air vaporizers.

In order to explore the feasibility of continuous operation of regasification and minimizing the footprint of the AAV, the authors in this study proposed an innovated design of AAV which embedded a defrosting duct in the middle of the fins. Through running a hot stream (MEG-water solution) in the defrosting channel, the AAV could perform defrosting invasively and shorten the period for defrosting without shutting off operation of the AAV. The design was tested in an outdoor pilot-scale experimental setup through evaporating LN<sub>2</sub> (Liquid nitrogen). Various operating conditions were tested, such as operating pressures, LN<sub>2</sub> flow rates, ambient conditions (e.g. relative humidity and temperature), defrosting conditions (e.g. flow rate and temperatures), etc.

## 7.2. Flow scheme and control system

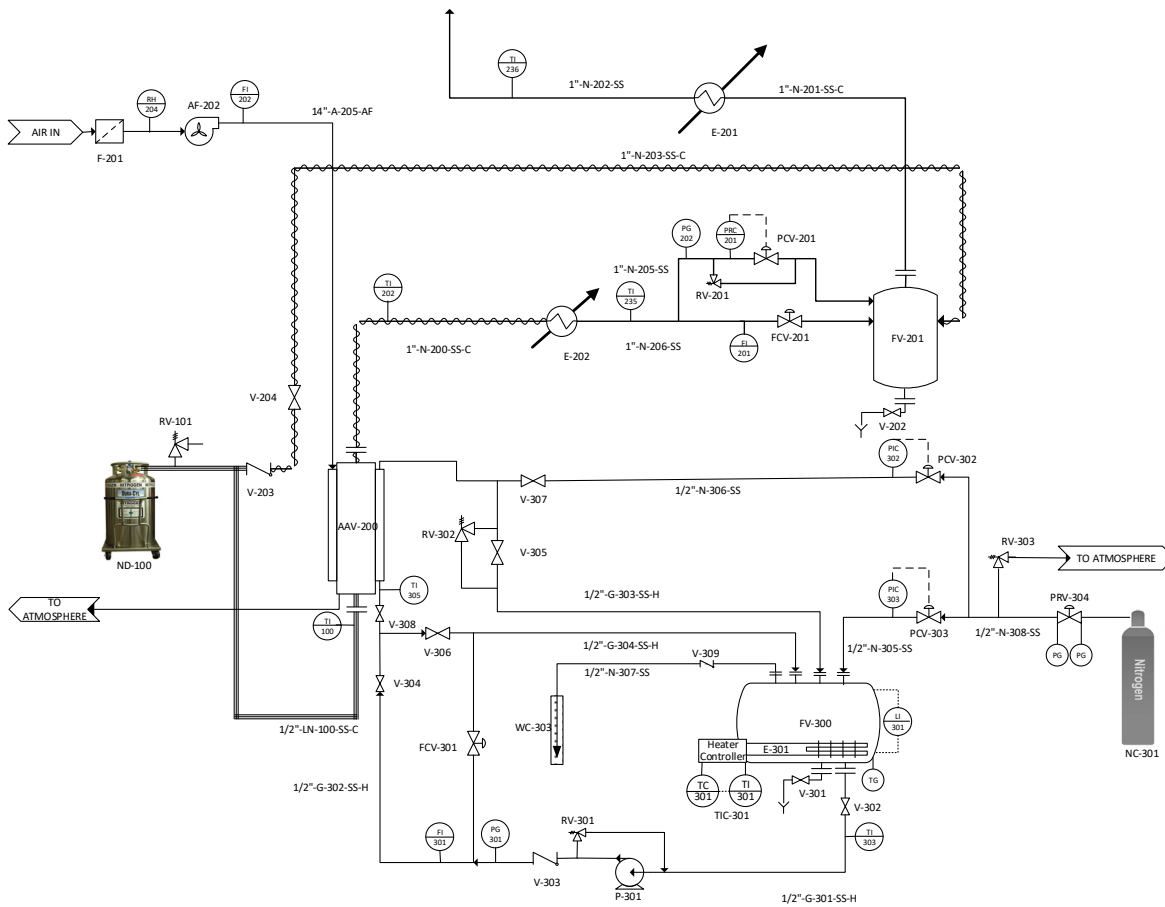


Figure 7-1 P&ID diagram of the pilot-scale experiment

The process design is illustrated in Figure 7-1. Because LNG is flammable and could have more safety concerns, liquid nitrogen was used as a substitute. There were mainly three streams in the process, viz. nitrogen, air and solution of Mono-ethylene glycol (MEG) & water. LN<sub>2</sub> was initially stored in a Dewar vessel (ND-100) with a storage capacity of 230 L and pressure range 1~15bar. The forced-draft AAV (AAV-200) was comprised of a single finned-tube (2 m high) and a transparent acrylic duct (diameter 300 mm) to enclose the vaporizer. Air flow (velocity range 0~7m/s) was driven by a blower (AF-202) to force ambient air through the acrylic duct to exchange heat with LN<sub>2</sub>. The auxiliary heater (E-201 & E-202) was placed at the downstream of nitrogen process line in order to heat up the output nitrogen to ambient temperature and vent it to atmosphere at the end. This could also protect the downstream instruments to avoid exposure to cold temperatures. After running the operation for a period (2~6 hours), frost could be formed on the

AAV fins, and could have affected the heat transfer rate. MEG solution was applied in the experiment for defrosting purpose. Pure MEG was diluted to 60% volumetric concentration which could provide the property of very low freezing point (-52.8°C). The MEG cycle was comprised by the MEG storage vessel (FV-300), MEG heater (E-301) and MEG pump (P-301). When performing defrosting, the hot MEG solution was introduced from the bottom of AAV, and run through the defrosting duct in fins to the top of the AAV. In defrosting process, the LN<sub>2</sub> evaporation was ongoing without operation shutdown. Once defrosting was completed, nitrogen (NC-301) was turned on to drain the MEG solution retained in the tubes back to the MEG storage vessel and to purge the MEG flow channel in order to avoid any frozen blockages when evaporating LN<sub>2</sub>.

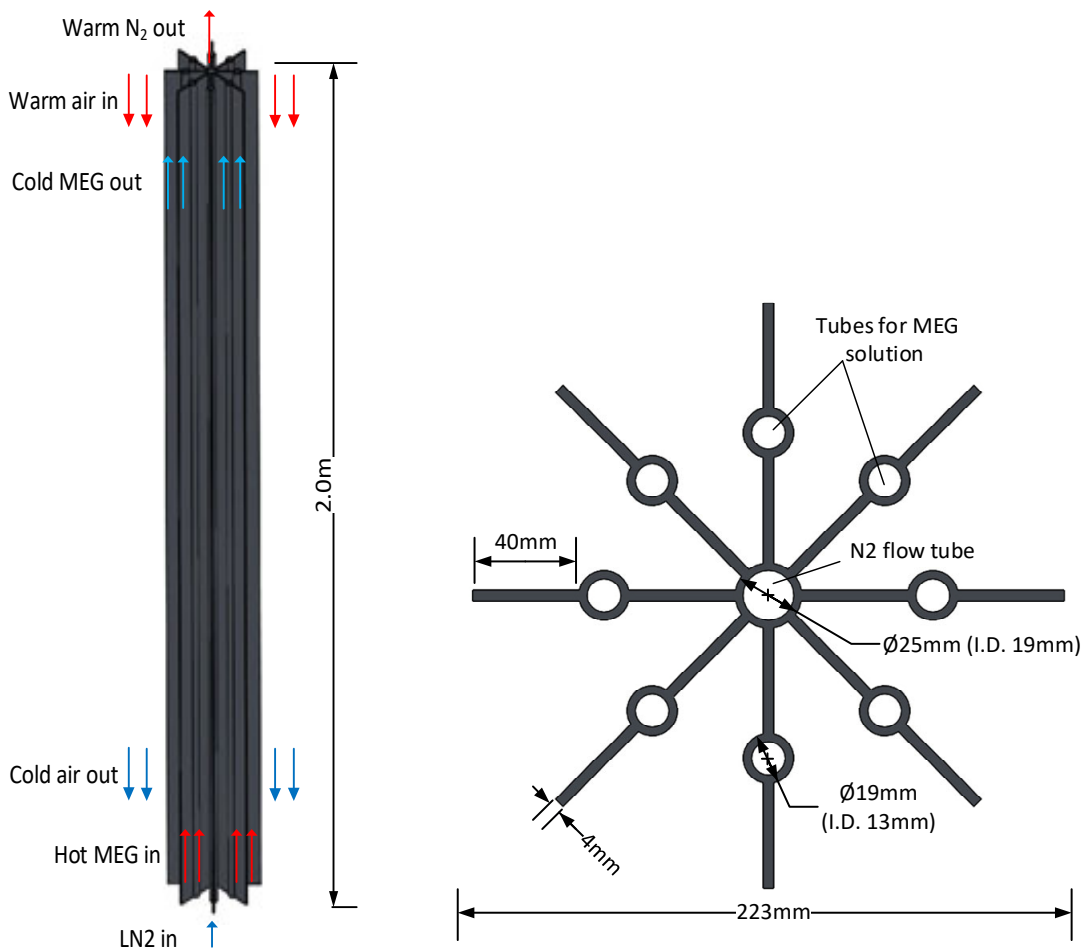


Figure 7-2. Flow scheme and schematic Diagram of finned tube design.

The vaporizer was made of aluminium alloy which could provide excellent heat transfer effect. The fin configurations are demonstrated in Figure 7-2. Eight pieces of fins (fin length 99mm) were welded onto the central tube (25mm diameter). A smaller tube (19mm diameter) used as defrosting stream duct was welded in the middle of the fin plates. The AAV operating pressure and capacity was designed as 15 bar and 10~25kg/hr, respectively. The flow rate of MEG-water solution was designed as 200~700L/min. The MEG cycle was performed periodically, and was only turned on when significant amount of frost was observed on the AAV. The MEG cycle was shut off when the vaporizer was completely defrosted and the fin surfaces were dried out.

When supplying LN<sub>2</sub> from the Dewar vessel, the physical status (liquid or gas) of the nitrogen was of great importance. The main issues for the AAV test rig were low nitrogen flow rate and relatively higher operating pressures which could result in flash losses and generating a lot of gas during the operation, thus the AAV may not be performed at the full potential cooling load. In order to ensure the liquid status of nitrogen in the process line at the AAV inlet, a double-jacketed and super-insulated vacuum line in combination with a phase separator was proposed, as illustrated in Figure 7-3. The outside of the equipment was insulated by a vacuum jacket. Both the cooling jacket and process line were supplied with LN<sub>2</sub> from the same pressurised Dewar. The process line was enclosed in the cooling jacket which could generate an LN<sub>2</sub> bath for chilling the process line from the tube outside. It could also help to recondense the gaseous form of nitrogen due to heat leak in the nitrogen transport line. The LN<sub>2</sub> level inside cooling jacket was maintained by a float valve (shown in Figure 7-3) which only allowed the gaseous nitrogen to be vented off and keep the cooling jacket filled with cold liquid.

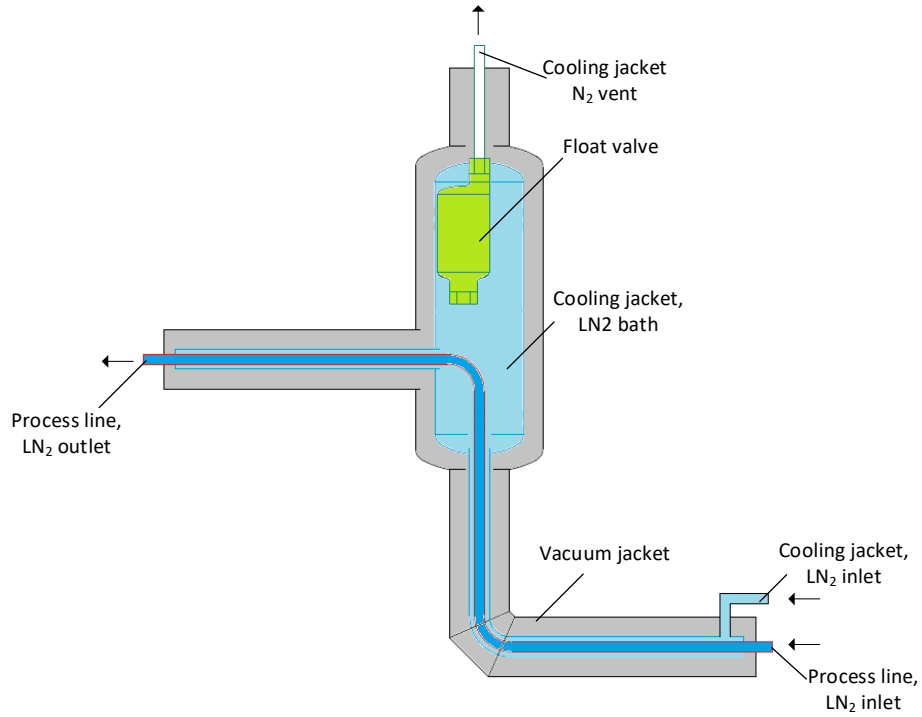


Figure 7-3. Schematic Diagram of phase separator

In order to test the effectiveness of the equipment, a thermal well (shown in Figure 7-4) was designed by placing a thermocouple (TI100 in P&ID diagram) at the center of the process line at AAV inlet which could measure the fluid temperature directly instead of the skin temperature of the metal.

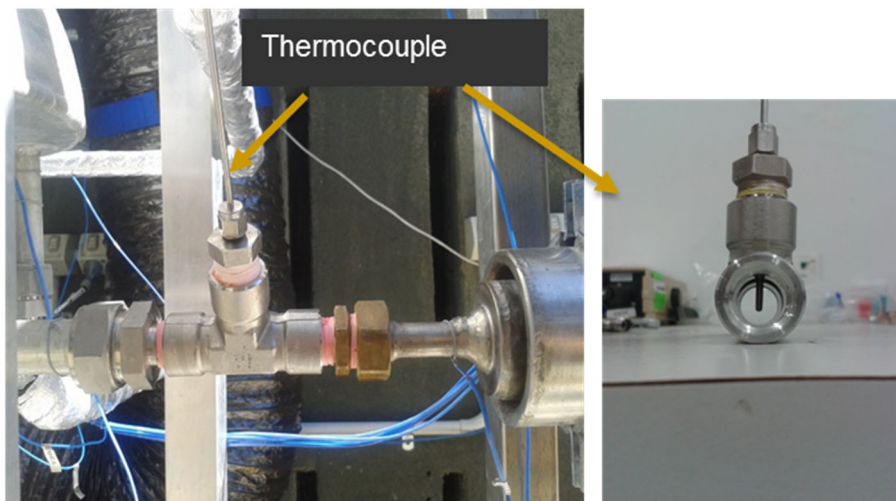


Figure 7-4. Thermocouple for measuring the LN<sub>2</sub> temperature at AAV inlet.

In order to explore the heat transfer performance of the AAV, different types of instruments were installed in the system, such as thermocouples, relative humidity sensors, flow meters, pressure gauges, etc. Details of all the instruments are listed in Appendix 2. The inlet and outlet nitrogen temperatures in the vaporizer were monitored by the thermocouples TI100 and TI202 (shown in Figure 7-1), respectively. Figure 7-5 illustrates the distribution of the sensors on the AAV body. TI203~TI205 and TI216 were the thermocouples to measure the temperature of air flow at different levels. The thermocouple arrays of TI206~TI210 and TI211~TI216 were placed to measure the temperature gradient of frost layer at AAV bottom and 0.2m height, respectively. The fin surface temperature was tested by the thermocouples TI217~TI231 at 6 different heights. At each level, temperatures of three different horizontal spots, i.e. central tube, MEG tube and fin end, were measured in order to investigate the temperature gradient on fins. RH201~203 were the relative humidity sensors to measure the moisture content at different heights. RH204 was installed to measure the ambient humidity and was located next to the air blower. All the sensors were connected with the Data Acquisition Unit (DAU), with the recording frequency set at 5 seconds intervals in order to track the temperature changes effectively.

Table 7-1. Details of instrumentation used in the AAV system

| Tag No.     | Description  |
|-------------|--|
| RH201~204   | Relative humidity sensor to measure the moisture content in air flow |
| TI100~TI305 | Thermocouples to measure the temperature profiles                    |
| TG302       | Temperature gauge to measure the temperature of MEG-water solution   |
| LI301       | Level indicator to show the solution level in MEG vessel             |
| PG202       | Pressure gauge to locally demonstrate the AAV operating pressure     |
| PRC201      | Pressure transmitter to measure and record the operating pressure    |
| FI202       | Air flow meter to monitor and record air flow rate                   |
| FI201       | Nitrogen flow meter  |
| FI301       | MEG solution flow meter  |
| PG301       | Pressure gauge to measure the MEG flow pressure at pump outlet       |

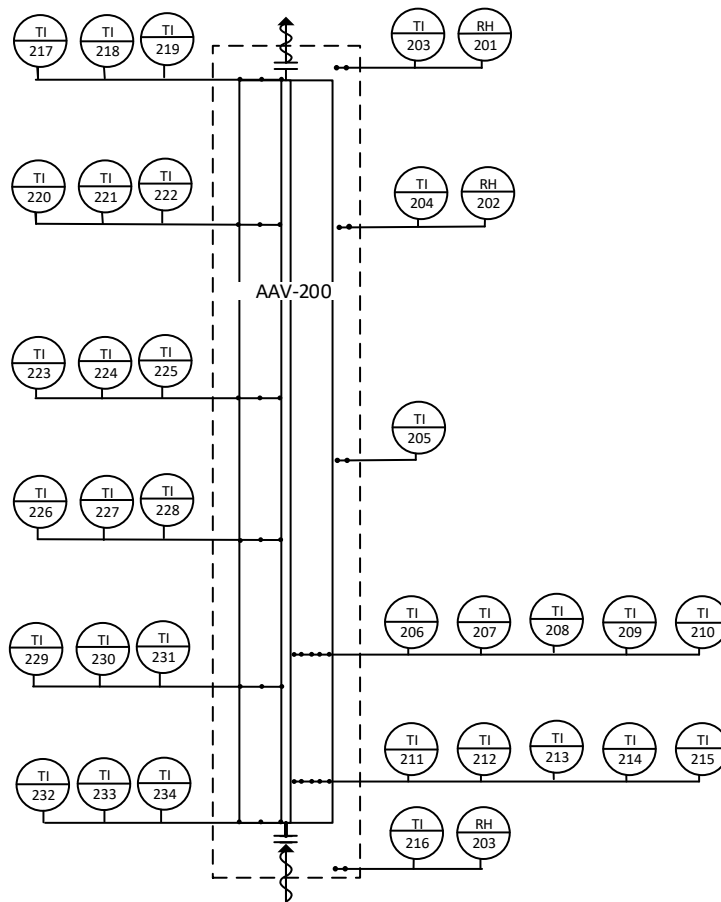


Figure 7-5. Distribution of thermocouples on vaporizer.

The test rig was located outdoors by occupying a footprint of 7.0m × 2.0m. The overall height of the vaporizer was 3.0m with a ground clearance of 1.0m in order to fit the connection of the LN<sub>2</sub> process line. The air blower was placed at one end of the site in order to avoid cold air from the AAV bottom bypassing to the air inlet. The operation was open to air in order to minimize the risk of operating cryogenic liquid and asphyxiation due to nitrogen displacement. Safety features including relief valve, check valve, flash vessel, gas vent etc., were considered properly. During the site preparation, bonding area was prepared in order to contain any possible leaks of chemicals, such as MEG-water solution and liquid nitrogen. The MEG vessels and the tubes for hot MEG solution and cold LN<sub>2</sub> process line were insulated properly by applying different insulation materials. The AAV pilot site photo is shown in Figure 7-6.





Figure 7-6. Site photo of the system of ambient air vaporizer

### 7.3. Operating data analysis (Commissioning operation)

Overall eleven different operating trials were conducted for both commissioning and normal operation. Test #1~6 was conducted in order to examine the equipment performance for cryogenic temperature, certify team members for operating LN<sub>2</sub>, test insulation used for LN<sub>2</sub> process line, explore the proper operating conditions, etc. Operation condition of Trials #1-6 are described in Table 7-2.

| Test number               | Test #1 | Test #2 | Test #3 | Test #4 | Test #5 | Test #6 |
|---------------------------|---------|---------|---------|---------|---------|---------|
| Test duration (hr)        | 1:30    | 1:30    | 1:00    | 1:30    | 1:40    | 2:40    |
| LN2 flowrate (L/min)      | 500     | 400     | 200     | 600     | 140     | 250     |
| Operating pressure (bar)  | 8       |         | 14      |         | 13      | 9       |
| Air Velocity (m/s)        | 4       | 6       | 5       |         | 7.1     | 1.8     |
| Ambient temperature (°C)  |         |         |         | 17.8    | 15      | 16.2    |
| Ambient relative humidity |         |         |         | 74.8    | 54.37   | 85%     |

(test #6), the temperature of LN<sub>2</sub> before the globe valve after 2 hrs was approximately -161°C, while the temperature after the globe valve was only about -120°C. The temperature increase could be because of the big metal body of the globe valve with a long handle (shown in Figure 7-10) which was causing significant heat leak. The nitrogen temperature at AAV outlet was kept constant at -44°C after 2 hrs operation.

As shown in Figure 7-8, the frost formation along the AAV started at the bottom of AAV especially at the central tube where the air velocity was too low. The maximum height of frost in this test (#6) was 1m after 2hr operation. Many reasons can reduce the frost to be formed along the AAV such as ambient conditions (ambient temperature, low air humidity, and also day time radiation flow).

The temperatures on fins was evaluated by averaging the temperature values measured at central tube, fin middle and fin end (fin edge) at the same AAV height. The minimum temperature was observed at the bottom of the AAV with -40°C (at 0m) as can be seen in Figure 7-9.

Table 7-2 . Operating condition (Test #1-6).

| Test number               | Test #1 | Test #2 | Test #3 | Test #4 | Test #5 | Test #6 |
|---------------------------|---------|---------|---------|---------|---------|---------|
| Test duration (hr)        | 1:30    | 1:30    | 1:00    | 1:30    | 1:40    | 2:40    |
| LN2 flowrate (L/min)      | 500     | 400     | 200     | 600     | 140     | 250     |
| Operating pressure (bar)  | 8       |         | 14      |         | 13      | 9       |
| Air Velocity (m/s)        | 4       | 6       | 5       |         | 7.1     | 1.8     |
| Ambient temperature (°C)  |         |         |         | 17.8    | 15      | 16.2    |
| Ambient relative humidity |         |         |         | 74.8    | 54.37   | 85%     |

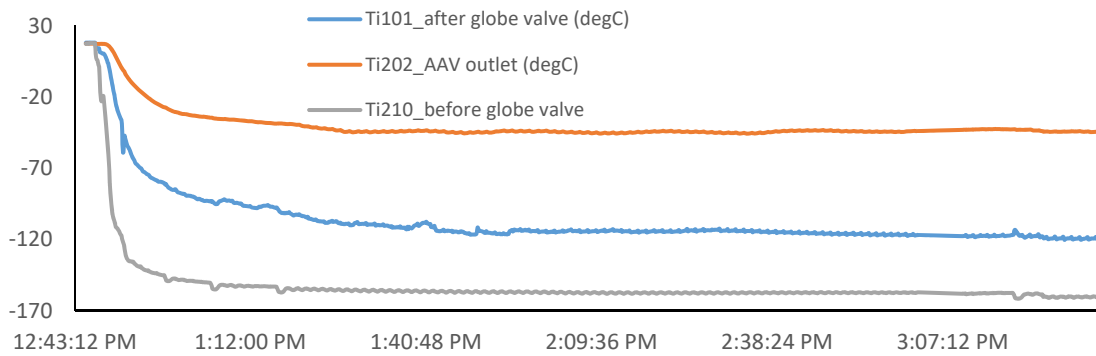


Figure 7-7. AAV inlet and outlet temperature profile test #6


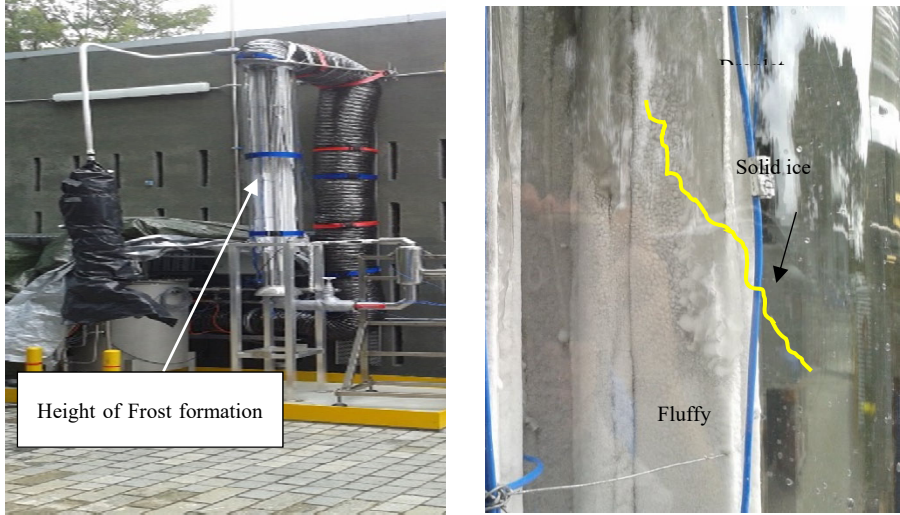
| Duration | Pics of frost formation  |
|----------|--|
| 50min    |   |
| 135 min  |  |

Figure 7-8. Frost formation from test #6



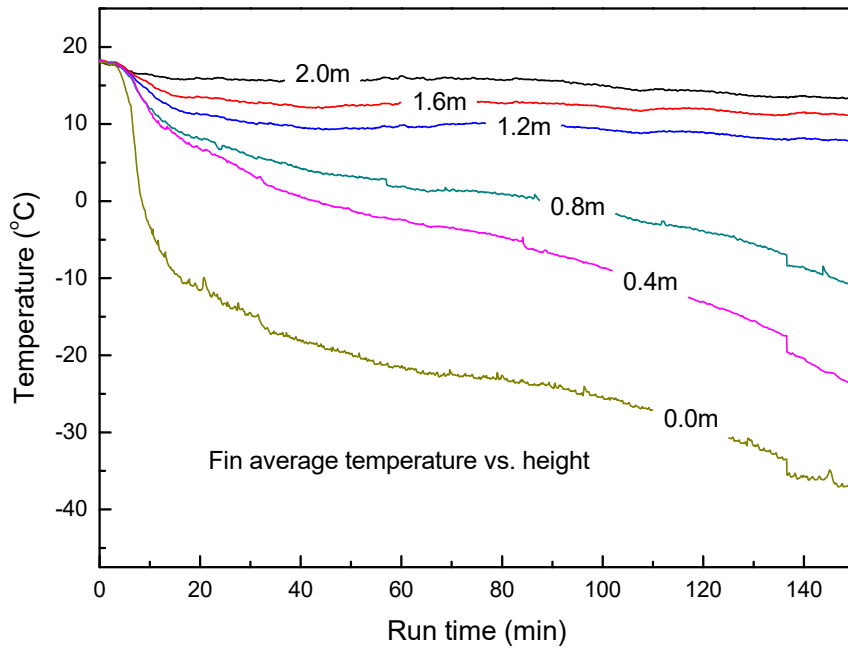


Figure 7-9. Fin average temperature

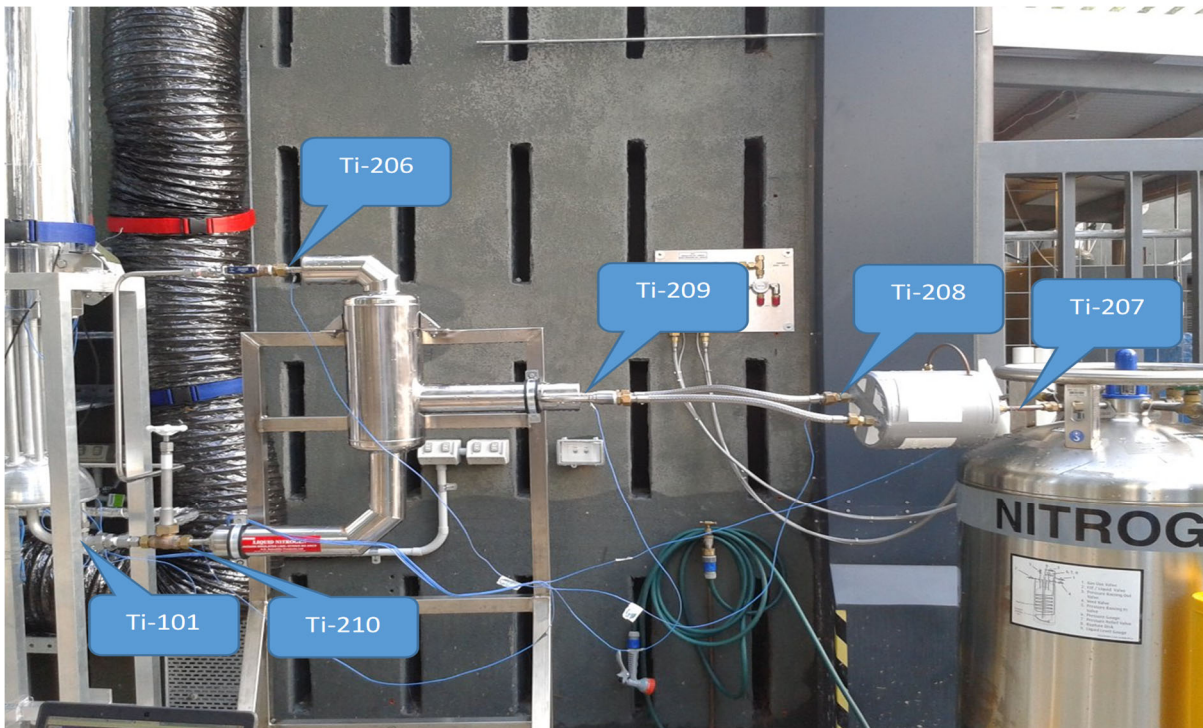


Figure 7-10. Temperature Sensors and globe valve location

### 7.3.1. Design modifications

During the initial tests (#1-6) of the AAV system, -120 C was the minimum temperature reached at the inlet of the vaporizer as described in Figure 7-10 (Ti101- after globe valve). The first 6 trials (commissioning trials) were conducted with low LN2 flowrates and relatively lower humidity, thus the frost formation was very low. In such cases, formation a thick layer of frost needs to be removed and that needs a long operation duration which was not possible due to the limitation of LN2 Dewar size.

Based on the initial results, and in order to increase frost formation along the vaporizer, several modifications were made to decrease the inlet temperature to the vaporizer (Ti101-after globe valve) and speed up the process of the frost formation. These modifications are discussed below:

#### 1. Humidify Air Flow

The system was modified by applying a mist generator in the air duct to create mist and increase the air humidity as shown in Figure 7-11. Through running a quick test without LN<sub>2</sub> flow, the relative humidity of air flow at AAV inlet could reach almost 100% in a relatively lower air velocity. Although the air inlet temperature could drop (within 10 °C) by humidifying the air flow, the humidity ratio is still higher.

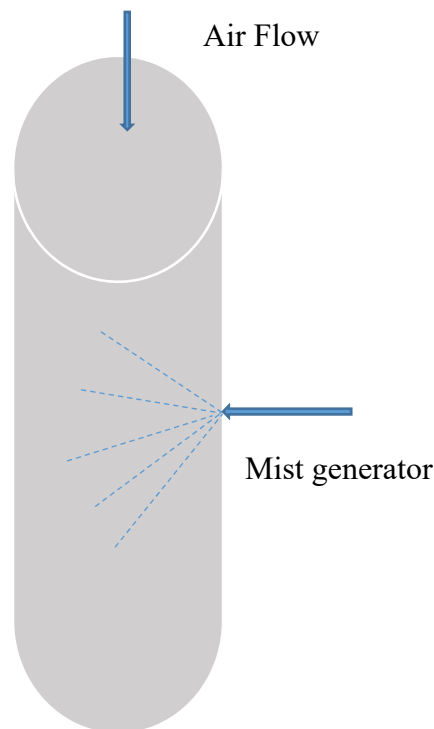


Figure 7-11. Spray head for air humidification

## 2. Globe Valve Removing

A thermocouple were placed initially at the LN<sub>2</sub> inlet to measure the skin temperature. As the temperatures differed between tube outer wall and inner fluid, a thermowell was installed by removing the globe valve and inserting a thermocouple probe to the centre of the process line in order to measure the real fluid temperature, as shown in Figure 7-12.

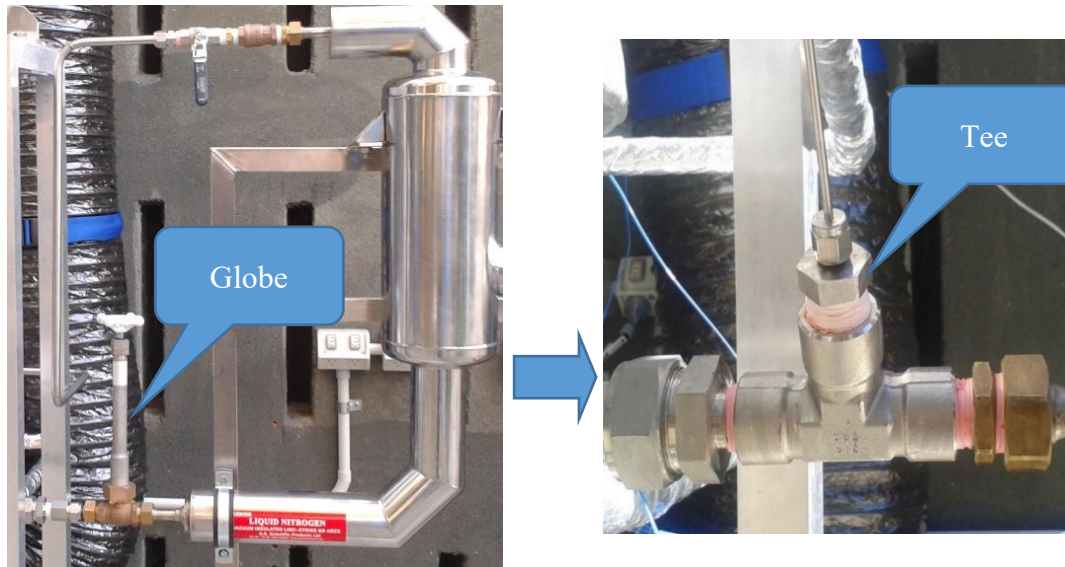


Figure 7-12. . Thermocouple of measuring LN<sub>2</sub> inlet temperature

## 3. Insulation

Cryogenic insulation (Cryogel) was installed at the LN<sub>2</sub> supply line and the vaporiser inlet in order to minimise the LN<sub>2</sub> evaporation. Removing the globe valve was also beneficial for minimizing the evaporation as it was very hard to insulate. Figure 7-13 shows the insulation of the cryogenic LN<sub>2</sub> process line.



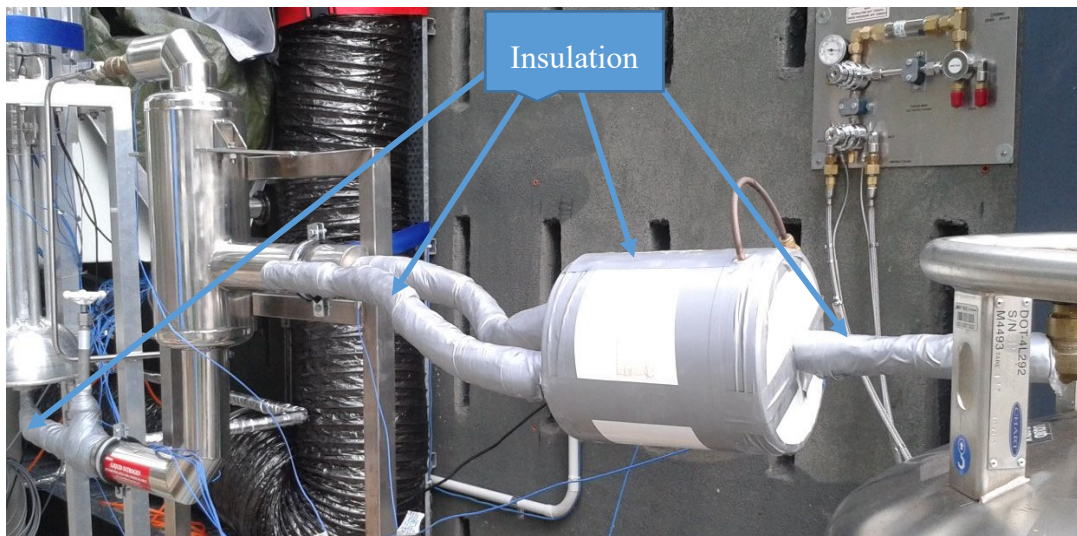
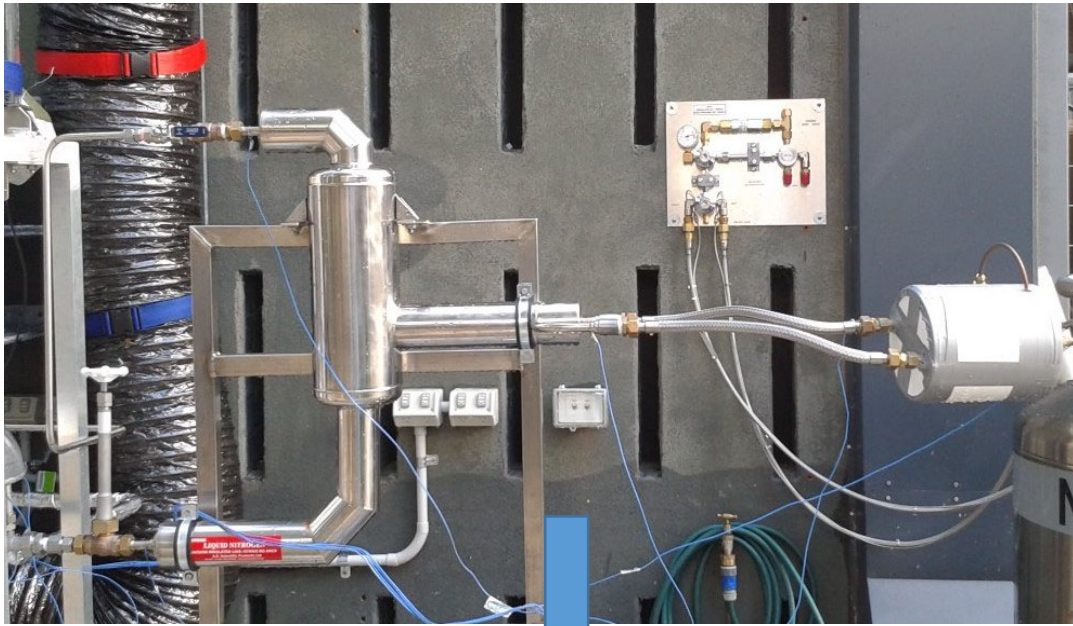


Figure 7-13. . LN2 line insulation



#### 7.4. Operating data analysis (Normal operation)

Test #7 ~12 were in normal operation status based upon the experience obtained from previous runs. The operating conditions are listed in Table 7-3. Different operating conditions, such as operation duration, nitrogen flow rate, operating pressure and forced/natural convection, were tested to investigate the heat transfer performance of AAV, and the frost formation and defrosting behaviours. In the initial trials of commissioning (Test #1~6), the amount of frost formed on AAV was very low and was not able to test the defrosting capacity completely. It was mainly because both nitrogen flow rate and air relative humidity were very low. In such cases, the amount of vapour condensed and frost formed on AAV was very limited. It required very long operating duration (possibly several days) to obtain a reasonable amount of frost for defrosting purpose, but the experiment was limited by the size of LN<sub>2</sub> Dewar (maximum capacity 230L). In order to speed up the process of frost formation and test the defrosting capability, a mist generator was applied in Test #10~12 to humidify the intake air before exchanging heat with the vaporizer.

Table 7-3. Operating conditions in different tests (7-12).

| Test number   | #7                  | #8                 | #9                  | #10                 | #11               | #12                 |
|---|---------------------|--------------------|---------------------|---------------------|-------------------|---------------------|
| Date of test  | 08/08/2017          | 18/08/2017         | 07/09/2017          | 15/09/2017          | 29/09/2017        | 02/11/2017          |
| Open & close time   | 12:50pm ~<br>3:30pm | 9:00am ~<br>2:30pm | 11:50am ~<br>2.00pm | 8:00am ~<br>11:00am | 1.30pm~<br>3:30pm | 6:00pm ~<br>12:30am |
| Operating duration  | 2hr 40min           | 5hr 30min          | 2hr 10min           | 3hr                 | 2hr               | 6hr 30min           |
| N <sub>2</sub> flow rate (L/min)  | 320                 | 250                | 250                 | 300/430             | 350               | 350                 |
| Operating pressure (bar)  | 11                  | 11.0               | 9.0                 | 11.0                | 14                | 7.0                 |
| Air velocity (m/s)  | 1.5                 | 1.2                | Natural convection  | 1.3                 | 1.3               | 1.3                 |
| Ambient temperature (°C)  | 15                  | 21.4               | 26.1                | 18.8                | 18.7              | 20.0                |
| Ambient relative humidity   | 45.0%               | 32.4%              | 28.3%               | 45.4%               | 43.4%             | 50.0%               |
| Note: In Test #10~12, intake air is humidified.<br>The unit of N <sub>2</sub> flow rate is in Normal Temperature and Pressure (20°C and 1 atm). |                     |                    |                     |                     |                   |                     |

Essentially, in order to achieve the continuous operation of LN<sub>2</sub> evaporation, defrosting process should be conducted intermittently and periodically without shutting off the LN<sub>2</sub> flow. Table 7-4

lists all the experimental conditions of defrosting operation. As each Dewar could only be operated approximately 7 hours (for LN2 flow rate at 300L/min), the defrosting must be performed before the Dewar was empty. The MEG flow duration was slightly longer than defrosting duration, because the MEG flow was firstly circulated in a bypass loop and then introduced to the vaporizer. As high temperature of MEG solution could damage the MEG flow meter and potentially corrode plastic components in the tubing system, the temperature of MEG solution was set as 50°C which was maintained by the MEG insertion heater. The MEG flow rate was designed as 200~800L/hr.

Table 7-4. Operating conditions of defrosting in different tests

| Test number   | #9                           | #10                 | #11                 | #12                 |
|---|------------------------------|---------------------|---------------------|---------------------|
| LN <sub>2</sub> flow conditions   | LN <sub>2</sub> flow ongoing |                     |                     |                     |
| Start time of defrosting  | @ run time<br>2.5hr / 5.0hr* | @ run time<br>2.0hr | @ run time<br>1.5hr | @ run time<br>5.7hr |
| MEG flow duration (min)   | 7.0 / 11.0                   | 7.0                 | 10.0                | 10.0                |
| MEG temperature (°C)  | 50.0                         | 50.0                | 44.0                | 50.0                |
| MEG flow rate (L/hr)  | 720 / 350                    | 610                 | 650                 | 600                 |
| * In Test #8, two defrosting processes was performed at run time of 2.5hr and 5.0hr separately. |                              |                     |                     |                     |

### 7.4.1. Liquid nitrogen flow

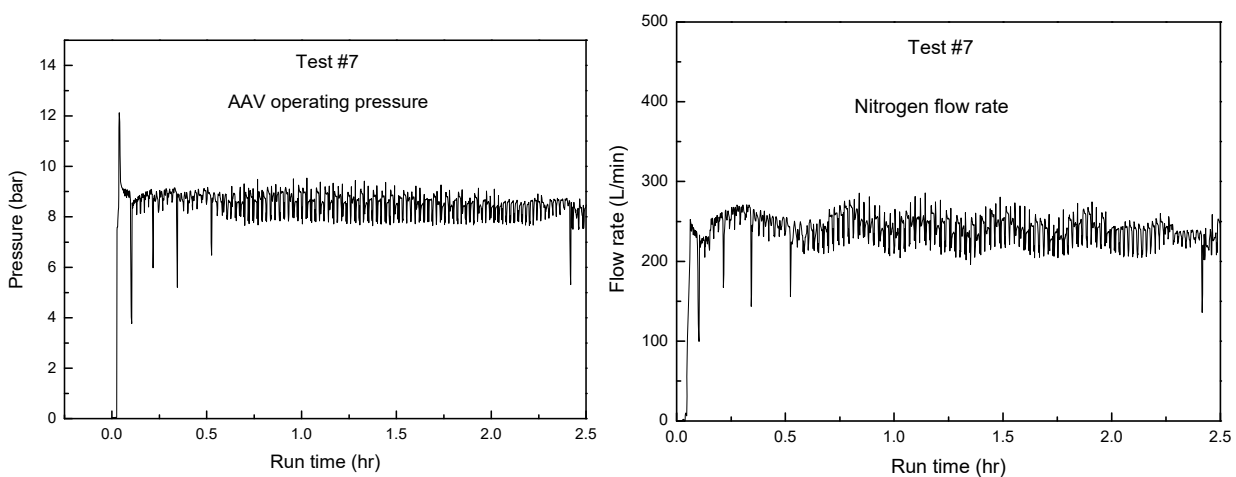


Figure 7-14. History of operating pressure and nitrogen flow rate of Test #7

The LN<sub>2</sub> flow of the AAV system was supplied by the pressurised Dewar. The flow rate was controlled by a needle valve (FCV201 in Figure 7-1) located downstream of the nitrogen flow after the vaporizer. Therefore, the operating pressure of the AAV was approximately equal to the pressure of LN<sub>2</sub> Dewar, although pressure was slightly reduced due to tube fittings and bends. Figure 7-14 shows the history of operating pressure and nitrogen flow rate in Test #6. The pressure fluctuation was around 0.5 bar which was possibly because of the pressure maintenance by the Dewar. As the Dewar pressure was controlled by the heating coil inside the Dewar insulation jacket, the heat transfer rate between ambient air and heating coil could be varied with time. This could also result in the fluctuation of nitrogen flow rate. Another periodical change (i.e. big wave) with a frequency of every 0.5 hr was observed when monitoring LN<sub>2</sub> flow rate. It was because the LN<sub>2</sub> supplies for both cooling jacket and process line were shared from the same Dewar. The flow in the process line could be bypassed from the phase separator. When the float valve (shown in Figure 7-3) was open, it meant to release the gaseous form of nitrogen in the cooling jacket, but it could also reduce the flow rate in the process line as the flow resistance in the separator was much smaller than that in the nitrogen process line of AAV. Once the cooling jacket was filled up with liquid, the float valve could be closed which forced the LN<sub>2</sub> to go through the process line only.

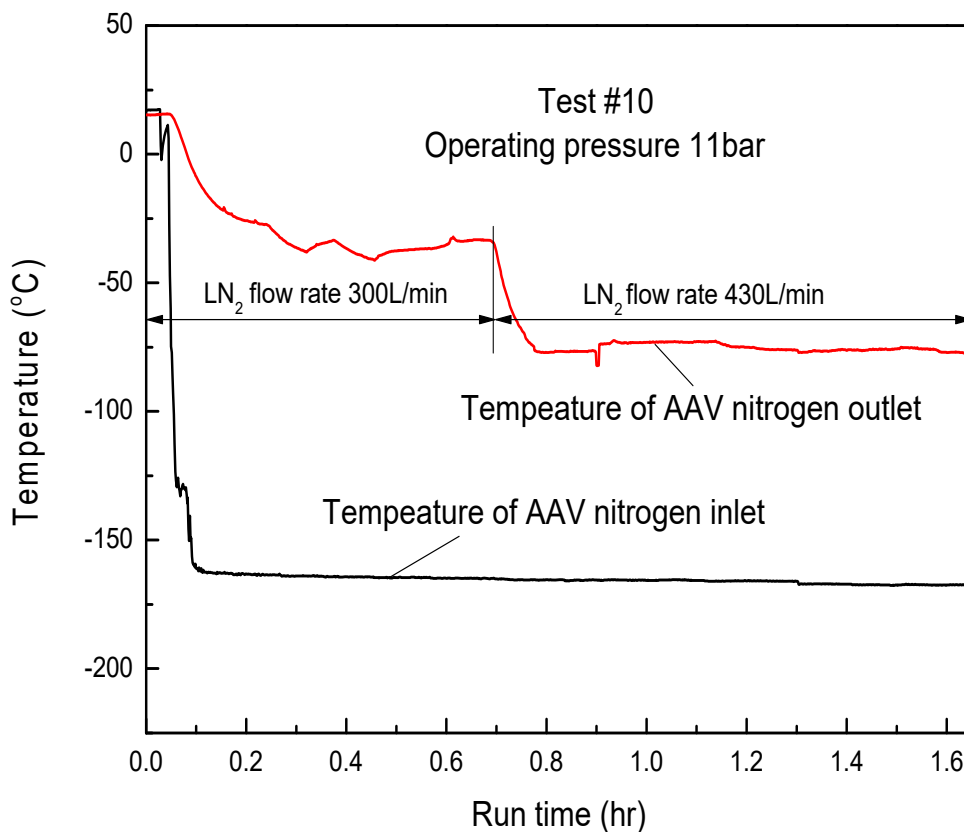


Figure 7-15. Temperatures of nitrogen inlet and outlet.

Figure 7-15 shows the history of nitrogen temperature change at AAV inlet and outlet in Test #10. Because the process line of connecting LN<sub>2</sub> Dewar with AAV was insulated properly and the phase separator was applied to ensure liquid-phase nitrogen supply, it could be observed that the nitrogen temperature at AAV inlet was at the saturation temperature for the specific operating pressure (nitrogen saturation temperature -167.9 °C at 11bar). In Test #10, two different nitrogen flow rates (300L/min and 430L/min) were tested. At the beginning, it could have taken around half an hour to cool down the system and stabilize the outlet temperature. Once changing the flow rate, the nitrogen temperature could be stabilized within a shorter period (approximate 10min). Afterwards, the outlet temperature was reduced very slowly which was due to frost formation on fins. At the flow rate of 430L/min, the temperature difference between nitrogen inlet and outlet was approximately 100 °C.

#### **7.4.2. Air flow**

The temperatures of air flow were measured at four different vertical levels, i.e. 0.0m (AAV air outlet), 1.0m, 1.6m and 2.0m (AAV air inlet), while the relative humidity was monitored at three different levels, i.e. 0.0m (AAV bottom), 1.6m and 2.0m. The ambient temperature and relative humidity was measured by placing the sensors close to the air blower in order to avoid any influence from the cold effluent air from the vaporizer. The intake air was perfectly humidified in Test #10~12. The measured value of both temperature and relative humidity is plotted in Figure 7-16 & Figure 7-17. With or without air humidification, the overall temperature drop of air flow was around 10 °C. It was also noticed that the temperature change at the bottom part (0~1.0m) was almost two times larger than the top part (1.0~2.0m). The relative humidity was increased when air travelling along the vaporizer. It was because the air temperature was reduced significantly while the humidity ratio (the mass of water vapour per unit mass of dry air) was not decreased largely. Without humidification, the air flow could only be saturated at the bottom part of the vaporizer where the frost was formed. When air flow was fairly humidified (in Test #10~12), the vapour in air flow was nearly saturated before entering AAV, but this led to the air inlet (at AAV height 2.0m) temperature becoming lower than ambient temperature. When air flow exchanging heat with LN<sub>2</sub> flow in vaporizer, minor increase of relative humidity was observed while air travelling through the AAV (shown in Figure 7-17).

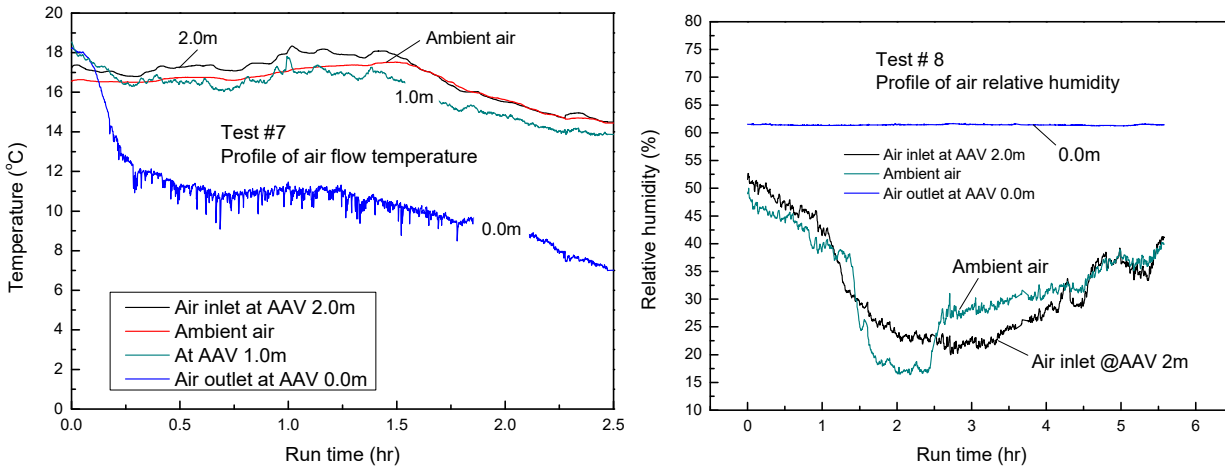


Figure 7-16. The temperatures and relative humidity of air flow in Test #7 & 8.

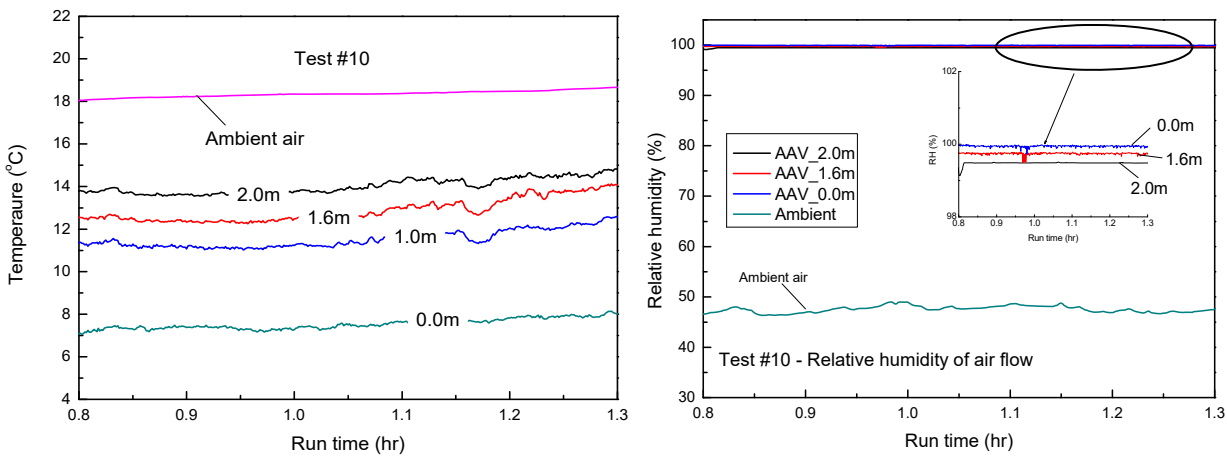


Figure 7-17. The temperatures and relative humidity of air flow in Test #10.

### 7.4.3. Temperature profile on fins

Fin temperatures of six different vertical levels were monitored on the vaporizer, with each level having three horizontal measuring spots, i.e. central tube, the middle of the fin and fin end (shown in Figure 7-5). The fin temperature plotted in Figure 7-18 was considered by averaging the three measured values. It was observed that the temperature of the fins was reduced by more than 50 °C whether or not the air flow was humidified. The fin temperature in the bottom part (below 1.0m) reduced much faster than the top part of the vaporizer. The fin temperature above a certain height (1.2m in Test #6, and 1.6m in Test #9) decreased very slowly after running for 0.5 hr, which implies the maximum height of the frost covering area on the AAV.

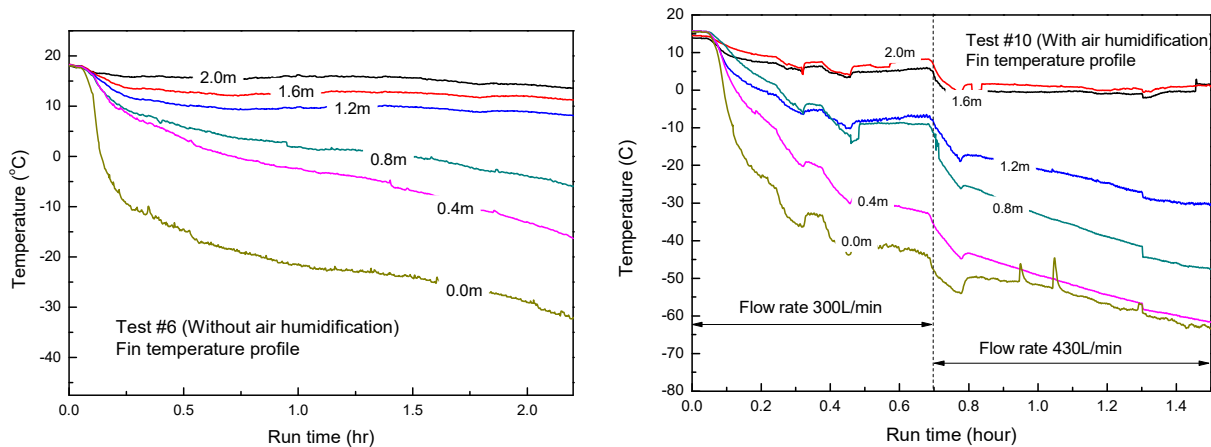


Figure 7-18. AAV Fin temperature profile in Test #6 and Test #10.

#### 7.4.4. Defrosting process

Defrosting process was turned on after running LN<sub>2</sub> evaporation for a few hours. In order to heat up the MEG solution evenly in the storage tank, a bypass loop for MEG circulation was turned on before conducting defrosting process. In Test #9, the hot defrosting stream was switched on at a run time of 1.64hr with a constant flow rate around 650L/hr, as shown in Figure 7-19. It took around 10min to defrost the vaporizer including drying the fin surface in order to delay the process of frost formation in next cycle. The temperature at MEG inlet in AAV was approximately 40 °C. The temperature difference between the MEG inlet and the MEG outlet was reduced with time. A temperature drop of about 2 °C could be observed at the final stage from which it could be confirmed that no blockage due to MEG-water solution frozen could occur during defrosting process. It was observed from the experiments that the frost started to melt from the top or middle part of the vaporizer rather than from the bottom part. During defrosting process, one phenomenon was captured that large ice/frost blocks were ripped off and dropping on the ground by gravity which was because the frost interface between frost layer and fin surface was melted. Test #11 was conducted at night time in order to avoid solar radiation and increase the amount of frost formation. The overall defrosting process could be completed effectively in around 10 minutes, which could demonstrate the defrosting capability for some extreme conditions.

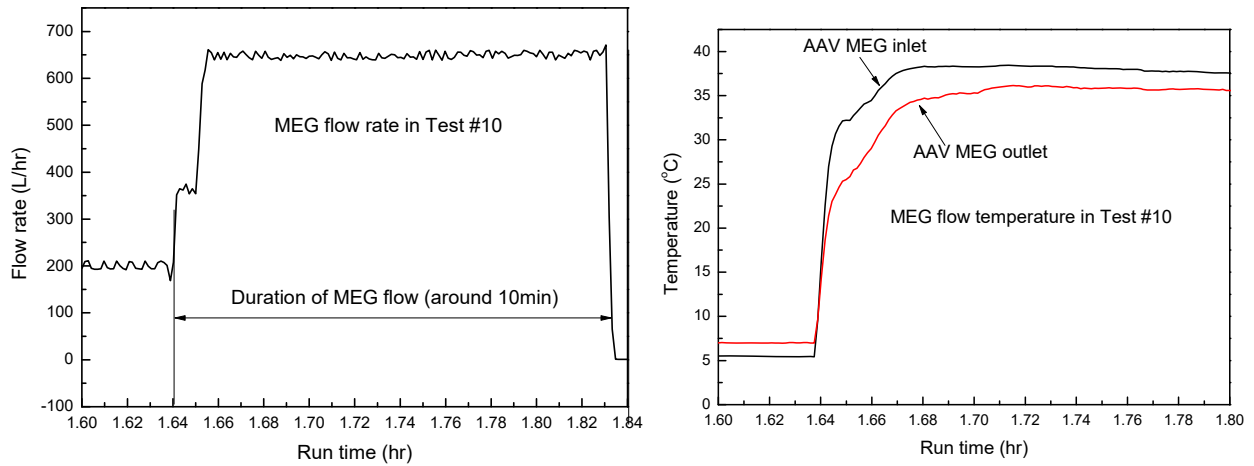


Figure 7-19. MEG flow rate and temperature change during defrosting process.

Fin temperature in defrosting stage of Test #10 are plotted in Figure 7-19. The fin temperature was increased rapidly in the initial stage (i.e. from 1.64hr to 1.72hr), and was then increased slowly when fin temperature was close to the frost melting point  $0^{\circ}\text{C}$ . It was because the defrosting process needed to overcome the latent heat of absorption for frost melting. It could also be observed in Figure 7-20 that the top part of finned tube (1.6m) reached  $0^{\circ}\text{C}$  earlier than the bottom part. It meant that the defrosting started to occur at the top or middle part of the vaporizer. It was observed that the frost on AAV was removed completely if the fin temperature was above  $0^{\circ}\text{C}$  which could be taken as a signal of completing defrosting. During defrosting process, the liquid nitrogen was supplied continuously in order to test the feasibility of non-stop operation of vaporization with intermittent defrosting. The temperature of nitrogen outlet during defrosting process was increased around  $20^{\circ}\text{C}$ , as shown in Figure 7-20.

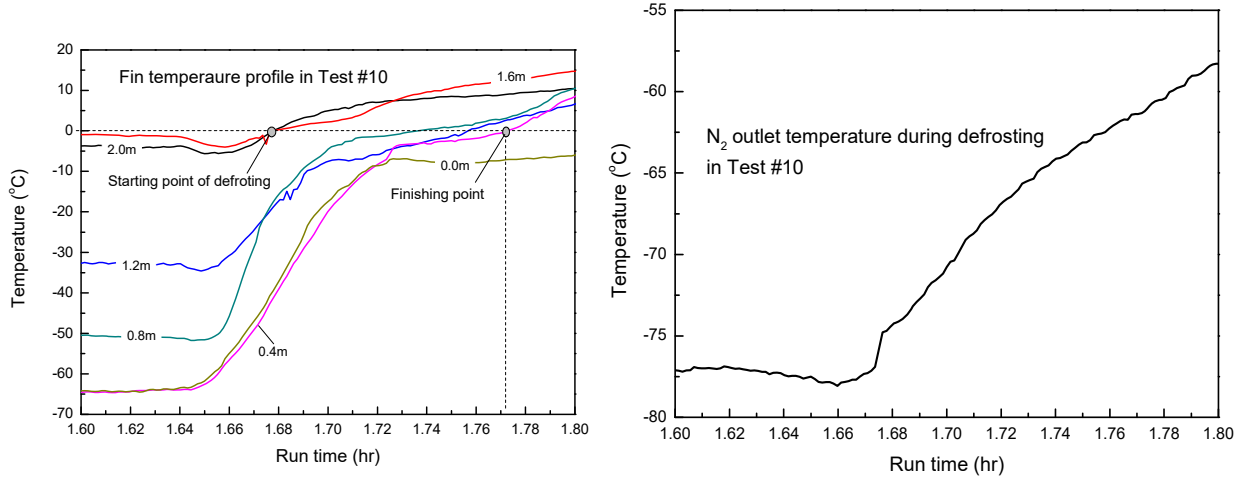


Figure 7-20. Temperature change of fin surface and Nitrogen outlet during defrosting process.

## 7.5. Discussion

### 7.5.1. Overall heat transfer coefficient

The overall heat transfer coefficient is one of the most important criteria to predict the performance of the vaporizer. As expressed in Equation 7.1[155], the total heat transfer rate ( $q$ ) is related to the quantities such as overall heat transfer coefficient ( $U$ ), surface area for heat transfer ( $A$ ), and inlet & outlet temperatures. Neglecting potential and kinetic energy changes and applying the steady flow energy equation, the total heat transfer rate could be expressed in Equation 7.2 where  $i$  is the fluid enthalpy,  $\dot{m}$  is the nitrogen flow rate,  $C_p$  is the specific heat capacity, and  $H_L$  is the latent heat. The temperature difference between the hot and cold fluids was evaluated by the LMTD (Log Mean Temperature Difference) associated with a counter flow heat exchanger, as expressed in Equation 7.3.

$$q = UA\Delta T_{lm} \quad 8.1$$

$$q = \dot{m}_{N_2}(i_{N_2,out} - i_{N_2,in}) = \dot{m}_{N_2}(C_{p,out}T_{N_2,out} - C_{p,in}T_{N_2,in}) + \dot{m}_{N_2}H_L \quad 8.2$$

$$\Delta T_{lm} = \frac{(T_{h,i} - T_{c,o}) - (T_{h,o} - T_{c,i})}{\ln[(T_{h,i} - T_{c,o}) / (T_{h,o} - T_{c,i})]} = \frac{(T_{air,in} - T_{N_2,out}) - (T_{air,out} - T_{N_2,in})}{\ln[(T_{air,in} - T_{N_2,out}) / (T_{air,out} - T_{N_2,in})]} \quad 8.3$$



The overall heat transfer coefficient changing with time in a typical test is demonstrated in Figure 7-21. Initially, the overall heat transfer coefficient was very high which was because of the relatively higher initial system temperature leading to high heat transfer rate. After running the test for approximately 1 hour, the value was stabilized at around 175W/m<sup>2</sup>.K with minor vibration. Afterwards, the overall heat transfer coefficient was reduced very slowly which was mainly due to frost formation.

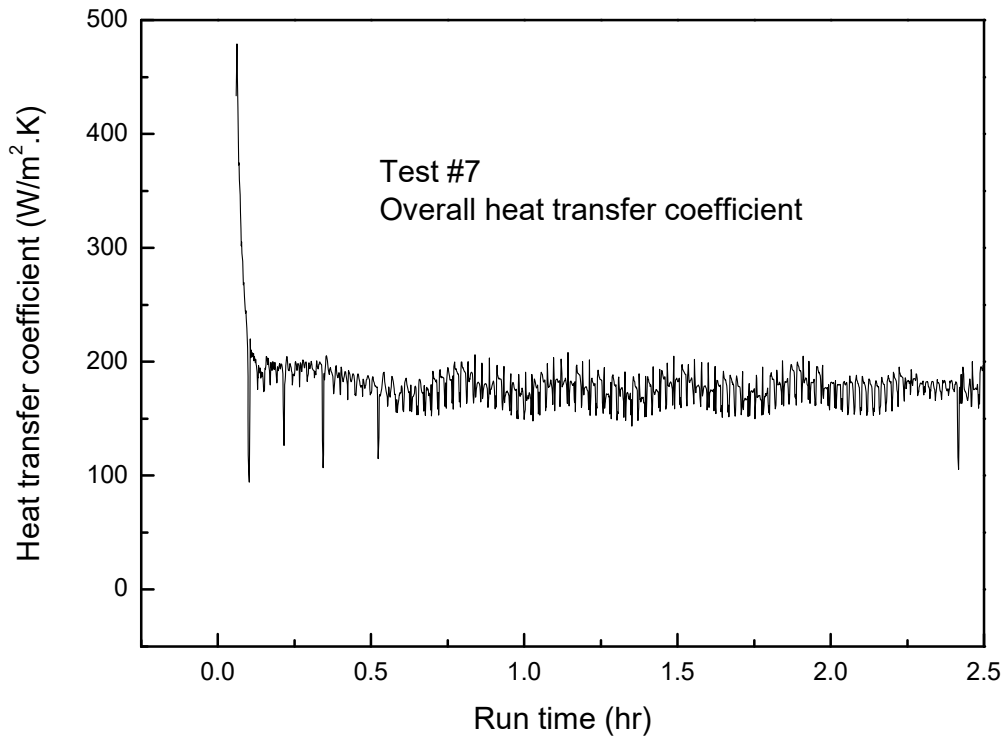


Figure 7-21. Overall heat transfer coefficient changing with time in Test #7

Table 7-5 listed the experimental results including nitrogen outlet temperature, air outlet temperature, and the overall heat transfer coefficient. In Test #6, the operating capacity was almost the same (250L/min) while the operating pressure was different. As air flow was humidified in Test #10~12, the overall heat transfer coefficient was increased by approximately 20% which was because latent heat released from ambient vapour condensation could contribute to LN<sub>2</sub> evaporation. The overall heat transfer coefficient in Test 12 was not as high as that in Test 10 ~11. It was because the test was conducted at night time which led to low ambient air temperature and low intensity of solar radiation.

Table 7-5. Overall heat transfer coefficient during LN2 evaporation.

| Test NO.  | N2 outlet Temp. (°C) | Air outlet Temp. (°C) | Overall heat transfer coefficient (W/m <sup>2</sup> .K) |
|---|----------------------|-----------------------|---|
| #6  | -44.51               | 10.19                 | 176.42  |
| #8  | -45.33               | 11.63                 | 135.56  |
| #10   | -37.11*              | 8.24*                 | 186.97*   |
|   | -75.14#              | 7.12#                 | 200.06#   |
| #11   | -55.61               | 8.65                  | 191.29  |
| #12   | -87.26               | 5.73                  | 136.1   |
| * The value is for nitrogen flow rate 300L/min. |                      |                       |   |
| # The value is for nitrogen flow rate 430L/min. |                      |                       |   |

### 7.5.2. Air humidification

One of the main objective of the test rig was to investigate the feasibility of defrosting in an innovated design of finned tube in order to achieve a continuous evaporation process. However, the test was limited by the volume of LN<sub>2</sub> Dewar. In order to speed up the process of defrosting, the air flow was humidified before entering the vaporiser by using a mist generator which could increase the air relative humidity and saturate the vapour at AAV air inlet, but this could lead to a decrease of air inlet temperature (shown in Figure 7-17). Humidity ratio of air flow was taken into consideration in order to understand the change of vapour content as air travelling through the vaporizer. As demonstrated in Figure 7-22, humidity ratio at AAV air inlet (2.0m) was increased by approximately 50% compared with ambient air. Because of vapour condensing when air passing through the vaporizer and exchanging heat with nitrogen flow, the humidity ratio of air flow was decreased from AAV top to bottom.

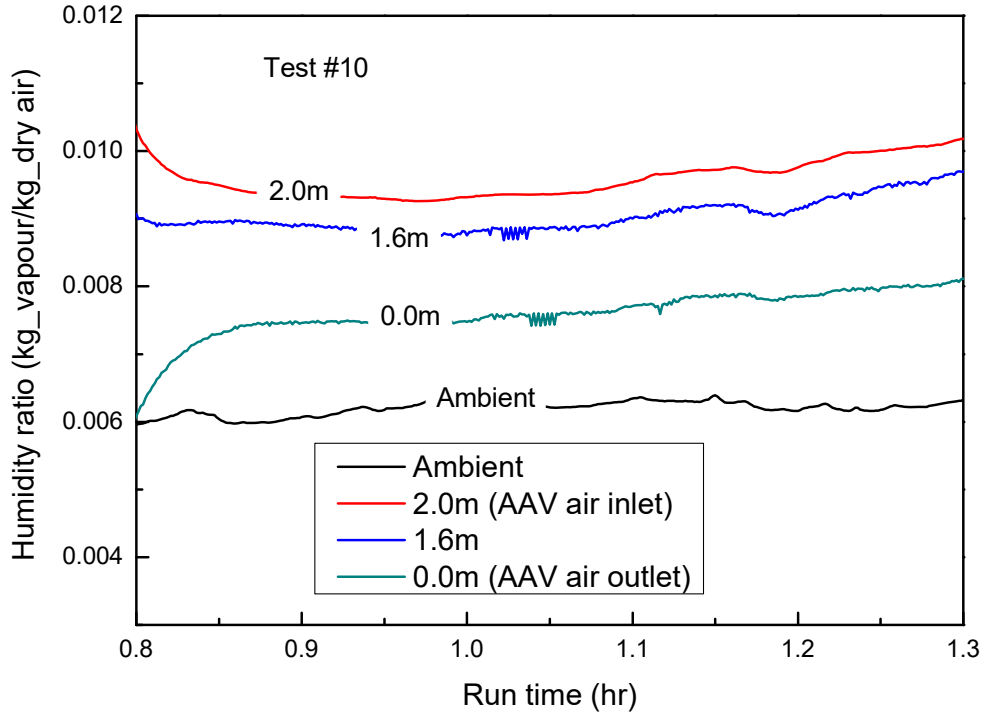


Figure 7-22. Humidity ratio change of air flow with time

Air humidification could obviously increase humidity ratio, and thus speed up the process of frost formation. Moreover, due to relatively more vapour condensed on the fin surface, the latent heat of vapour condensation and solidification could potentially enhance heat transfer between air flow and nitrogen flow. The heat transfer rate was evaluated by calculating the enthalpy change between the inlets and outlets of air flow and nitrogen flow, respectively. Besides, solar irradiation and environmental radiation could also provide heat for the evaporating LN<sub>2</sub> which could enhance heat transfer rate largely. The data of daily solar irradiation in Perth metro area is available from Bureau of Meteorology [156]. Through checking the database, the sunrise & sunset time and solar exposure on the date of Test #10 were 6:15am & 06:08pm and 19.5MJ/m<sup>2</sup>, respectively, so the solar irradiation rate was calculated as 455.8W/m<sup>2</sup>. The amount of radiation heat transfer rate occurring on the fin surface of AAV could be calculated in Equation 4 where  $q_{rad}$  is the radiation heat flux (W/m<sup>2</sup>);  $\alpha_{Al}$  is the absorptivity of aluminium sheet ( $\alpha_{Al}=0.5$ );  $G_{solar}$  is the solar irradiation rate ( $G_{solar}=455.8\text{W/m}^2$ );  $\varepsilon_{air}$  is the air emissivity ( $\varepsilon_{air}=1$ );  $\sigma$  is the Stefan-Boltzmann constant ( $\sigma=5.67\text{e-}08\text{W/m}^2\cdot\text{K}^4$ );  $T_{air}$  and  $T_{Al}$  are the air ambient temperature and fin surface temperature respectively which are varied with time.

$$q_{rad} = \alpha_{Al} \cdot G_{solar} + \varepsilon_{air} \cdot \sigma(T_{air}^4 - T_{Al}^4) \quad 8.4$$

The calculation results are plotted in Figure 7-23. The heat transfer rates of nitrogen flow and ambient environment (including convection heat transfer and irradiation) were comparable. If air flow was not humidified, the heat transfer rate was much lower than that with air humidification. It could be concluded that humidifying the intake air could enhance the overall heat transfer effect on AAV which is because the latent heat released from water vapour condensing or solidification could provide more heat transfer rate for LN<sub>2</sub> evaporation, although it could speed up the process of frost/ice formation and deteriorate heat transfer effect in the later operating stage.

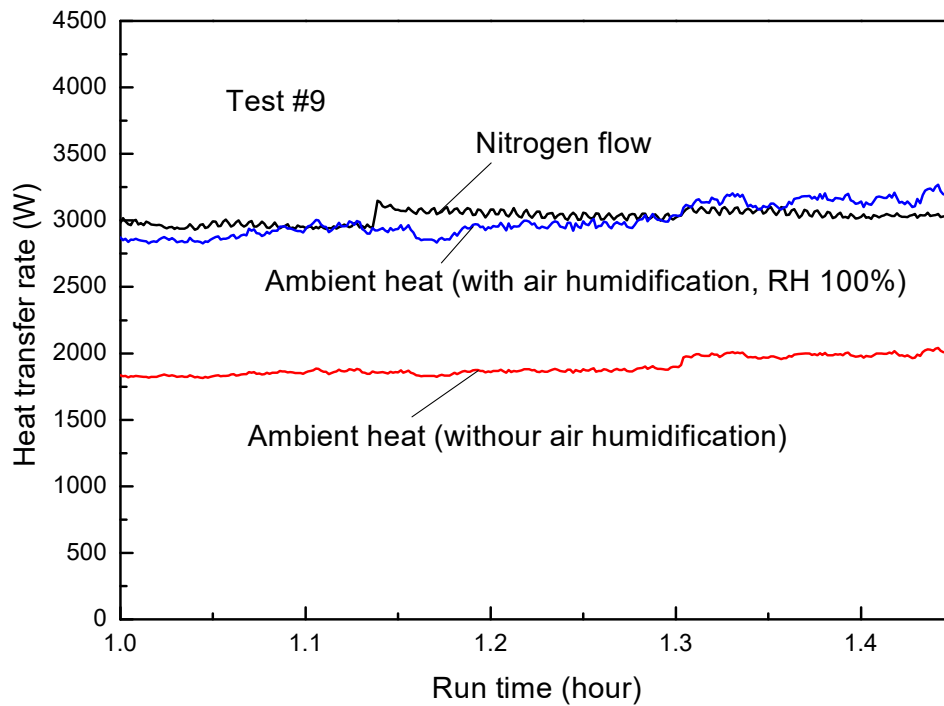


Figure 7-23. Energy balance between nitrogen flow and air flow.

### 7.5.3. Frost formation

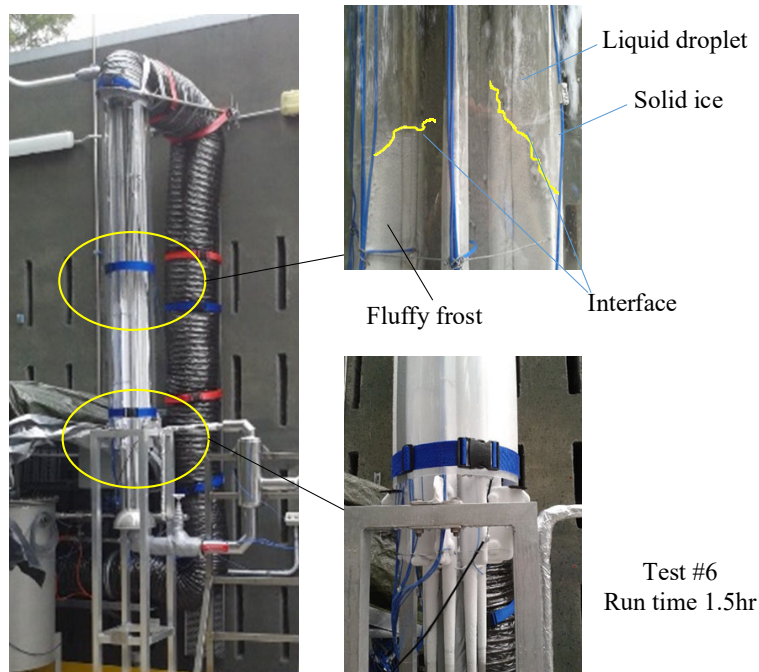


Figure 7-24. Frost formation on the AAV in Test #6.

Frost formation was tested and monitored under different experimental conditions in different tests, such as ambient conditions (air temperature, air relative humidity, and day/night time operation) and LN<sub>2</sub> flow conditions (flow rate and operating pressure). In Test #7, the maximum height of frost formation on AAV was around 1.0m after running for 0.5hr, and was not increased any further afterwards (total 2.5 operation period), shown in Figure 7-24. It was because fin temperature above 1.0m was not reduced as faster as the bottom part of AAV. An interface of three phases (liquid droplet, solid ice and fluffy frost) was observed. Although increasing the nitrogen flow rate from 300L/min to 430L/min in Test #10, the maximum height of frost formation reaches around 1.85m and did not cover all the fin area as shown in Figure 7-25 .a. This was because solar irradiation in clear sky and environmental radiation during day time could provide a comparable heat transfer rate as forced convection of air flow. Test #12 was conducted during the night time in order to minimize the radiation effect. It was observed that the frost could cover all the finned area from top to bottom, as shown in Figure 7-25.b.

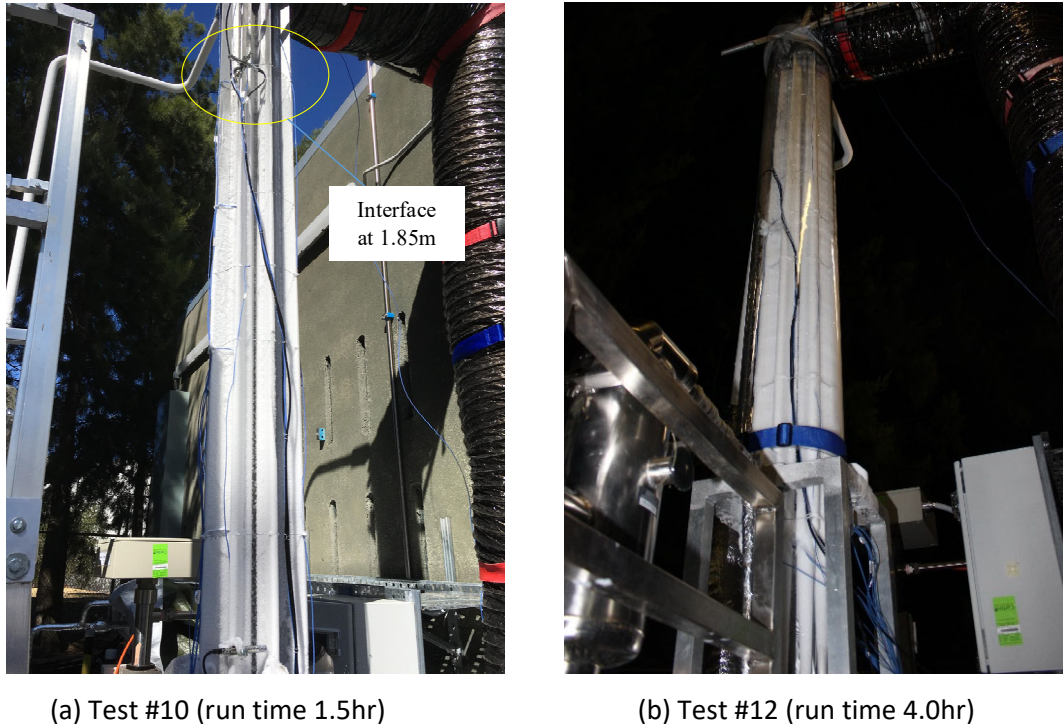


Figure 7-25. Frost formation in Test #10 (a) and Test #12 (b).

## 7.6. Conclusions

In this study, an innovative design of AAV focusing upon invasive defrosting has been tested in a pilot-scale experiment outdoors. Different operating conditions, such as air flow, nitrogen flow and MEG solution flow, have been tested to investigate the vaporizer performance and defrosting capacity. The following conclusions have been drawn. Firstly, the hot MEG solution could defrost the vaporizer effectively. No blockage due to MEG freezing were found during defrosting process. Secondly, air humidification could saturate the vapour of air supply at AAV top, and could speed up the process of frost formation remarkably. Latent heat released from vapour condensing and solidification could help to increase heat transfer rate to some extent especially at the beginning of operation. Thirdly, the defrosting process was completely successful in 10min including drying up the fin surface. During the process, the hot MEG solution only needed to melt the interface of frost layer rather than to melt all the frost/ice block. This pilot-scale experiment could provide an in-depth insight of continuous process of LNG regasification in AAVs by using proper invasive defrosting method.

## 8. Chapter 8: Conclusions and recommendations

The first part of this chapter presents the overall conclusions from the studies reported in the previous chapters while the second part presents the recommendations for future work.

### 8.1. Conclusions

Natural gas plays a critical role in the global energy market. Although the primary use of natural gas is as a fuel, it is also a source of hydrocarbons for petrochemical feedstocks and a major source of elemental sulfur, an important industrial chemical. Its popularity as an energy source is expected to grow substantially in the future because natural gas presents many environmental advantages over petroleum and coal.

This thesis extensively comprises the pathway of natural gas processing for removing of sour gases using different processes and solvents, also reducing water content, reinjection CO<sub>2</sub> for EOR or storage purposes and LNG regasification. Based on the results obtained, MEG can be used as an alternative to remove sour gases (CO<sub>2</sub> and H<sub>2</sub>S) from streams of natural gas in an absorption process. Beside, MEG can reduce the water content of natural gas to less than 0.03 mole% to meet the pipeline specifications

A simulation work was developed using Aspen HYSYS and Peng-Robinson equation of state has been used due to containing enhanced binary interaction parameters for all hydrocarbons–non-hydrocarbons components pairs and the high accuracy results. The simulation work achieved high acid gases and water removal using MEG solutions at different temperatures and concentrations. Water content was reduced from 1 mole% to less than 0.003 mole%. The total recovery of CO<sub>2</sub> and H<sub>2</sub>S were 98% and 99.7% respectively.

In addition, aromatic compounds have been employed for CO<sub>2</sub> /H<sub>2</sub>S separation process. H<sub>2</sub>S needs to be removed from CO<sub>2</sub> before reinjecting underground for storage or for EOR purposes. Based on the results obtained, high purity of CO<sub>2</sub> stream has been achieved using aromatic compounds due to increasing the relative volatility of CO<sub>2</sub>/H<sub>2</sub>S which makes the separation process easier.

Furthermore, this thesis consists a simulation study of sour gas removal from natural gas using low temperature distillation process. The study presents a modified scheme for the separation of sour gases based on an existing scheme of Ryan-Holmes. A great advantage of this process lies in the production of high purity of CO<sub>2</sub> at the high pressure required for enhanced oil recovery processes. Importantly, the reported process produced pure methane and ethane containing <50 ppm CO<sub>2</sub>, with high purity (>90%) of CO<sub>2</sub> stream.

Moreover, the removed CO<sub>2</sub> from natural gas processes which needs to be reinjected to underground to control the environment emissions and address climate changes. Therefore, an experimental study has been conducted to study the effect of the porosity in the real rock in underground reservoir on CO<sub>2</sub> injection and examine the suitability of a particular reservoir in WA for CO<sub>2</sub> reinjection by studying the wettability properties of CO<sub>2</sub>/brine/Sandstone. The advancing-receding contact angles of brine/CO<sub>2</sub> and sandstone as a function of pressure, temperature, and salinity were investigated in this study. The results show that the contact angle of sandstone was systematically higher than that of pure quartz at any pressure or temperature because of the effect of pores in sandstone. The contact angles also increased with increasing pressure and temperature and decreased with increasing the salinity.

Finally, LNG regasification is an essential process required before it can be used as a sale gas or in power generation plant. For this purpose, a pilot plant has been designed, constructed and operated in order to test the efficiency of a modified ambient air vaporizer. Liquid nitrogen was used instead of LNG for safety purposes. Twelve experiments were conducted to investigate the ability of air vaporizer to re-gasify stream of liquid nitrogen at -169 °C and to melt the forming frost during the regasification process. The experiments were classified into commissioning tests (1-6) and normal operation tests (7-12). The results conclude that the vaporizer is able to vaporize LN<sub>2</sub> efficiently and the defrosting process was completely successful in less than 10 min during continuous vaporization process.

## **8.2. Recommendations**

For further academic studies, the following activities are recommended:

1. The optimisation of the sour gases removal processes should also include economic aspects to identify the feasibility of the proposed optimisation approach. This approach permits the actual cost sources at the equipment level to be recognized such as the capital, operating, maintenance costs and cost linked with the energy loss.
2. Testing different solvents at different operating conditions for sour gas separation process to optimize the energy consumption and to minimize the plant footprint.
3. Modelling the sour gases removal processes using another simulation software such as ProMax or SIMSCI Pro-II and comparing the results with Aspen HYSYS is another option to optimise the process efficiency.
4. Further studies can be conducted on pore rocks with different pore sizes and structures to better understand the variations in the wettability in the presence of porosity.



5. Considering scaling up the existing pilot plant of Ambient Air Vaporizer and using LNG to test the vaporizer efficiency for both vaporization and defrosting process.

## 9. References

1. Holmes, A.S. and J.M. Ryan, *Distillative separation of carbon dioxide from light hydrocarbons*. 1982, Google Patents.
2. Patel, D., et al., *LNG vaporizer selection based on site ambient conditions*. Proceedings of the LNG, 2013. **17**: p. 16-19.
3. Shah, K., et al. *Considerations for ambient air based technologies for LNG regasification terminals*. in *Proceedings of the 8th Tropical Conference on Natural Gas Utilization, New Orleans, LA, USA*. 2008.
4. Altman, S.J., et al., *Chemical and hydrodynamic mechanisms for long-term geological carbon storage*. The Journal of Physical Chemistry C, 2014. **118**(28): p. 15103-15113.
5. Kidnay, A.J., W.R. Parrish, and D.G. McCartney, *Fundamentals of natural gas processing*. 2006: CRC press.
6. Mokhatab, S. and W.A. Poe, *Handbook of natural gas transmission and processing*. 2012: Gulf professional publishing.
7. Rios, J.A., et al. *Removal of trace mercury contaminants from gas and liquid streams in the LNG and gas processing industry*. in *PROCEEDINGS OF THE ANNUAL CONVENTION-GAS PROCESSORS ASSOCIATION*. 1998. GAS PROCESSORS ASSOCIATION.
8. Kohl, A. and R. Nielsen, *Liquid phase oxidation processes for hydrogen sulfide removal*. Gas Purification, Fifth Edition. Gulf Publishing Company, Houston, Texas, USA, 1997: p. 731-865.
9. Carlsson, A., T. Last, and C. Smit. *Design and Operation of Sour Gas Treating Plants for H<sub>2</sub>S, CO<sub>2</sub>, COS, and Mercaptans*. in *86th GPA Annual Convention, San Antonio, TX, USA (March 11-14, 2007)*. 2007.
10. Polasek, J. and J. Bullin, *Selecting amines for sweetening units*. ENERGY PROGRESS., 1984. **4**(3): p. 146-149.
11. Bord, N., et al., *Determination of diethanolamine or N-methyldiethanolamine in high ammonium concentration matrices by capillary electrophoresis with indirect UV detection: application to the analysis of refinery process waters*. Analytical and bioanalytical chemistry, 2004. **380**(2): p. 325-332.
12. Kerry, F.G., *Industrial gas handbook: gas separation and purification*. 2007: CRC press.
13. Shimekit, B. and H. Mukhtar, *Natural gas purification technologies-major advances for CO<sub>2</sub> separation and future directions*. 2012: INTECH Open Access Publisher Croatia, Europe.
14. Hermann, W., et al., *An assessment of carbon capture technology and research opportunities*. Physical Adsorption, 2005. **25**(11).
15. Baker, R.W., *Future directions of membrane gas separation technology*. Industrial & engineering chemistry research, 2002. **41**(6): p. 1393-1411.
16. Bocquet, P.E., *Process of removing carbon dioxide from natural gas*. 1959, Google Patents.

17. Goddin Jr, C.S., *Cryogenic distillative removal of CO<sub>2</sub> from high CO<sub>2</sub> content hydrocarbon containing streams*. 1984, Google Patents.
18. Eggeman, T. and S. Chafin. *Pitfalls of CO<sub>2</sub> freezing prediction*. in *82nd Annual Convention of the Gas Processors Association*.—San Antonio. Texas.—19 p. 2003.
19. Heichberger, A.N., *Method and apparatus for carbon dioxide liquefaction and evaporation*. 1987, Google Patents.
20. Holmes, A.S. and J.M. Ryan, *Cryogenic distillative separation of acid gases from methane*. 1982, Google Patents.
21. O'brien, J.V., *Distillative separation of methane and carbon dioxide*. 1983, Google Patents.
22. O'brien, J.V., A.S. Holmes, and R.B. Hopewell, *Process for the separation of landfill gas*. 1987, Google Patents.
23. Durr, C.A., D.B. Manley, and R.L. McKee, *Carbon dioxide recovery process*. 1994, Google Patents.
24. Sapper, R. and H. Kick, *Process for separating CO<sub>2</sub> from a gaseous mixture*. 1987, Google Patents.
25. Sapper, R., *Separation of CO<sub>2</sub> from a gaseous mixture*. 1987, Google Patents.
26. Valencia, J.A. and R.D. Denton, *Method of separating acid gases, particularly carbon dioxide, from methane by the addition of a light gas such as helium*. 1985, Google Patents.
27. Eakman, J.M. and H.A. Marshall, *Separation of carbon dioxide and other acid gas components from hydrocarbon feeds*. 1979, Google Patents.
28. Gottier, G.N., *Process for removal of carbon dioxide from mixtures containing carbon dioxide and methane*. 1988, Google Patents.
29. Amin, R. and A.F. Kennaird, *Process and device for production of LNG by removal of freezable solids*. 2008, Google Patents.
30. Hart, A. and R. Amin, *Process and apparatus for removal of sour species from a natural gas stream*. 2010, Google Patents.
31. Amin, R., A.T. Jackson, and T. Kennaird. *The Cryocell: an advanced gas sweetening technology*. in *International Petroleum Technology Conference*. 2005. International Petroleum Technology Conference.
32. Haut, R. and E. Thomas, *Development and application of the controlled-freeze-zone process*. SPE production engineering, 1989. **4**(03): p. 265-271.
33. Potts Jr, W.A. and E.R. Thomas, *Method for separating a multi-component feed stream using distillation and controlled freezing zone*. 1992, Google Patents.
34. Cole, E.T., E.R. Thomas, and R.R. Bowen, *Process for liquefying a natural gas stream containing at least one freezable component*. 1999, Google Patents.
35. Takeuchi, Y., et al., *Study on solidification of carbon dioxide using cold energy of liquefied natural gas*. Heat Transfer—Asian Research: Co-sponsored by the Society of Chemical Engineers of Japan and the Heat Transfer Division of ASME, 2000. **29**(4): p. 249-268.
36. Katz, D.L.V., *Handbook of natural gas engineering*. 1959: McGraw-Hill.
37. Berstad, D., P. Nekså, and R. Anantharaman, *Low-temperature CO<sub>2</sub> removal from natural gas*. Energy Procedia, 2012. **26**: p. 41-48.
38. Tusiani, M.D. and G. Shearer, *LNG: a nontechnical guide*. 2007: PennWell Books.

39. ZareNezhad, B. and N. Hosseinpour, *An extractive distillation technique for producing CO<sub>2</sub> enriched injection gas in enhanced oil recovery (EOR) fields*. *Energy Conversion and Management*, 2009. **50**(6): p. 1491-1496.
40. Finn, A.J. and J. O'Brien. *Processing of carbon dioxide rich gas*. in *GPA Annual Conference*. 2014.
41. Sun, J., et al., *Simulation Studies of Process Improvement of Three-Tower Low-Temperature Distillation Process to Minimize Energy Consumption for Separation of Produced Gas of CO<sub>2</sub>-Enhanced Oil Recovery (EOR)*. *The Canadian Journal of Chemical Engineering*, 2015. **93**(7): p. 1266-1274.
42. Emmett, R.C., *The Transportation of Energy Materials in the United States: A Bibliography*. Vol. 11. 1978: Argonne National Laboratory, Energy and Environmental Systems Division.
43. Chen, S., et al., *Optimal parametric design for water-alternating-gas (WAG) process in a CO<sub>2</sub>-miscible flooding reservoir*. *Journal of Canadian Petroleum Technology*, 2010. **49**(10): p. 75-82.
44. LaForce, T.C., *Insight from analytical solutions for improved simulation of miscible WAG flooding in one dimension*. *Computational Geosciences*, 2012. **16**(4): p. 1007-1020.
45. Chiquet, P., D. Broseta, and S. Thibeau, *Wettability alteration of caprock minerals by carbon dioxide*. *Geofluids*, 2007. **7**(2): p. 112-122.
46. Chalbaud, C., et al. *Wettability impact on CO<sub>2</sub> storage in aquifers: visualisation and quantification using micromodel tests, pore network model and reservoir simulations*. in *International symposium of the society of core analysts, Calgary, Canada*. 2007.
47. Hirasaki, G., *Wettability: fundamentals and surface forces*. *SPE Formation Evaluation*, 1991. **6**(02): p. 217-226.
48. Hoffert, M.I., et al., *Advanced technology paths to global climate stability: energy for a greenhouse planet*. *science*, 2002. **298**(5595): p. 981-987.
49. Chunbao Charles, X. and D.-q. Cang, *A brief overview of low CO<sub>2</sub> emission technologies for iron and steel making*. *Journal of Iron and Steel Research, International*, 2010. **17**(3): p. 1-7.
50. Mahdavian, M., et al., *Simulation of CO<sub>2</sub> and H<sub>2</sub>S Removal Using Methanol in Hollow Fiber Membrane Gas Absorber (HFMGGA)*. 2011.
51. Pires, J., et al., *Recent developments on carbon capture and storage: an overview*. *Chemical Engineering Research and Design*, 2011. **89**(9): p. 1446-1460.
52. Wong, S. and R. Bioletti, *Carbon dioxide separation technologies*. Alberta Research Council, 2002.
53. Coninck, H.d. and S. Bakker, *CO<sub>2</sub> Capture and Storage—State-Of-The-Art in the Climate Negotiations*. 2005, December.
54. IPCC, *Working Group III of the Intergovernmental Panel on Climate Change*. 2005: p. 1-443.
55. Burgers, W., et al., *Worldwide development potential for sour gas*. *Energy Procedia*, 2011. **4**: p. 2178-2184.
56. Gibbins, J., and Hannah Chalmers *Carbon capture and storage*. *Energy Policy* 2008. **36.12** p. 4317-4322.
57. Ryan, J.M. and A.S. Holmes, *Distillative separation of carbon dioxide from hydrogen sulfide*. 1981, Google Patents.
58. Aspelund, A. and K. Jordal, *Gas conditioning—the interface between CO<sub>2</sub> capture and transport*. *International Journal of Greenhouse Gas Control*, 2007. **1**(3): p. 343-354.

59. Yao, J., J.J. Chen, and D.G. Elliot, *Method and apparatus for purification of high CO<sub>2</sub> content gas*. 1986, Google Patents.
60. John, S., et al., *Energy efficiency of hydrogen sulfide decomposition in a pulsed corona discharge reactor*. Chemical Engineering Science, 2009. **64**(23): p. 4826-4834.
61. Mandal, B.P., A. Biswas, and S. Bandyopadhyay, *Selective absorption of H<sub>2</sub>S from gas streams containing H<sub>2</sub>S and CO<sub>2</sub> into aqueous solutions of N-methyldiethanolamine and 2-amino-2-methyl-1-propanol*. Separation and purification technology, 2004. **35**(3): p. 191-202.
62. Truong, L.-A. and N. Abatzoglou, *A H<sub>2</sub>S reactive adsorption process for the purification of biogas prior to its use as a bioenergy vector*. Biomass and Bioenergy, 2005. **29**(2): p. 142-151.
63. Quinn, R., *Ion exchange resins as reversible acid gas absorbents*. Separation science and technology, 2003. **38**(14): p. 3385-3407.
64. Brouwers, J., R. van Wissen, and M. Golombok, *Novel centrifugal process removes gas contaminants*. Oil and Gas Journal, 2006. **104**(42): p. 37.
65. Shiflett, M.B., A.M.S. Niehaus, and A. Yokozeki, *Separation of CO<sub>2</sub> and H<sub>2</sub>S using room-temperature ionic liquid [bmim][MeSO<sub>4</sub>]*. Journal of Chemical & Engineering Data, 2010. **55**(11): p. 4785-4793.
66. Tomadakis, M.M., et al., *Pressure-swing adsorption separation of H<sub>2</sub>S from CO<sub>2</sub> with molecular sieves 4A, 5A, and 13X*. Separation Science and Technology, 2011. **46**(3): p. 428-433.
67. Holmes, A.S. and J.M. Ryan, *Distillative separations of gas mixtures containing methane, carbon dioxide and other components*. 1984, Google Patents.
68. Abdulrahman, R. and I. Sebastine, *Natural gas sweetening process simulation and optimization: A case study of Khurmala field in Iraqi Kurdistan region*. Journal of Natural Gas Science and Engineering, 2013. **14**: p. 116-120.
69. HYSYS, H., v7.2, *User Guide*. Aspen Technology Inc, 2010.
70. Vitu, S., et al., *Predicting the phase equilibria of CO<sub>2</sub>+ hydrocarbon systems with the PPR78 model (PR EOS and k<sub>ij</sub> calculated through a group contribution method)*. The Journal of Supercritical Fluids, 2008. **45**(1): p. 1-26.
71. Jaubert, J.N., R. Privat, and F. Mutelet, *Predicting the phase equilibria of synthetic petroleum fluids with the PPR78 approach*. AIChE journal, 2010. **56**(12): p. 3225-3235.
72. Privat, R., F. Mutelet, and J.-N. Jaubert, *Addition of the hydrogen sulfide group to the PPR78 model (predictive 1978, Peng–Robinson equation of state with temperature dependent k<sub>ij</sub> calculated through a group contribution method)*. Industrial & Engineering Chemistry Research, 2008. **47**(24): p. 10041-10052.
73. Ebrahimzadeh, E., et al., *Alternative extractive distillation system for CO<sub>2</sub>–ethane azeotrope separation in enhanced oil recovery processes*. Applied Thermal Engineering, 2016. **96**: p. 39-47.
74. Kidnay, A.J., W.R. Parrish, and D.G. McCartney, *Fundamentals of natural gas processing*. Vol. 218. 2011: CRC Press.
75. Lastari, F., et al., *Extractive distillation for CO<sub>2</sub>–ethane azeotrope separation*. Chemical Engineering and Processing: Process Intensification, 2012. **52**: p. 155-161.
76. Holmes, A., et al., *Process improves acid gas separation*. Hydrocarbon Process.:(United States), 1982. **61**.
77. Barifcani, A. and M. TADE, *A process for separating components of a sour natural gas*. 2016, Google Patents.

78. HYSYS. 2017, Aspen Technology Inc.
79. Stewart, M. and K. Arnold, *Gas sweetening and processing field manual*. 2011: Gulf Professional Publishing.
80. Kohl, A.L. and R. Nielsen, *Gas purification*. 1997: Gulf Professional Publishing.
81. Bernardo, P., E. Drioli, and G. Golemme, *Membrane gas separation: a review/state of the art*. *Industrial & Engineering Chemistry Research*, 2009. **48**(10): p. 4638-4663.
82. Tagliabue, M., et al., *Natural gas treating by selective adsorption: Material science and chemical engineering interplay*. *Chemical Engineering Journal*, 2009. **155**(3): p. 553-566.
83. Faiz, R. and M. Al-Marzouqi, *Insights on natural gas purification: Simultaneous absorption of CO<sub>2</sub> and H<sub>2</sub>S using membrane contactors*. *Separation and purification technology*, 2011. **76**(3): p. 351-361.
84. Kelley, B., et al., *Controlled Freeze Zone™ for developing sour gas reserves*. *Energy Procedia*, 2011. **4**: p. 824-829.
85. Øi, L.E. and E. Tyvand Selstø. *Process simulation of glycol regeneration*. in *GPA Europe's meeting in Bergen* < [www.escet.urjc.es/~sop/alumnos/proyectos/descargas/propuesta06.pdf](http://www.escet.urjc.es/~sop/alumnos/proyectos/descargas/propuesta06.pdf)> (accessed 06/07/2010). 2002.
86. Rohani, S.S.M., *Natural Gas Dehydration Using Silicagel: Fabrication of Dehydration Unit*. 2009, UMP.
87. Giavarini, C. and K. Hester, *Gas hydrates: Immense energy potential and environmental challenges*. 2011: Springer Science & Business Media.
88. Carroll, J., *Natural gas hydrates: a guide for engineers*. 2020: Gulf Professional Publishing.
89. IEA, *World Energy Outlook Special Report*. 2013: p. 1-126.
90. Ofori, A.E. and T.W. Engler. *Effects of CO<sub>2</sub> sequestration on the petrophysical properties of an aquifer rock*. in *Canadian Unconventional Resources Conference*. 2011. Society of Petroleum Engineers.
91. Arts, R., et al., *The feasibility of CO<sub>2</sub> storage in the depleted P18-4 gas field offshore the Netherlands (the ROAD project)*. *International Journal of Greenhouse Gas Control*, 2012. **11**: p. S10-S20.
92. van Bergen, F., et al., *Production of gas from coal seams in the Upper Silesian Coal Basin in Poland in the post-injection period of an ECBM pilot site*. *International Journal of Coal Geology*, 2009. **77**(1): p. 175-187.
93. P. Tomski, V.K., M. Moore,, *Atlantic Council* 2013: p. 1–15.
94. Iglauer, S., A. Paluszny, and M. Blunt, *Simultaneous oil recovery and residual gas storage: A pore-level analysis using in situ X-ray micro-tomography*. *Fuel*, 2013. **103**: p. 905-914.
95. Hesse, M., F. Orr, and H. Tchelep, *Gravity currents with residual trapping*. *Journal of Fluid Mechanics*, 2008. **611**: p. 35-60.
96. Iglauer, S., et al., *Residual CO<sub>2</sub> imaged with X-ray micro-tomography*. *Geophysical Research Letters*, 2011. **38**(21).
97. Iglauer, S., *Mass Transfer*. 2011: p. 233-257.

98. Gaus, I., *Role and impact of CO<sub>2</sub>-rock interactions during CO<sub>2</sub> storage in sedimentary rocks*. International journal of greenhouse gas control, 2010. **4**(1): p. 73-89.
99. Anderson, W., *Wettability literature survey-part 2: Wettability measurement*. Journal of petroleum technology, 1986. **38**(11): p. 1,246-1,262.
100. Morrow, N.R., *Wettability and its effect on oil recovery*. Journal of Petroleum Technology, 1990. **42**(12): p. 1,476-1,484.
101. Arendt, B., D. Dittmar, and R. Eggers, *Interaction of interfacial convection and mass transfer effects in the system CO<sub>2</sub>-water*. International journal of heat and mass transfer, 2004. **47**(17): p. 3649-3657.
102. Iglauer, S., *CO<sub>2</sub>-Water-Rock Wettability: Variability, Influencing Factors, and Implications for CO<sub>2</sub> Geostorage*. Accounts of Chemical Research, 2017. **50**(5): p. 1134-1142.
103. Chalbaud, C., et al., *Interfacial tension measurements and wettability evaluation for geological CO<sub>2</sub> storage*. Advances in Water Resources, 2009. **32**(1): p. 98-109.
104. Yang, D., Y. Gu, and P. Tontiwachwuthikul, *Wettability determination of the crude oil- reservoir brine- reservoir rock system with dissolution of CO<sub>2</sub> at high pressures and elevated temperatures*. Energy & Fuels, 2008. **22**(4): p. 2362-2371.
105. Roshan, H., et al., *On wettability of shale rocks*. Journal of colloid and interface science, 2016. **475**: p. 104-111.
106. Cassie, A. and S. Baxter, *Wettability of porous surfaces*. Transactions of the Faraday Society, 1944. **40**: p. 546-551.
107. Wenzel, R.N., *Resistance of solid surfaces to wetting by water*. Industrial & Engineering Chemistry, 1936. **28**(8): p. 988-994.
108. Al-Yaseri, A.Z., et al., *Receding and advancing (CO<sub>2</sub>+ brine+ quartz) contact angles as a function of pressure, temperature, surface roughness, salt type and salinity*. The Journal of Chemical Thermodynamics, 2016. **93**: p. 416-423.
109. Cassie, A., *Contact angles*. Discussions of the Faraday Society, 1948. **3**: p. 11-16.
110. Tamai, Y. and K. Aratani, *Experimental study of the relation between contact angle and surface roughness*. The Journal of Physical Chemistry, 1972. **76**(22): p. 3267-3271.
111. Bartell, F. and J. Shepard, *Surface roughness as related to hysteresis of contact angles. II. The systems paraffin-3 molar calcium chloride solution-air and paraffin-glycerol-air*. The Journal of Physical Chemistry, 1953. **57**(4): p. 455-458.
112. Hong, K.T., H. Imadojemu, and R. Webb, *Effects of oxidation and surface roughness on contact angle*. Experimental Thermal and Fluid Science, 1994. **8**(4): p. 279-285.
113. Drelich, J. and J.D. Miller, *The effect of solid surface heterogeneity and roughness on the contact angle/drop (bubble) size relationship*. Journal of Colloid and Interface Science, 1994. **164**(1): p. 252-259.
114. Love, J.C., et al., *Self-assembled monolayers of thiolates on metals as a form of nanotechnology*. Chemical reviews, 2005. **105**(4): p. 1103-1170.
115. Iglauer, S., et al., *Contamination of silica surfaces: impact on water-CO<sub>2</sub>-quartz and glass contact angle measurements*. International Journal of Greenhouse Gas Control, 2014. **22**: p. 325-328.

116. Sarmadivaleh, M., A.Z. Al-Yaseri, and S. Iglauer, *Influence of temperature and pressure on quartz–water–CO<sub>2</sub> contact angle and CO<sub>2</sub>–water interfacial tension*. Journal of colloid and interface science, 2015. **441**: p. 59-64.
117. Bikkina, P.K., *Int. J. Greenhouse Gas Control* 2012. **7**: p. 263-264.
118. El-Maghraby, R., et al., *A fast method to equilibrate carbon dioxide with brine at high pressure and elevated temperature including solubility measurements*. The Journal of Supercritical Fluids, 2012. **62**: p. 55-59.
119. Al-Yaseri, A., et al., *N<sub>2</sub>+ CO<sub>2</sub>+ NaCl brine interfacial tensions and contact angles on quartz at CO<sub>2</sub> storage site conditions in the Gippsland basin, Victoria/Australia*. Journal of Petroleum Science and Engineering, 2015. **129**: p. 58-62.
120. G. Macdougall, C.O., *Proc. Soc. Lond*, 1942. **180**: p. 152-174.
121. Lander, L.M., et al., *A systematic comparison of contact angle methods*. Langmuir, 1993. **9**(8): p. 2237-2239.
122. Extrand, C.W. and Y. Kumagai, *Liquid drops on an inclined plane: the relation between contact angles, drop shape, and retentive force*. Journal of Colloid and Interface Science, 1995. **170**(2): p. 515-521.
123. Al-Yaseri, A.Z., et al., *Dependence of quartz wettability on fluid density*. Geophysical Research Letters, 2016. **43**(8): p. 3771-3776.
124. Grate, J.W., et al., *Correlation of oil–water and air–water contact angles of diverse silanized surfaces and relationship to fluid interfacial tensions*. Langmuir, 2012. **28**(18): p. 7182-7188.
125. Iglauer, S., M. Mathew, and F. Bresme, *Molecular dynamics computations of brine–CO<sub>2</sub> interfacial tensions and brine–CO<sub>2</sub>–quartz contact angles and their effects on structural and residual trapping mechanisms in carbon geo-sequestration*. Journal of colloid and interface science, 2012. **386**(1): p. 405-414.
126. Saraji, S., et al., *Wettability of supercritical carbon dioxide/water/quartz systems: Simultaneous measurement of contact angle and interfacial tension at reservoir conditions*. Langmuir, 2013. **29**(23): p. 6856-6866.
127. Farokhpoor, R., et al., *Wettability behaviour of CO<sub>2</sub> at storage conditions*. International Journal of Greenhouse Gas Control, 2013. **12**: p. 18-25.
128. Espinoza, D.N. and J.C. Santamarina, *Water-CO<sub>2</sub>-mineral systems: Interfacial tension, contact angle, and diffusion—Implications to CO<sub>2</sub> geological storage*. Water resources research, 2010. **46**(7).
129. Claypool, G.E. and P.R. Reed, *Thermal-analysis technique for source-rock evaluation: quantitative estimate of organic richness and effects of lithologic variation: GEOLOGIC NOTES*. AAPG Bulletin, 1976. **60**(4): p. 608-612.
130. Arif, M., et al., *Influence of shale-total organic content on CO<sub>2</sub> geo-storage potential*. Geophysical Research Letters, 2017. **44**(17): p. 8769-8775.
131. Verheijen, H. and M. Prins, *Reversible electrowetting and trapping of charge: model and experiments*. Langmuir, 1999. **15**(20): p. 6616-6620.
132. Kaveh, N.S., et al., *Wettability evaluation of a CO<sub>2</sub>/water/bentheimer sandstone system: Contact angle, dissolution, and bubble size*. Energy & Fuels, 2014. **28**(6): p. 4002-4020.
133. Al-Yaseri, A.Z., et al., *Effect of the Temperature on CO<sub>2</sub>/Brine/Dolomite Wettability: Hydrophilic versus Hydrophobic Surfaces*. Energy & Fuels, 2017. **31**(6): p. 6329-6333.

134. Milne, A. and A. Amirfazli, *The Cassie equation: How it is meant to be used*. Advances in colloid and interface science, 2012. **170**(1): p. 48-55.
135. Petroleum, B., *BP statistical review of world energy*. 2017, London: British Petroleum.
136. Boris Ertl, C.D., David Coyle, Isa Mohammed, Stanley Huang, *New LNG Receiving Terminal Concepts*. Conference Proceeding: World Petroleum Congress. Block 3, Forum 14 paper, 2006.
137. Shah, K., Wong, J., Minton, B., *Consideration for ambient air based technologies for LNG regasification terminals*. AIChE Spring meeting, 2008.
138. Angtuaco, D.P.J.M.D.R.J., *LNG VAPORIZER SELECTION BASED ON SITE AMBIENT CONDITIONS*, in *17th International Conference on LNG*. 2013: Houston.
139. Sunder, S., M. AHUJA, and J. GAUTIER. *LNG Receiving Terminal at Dahej, Gujarat, India*. in *13th Proceedings of the Thirteenth Conference & Exhibition on Liquefied Natural Gas*. 2001.
140. CHIV, *Estimated condensation rate for ambient air vaporization*. CH IV International report, 2007.
141. CHIV, *Oregon LNG import terminal vaporizer alternatives study*. CH IV international report, 2007.
142. CHIV, *Oregon LNG Terminal Resource 13-Engineering and Design Material*. 2008.
143. Corpus Christi Liquefaction, L., *Corpus Christi Liquefaction Project\_Draft Resource Report 1-General Project Description*. 2012.
144. Jeong, H., et al., *Experimental study on the characteristics of longitudinal fin air-heating vaporizers in different seasons*. Journal of Mechanical Science and Technology, 2008. **22**(5): p. 981-990.
145. Jeong, H., et al., *Natural convection heat transfer estimation from a longitudinally finned vertical pipe using CFD*. Journal of Mechanical Science and Technology, 2009. **23**(6): p. 1517-1527.
146. Jeong, H.-M., et al., *Optimum design of vaporizer fin with Liquefied Natural Gas by numerical analysis*. Journal of Mechanical Science and Technology, 2006. **20**(4): p. 545-553.
147. Liu, S., W. Jiao, and H. Wang, *Three-dimensional numerical analysis of the coupled heat transfer performance of LNG ambient air vaporizer*. Renewable Energy, 2016. **87, Part 3**: p. 1105-1112.
148. Pandey, A.S., et al. *Performance testing and analysis of vertical ambient air vaporizers*. in *IOP Conference Series: Materials Science and Engineering*. 2017. IOP Publishing.
149. Liu, Z., Y. Dong, and Y. Li, *An experimental study of frost formation on cryogenic surfaces under natural convection conditions*. International Journal of Heat and Mass Transfer, 2016. **97**: p. 569-577.
150. Barron, R.F. and L. Han, *Heat and mass transfer to a cryosurface in free convection*. Journal of Heat Transfer, 1965. **87**(4): p. 499-506.
151. Kim, K.-H., et al., *Analysis of heat transfer and frost layer formation on a cryogenic tank wall exposed to the humid atmospheric air*. Applied Thermal Engineering, 2009. **29**(10): p. 2072-2079.
152. Faka, S.A., *Intermittent De-Icing During Continuous Regasification of a Cryogenic Fluid Using Ambient Air*. 2007, Google Patents.
153. Faka, S.A., *Mechanical Defrosting During Continuous Regasification of a Cryogenic Fluid Using Ambient Air*. 2009, Google Patents.
154. Jhee, S., K.-S. Lee, and W.-S. Kim, *Effect of surface treatments on the frosting/defrosting behavior of a fin-tube heat exchanger*. International Journal of Refrigeration, 2002. **25**(8): p. 1047-1053.



155. Bergman, T.L. and F.P. Incropera, *Fundamentals of heat and mass transfer*. 2011: John Wiley & Sons.
156. Bureau of Meteorology. <http://www.bom.gov.au/climate/data/>.

## Appendix 1 :Statement of Contributions of Others

### Statement of Contributions of Joint Authorship

Alnili, F. and Barifcani, A., 2018. Efficient separation scheme for binary mixture of CO<sub>2</sub> and H<sub>2</sub>S using aromatic components. *Separation Science and Technology*, 53(2), pp.312-319.

### **Statement of Contribution of Others for “Efficient separation scheme for binary mixture of CO<sub>2</sub> and H<sub>2</sub>S using aromatic components”.**

30<sup>th</sup> June 2020

**Firas Alnili** (PhD Candidate)

Writing and compilation of manuscript, established methodology, data analysis, preparation of tables and figures.

**Ahmed Barifcani:**  
(Main supervisor)

Supervised and assisted with manuscript compilation, editing and co-author of manuscript.

Chapter Three of this thesis is an exact copy of the journal paper referred to above.

Statement of Contributions of joint Authorship

Alnili, F., James, P. and Barifcani, A., 2019. Natural gas sweetening using low temperature distillation: simulation and configuration. *Separation Science and Technology*, pp.1-8.

**Statement of Contribution of Others for " Natural gas sweetening using low temperature distillation: simulation and configuration"**

30<sup>th</sup> June 2020

**Firas Alnili** (PhD Candidate)

Writing and compilation of manuscript, established methodology, data analysis, preparation of tables and figures.

Paul James (Co-Author)

Established methodology, data analysis, Editing and Co-Author of manuscript.

**Ahmed Barifcani:** (Main supervisor)

Supervised and assisted with manuscript compilation, editing and co-author of manuscript.

Chapter Four of this thesis is an exact copy of the journal paper referred to above.

Statement of Contributions of joint Authorship.

Alnili, F. and Barifcani, A., 2018. Simulation study of sweetening and dehydration of natural gas stream using MEG solution. *The Canadian Journal of Chemical Engineering*, 96(9), pp.2000-2006.

**Statement of Contribution of Others for "Simulation study of sweetening and dehydration of natural gas stream using MEG solution"**

30<sup>th</sup> June 2020

**Firas Alnili** (PhD Candidate)

Writing and compilation of manuscript, established methodology, data analysis, preparation of tables and figures.

**Ahmed Barifcani:**

(Main supervisor)

Supervised and assisted with manuscript compilation, editing and co-author of manuscript.

Chapter Five of this thesis is an exact copy of the journal paper referred to above.

Statement of Contributions of Joint Authorship.

Alnili, F., Al-Yaseri, A., Roshan, H., Rahman, T., Verall, M., Lebedev, M., Sarmadivaleh, M., Iglauer,

S. and Barifcani, A., 2018. Carbon dioxide/brine wettability of porous sandstone versus solid quartz: An experimental and theoretical investigation. *Journal of colloid and interface science*, 524, pp.188- 194.

**Statement of Contribution of Others for". Carbon dioxide/brine wettability of porous sandstone versus solid quartz: An experimental and theoretical investigation"**

*Chapter Six of this thesis is an exact copy of the journal paper referred to above.*

30<sup>th</sup> June 2020

Firas Alnili

(PhD Candidate)

Writing and compilation of manuscript, established methodology, data analysis, Equation Derivation, preparation of tables and figures.


Ahmed Al-Yaseri

Hamid Roshanm

Rahman T.

Lebedev M.

Sarmadivaleh, M.



(Co-author)

Established methodology, AFM and SEM imaging, Equation Derivation, Data Analysis and Co-author of manuscript.

Stefan Iglauer (Co-Supervisor)

Supervised and assisted with manuscript compilation, editing and co-author of manuscript

Ahmed Barifcani: (Main supervisor)

Supervised and assisted with manuscript compilation, editing and co-author of manuscript.

## Appendix 2 :Equipment used in LNG vaporization (Chapter 7)

### Liquid Nitrogen Dewar and phase separator

Liquid Nitrogen (LN<sub>2</sub>) was used as an alternative for LNG for safety purposes. In this project, LN<sub>2</sub> Dewar with 240 L capacity and 16 bar pressure was used to supply LN<sub>2</sub> to AAV as shown in **Error! Reference source not found.** LN<sub>2</sub> was supplied to the inlet of the finned tube from Dewar where the Dewar pressure was maintained by a pressure regulating device. Because of the temperature difference between LN<sub>2</sub> and ambient temperature, and low nitrogen flowrate, LN<sub>2</sub> may be vaporized in the process line before reaching the AAV inlet which may not be able to provide enough cooling load for AAV operation. Thus, a double-jacketed and super-insulated vacuum line combined with a phase separator was used as described in Fig 1. The phase separator can be described as a shell and tube exchanger, connecting the LN<sub>2</sub> Dewar to the AAV inlet in order to ensure the nitrogen supply in liquid phase. . The process line of LN<sub>2</sub> is shut off by switching off the globe valve in order to fill up the cooling jacket with LN<sub>2</sub> bath as shown in Fig 2. The phase separator was designed by BOC team and manufactured in UK.

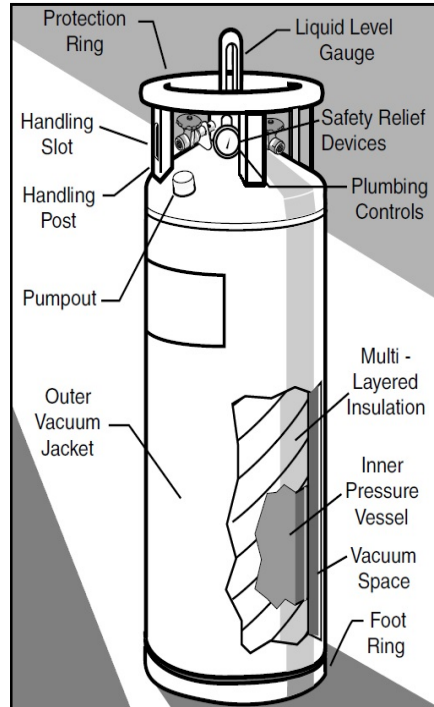


Figure 1. Liquid Nitrogen Dewar

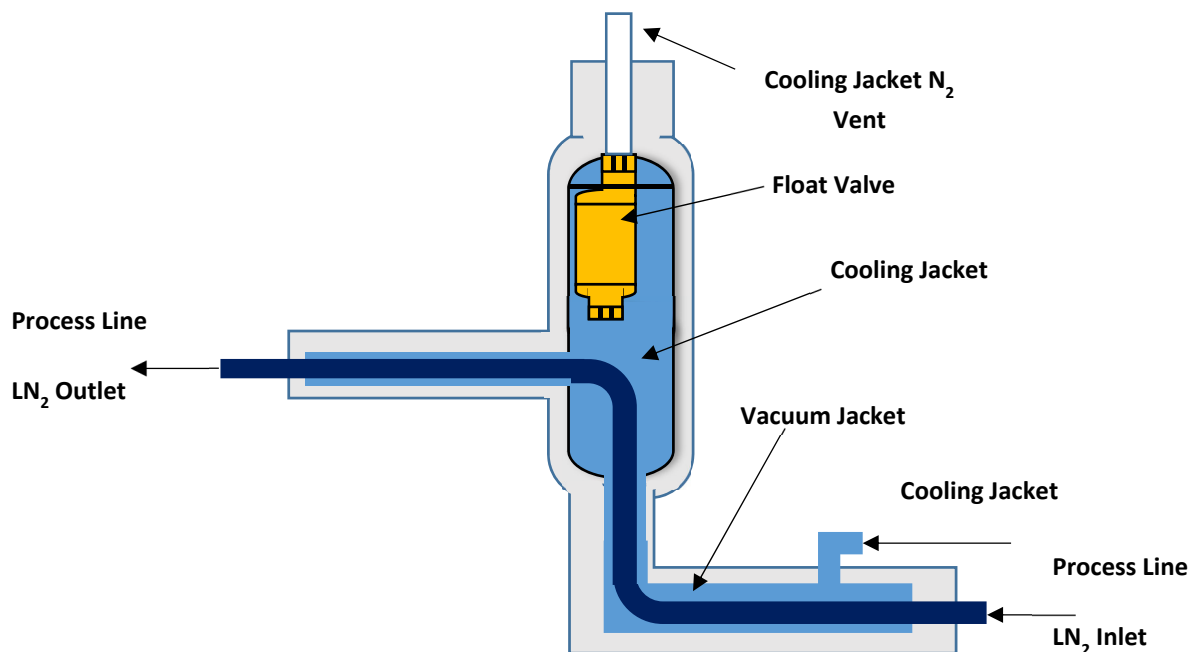
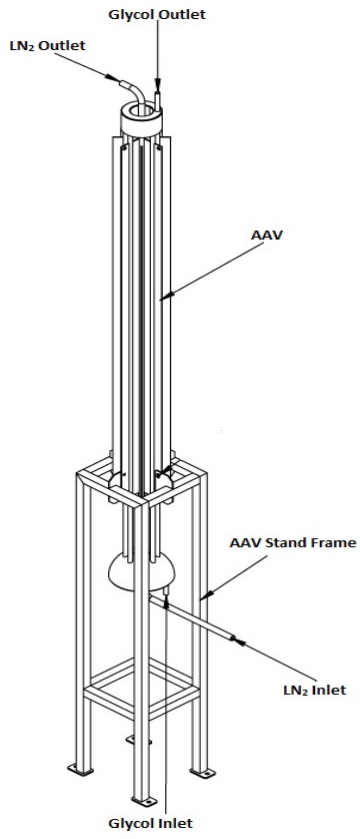


Fig. 2. Phase Separator

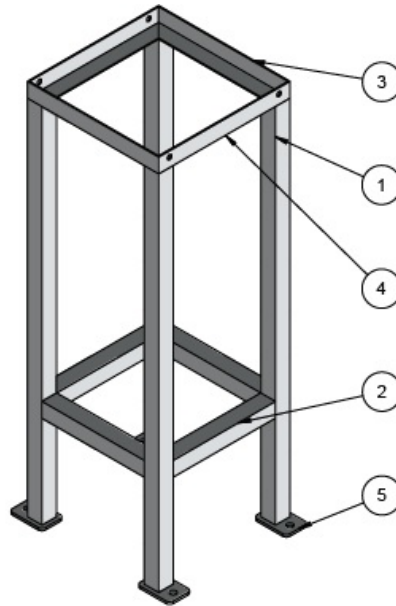
### **Ambient Air Vaporizer (AAV)**

An innovative ambient air vaporizer has been designed in this project based on Woodside Patent (The AAV is basically similar to the conventional AAV which comprises a central single finned-tube (2m height, tube diameter 25mm, 8 fins). An intrusive defrosting concept was involved by applying a minor channel (19mm OD) to allow hot fluid (defrosting stream) to flow through (shown in Fig. 3). The reason behind choosing a tubular channels for defrosting instead of rectangular channels (as described in the Patent [9] is to hold high pressure as the rectangular channel has a weak points for high pressure flow particularly at the edges. In addition, the vaporizer was mounted on a square base frame (1m height) which was bolted on the ground as shown in Fig. 3. The vaporizer also consists a dome-shaped MEG distributor at AAV bottom and a ring-shaped MEG collector at AAV top.





AAV



AAV Stand

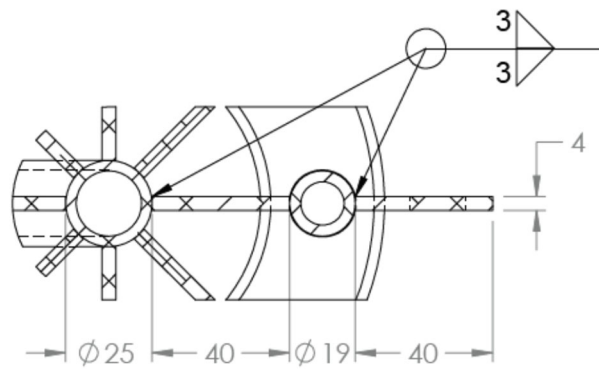
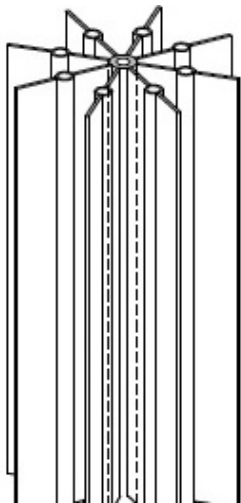


Fig. 3. Fin design

This AAV is manufactured by QSM Fabrication Company. The vaporizer has been tested to hold high pressure up to 24 bar (operating pressure 10 bar) by QSM in present of our team before using it for operation.

### **MEG Heating System**

In the process, frost can be formed due to condensing of water vapour in the air on the fins surface. A solution of MEG and water is used as a hot fluid to perform defrosting to realise continuous evaporation without shutting off LN<sub>2</sub> flow. However, MEG is only switched on when heat transfer is reduced up to a certain point (e.g. nitrogen outflow temperature is lower than -150°C). In order to maintain the MEG temperature as 50°C, an insulated storage tank (FV-300, capacity 150L) with an integrated heater (E-301, power 970W) is applied. A mixture of MEG (60 % by volume) and water at 50° C is pumped by a gear pump (P-301) through Line 9 to the defrosting channels. MEG to water percentage was selected based on the low freezing point of this mixture ( $\approx -52.8^{\circ}\text{C}$ ) to prevent MEG freezing during the defrosting process. The flow rate and temperature of MEG solution were designed as 200~600L/hr and 50°C, respectively. While flowing through the ducts in fins, MEG heats LN<sub>2</sub> and frost simultaneously. Once the system is completely defrosted, the glycol flow is stopped and return to the vessel through line 10 by gravity or nitrogen pushing provided by nitrogen cylinder (NC-301) as illustrated in Fig. 4. All parts need to be suitable for outside weather conditions.

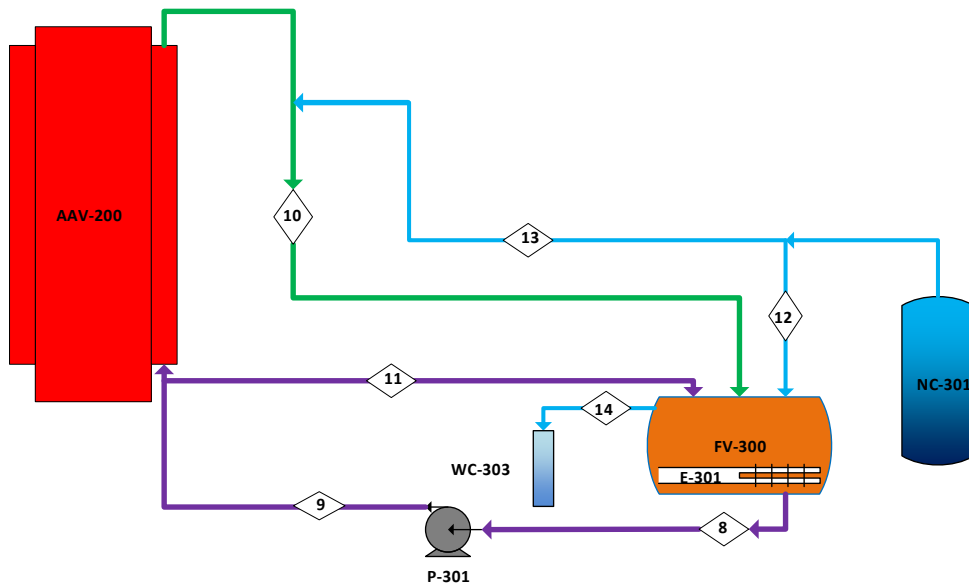


Fig. 4. MEG heating System

### **Nitrogen blanketing**

Nitrogen blanketing is required for the MEG storage drum to avoid any interaction with air and thus cause MEG degradation. Nitrogen Cylinder, NC-301 is used to supply nitrogen for the purpose through line 12 as shown in Fig. 4. Another use for Nitrogen cylinder is to purge glycol solution out of the AAV through line 13 at the end of defrosting cycle. The pressurised nitrogen is contained in an open water column, WC-303 connected at one end of MEG storage drum.

### **Air Blower and Air Duct**

As mentioned above, ambient air is supplied through an air duct to the top of AAV by an air blower (AF-202), shown in Fig. 5, which could supply variable air flow rate. Air filter is also attached to the back of the air blower (sanction part) to avoid entry of any big particles which might damage the air blower. The air blower was covered by an enclosure base plate to protect the air blower from weather conditions.

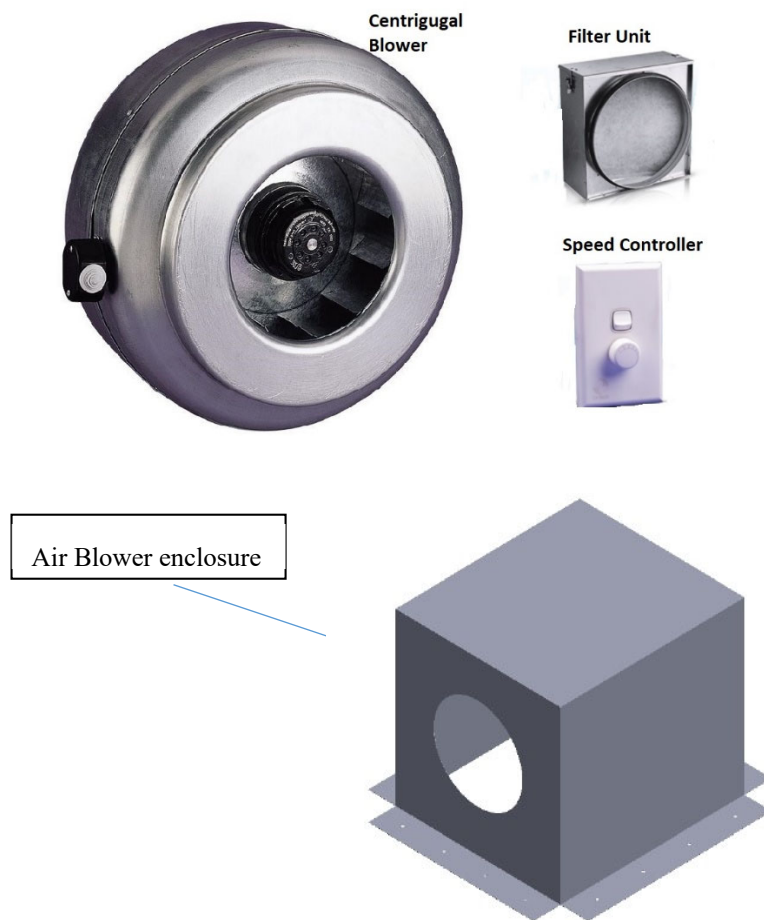


Fig. 5 Centrifugal Air Blower

### Equipment data and control system

- **Data Logger**

A data logger has been used to record all the measurements in the system over the time, such as temperatures, pressures, relative humidity, flow rates and more as described in **Error! Reference source not found.** 6 Data loggers could continuously monitor conditions remotely without having people to be on site. Environmental consultants, building managers, energy auditors, research scientists, and many more professionals all rely on data loggers because of the low cost, easy use and reliability. All instruments in this project such as thermocouples, sensors and flowmeters was connected to the Data Logger.



Fig. 6. Data Logger (DT80S2)

- **Thermocouples and relative humidity sensors**

Series of thermocouples and humidity sensors have been located at different heights in the AAV system (shown in Fig. 7) to record the temperature and humidity with time. The relative Humidity sensors with the type of HMP110 have been used to measure the relative humidity of the heating air. This type of sensors are able to measure the relative humidity between 0-100 % and the temperature between -40 to 80 °C. Some other thermocouples and humidity sensors are located at different places outside the vaporizer, for instance, the outlet of liquid nitrogen Dewar, inlet and outlet the phase separator, the outlet of the vaporizer.

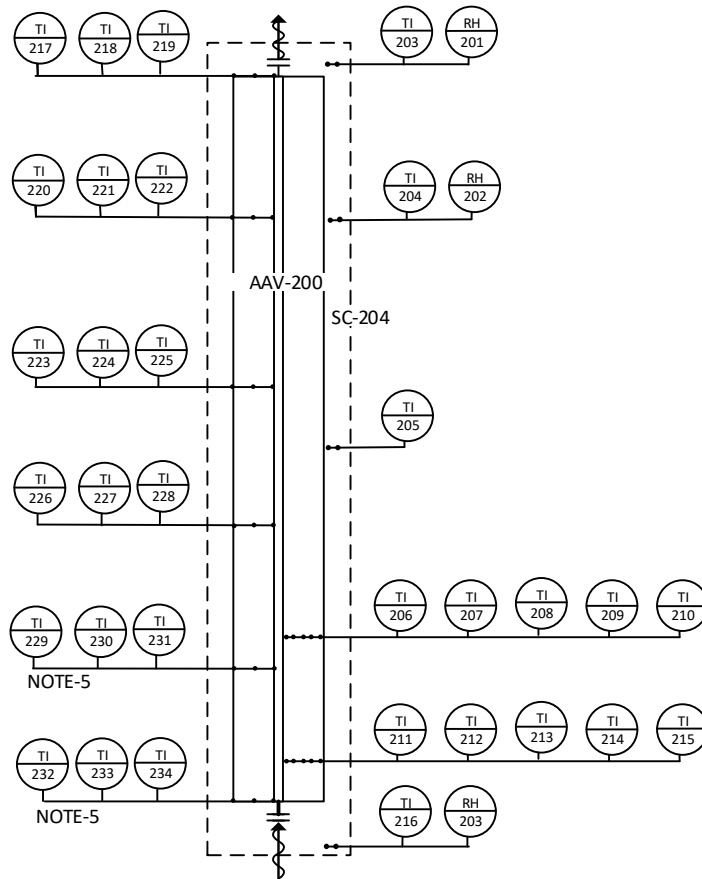


Fig. 7. Thermocouples and Humidity sensors location

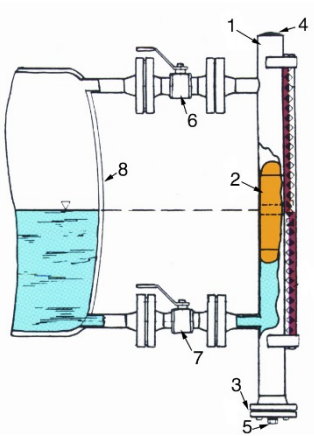
- **Flowmeters and Other instruments**

For the liquid and gas flow rate, flow meters have been used for this purpose. MEG flow meter has been recorded using FMG-Oval Gear Pulse Flowmeter size (1/2") which can read the flow rate between 15 L/hr - 750 L/hr in temperature range 0 °C to 80 °C. In order to measure the liquid nitrogen flow rate that enters the vaporizer, ‘Azbil In-Line Multi parameter Vortex Volumetric Mass Flow Meter’ has been used. This flow meter is able to measure the flow rate between 0.5 m<sup>3</sup>/hr – 10 m<sup>3</sup>/hr and comes with a digital display and works with a temperature range 80 °C to -200 °C. In addition, other instruments used in this project such as MEG level indicator and differential pressure transmitter. For MEG level in MEG vessel, Magnetic Rotor Level Indicator was used to indicate the MEG level. The differential pressure transmitter (Magnesense MS2) is used to measure the air flow rate in the air duct. Fig. 8 shows all flowmeters and level indicator instruments.



MEG Flowmeter

Nitrogen Flowmeter



MEG level indicator



Differential Pressure Transmitter

Fig. 8. Flowmeters and level indicator

## **Insulation**

Insulating is the important procedure in such process in order to minimize the heat leak and maintain the temperature at a certain point of different fluids and also prevent the probability of any injury for the site workers as the system works at very low temperature (-170 °C). Different insulation materials have been used to insulate different parts of the system. MEG vessel was insulated to maintain the temperature inside the vessel at 50 °C, Earthwool insulation (Earthwool R-4.0 195 x 430mm 8.98m<sup>2</sup> Ceiling insulation batts, was used for this purpose and the insulation material then was wrapped using Aluminium tape to hold the insulation material around the vessel as. All tubes in the system have also been insulated using different types of insulation material. Ormonoid 10 x 75mm x 6m Abelflex Expansion Joint Filler was used to insulate the MEG system pipelines. The most important part of insulation process is the cold lines. All tubes in the cold line should be insulated properly by using efficient insulation material as it was a challenge to maintain Nitrogen entering the vaporizer in a liquid phase due to the huge temperature difference between ambient air and liquid nitrogen. Cryogel Z insulation material was used to insulate the cold section of this project as shown in Fig. 9. Cold line insulation was selected based on the a unique specification such as wide temperature range ( -265°C – 125°C), extremely low thermal conductivity (55 W/m at 23°C), high flexibility, compression resistance, and easily use[12]. Many LNG facilities has turned to Cryogel Z for the ability of solving the difficult insulation problems[12].





Fig. 9. Insulation Material

### **Safety Precaution**

Due to the high operating pressure (up to 15 bar) and cryogenic temperature (-170 C), safety precaution should be taken in consideration. Many safety procedures were applied in this plant. Firstly, a back pressure control valve was installed to control the pressure in the system at a certain pressure (operating pressure). Secondly, an auxiliary heater (E-202) was installed at the AAV outlet to heat up the outflow nitrogen in order to prevent the instruments such as back pressure control valve and LN2 flow meter from any possible damage due to low temperature. In addition, nitrogen outlet stream is released in a flush vessel (FV-201) at atmospheric pressure in case of existing nitrogen in a liquid phase and then passing through another heater (E-201) installed at the top of vessel (FV-201) to heat the outlet stream up to 5 C and the heated nitrogen is then released to the atmosphere. Several safety valves was installed in the system to prevent any unexpected increase in pressure, as shown in Fig. 10.

For the operators when operating liquid nitrogen, cryogenic gloves, face shield, lab coat and enclosed shoes (Fig. 11) are required to prevent frost bite and cold burn.

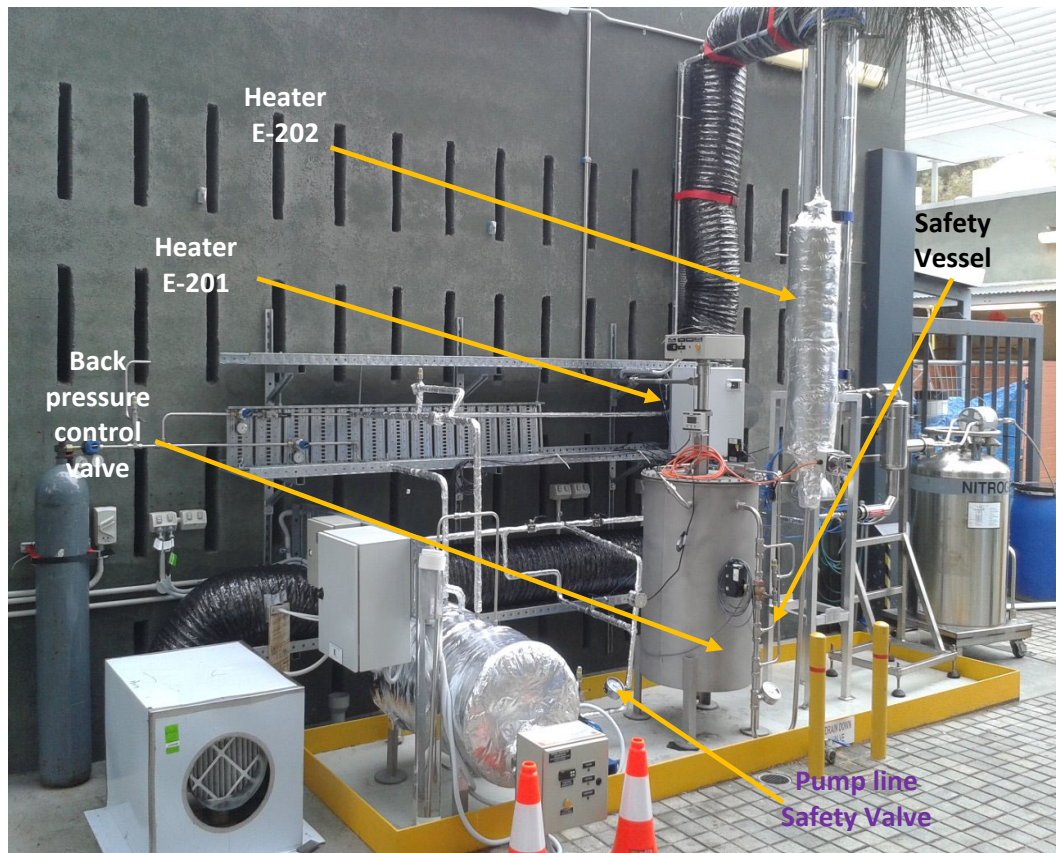


Fig. 10. Safety heaters and Back pressure control valve.



Fig. 11. Personal Protective Equipment (PPE)